DESIGN AND FABRICATION OF LANTHANUM-DOPED Sn-Ag-Cu LEAD-FREE SOLDER FOR THE NEXT GENERATION OF MICROELECTRONICS APPLICATIONS IN SEVERE ENVIRONMENT

A Dissertation
Presented to
The Academic Faculty

by

Muhammad Sadiq

In Partial Fulfillment
of the Requirements for the Degree
Doctor of Philosophy in the
George W. Woodruff School of Mechanical Engineering

Georgia Institute of Technology
August 2012

DESIGN AND FABRICATION OF LANTHANUM-DOPED Sn-Ag-Cu LEAD-FREE SOLDER FOR THE NEXT GENERATION OF MICROELECTRONICS APPLICATIONS IN SEVERE ENVIRONMENT

Approved by:

Dr. Mohammed Cherkaoui, Advisor
School of Mechanical Engineering
Georgia Institute of Technology

Dr. Abdallah Ougazzaden
School of Electrical and Computer Engineering
Georgia Institute of Technology

Dr. Richard Neu
School of Mechanical Engineering
Georgia Institute of Technology

Dr. Esteban Busso
Center for Materials
School of Mines, Paris

Dr. Ting Zhu
School of Mechanical Engineering
Georgia Institute of Technology

Date Approved: May 18, 2012

Dedicated to my Parents

ACKNOWLEDGEMENTS

First of all, I would like to thank Dr. Mohammed Cherkaoui for providing me an opportunity to work under his supervision. His support, guidance and motivation have always been a great inspiration during the entire work.

I would like to thank Dr. Abdallah Ougazzaden, Dr. Richard Neu, Dr. Ting Zhu and Dr. Esteban Busso who accepted my request to be the part of my PhD reading committee. I strongly appreciate their suggestions and remarks.

I would like to thank Stephanie Blanc, Suriyakan Kleitz and the whole techno-group of Schlumberger for providing me an opportunity to work on such a challenging project.

I am extremely thankful to Dr. Raphael Pesci for all his contributions, support and motivation during the entire experimental work. His "friendly" attitude gave me the real motivation to work in a friendly environment.

I am thankful to Dr. El Mostafa Daya and Dr. Jean-Marc Raulot for their enriching discussions and valuable remarks.

I would like to thank Jean-Sebastien Lecomte for his help in Nanoindentation, Claude Guyomard for the die design, Olivier Naegelen for the sample casting and Marc Wary for the polishing and etching processes. I am also thankful to Abderrahim Nachit and Ammar for their help in electrical characterization.

I am thankful to Dr. Pei Min for his help in coarsening models and David Macel for his support in Wettability testing.

My experience at Georgia Tech was made more pleasant by my colleagues Wei, David, Mathieu, Bhasker, Malek, Liaqat, Sajid, Rafiq, Armaghan, Aamer, Jawad, Khuda Bux, Mohsin and Fahd. I would like to thank all of them.

I would like to offer Special thanks to my brother Muhammad Arif for all his help and support in editing and organizing my thesis.

I would like to thank the whole team of Georgia Institute of Technology who helped me in everything to make this period more interesting and enjoyable.

TABLE OF CONTENTS

LIST OF TABLES

LIST OF FIGURES

SUMMARY

Tin-Lead solder (Sn-Pb) has long been used in the Electronics industry. But, due to its toxic nature and environmental effects, certain restrictions are made on its use by the European Rehabilitation of Hazardous Substances (RoHS) directive, and therefore, many researchers are looking to replace it. The urgent need for removing lead from solder alloys led to the very fast introduction of lead-free solder alloys without a deep knowledge of their behavior. Therefore, an extensive knowledge and understanding of the mechanical behavior of the emerging generation of lead-free solders is required to satisfy the demands of structural reliability.

Sn-Ag-Cu (SAC) solders are widely used as lead-free replacements but their coarse microstructure and formation of hard and brittle Inter-Metallic Compounds (IMCs) have limited their use in high temperature applications. Many additives are studied to refine the microstructure and improve the mechanical properties of SAC solders including iron (Fe), bismuth (Bi), antimony (Sb) and indium (In) etc. Whereas many researchers studied the impact of novel rare earth (RE) elements like lanthanum (La), cerium (Ce) and lutetium (Lu) on SAC solders. These RE elements are known as “vitamins of metals” because of their special surface active properties. They reduce the surface free energy, refine the grain size and improve the mechanical properties of many lead free solder alloys like Sn-Ag, Sn-Cu and SAC but still a systematic study is required to explore the special effects of “La” on the eutectic SAC alloys.

The objective of this PhD thesis is to extend the current knowledge about lead free solders of SAC alloys towards lanthanum doping with varying environmental conditions implemented during service. This thesis is divided into six main parts.

PART-I:

This part includes the basic ideas and definitions of soldering techniques and solders alloys. Around ten alloys systems are presented here. Different soldering techniques like wave soldering, reflow soldering and liquid phase bonding etc. are described in detail. Previous studies from the literature are critically analyzed in terms of high temperatures applications of Sn-Ag, Sn-Cu and SAC alloys. RE elements are presented here as potential additives to improve the currently available tertiary SAC lead-free solders.

PART-II:

Understand the microstructure evolution of SAC and SAC-La alloys with Inter-Metallic Compounds (IMCs) coarsening and grain size (growth) due to high temperature aging. Scanning Electron Microscopy with Energy Dispersive Spectroscopy (EDS) mapping and Optical Microscopy (OM) with cross polarized light is implemented to follow it. A quantitative measure is provided for this work in terms of IMCs particles size, volume fraction, interparticle spacing, grain size etc. Isothermal aging at 150°C and 200°C is used and different aging times from 10 hours up to 200 hours are selected. Similar quantitative data for the grain size during thermal aging is presented for SAC and SAC-La doped alloys.

PART-III:

A good set of high mechanical properties including yield stress, tensile strength and creep behavior is expected which is the response of fine microstructure as discussed in Part-II. Controlled coarsening of IMCs during thermal aging is expected to affect the mechanical behavior of the solder joints during service. In this part, mechanical properties like yield stress, tensile strength and ductility, for as cast and thermally aged specimens, at low strain rate are evaluated for

different environmental conditions varying from -60°C to 140°C. Quasi-static tensile tests at different strain rates are carried out with an MTS tensile machine equipped with a 5kN load cell.

PART-IV:

During service, these solder joints have to withstand at elevated temperatures for longer period of times. In this situation, creep resistance becomes an important mechanical property of SAC alloys, which is strongly affected by the growth of IMCs due to thermal coarsening. 3 different temperatures of 40°C, 80°C and 120°C were selected for the entire creep behavior and the stress range varies from 10Mpa up to 16Mpa. All 3 zones, primary, secondary and tertiary creep curves were identified and the samples were loaded till rupture.

Therefore, in this section, the creep behavior of these alloys is explored to further understand the impact of lanthanum doping. Alloys with the best-fit to requirements with refined microstructure, improved mechanical properties and better creep life are suggested as the best additives of lanthanum doped SAC compositions. Dorn and back-stress creep models are used here.

PART-V:

Nanoindentation is implemented to explore the Young's modulus and hardness of individual phases for soft tin matrix, eutectic zone, Ag_3Sn and Cu_6Sn_5 IMCs. Visual matrix technique is implemented to follow the predefined indentation locations under the OM. AFM images are used to confirm the indenter testing. Pile-up effects on the soft matrix are incorporated into both Young's modulus and hardness measurements. A much better agreement is found with the previous studies.

High temperature nanoindentation was followed to explore the thermal properties like activation energy and also determine the variation of Young's modulus and hardness as function of temperature. Creep behavior was also investigated using nanoindentation by allowing dwell time during peak loadings.

PART-VI:

Wettability or solderability is an important parameter in characterizing the solder alloys. Most of the solder alloys have good mechanical properties when tested in bulk but their wetting behavior when soldered on boards is not good. These solder compositions are not highly recommended for the solder joints reliability. Therefore, after completing sufficient study over the bulk SAC and SAC-La doped alloys; an extensive experimental work was performed to explore the wetting behavior of all solder alloys compositions. Surface tensions, wetting forces and contact angles measurements were made at 250°C and 260°C.

Wetting balance test was used during this part and significant improvements were made in the contact angles and wetting forces due to lanthanum doping.

CHAPTER 1

INTRODUCTION

1.1 Motivation and Problem Identification

Tin-lead (SnPb) solders for metal interconnections were first used about 2000 years ago. At present, the use of solders has become indispensable for the interconnection and packaging of virtually all electronic devices and circuits. Pb-bearing solders and especially the eutectic or near-eutectic SnPb alloys have been used extensively in the assembly of modern electronic circuits. Research into the science and engineering of soldering has taken a major change in direction ever since the mandatory requirements for Pb-free imports were introduced by countries such as Japan and those in the European Union. This is because Pb and Pb-containing compounds, as cited by the Environmental Protection Agency (EPA) of the US, is one of the top 17 chemicals posing the greatest threat to human beings and the environment [M. H. Chen 2003]. In the electronics industry, the Pb generated by the disposal of electronic assemblies is considered as hazardous to the environment.

The new lead-free solders are mostly Sn-containing binary and ternary alloys [Yu et al. 2004]. Due to better thermo-mechanical properties, SAC alloys are considered as the best choice [Martin 2006] and therefore covers a big market place as compared to its other competitive alloys and is shown in Figure 1.1 [Soldertec Report, European Lead-Free Roadmap, 2002]. But,

because of their coarse microstructure, iron (Fe), cobalt (Co) and nickel (Ni) have been used as refining elements and their effect on the microstructure have been investigated [Anderson et al. 2001]. Many combinations like indium (In), antimony (Sb), bismuth (Bi), copper (Cu) and silver (Ag) are also used as alloying elements [Yu et al. 2004].

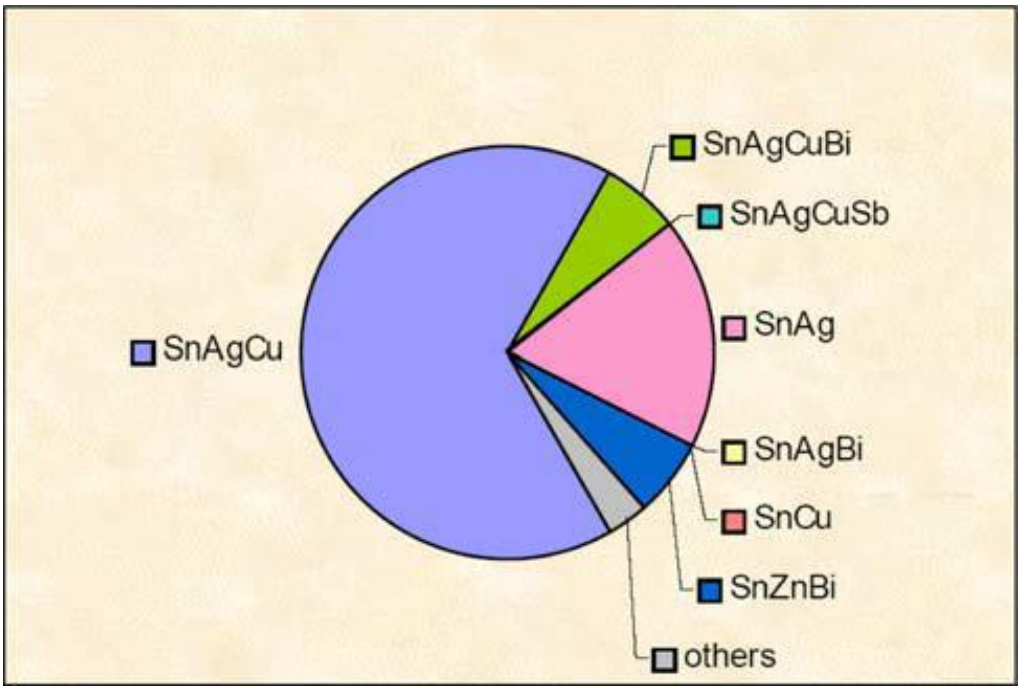

Figure 1.1: The market share of different lead-free solders

In electronic assemblies, solder joints serve as both electronic connection and mechanical support for components and substrates. They play crucial roles in the reliability of joint assemblies in electronic packaging because they provide electrical, thermal and mechanical continuity in electronic assemblies. During service, they are subjected to many thermo-mechanical stresses and hence stand as one of the weakest point in assembly and usually determine the lifetime of the whole component, the reliability of which depends on packaging specificities and application environments. This has been investigated that, in high reliability applications, failure mechanisms leading to the damage of solder joints are mainly thermo

mechanical phenomena. Fatigue, thermal diffusion and thermal coefficient mismatch also can reduce solder strength.

With the development of lead-free solders to be used in the electronic packaging industry, there are several challenges to be met. The sustained trend towards miniaturization and functional density enhancement requires much smaller solder joints and fine-pitch interconnections for microelectronic packaging in electronic devices. The miniaturization of these electronic devices demands better solder-joint reliability. These ultrafine solder joints packaged in a narrow space will lead to a high homologous temperature during service which may lead to coarsening of the microstructure of the solder joints. So, solder alloys to be utilized in high density packaging electronic devices must stand up to relatively high service temperatures. That is, high temperature solder alloys must be developed to face the challenges of the extensive miniaturization of microelectronic packaging in electronic devices.

During the switching on and off electronic devices, the electrical circuits heat up and cool down, thus experiencing low cycle thermo-mechanical fatigue (TMF) due to stresses that develop as a consequence of the coefficient of thermal expansion (CTE) mismatch between the solder, the substrate and the components. These thermal cycles cause plastic straining of solder joints which experience long hold times at stress extremes at two significantly different temperatures. So, this stress may be sufficient to cause low strain rate creep deformation of the solder during the hold time at higher temperature due to which IMCs grow and deteriorate the mechanical properties of SAC alloys.

Several preliminary studies have been performed on RE doping in SnAg and SAC solder materials but no systematic work has been done, especially on the microstructure and mechanical

behavior of these materials due to which the electronics industry, public interest and governmental organizations are concerned about the lack of research to date on the potential environmental effects of the alternatives to tin-lead (SnPb) solder. Therefore, an extensive knowledge and understanding of the mechanical behavior of the emerging generation of lead-free solders is required to satisfy the demands of structural reliability.

1.2 Objectives

As discussed above, due to better thermomechanical properties, SAC alloys are considered as the best choice [Yu et al. 200 and Rist et al. 2006]. But, because of their coarse microstructures, iron (Fe), cobalt (Co) and nickel (Ni) have been used as refining elements and their effect on the microstructure have been investigated [Anderson et al. 2001]. Many combinations like indium (In), antimony (Sb), bismuth (Bi), copper (Cu) and silver (Ag) are also used as alloying elements [Yu et al. 2004]. Extensive knowledge and understanding of the mechanical behavior of the emerging generation of SAC lead-free solders with RE doping is required to satisfy the demands of structural reliability.

Main Objectives of This Research

The main objectives of this thesis include the study of the microstructure evolution due to thermal aging, evaluation of mechanical properties, nanoindentation applied to individual phase properties, creep behavior and wettability testing of SAC and SAC-La doped alloys.

The steps to achieve these objectives are:

- Design and prepare lanthanum doped solder alloys that are mixtures of pure SAC and pure lanthanum with different mixing ratios.

- Develop test specimen preparation procedures that produce dog-bone shape specimens with consistent microstructure comparable to the lead-free solder materials used in commercial electronic assemblies.
- Measure isothermal aging effects on the microstructure evolution for different aging times and different chemical compositions.
- Perform uni-axial tensile testing to determine the mechanical properties like yield stress, tensile strength and ductility etc. for different environmental conditions close to the service conditions.
- Perform nanoindentation to investigate the individual phase Young's modulus, hardness, creep strain and strain rate sensitivity index etc. in varying environmental conditions.
- Investigate the special pile-up effects and incorporate them into obtained results for Young's modus and hardness.
- Investigate the creep behavior of all compositions using tensile creep tests and fit the experimental results to Dorn creep models. Also investigate the back stress phenomenon due to hard and brittle IMCs and develop the back-stress creep models.
- Investigate the wettability behavior in terms of surface tensions, wetting force and contact angles at different temperatures.

1.3 RE Additives

Many solder properties are linked to its microstructure, which further depends on the thermal aging. The typical SEM micrograph of an undoped SAC alloy is given in Figure 1.2 with matrix (dark black) and IMCs (white).

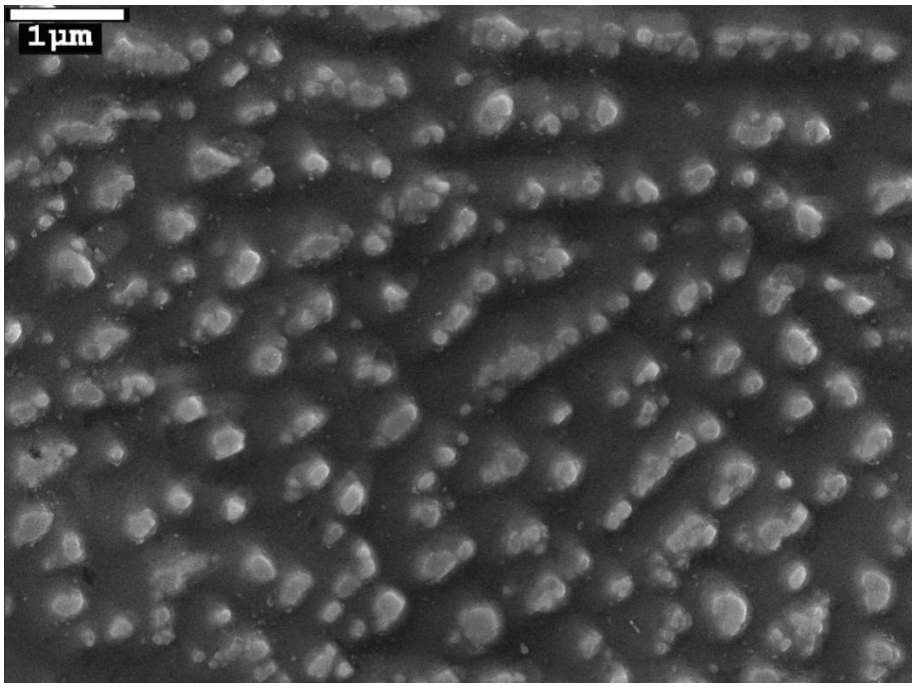

Figure 1.2: SEM micrograph of SAC alloy with matrix (black) and IMCs (white)

Since solder joints are exposed to high temperatures, the IMCs grow and deteriorate the mechanical properties of SAC alloys. RE elements, mostly lanthanum (La), are considered as the best additives due to their lower cost, wide availability and low melting point as compare to the other RE elements [Dudek 2006]. They are widely used to control the growth of these IMCs at high temperatures, but over-doping can deteriorate the solder mechanical properties. They have been used in different studies for both as cast and isothermal aging, e.g. Cerium (Ce) and Lanthanum (La) are used in the Sn-9Zn alloys. Lutetium (Lu) is also used in many studies to improve the Sn-Au and Sn-Ag solder alloys. In [Z. Chen et al. 2003] the addition of small traces of RE elements reduce the size of Ag_3Sn and Cu_6Sn_5 IMCs, while in [Min Pei 2007] impact of lanthanum on the microstructure evolution due to isothermal aging is studied for eutectic Sn-3.5Ag alloy. In [Choi et al. 1999] the impact of isothermal long-term aging is studied for the growth of intermetallic interfacial layers of Sn-Ag and Sn-Pb eutectic solders on Cu substrates. Similarly, in [C. Wu et al. 2004] the impact of isothermal aging is studied on RE-doped Sn-Cu

alloys and [Hao et al. 2008] have systematically investigated the evolution of microstructure and IMCs for SAC solder modified with trace amounts of the RE element Er (addition of 0.15 wt.% Er to SAC387) during isothermal aging. All these elements refine the grain size leading to a fine microstructure which ultimately improves the mechanical properties of SAC lead-free solders, including yield stress, tensile strength and creep behavior at elevated temperatures and thus increase the solder joint reliability [Ma et al. 2002 and C. M. L. Wu & Wong 2007]. In [Cai et al. 2010] the impact of isothermal aging on mechanical properties of SAC alloys is studied with quite consistent results to the other works.

The benefits of RE elements applied as additives to Sn based alloys could be summarized into three main areas [Kanchanomai et al. 2002]: improving wetting ability, reducing intermetallic growth, and refining microstructure. Initially, RE elements were used to increase the solderability of lead-free solders with exceptional results achieved. Even without using any flux, studies show that SnAg or SnAu solder with RE additives form a direct bond to different inorganic surfaces (nitrides, carbides, oxides, etc.) with interfacial bond strength more than 6.9-13.8 Mpa [Mavoori et al. 2002 and Jin 2003]. A Transmission Electron Microscopy study found that the Lutetium atoms go to the interface and thus form a layer of chemical bonding with Lu_2O_3 when the RE doped solders interacts with silica [Ramirez et al. 2002]. Several other researchers have found that RE doping can enhance the solderability characteristics with Cu. It actually happens by decreasing the interfacial tension between the solder alloy and the Cu substrate due to Cu and RE interaction. [C. M. L. Wu et al. 2002b, C. M. L. Wu et al. 2002a and Wang et al. 2002].

Being surface activation agents, even small amounts of La greatly increase the reliability of the solder [Ma et al. 2002]. They tend to accumulate at the solder/copper interface during

reflow and provide a barrier for the formation of tin copper intermetallics. Moreover, after high temperature aging, tin-copper intermetallics in RE element doped solder joint has much lower growth rate than the joints without RE elements. IMC is harmful to the reliability of solder joint due to its brittle character, and RE element enhanced solder joints will have higher reliability [Min Pei 2007]. In [Xia et al. 2002], they showed a huge refinement of the microstructure by adding RE elements.

There has been some study on the issue of wettability of solders and some models predicted that there would be significant changes in the contact angles at the three phase junction points. Some researchers also mentioned that the plane with maximum surface tension will grow the slowest during solidification. This is because of the absorbing effects of the surface-active elements [Min Pei 2007]. Some researchers found that the atomic radius difference between Sn and RE makes them unlikely to form replacement atom type solid-solutions, and the RE atoms will gather at defects, such as dendrite boundaries [ZG Chen et al. 2002].

As mentioned above, the microstructure refinement is noticed due to RE additions, which causes a significant increase in the mechanical properties of solder alloys [Zhu et al. 1994]. Similarly, an improvement in creep resistance is expected by refinement of microstructure. The refined grain and particles decrease the distance for dislocations to pile up, consequently the doped solders have better creep resistance, longer creep rupture time, and higher strength in tension with less elongation.

Other than the refinement of microstructure, RE can also affect mechanical properties in other ways. For example a web-like sub-grain in SAC387 solder was found with lower than 0.1 wt % of RE elements at slow cooling rate [Z. Chen et al. 2003]. This structure limits the

movement of the dendrites, hinders Sn diffusion and increases the creep property of the solder, but increasing RE elements can reduce the creep rupture life, due to RE aggregation at the grain boundary in snow flake shape.

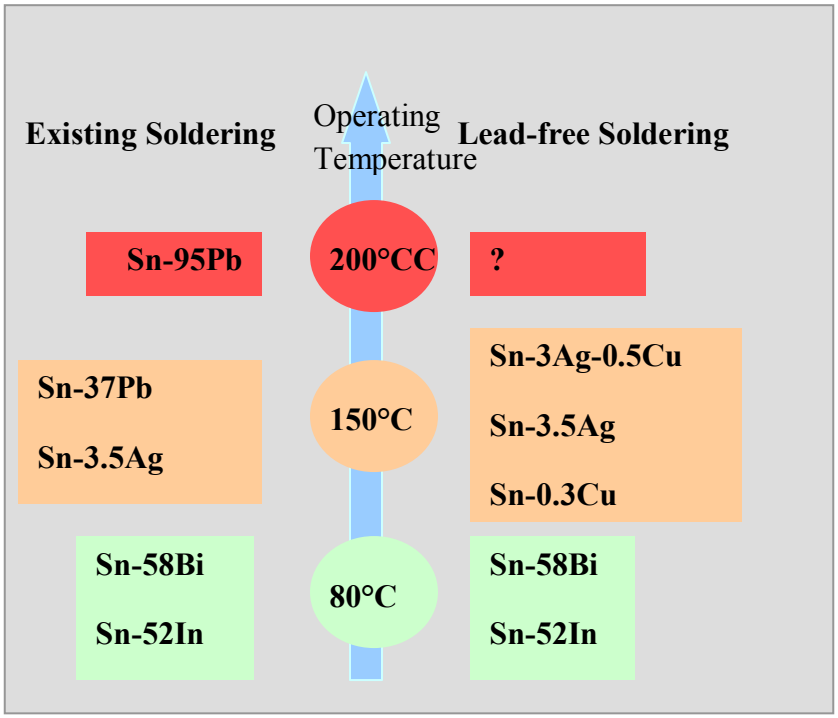

Figure 1.3: Comparison of melting point temperatures of lead solders and lead-free solders

Currently, there are many solder alternatives to low temperature Sn-Pb alloys as shown in the Figure 1.3 but almost no choice for Sn-95Pb. This work is done to take SAC alloy and improve its behavior for making a good alternative for Sn-95Pb.

1.4 Special Adsorption Effects of RE-Additives

RE elements are active and they accumulate at the interface of IMCs. Due to their adsorption phenomenon, they greatly affect the microstructure of lead-free solders [Gebarhardt et al. 1959]. This adsorption is different at different planes and is maximized for the plane with

maximum surface tension. It can be calculated, for a plane k, by the following equation (1.1), [Zhai et al. 1999]:

$$\Gamma^K = -\frac{C}{RT}\frac{d\gamma^K}{dC} \quad \text{..... (1.1)}$$

where Γ^K is the adsorption of surface active material at a plane K, C is the concentration of surface-active material, T is the absolute temperature, R is the universal gas constant and γ^K is the surface tension of plane K.

By integrating equation (1.1), we can determine the adsorption of Lanthanum on the plane K,

$$\gamma_C{}^K = \gamma_0{}^K - RT\int_0^C \frac{\Gamma^K}{C}dC \quad \text{..... (1.2)}$$

where $\gamma_0{}^K$ and $\gamma_C{}^K$ are the surface tension of plane K before and after the adsorption of RE elements respectively. From (1.2), the free surface energy is calculated as,

$$\sum_K \gamma_C{}^K A_K = \sum_K (\gamma_0{}^K - RT\int_0^C \frac{\Gamma^K}{C}dC)A_K \quad \text{..... (1.3)}$$

where A_K is the area of plane K. From equation (1.3), in order to minimize this energy, the following term should be maximized,

$$\sum_K A_K \int \frac{\Gamma^K}{C}dC \quad \text{..... (1.4)}$$

Thus, small quantities of lanthanum not only decrease the difference of the surface free energy of the crystal but also prevent the later from further growth on these planes. This refinement can then enhance the hardness, tensile and creep properties of lead-free solders.

1.5 Chapter Structure

CHAPTER 1 is the introduction of the whole thesis. A short description of each chapter is given. The overall objective of the whole thesis is presented. RE elements are discussed as potential additives with special adsorption effects.

CHAPTER 2 is based on the soldering background and the need of lead-free solders. The most competent alloys are presented here. Different soldering methods are described in detail with their respective limitations.

CHAPTER 3 is dedicated to the experimental design of this research work. Special 3-parts aluminium-steel die is used to cast the testing samples. Quenching process, cooling profiles and sample preparation processes are described in detail. Electrical properties measurements and Differential Scanning Calorimeter (DSC) equipments are presented.

CHAPTER 4 is the characterization of all 5 compositions used in this study. Isothermal aging at 150°C and 200°C and different aging times starting from 10 hours up to 200 hours are studied. This characterization is provided in terms of microstructure evolution during isothermal aging. IMCs particles size, volume fraction, interparticle spacing, grain size etc. are presented both qualitatively and quantitatively in this chapter supported with extensive EDS analysis and elemental mappings.

CHAPTER 5 is based on the models to predict the IMCs size caused due to thermal coarsening. Experimental data is used to get a good fitting and use them for the longer thermal aging times. Again the isothermal aging study is carried out at 150°C and 200°C.

CHAPTER 6 is based on evaluating the mechanical properties of SAC and SAC-La doped alloys. Quasi-static tensile testing is used during this work. Slow strain rate (near to actual soldering joints) is used. As cast, isothermally aged and thermal cycles specimens are used in this part. Different environmental conditions from -60°C up to 140°C are applied during testing.

CHAPTER 7 is dedicated to perform the tensile creep tests of SAC and SAC-La alloys. The temperatures used in this study are 40°C, 80°C and 120°C and the constant stress is ranging from 10Mpa up to 20Mpa. Dorn creep models are used for the data fitting from experiments. Back stress creep models are used to incorporate the special back-stress effects due to IMCs and validated with the creep experiments already performed.

CHAPTER 8 is based on the novel nanoindentation approach to evaluate the individual phase mechanical properties in varying environmental conditions of 20°C, 45°C, 65°C and 85°C. The important pile-up effects are introduced into both Young's modulus and hardness measurements. The results produced are in a better agreement with the previous studies.

CHAPTER 9 is dedicated to perform the wettability tests for SAC and SAC-La doped alloys. This study was performed at 250°C and 260°C. Surface tension, wetting force and contact angle measurements are presented in this chapter.

CHAPTER 10 describes the scientific contributions, main conclusions of the whole project with future recommendations.

Appendixes, Lists of figures and tables are made at the beginning whereas References for the whole thesis are provided in the end of the thesis.

1.6 Summary

Lead-free solders were proposed after Sn-Pb solders were banned by the RoHS legislations. Many lead-free solders, with binary and tertiary combinations of Sn based alloys were selected as good replacements. Sn-3.5Ag and SAC305 were considered as potential substitutes for lead content solders but their coarse microstructure with Sn matrix and hard Ag_3Sn and Cu_6Sn_5 intermetallic compounds (IMCs) makes certain issues/problems in high temperature applications. Other alloys include SnSb, SnAu, SnZn with different additives for application-specific problems. Most of the alloys suggested have certain limitations in terms of mechanical, electrical, thermal and chemical properties that provide an opportunity to go for the surface active elements, known as the vitamins of metals i.e. the novel RE additives.

Mostly used RE additives are the lanthanum and cerium. RE elements are mostly found with small quantity of lanthanum and high quantity of cerium. Due to the high processing cost of separation of these two elements many researchers have used them in combination. In our study, however, we used lanthanum (with no cerium) and got the 200g ingots of lanthanum doped SAC alloys from Atlantic Metals and Alloys, USA, in order to explore the impact of pure La on SAC alloys. For our work, four different combinations of lanthanum were selected for the SAC alloy, and thus the entire work was perfomed for 5 different alloy compositions. These are described in detail in chapter 3 (Experimental Design).

CHAPTER 2

SOLDERING BACKGROUND

2.1 Pin in Paste Method

There are the two famous techniques used since long in the metal joining process in electrical components called surface mount technology (SMT) and plated thru-hole (PTH). This method of PIN IN PASTE is the combination of SMT and PTH. The process involves a pin that is placed with the paste just above the hole where the joint is needed as described in Figure 2.1 (a) whereas as Figure 2.1 (b) shows the final shape with all the necessary dimensions for a single pin.

There are a couple of important steps followed in channel. The stencil is applied for printing process first. After that, solid paste printing is used by squeegee. This is carried out in the paste printing machine. Later, components placing are used with a pick and place machine and is followed by the reflow soldering oven. Similar process is used for the paste printing on pads for the SMT. At the end of this process, PCB is fully assembled and TH process is not required [Owen 1993].

2.2 Press Fit Method

As clear from the name of this method, the joint is made by a pin after pressing into PTH inside the printed circuit board (PCB). Quite obvious from the mechanical pressing point of

view, for a good joint, the diameter (or cross-section) of the pin would be slightly larger than the PTH in the PCB. After pressing the pin into the hole with the required amount of force, the excess material of the pin is either adjusted by some deformation (compensation) of the pin or the hole itself.

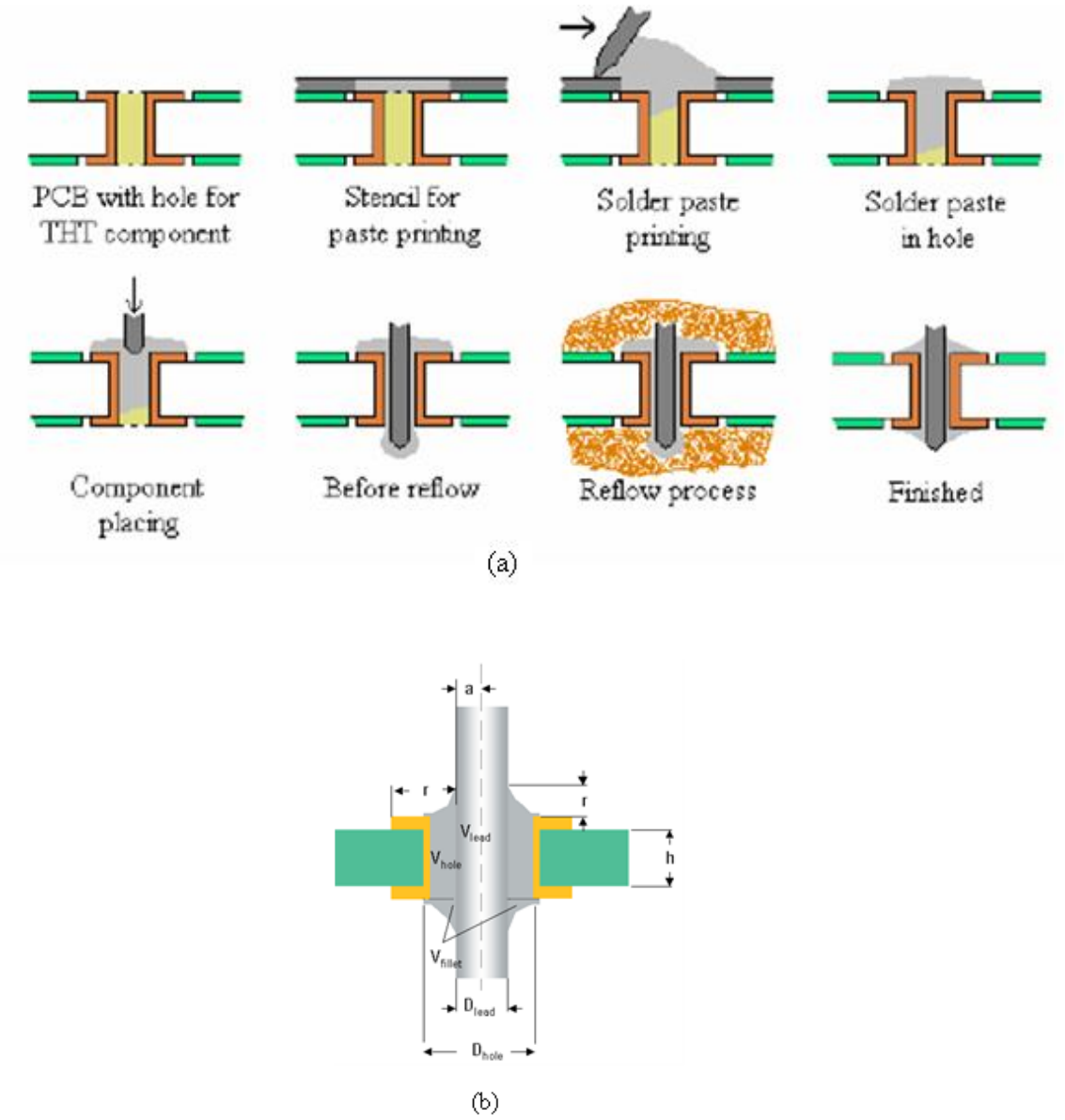

Figure 2.1: Pin-in-Paste technology steps (a) and final shape (b)

Important Features of Press Fit Method

- This is quite easily repairable and of course continuously adjustable
- Other components are press fit components
- The connector is too large for surface-mount techniques
- This technique is quite cheap, safe and fast in comparison to hand soldering
- Other components on the board may be damaged by high temperatures of soldering processes
- The use of soldering fluxes is restricted due to stringent environmental regulations

2.3 Reflow Soldering Method

Reflow soldering is a widely joining technique with a solder paste where the solder paste is a sticky mixture with mixture of powdered solder and flux. This is used to temporarily attach one or many electrical components to their pads. Afterwards, the whole assembly is subjected to controlled heat which actually melts the solder and thus making a permanent connection to the joint.

The heating process or method could be performed by passing the whole assembly thru a heating oven. In some cases an infrared lamp is used or individual joints are made with a hot air pencil. The heating temperature and reflow time are adjustable as per alloy compositions.

Generally, the reflow soldering is used mostly for connecting SMT components to the circuit board. The basic idea is to cause the melting of solder and also heat the adjacent surfaces. Care is needed not to overheat the assembly or damage the electrical components. The important

steps used in most of the reflow soldering processes are explained below. They are called the "zones" of reflow soldering. Each of them has their individual heating profile with certain peaks and heating rates.

The main objectives are the following,

- In order to activate the flux and also remove its volatiles
- To make the pieces to be joined sufficiently hot upto a high temperature necessary for the soldering operation
- To provide a consistent temperature to solder for the even flow onto the pieces to be soldered
- To reflow the solder paste to form a liquid solder volume sufficient to create a sound joint

Finally, the assembly is cooled to solidify the solder joints and make it possible to handle the board.

2.3.1 Pre-Heat

The first and probably the most important step of this joining method is the pre-heat. It involves a rapid rise in temperature. This helps in evaporating the solvent from the paste and also burns off the contaminants present in a large amount. This is performed in the first heating zone of the heating chamber or oven.

In the next zone, the heating is programmed in a way to provide a constant (uniform temperature) with full pre-heating of the assembly. This generally reaches to a temperature between 100°C and 150°C. The time taken to reach this range is controlled by the heating rate

provided during the process. Fast heating rate may cause thermal stresses in the assembly which may lead to thermal shocks and the multilayer ceramic capacitors can be vulnerable to cracking and therefore in most of the cases a heating rate of about 2°C/s (or less) is used. This slow heating rate is also recommended to avoid the spattering of solder paste.

This section, also referred to as the dry-out, soak, reflow or activation zone, ensures that the solder paste is fully dried before hitting reflow temperatures, and acts as a flux activation zone for many solder pastes. Pre-heating may also cause some slumping of the paste, depending on the specification and quality of the solder paste used.

An important aim is to ensure that all joints stabilize at the dwell temperature. Smaller joints hotter than the dwell temperature will cool down, while larger joints heat up. At the end of the dwell time, all joints are intended to be at the same temperature. In general, the tighter the temperature spread is at the end of the preheat zone, the smaller it will be at the top of the reflow spike zone. In most designs,

- the preheating function will occupy 60–70% of the total heated length
- the first heated zone will do most of the work, as it has to take in assemblies at room temperature, 'off the street'.

2.3.2 Reflow

The final heated zones are used to provide a spike (rapid rise) in temperature, when the solder paste reflows and wets the surfaces of both component and board pads. Surface tension will determine the shape of the joints and in some cases the surface tension forces during wetting can generate component movement.

Solder reflow starts happening when the paste is taken to a temperature above the melting point of the solder, but this temperature increase must exceed by approximately 20°C than the melting point of solder to ensure quality reflow.

The length of time for which the solder joint is above the liquidus temperatures is referred as the “wetting time”. This is normally 30–60 seconds for most pastes. If the wetting time is excessive, intermetallics may occur in the joint, which result in brittle solder joints.

2.3.3 Cooling

Once the product has reached the end of the heated zones, the process involves “ramping down”, or slow cooling, until the assembly reaches a suitable temperature. The first stage down to the liquidus temperature of the solder is critical and solder is weak mechanically above 150°C, so care has to be taken to avoid rapid changes of temperature and draughts. Final cooling is both to reduce possible oxidation and make handling safe.

2.3.4 Reflow Temperature Profile

As an assembly moves through a soldering system, it is exposed to a controlled rise and fall in temperature. A plot of temperature against time is called a 'temperature profile’. A typical target profile for reflow soldering indicating both temperature rise and fall and the time above liquidus is shown for an RMA paste in Figure 2.2. Figure 2.3 is a target profile for a reduced solids paste, which is able to tolerate less preheat.

The ideal temperature profile is usually based on three factors: peak temperature, maximum rate of change of temperature and time above liquidus.

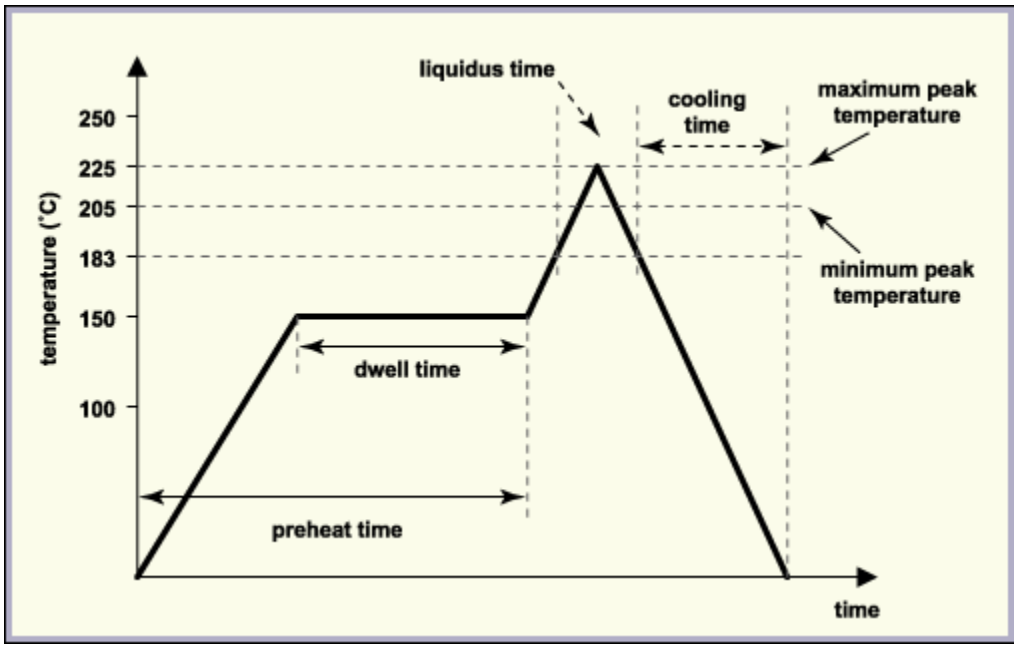

Figure 2.2: Target reflow profile for a typical RMA-style flux [Martin Tarr Reflow Soldering]

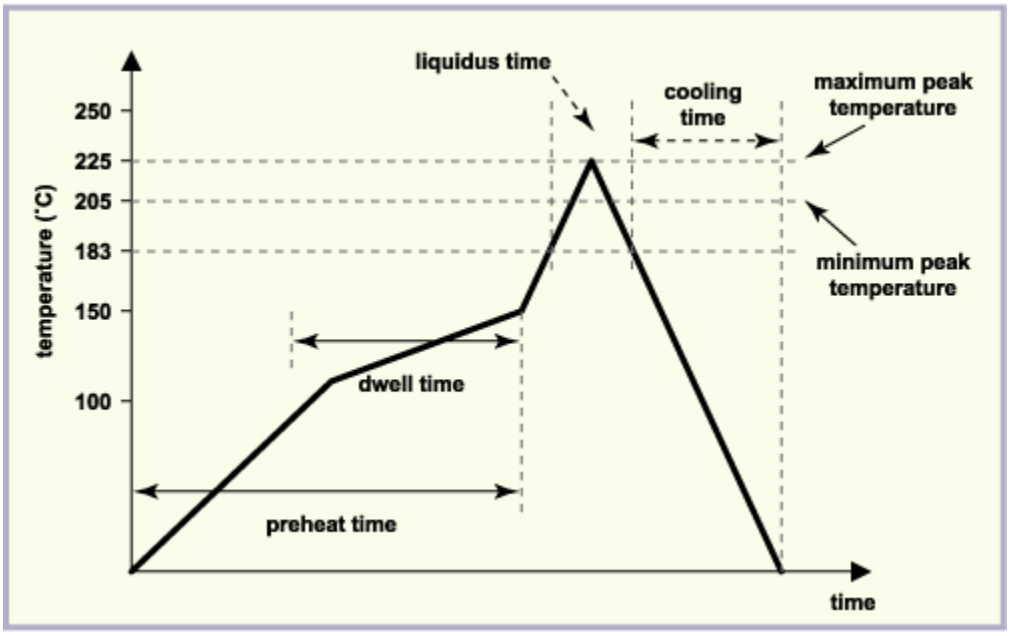

Figure 2.3: Target reflow profile for a typical reduced-solids flux [Martin Tarr Reflow Soldering]

2.3.5 Peak Temperature

For a solder with a melting point of 179–183°C, the maximum allowable peak temperature is usually 220–230°C and the minimum peak is 195–205°C. If the board gets too hot,

- the edges may turn brown
- damage may be caused to SMT components
- intermetallic growth is promoted

If the assembly does not get hot enough, the solder paste will not reflow adequately.

The maximum slope or "ramp rate" specifies how fast the assembly temperature is allowed to change. Many components, especially chip ceramic capacitors, will crack if their temperature is changed too quickly. In order to maximize throughput, the thermal profile is usually designed to have a slope just under the maximum allowable, between 1–3°C/s.

The negative slope "ramp down" on cooling should theoretically be the same as the heat-up rate but most companies have profiles with higher negative slopes, especially with ovens that have a short cooling zone. Perhaps, as seems to be the case with vapour phase systems, the ramp rate may be less critical above certain temperatures.

Most companies aim for a time above liquidus of 30–60 seconds but 90–120 seconds is more typical of larger assemblies. This allows a margin of safety against both oven temperature drops and the chance that the coolest spot on the assembly has not been located during set-up.

However, most solder experts believe that the shorter the time above liquidus the better, as the growth of tin–copper intermetallics leads to a tin-depleted and brittle solder joint.

In practice, an “ideal” profile is impossible to achieve over a range of components, and a temperature profile is best displayed as a band of temperatures (Figure 2.4), within which all joints should be maintained. So long as no joint temperature actually falls outside the profile band, it can be assumed that an assembly has been properly soldered.

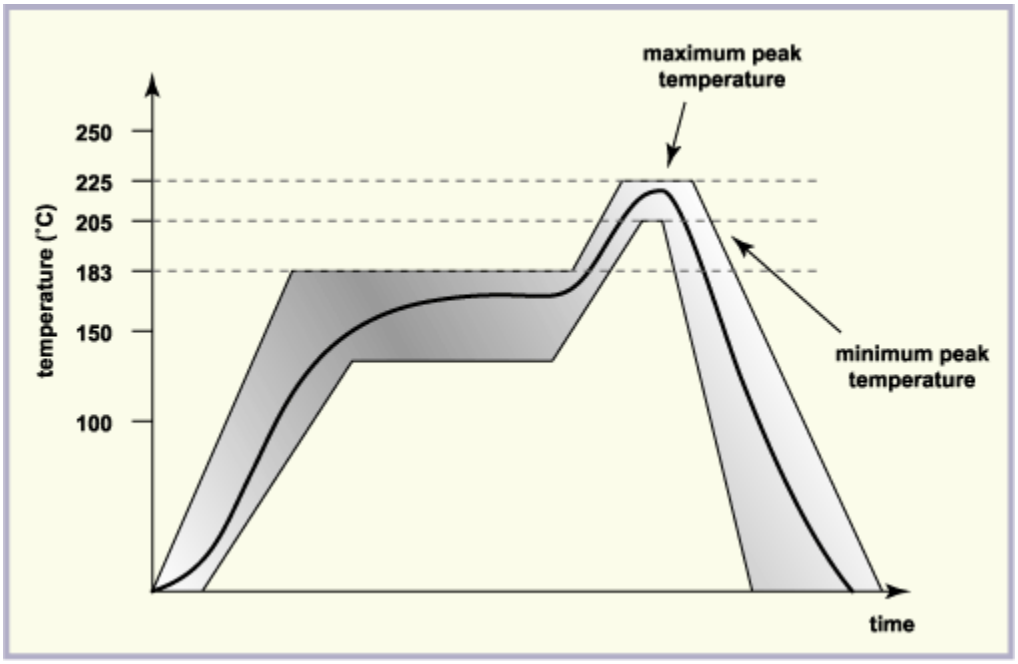

Figure 2.4: A profile „band’ during reflow soldering [Martin Tarr Reflow Soldering]

2.4 Wave Soldering Method

Selective wave soldering is a process for soldering thru-hole components on the bottom side of an assembly. In a selective soldering process, a robot system is used to pick up the assembly and drag it over a single point select wave, or dips the assembly into multiple nozzles that are mounted on a product specific nozzle plate. In contrast, the soldering process utilizing traditional wave soldering equipment consists of transporting the entire assembly, by means of a

conveyor system, over a liquid solder wave. The complete sequence of operation is given in Figure 2.5.

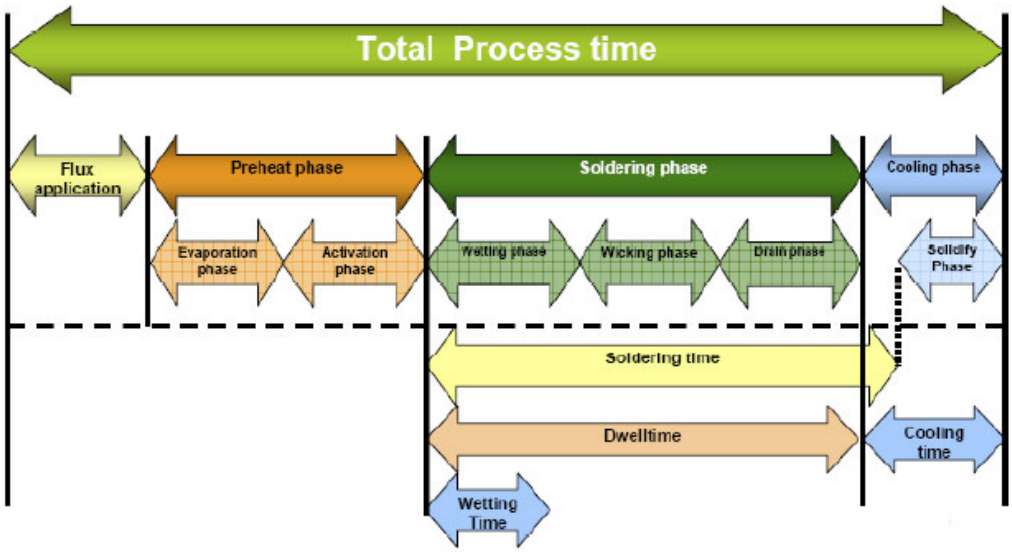

Figure 2.5: Wave soldering sequence of operations

Selective soldering machines accomplish this by providing flux, solder and in some cases preheat to only the areas requiring solder. Benefit is that no special tooling is required, the processes are tailored to the needs of each component and the overall quality is improved.

The decision to choose selective soldering versus wave soldering can be made by considering the number of components or points, the difficulty of the process and the required cycle time. If there are only selective number of points or components on the bottom side and they are in close proximity to SMT devices, selective soldering may be a good solution. If a large volume of points require soldering in a short period of time and the keep out zones are open, then wave soldering may be the solution.

Basic Advantage of Selective Wave Soldering

The implementation of lead-free alloys will affect the thermal load of components and board material due to higher process temperatures. Not all of the components can withstand the high temperatures that they may be exposed to during wave and reflow processes. For this reason, selective soldering becomes interesting since in this process only the areas that come into contact with the lead-free solder will reach higher temperatures while other sections and components remain significantly below critical temperature levels.

2.4.1 Solder Wave

The solder only wets to, or forms joints on, solderable metallic surfaces as shown in Figure 2.6. Consequently, no soldering takes place on the board surface, which is non-metallic. Poor soldering can occur on any metallic surfaces that are contaminated or have poor solderability.

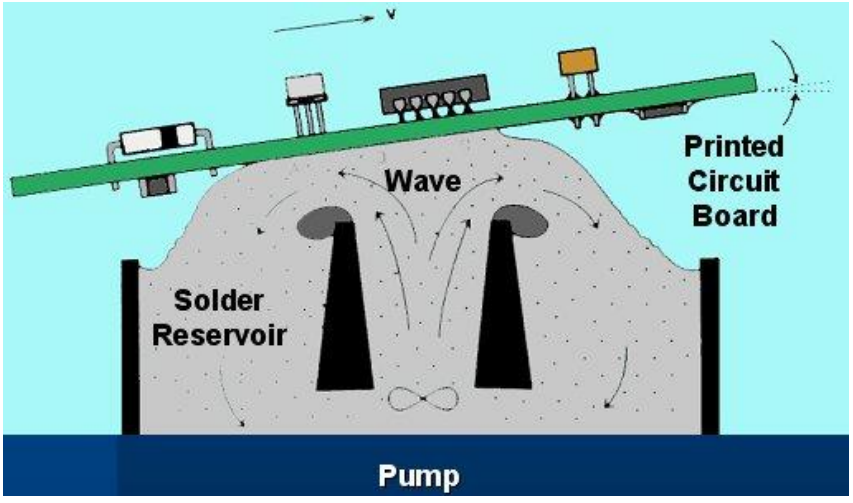

Figure 2.6: Solder wave during wave soldering

2.4.2 Dual Wave

For wave soldering of surface mount assemblies where, in addition to the usual leaded components, small chip components are glued to the bottom of the board, two solder waves are sometimes used. The first solder wave is usually a high, rather narrow wave made turbulent by some mechanical means. This is achieved by pumping the solder through rows of small fixed or moving holes at the outlet of the nozzle or by means of a unidirectional hollow jet wave. The jet wave's flow trajectory is usually aimed in the same direction as the board's travel direction. This first turbulent wave is followed by an asymmetrical laminar wave. The turbulent action of the first wave causes the solder to move in and around all the chip components to help ensure that all solder joints get soldered. The schematic is given in Figure 2.7.

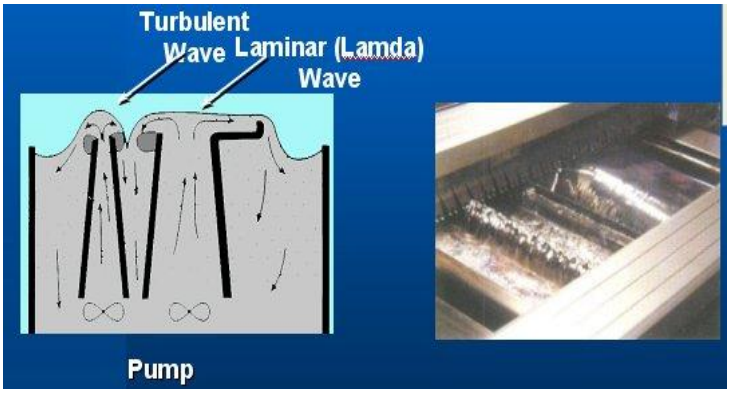

Figure 2.7: Dual Wave during wave soldering

2.4.3 Conveyor Angle

The assembly is conveyed, usually up to 4° to 12° slope (Figure 2.8), until its bottom surface contacts the crest of the solder wave, where the pads, protruding leads, plated holes, and bottom side surface mounted components are soldered.

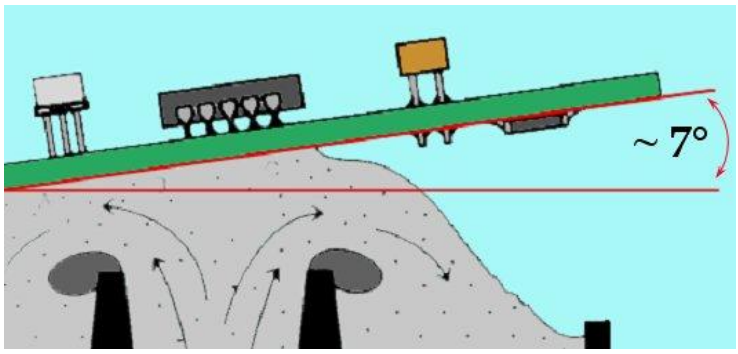

Figure 2.8: Conveyor angle during wave soldering

2.5 Fluxing During Soldering

Fluxing is an important parameter and is recommended by most of the solder manufacturers. Other than cleaning the solder joint, following 2 are the most important justifications for fluxing,

- Prevents oxidation
- Acts as a wetting agent

This is important to note that under fluxing or over fluxing may destroy the whole board as shown in Figure 2.9.

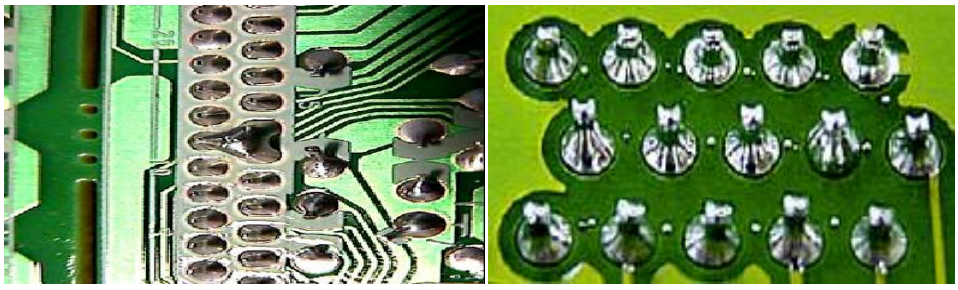

Figure 2.9: (a) too little flux and (b) too much flux

Types of fluxing in the wave soldering

(i) Foam fluxing

(ii) Spray fluxing

2.5.1 Foam Fluxing Process

As the assembly is conveyed over the foam fluxer chimney, the bottom of the board touches the foam head and becomes coated with flux as shown in Figure 2.10 below. A short distance after the exit end of the fluxer, an air knife is usually used, made from a tube with small diameter holes drilled in a row along its length. Low pressure air is directed upward at a slight angle toward the entry end of the machine to remove excess flux and drippings without disturbing the components. If the flux is not adequately removed, it can affect preheating, solder joint quality (too much flux can inhibit soldering), and cleanability (what is placed on the PWA typically has to be removed later on). When an air knife is used at this point, it is typically not heated (due to the flammability of the flux solvents) and is often set to hit the PWA surface at angles of approximately 45° to 60°. This is done to both "squeegee" the excess flux away and drive some material up the PTH to aid in solder flow to the topside connections.

2.5.2 Spray Fluxing Process

Spray fluxing is widely used for the application of low solids fluxes because of the ability to better control the flux deposit for no-clean applications. Low solids fluxes with solids content in the range of 1-3% often contain no rosin. These are more expensive than foam or wave fluxers. The schematic is provided in Figure 2.11.

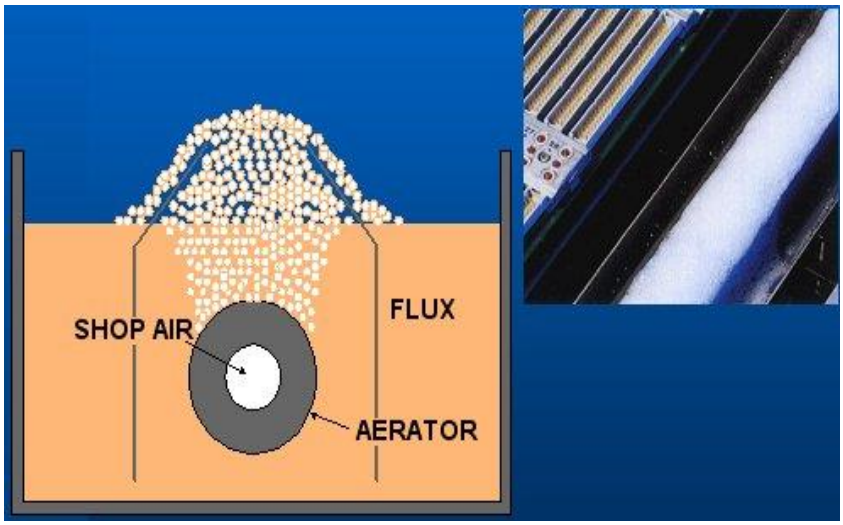

Figure 2.10: Foam fluxing process

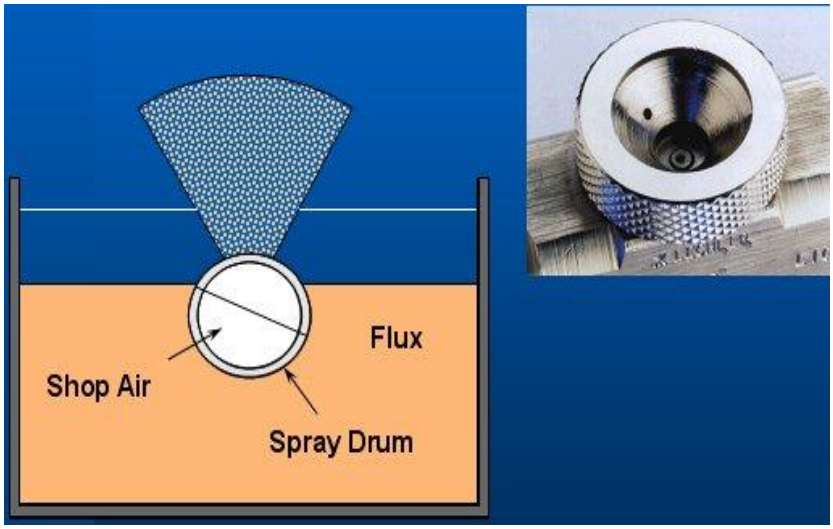

Figure 2.11: Spray fluxing process

2.6 Transient Liquid Phase Diffusion Bonding Method

Liquid-state diffusion bonding relies on the formation of a liquid phase at the bond line during an isothermal bonding cycle. This liquid phase then infuses the base material and eventually solidifies as a consequence of continued diffusion of the solute in to the bulk material

at constant temperature. Therefore, this process is called Transient Liquid Phase (TLP) diffusion bonding.

Despite the presence of a liquid phase, this process is not a subdivision of brazing or fusion welding as the formation and annihilation of the liquid phase occurs at a constant temperature and below the melting point of the base material. The liquid phase in TLP diffusion bonding, generally, is formed by inserting an interlayer which forms a low melting point phase, *e.g.* eutectic or peritectic, after preliminary interdiffusion of the interlayer and the base metal at a temperature above the eutectic temperature. Note that the liquid phase could, alternatively, be formed by inserting an interlayer with an appropriate initial composition *e.g.* eutectic composition which melts at the bonding temperature.

This Figure 2.12 represents the schematics of the Transient Liquid Phase (TLP) bonding process (a) conventional implementation, with single layer of low melting point element (B) and thicker layers of high melting point element (A), which are deposited on substrates composed of (potentially) different materials than A; (b) multi layer implementation, wherein the diffusion distances and associated reactions times at a given temperature are reduced;(c) nanoparticle materials (B), accomplishing both a reduction in the melting point of B as well as further reducing the diffusion distances and reaction times; and (d) schematic of the TLP bonding sequence for the case of (a), showing how the composition of the bonding layer becomes more progressively rich in A as solidification and homogenization proceed. The key point is that the melting point of bondline (after a slight initial reduction) progressively increases towards that of A.

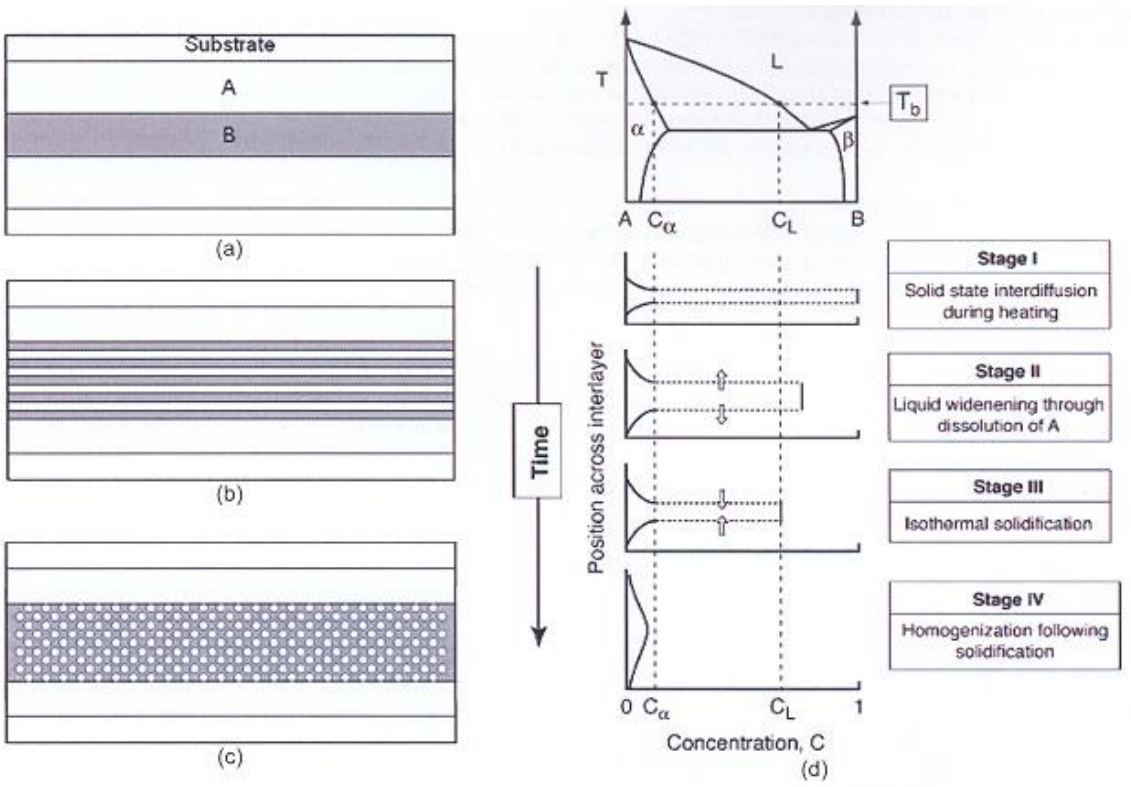

Figure 2.12: Transient Liquid Phase diffusion bonding process (phase diagram)

2.7 Metallo-Organic Nanoparticles Bonding

A novel bonding process using Ag metallo-organic nanoparticles is used as a new application of nanotechnologies towards next generation soldering techniques. When particles are reduced in size to less than 10 nanometer, their characteristics are different from those of the bulk state [Goldstein 1992]. For example, the melting point and the sintering temperature are detectably lower than for the bulk state as shown in Figure 2.13 [Buffat & Borel 1976 and Zou et al. 2009]. When the particle size becomes small, the number of atoms included in the particle decreases and the ratio of surface area to volume increases. Therefore, the melting point of a nanoparticle reduces near linearly with the inverse of the particle radius due to surface energy contribution [Allen 1986]. A small particle also has a large change in vapor pressure caused by

its high radius of curvature. It was first shown theoretically by Thomson and after lead to the Kelvin equation using Gibbs approach. It has long been known that small particles have a natural propensity to sinter or Ostwald ripen for the purpose of reducing total free energy. This is called the Gibbs–Thomson effect.

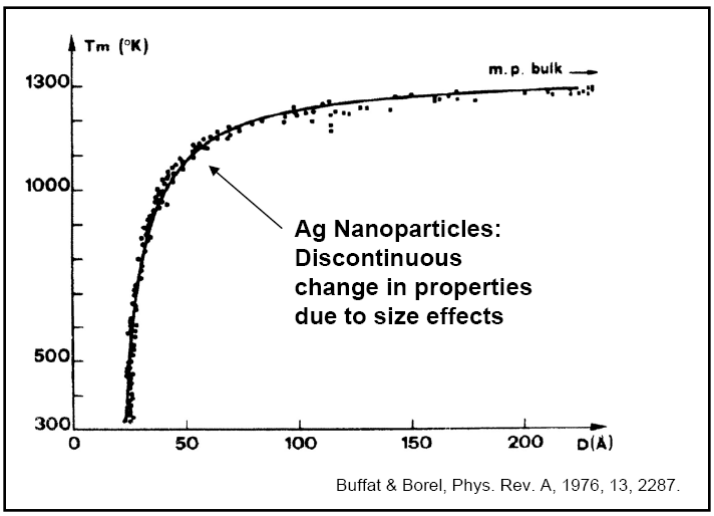

Figure 2.13: Melting temperature vs. nanoparticles diameter

The nanoparticles used are chemically synthesized Ag metallo-organic nanoparticles, which consists of an Ag nanoparticle covered with an organic element derived from Myristyl alcohol (hereafter described as organic shell) [Nagasawa 2002]. The organic shell has the function of preventing the self-cohesion [Lopes WA. Phys Rev E 2001; 65:031606.] that is a significant problem in handling nanoparticles. Removing the organic shell is necessary in order to bring out the activated property of the nanoparticles at a bonding temperature.

Experimental Procedure

Nanoparticles of Ag are employed (Figure 2.14) with standard paste constituents. It gives the processing temperature of almost 275°C which is slightly greater than the peak temperature of most of the components (260°C). These particles are schematically shown in Figure 2.15.

Chemical bonds between the Ag nanoparticle and the organic shell function as a passivation layer that prevents self cohesion of the nanoparticles. An image of nanoparticles obtained with transmission electron microscopy (TEM) is shown in Figure 2.16.

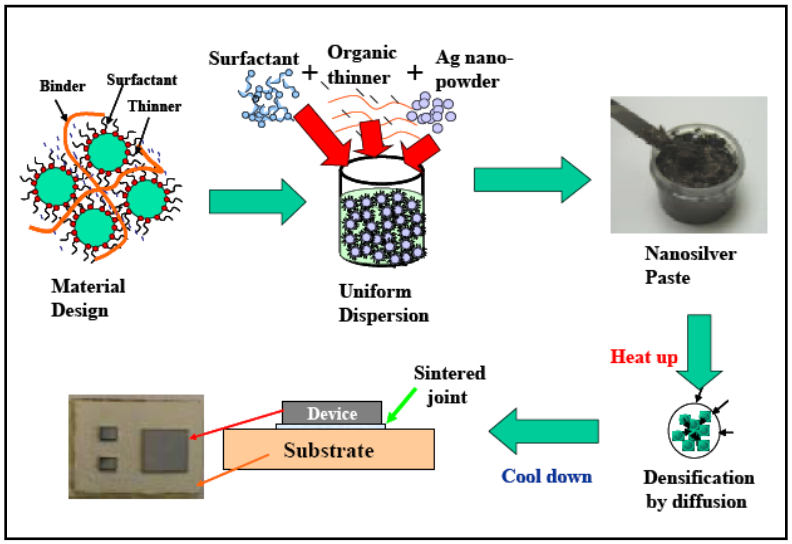

Figure 2.14: Ag particles with standard paste constituents

The average size of Ag nanoparticles is around 11 nm and the particles are isolated from each other. The Ag nanoparticulate paste is usually prepared by mixing an organic solvent with the nanoparticles. Ag fine particles (average particle size of 100 nm) are used as a reference material to consider the effect of particle size on bondability.

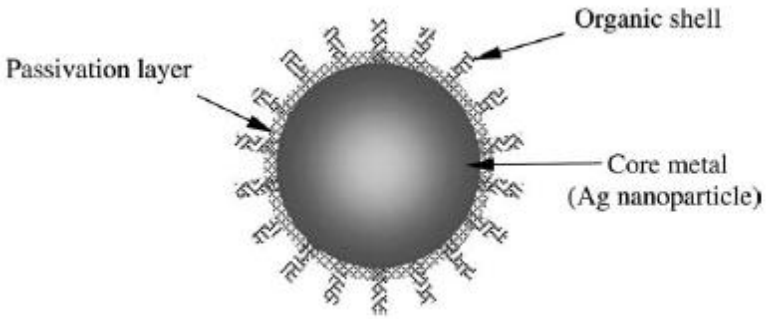

Figure 2.15: Schematic view of Ag metallo-organic nanoparticle

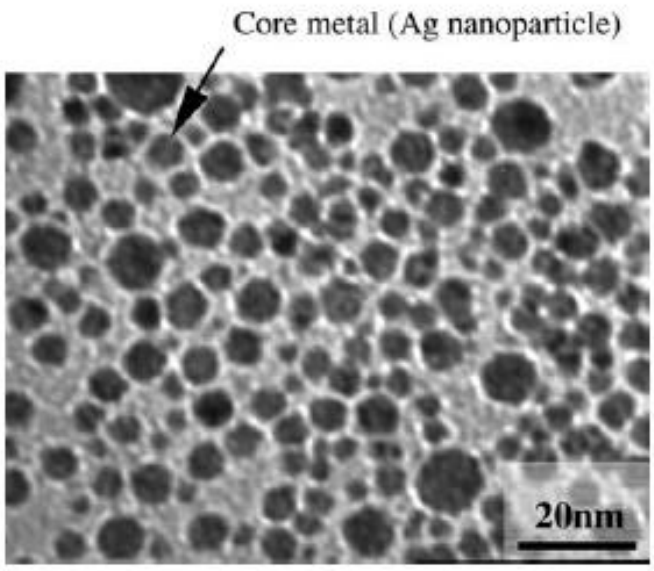

Figure 2.16: TEM image of Ag metallo-organic nanoparticles

2.8 Solder Alloys

There are a huge number of alloys that are implemented since the lead solder is banned. These new alloys are lead free in a way that they don't have any lead composition but these lead free solders do not fulfill the needs and challenges of modern electronics manufacturing. Many of them are not good for high temperature applications whereas some of them have processing issues due to the doping of certain elements. In general, the major issues and problems are presented below in Figure 2.17. Similarly, the adding elements have a major issue of their high melting temperatures. This causes high thermal stresses in the alloys which may affect the entire structural reliability of the components. Most important additives with their respective melting points are provided in Figure 2.18.

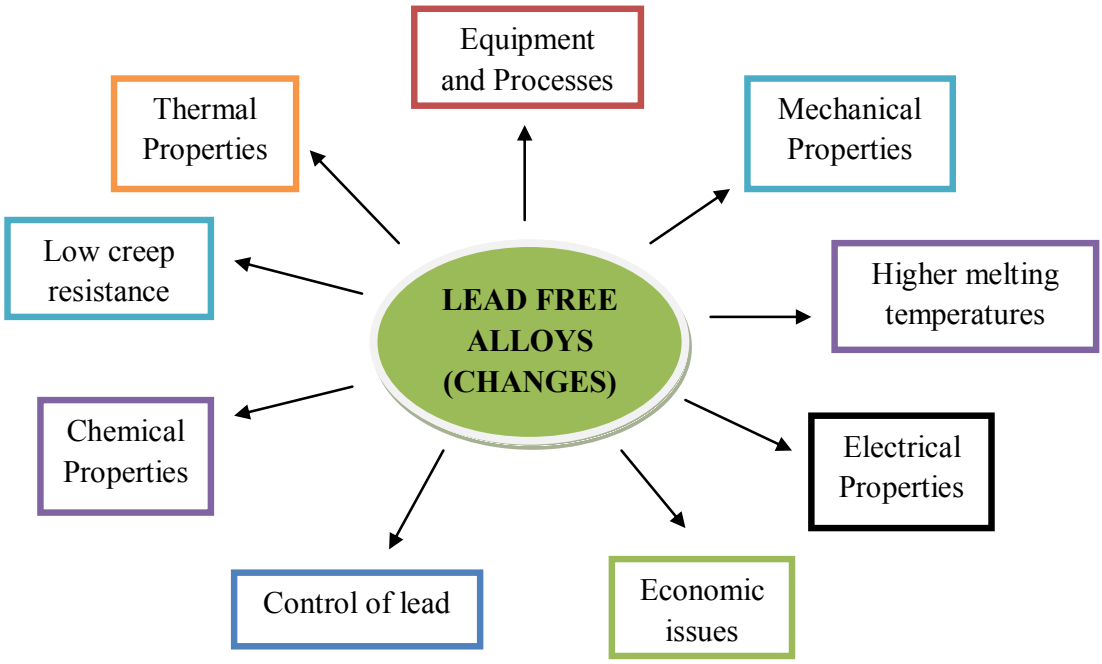

Figure 2.17: Lead-free solder alloys major problems

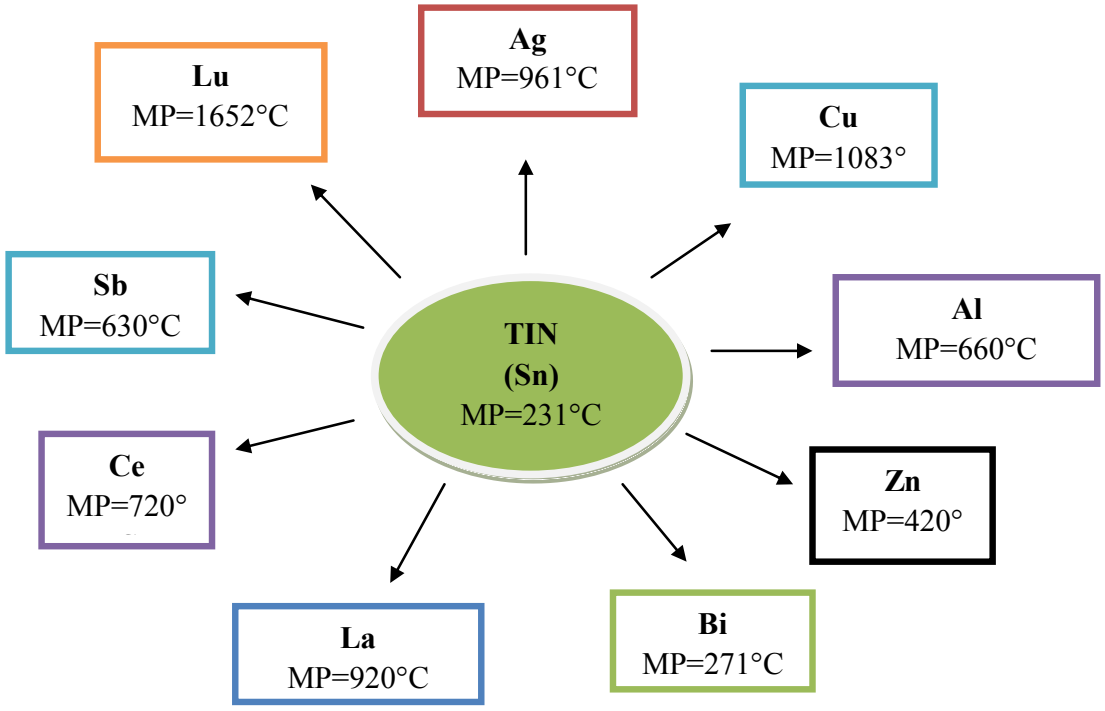

Figure 2.18: Melting points of different lead-free solder additives

The alloy composition (selection) is a critical job. After analyzing the phase diagram of each binary and tertiary alloys and varying the liquidus and solidus temperatures by changing the minute composition of any of the constituent even makes it broader. The best lead-free solder alloys used in different applications like automotive, aerospace, consumable electronics, and pipelines industries are given in the Table 2.1.

Table 2.1: Lead-free solder alloys

Alloy Composition	Liquidus Temperature (°C)	Solidus Temperature (°C)	Eutectic
Sn–3.5Ag	221	221	Yes
Sn-0.7Cu	227	227	Yes
Sn-10Au	217	217	Yes
Sn-9Zn	199	199	Yes
Sn-57Bi	139	139	Yes
Sn-51In	120	120	Yes
Sn25Ag10Sb	233	233	Yes
Sn3Ag0.5Cu	217	220	Near
Sn3.5Ag0.7Cu	217	220	Near
Sn3.5Ag0.9Cu	217	217	Yes
Sn3.4Ag4.8Bi	211	213	No
Sn7.6Zn8.8In	181	187	No
Sn5.5Zn4.5In3.5Bi	174	186	No

2.9 Solder Manufacturing

Solder alloys are available in different shapes that depend on their respective applications. The most important are the following; Solder bar, Solder wire, Solder powder, Solder paste [Carabello M. Christopher]**.** The manufacturing of all these shapes of solder alloys is a complex process. As temperature, mechanical processing (like annealing, rolling etc.) can significantly change the solder properties therefore different processes are suggested keeping in mind the final properties of each shape. This is important to mention that the same solder alloys can have different set of properties if formed in different shapes.

Once the required shape is formed, the solders are placed in an environment not to cause any kind of oxidation otherwise the desired properties could be altered. In some cases, particular flux is used for the purification and avoiding oxidation during the soldering process. Particular fluxes re checked for the compatibility with respective alloy compositions.

2.10 Summary

Different joining techniques are explained in this part. All of them have their advantages and certain limitations.

Pin-in-paste is a good combination of both surface mount technology (SMT) and thru-hole (TH) technology. The biggest advantage of this technique is that it is simple and needs easy handling. On the other hand, some important **disadvantages** are listed as follows,

- Reliability is still an issue because of choosing a proper solder paste.
- In case of Au/Sn solder paste the method is very expensive and is not feasible.

- Very precise volume calculation of the solder paste is required.
- Pin, paste and board compatibility is crucial to make solid joints.
- Thermal stresses can damage the board.

Press fit approach is another joining technique used in the electrical components. Some of the major advantages and disadvantages are provided below,

Advantages	**Disadvantages**
No thermal load	Extremely precise dimensions are required for both holes and press fit pins.
No solder vapors and welding fluxes	Very precise press forces are required to make suitable joints.
No cold soldering joints	Stuffing operations.
Direct mechanical fixing via press-fit zones	Board's handling.
Long connector pins remain free of brazing solder that could be used as rear mating connection	Bent connector or the misalignment of connectors can damage the whole board.
No short circuit due to solder bridges	Highly operator dependant.
Can be repaired without problems	Visual and tactile acuity
Well defined geometry (impedance of the connection is well defined)	
Environmentally compatible since the PCB do not have to be washed	

Very easy to recycle	

Selective wave soldering is already explained. It is of particular interest in the wave soldering process. Some of the critical advantages and inconvenient are listed below,

Advantages	Disadvantages
Quantifiable application of the flux deposit (SPC)	Cracks in the solder can occur and are usually caused by stress on the solder and can cause a loss of conductivity.
Not in-process QC of the flux	Cavities, pores in the solder, can be caused by contaminated surfaces, insufficient flux and insufficient preheating.
No thinner consumption	Cavities can reduce strength and conductivity.
Direct application from can	Improper solder temperature or conveyor speed can cause an undesired thickness.
Reduced flux consumption	If the solder is too thin, then it is susceptible to stress and may not support the required load. If it is too thick, then unwanted shorts and bridging can occur.
No flux drippings over the preheat	Poor conduction in the solder can be caused by contaminated solder and can cause the product to be disfunctional.
	Excess heat can cause the circuit board to delaminate, become brittle and become warped. Excess heat can also damage components that are sensitive to heat.

Transient Liquid Phase Bonding

Liquid-state diffusion bonding relies on the formation of a liquid phase at the bond line during an isothermal bonding cycle. This liquid phase then infuses the base material and eventually solidifies as a consequence of continued diffusion of the solute in to the bulk material at constant temperature. Therefore, this process is called Transient Liquid Phase (TLP) diffusion bonding.

Advantages	Disadvantages
Base metal properties at joint	Long bonding times (several hours)
No interface remains after bonding	Restricted to high temperatures (T/Tm=0.6)
Self homogenizing	Fast diffusers are required (preferably interstitial elements)
Low joint pressure required	Rapid heat up is required
Intermetallics formation can be avoided	Close fit-up are required
Minimum surface preparation	Post bonding heat treatment for age hardening alloys is required
Large and complex shapes bonded simultaneously	

Metallo-organic Ag nanoparticles approach is presented with certain limitations. Its experimental procedure is described in detail. Some of the most important binary and tertiary alloys are presented.

CHAPTER 3

EXPERIMENTAL DESIGN

3.1 Alloy Compositions

Good samples preparation is crucial in order to get good results from the characterization of the alloys like elemental compositions, intermetallic compounds size, distribution, interparticles spacing, grain size, mechanical properties etc. In this chapter, the overall experimental work for the tools and equipments used is described in detail. The core alloy used in this work has the following elemental composition.

Table 3.1: Elemental compositions of the core SAC alloy

Sn (wt %)	Ag (wt %)	Cu (wt %)
96.5	3.0	0.5

There are 3 major parameters that control the microstructure and mechanical properties of lead-free solder alloys used in this study. They are RE additions, thermal aging temperature and thermal aging time. The 3-D experimental design sample space is given in Figure 3.1. The first parameter is to understand and explore the impact of lanthanum (La) doping on SAC alloys. Therefore, 4 different La compositions are selected for this study along with an undoped SAC alloy.

These 5 SAC and SAC-La doped alloys are given in Table 3.2. These alloy compositions are purchased in the form of 200 grams ingots, as shown in Figure 3.2, from Atlantic Metals and alloys. Similarly, the thermal aging temperature varies from -60°C upto 200°C for different properties evaluations. The thermal aging time varies from 10 hours up to 200 hours.

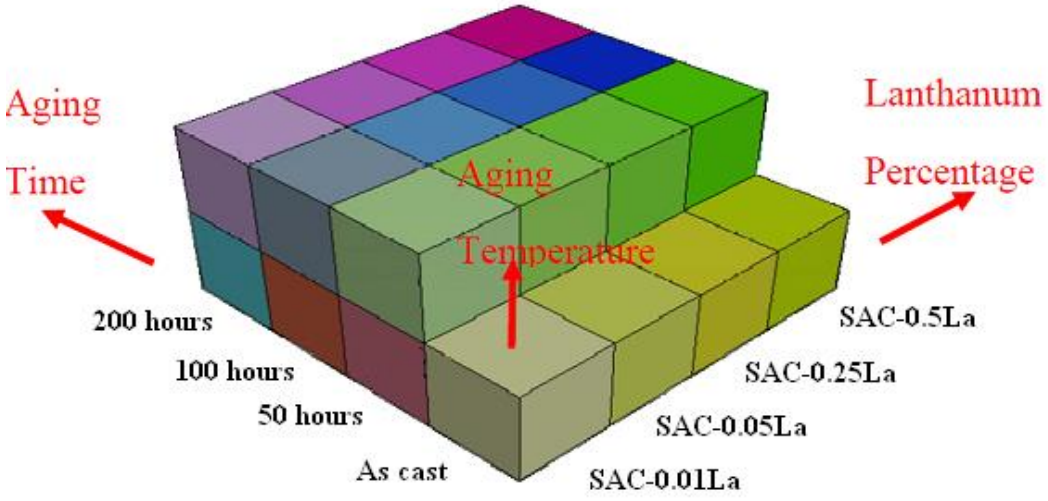

Figure 3.1: Experiment design sample space

3.2 Die Design

The die is designed in such a way that it provides high cooling rate during the solidification process. It is easily bolted using 4 right handed nut-bolts. The path for the flow of molten material is kept smooth and is always lubricated before putting it in the heating chamber. There are 5 risers equally spaced above the samples cavities to get the extra material at the top of the die. This design function additionally provides a place for the thermocouple.

Table 3.2: Selected SAC-La compositions

Sn (wt %)	Ag (wt %)	Cu (wt %)	La (wt %)
96.5	3.0	0.5	0
96.5	3.0	0.5	0.01
96.5	3.0	0.5	0.05
96.5	3.0	0.5	0.25
96.5	3.0	0.5	0.5

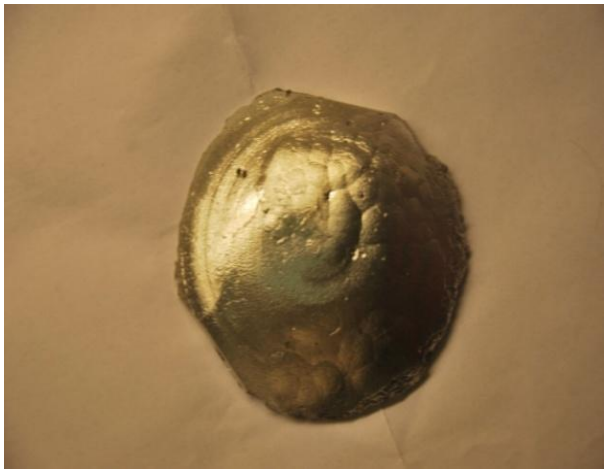

Figure 3.2: 200 grams ingots for SAC-La alloys

The die is composed of 3 parts, two parts in aluminium and a central steel plate, as given in Figures 3.3-3.5, and is used to follow the “cast by melt” die casting to make dog-bone shape tensile specimens for the entire study. There are many advantages to use this die and follow the casting (water quenching) process as given below,

i) To get the samples following the same thermal profile (cooling rate) as that of the actual soldering joint process. This way we can easily control the microstructure of all samples.

ii) We can have 5 specimens for each cast. As this study needs many samples for every composition during the experimental study, thus it saves time.

iii) Small specimen dimensions and re-use of broken samples minimize the waste of solder alloys.

iv) Net shape technique that requires no further machining operations on specimen.

3.3 Sample Casting

A temperature of 260°C is applied in the heating chamber as shown in Figure 3.6 and the die is heated for about 45 minutes before putting the molten metal into it. The 200 grams ingots are put in a crucible and then placed in the oven at 260°C for about 25 minutes as shown in Figure 3.6.

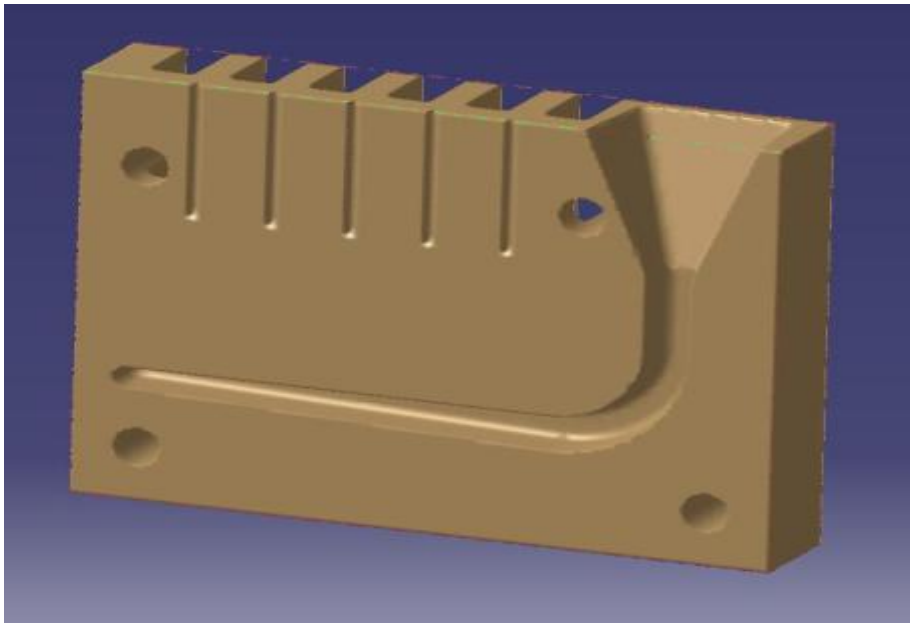

Figure 3.3: Back part of the die with material flow path and risers

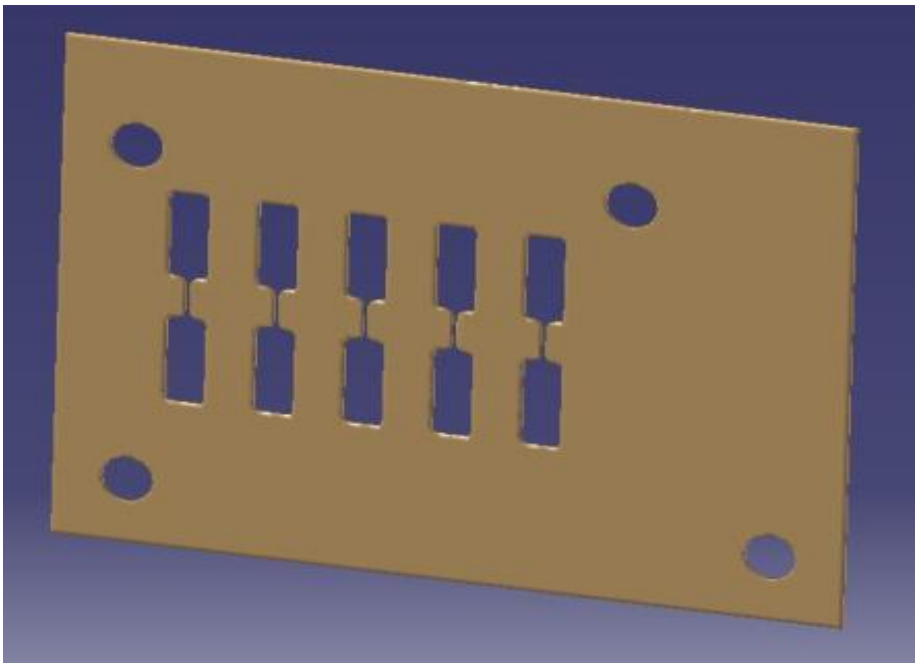

Figure 3.4: Central steel plate with sample cavities (2mm thickness)

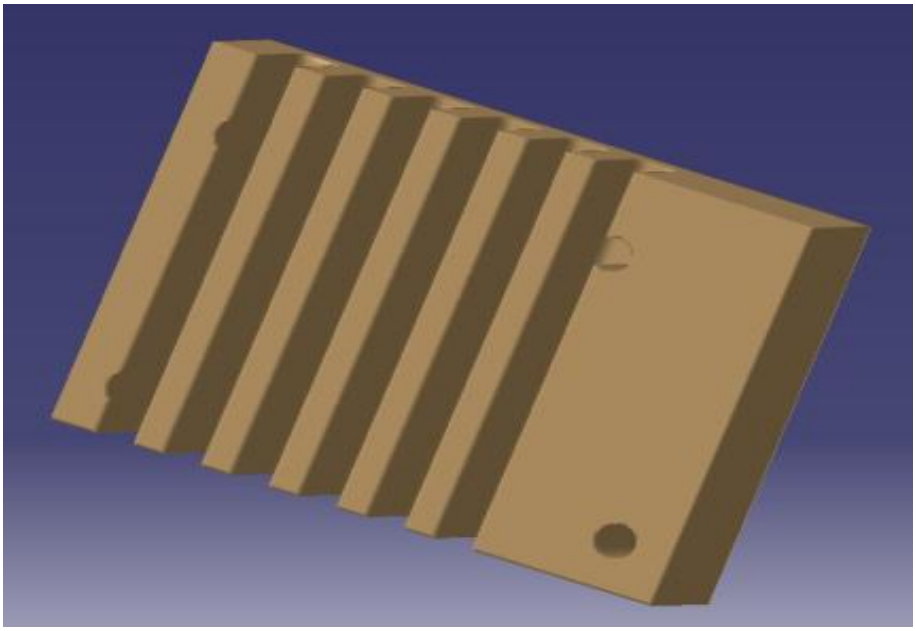

Figure 3.5: Front part of the die with cooling profile

Figure 3.6: Die casting and water quenching of test specimens

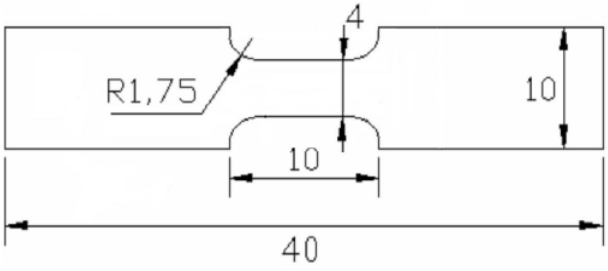

Figure 3.7: Dog-bon shape tensile test specimen

Water at a temperature of 15°C is used for quenching; the cooling rate of the specimens is measured with a K-type thermocouple which is connected to computer to record the cooling rate. The computer recorded the temperature reading at the time when the die was removed from the hot plate; history curve is shown in Figure 3.8. Only a small part of the die is dipped into the

water to get a slow cooling rate of about 3°C/s, which is close to the actual soldering process. Fast cooling rates (e.g. complete water quenching) result in much higher flow stress compared to pure Sn, while low cooling rates (e.g. furnace cooling) increases the strength modestly [Zhang Yifei, 2010]. The strengthening effect is largely due to Ag and determined by the size of Ag_3Sn intermetallic plates and Ag content in the Sn-rich matrix phase [Chen & Dutta 2008 and Korhonen et al. 2004]. In general, the intermetallic compound particles possess much higher strength than the Sn matrix [Tsai et al. 2005 and Fields & Low 1991].

The thickness of the resulting specimens is 2mm. The batch of 5 casted specimens is given in Figure 3.6 whereas a single specimen, after proper cutting, is given in Figure 3.7; all dimensions are in mm. The dog bone sample is left at room temperature (about 25°C) for one whole day to release some of the residual stresses (due to quenching) and then stored in a freezer thereafter.

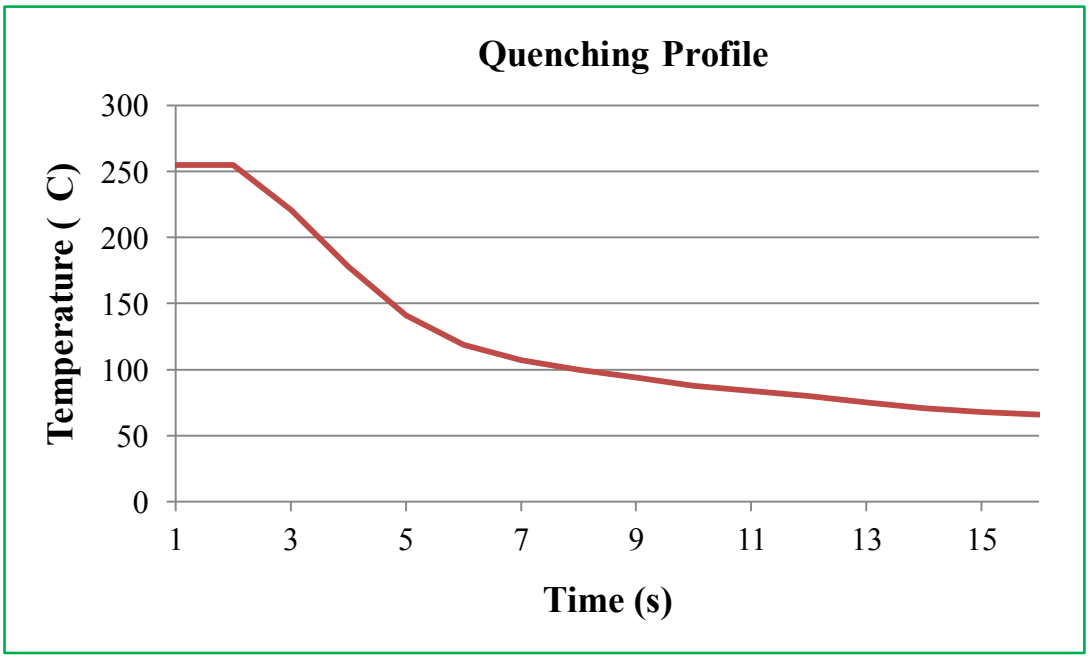

Figure 3.8: Sample quenching profile

3.4 Sample Preparation

After casting the specimens, it is necessary to get high quality surface finishing. For the as cast specimens, some scratches are produced during separation of the central plate of the die. These scratches can have a major impact on the surface quality and therefore alter the microscopy results. The Scanning Electron Microscope used in this study is the JEOL JSM-7000F as given in Figure 3.9 and Optical Microscope used is the Olympus OM as given in Figure 3.10. Both SEM and OM needs almost scratch free surface, therefore, sample polishing is important before subjecting it to any characterization study.

SAC and SAC-La samples are quite fragile once casted. During polishing, it becomes difficult to properly handle the specimens and avoid any distortion. Therefore, the specimens used for microstructure analysis were mounted in a slow-curing transparent epoxy that took about few hours to harden at room temperature. Later on, an initial grinding is performed to remove big scratches and also remove some oxidized layers. This needs extreme care, as not to push the samples too much, otherwise some extra scratches can be produced which may take quite long in the polishing to get the scratch free surface. Polishing was then conducted manualy with regular metallographic rotating polishing disks as shown in Figure 3.11. Silicon carbide (SiC) sand papers were used for the initial grinding of specimens, and were selected in a sequence of 320, 600, 800, 1000 and 1200 in grit size. During grinding process, some heat is generated which may also damage the surface. In order to avoid any effects, tap water was used during the sand paper grinding for lubrication purposes.

The polishing process started with polycrystalline diamond suspension as the abrasive (particle size: 6.0 μm) on woven silk cloth, right after the 1200 SiC sand paper grinding. Later on, abrasives of 3μm and 1μm were followed to get extra shining surface.

Figure 3.9: JEOL JSM-7000F Field Emission SEM

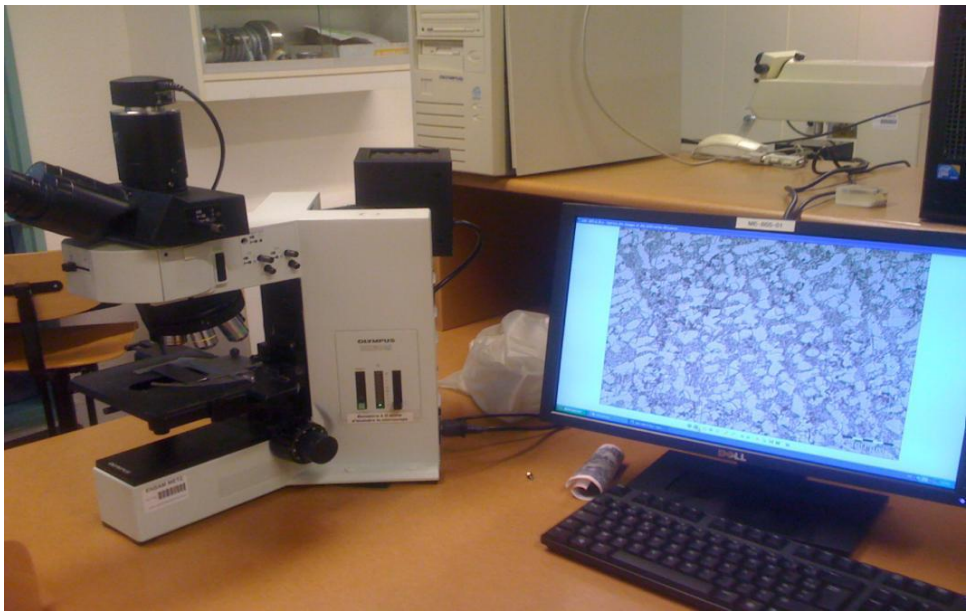

Figure 3.10: Olympus Optical Microscope

After polishing, the specimen surface was thoroughly cleaned by distilled water in order to remove any residue left in the process.

The resin could be used in the process where no thermal aging is involved. In case of thermal aging, no resin was used and the samples were polished with a scotch tap attached on its surface to get extra handling grip during polishing. The disc rotating speed is adjustable and was therefore quite slow in comparison to the speed of polishing where resin was used for handling samples.

After sample polishing, it is necessary to perform the chemical etching of all compositions. The chemical etchant used in this study is 5% hydrochloric acid and 95% ethanol solution. The etching time is different for each composition. It varies from 10 seconds upto 1 minute. This etching time is more for alloys with La composition. The average etching time for SAC and SAC-La doped alloys is given in Table 3.3.

Table 3.3: Etching time for SAC and SAC-La doped alloys

Alloy (wt %)	**Etching time (s)**
SAC	9
SAC-0.01La	14
SAC-0.05La	18
SAC-0.25La	28
SAC-0.5La	58

It is necessary to point out that the microstructures of solder alloys can evolve rapidly even at room temperature due to aging after solidification. Therefore, specimens must be prepared in a timely manner if one wants to capture the initial microstructure and ensure microstructure evolution without significant aging effects. Moreover, the samples are always placed in the vacuum chamber to avoid any oxidation or contamination effects.

Figure 3.11: Sample polishing rotating discs

3.5 Electrical Resistivity

As the La doping varies for all compositions so it is important to study the impact of La doping on electrical properties like electrical resistivity at different voltages and current specifications. The electrical resistivity is calculated using 4 points method. It is generally in a range of 10-15 μΩcm and is found for all compositions within this range.

Solder being an alloy to create a mechanical joint between 2 different metals also provides an electrical connectivity between them. This requires an alloy with a reasonable electrical conductivity both at room and elevated temperatures during service. Extensive thermal

aging study has been made for all compositions and therefore electrical resistivity was calculated with regular intervals. The “Rohde and Schwarz Signal generator and signal analyzer” used in this study are shown in Figures 3.12-3.13. The detailed results can be seen in Appendix E.

Figure 3.12: Rohde & Schwarz FSW signal and spectrum analyzer

Figure 3.13: Rohde & Schwarz signal generator

3.6 Differential Scanning Calorimeter Tests

As the melting point of all solder alloys is crucial in high temperature applications, therefore a difference of 10 to 15°C is always recommended between the solidus temperature and

the service conditions. It is important to perform the DSC tests and see the variation of both solidus and liquidus temperatures of all alloy compositions.

It is concluded that the melting point does not vary more than 2°C for all La compositions. The thermal cycle used in DSC tests have a heating/cooling rate of 5°C/min and the 2 peaks were 20°C and 300°C. As compared to the melting temperature of 217°C for SAC, a relatively high temperature was selected to ensure complete melting. The DSC curves are given Appendix C.

3.7 Summary

Being an experimental thesis, there was a great deal of experimental setups, equipments, tools and sample preparation and characterization in this work. Detailed Die design used for the sample casting is presented. The overall casting process with water quenching and thermal profiles is described that explains how to control the cooling rate with thermocouples attached within the die during the casting process.

Microscopic techniques like Optical Microscope, Scanning Electron Microscope etc. are explained in detail. Sample preparations with cutting, fine polishing and good chemical etching is also described. Electrical properties of the solders alloys play an important role in overall performance of solder joints. Therefore, electrical properties are evaluated using 4 points average method.

Melting point is considered as a critical parameter specifying the limiting temperature during service of the soldered components. Differential Scanning Calorimeter tests are performed for all SAC and SAC-La doped alloys. Small difference for the melting temperature between the SAC and SAC-La doped alloys was observed.

CHAPTER 4

MICROSTRUCTURE EVOLUTION

4.1 SAC Alloy Phase Diagram

Melting point is one of the most important properties of any solder alloy. Since SAC is considered as the best replacement of SnPb, therefore its melting point is of utmost importance for many researchers. For many lead-free solder alloys, the researchers always start with the melting point and then follow the respective liquidus and solidus temperatures of different binary and tertiary systems. SAC, a tertiary system, is based on the Sn-rich, Sn-Cu and/or Sn-Ag binary eutectics.The addition of Cu into SAC performs 2 important functions; it reduces the melting point and improves the wettability performance [Suganuma 2003]. The melting point, as pointed out by many studies and also in this work, is identified to be 217°C.

Millet et al. discovered first the eutectic composition of SAC alloy using DTA [Miller et al. 1994]. The melting temperature of eutectic composition was identified to be 217°C and the elemental composition (wt %) was 4.7 for Ag and 1.7 for Cu in the tertiary system. Similarly, Loomans and Fine [Loomans & Fine 2000] further refined this composition to (wt %) 3.5 Ag and 0.9 Cu by using the thermal analysis monovariant SnCu and SnAg binary eutectics. Afterwards, Moon et al. [Moon et al. 2000] confirmed their work by using simulated DTA curves and thermodynamic calculations with combined thermal analysis. Thus the new melting point

was stated as 217.2 ± 0.2 °C with a standard deviation of 2 σ. The 3D SAC ternary phase diagram is shown in Figure 4.1.

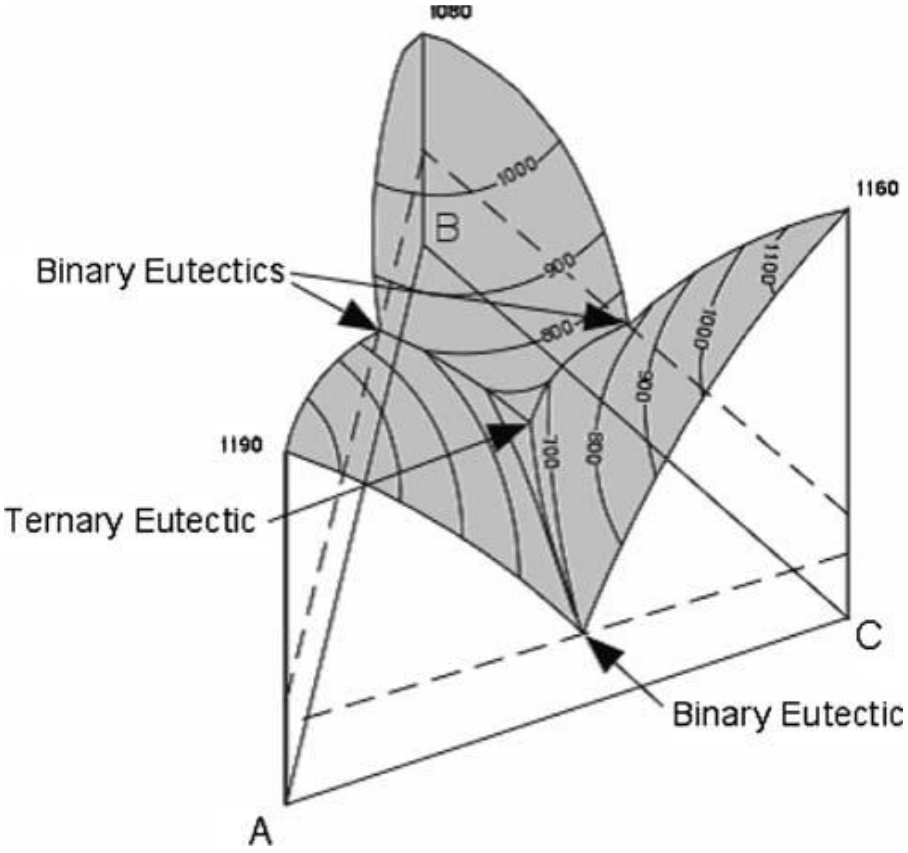

Figure 4.1: Typical 3-D Ternary Phase Diagram

The shaded area shown as contours on the top surface shows isothermal lines in Figure 4.1. These lines converge at the lowest point and are the eutectic point of the ternary alloy system. The main eutectic reaction is formulated as [Zhang 2010],

$$L \rightarrow Ag3Sn + Cu6Sn5 + Sn\ (Matrix)$$

There are three main sectors in the diagram, the three binary eutectic points and the ternary eutectic point, where they represent the phase diagrams of the binary combinations of SnAg, SnCu and AgCu. There are 3 constituent elements in the SAC alloy, each element

concentration (particularly Cu and Ag) will fall to a certain point in the ternary phase diagram. This happens for the alloys which are used as the mainstream substituents for SnPb solder. This is shown as the red box in the ternary phase diagram of SAC in Figure 4.2 and is called as the near eutectic composition [Zhang 2010].

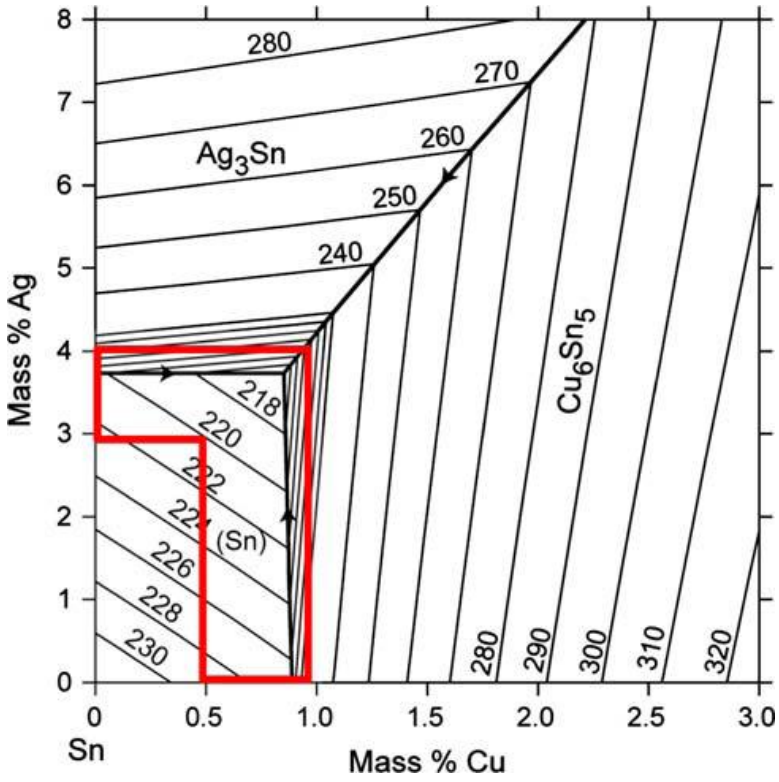

Figure 4.2: Top View of SAC Ternary Phase Diagram

4.2 SAC Alloy Microstructure

The microstructure of the SAC alloy is composed of a soft Sn matrix (almost 90 %) and hard IMCs of Ag and Cu with Sn [C.M.T. Law et al. 2003]. Figure 4.3 shows the SEM image of a SAC alloy: the black zone is the matrix mainly composed of Sn and the white particles are the IMCs. These IMCs, rich in Ag and Cu, are brittle in nature in comparison to the soft Sn matrix and dictate the mechanical properties of lead-free solders [Wu et al. 2004].

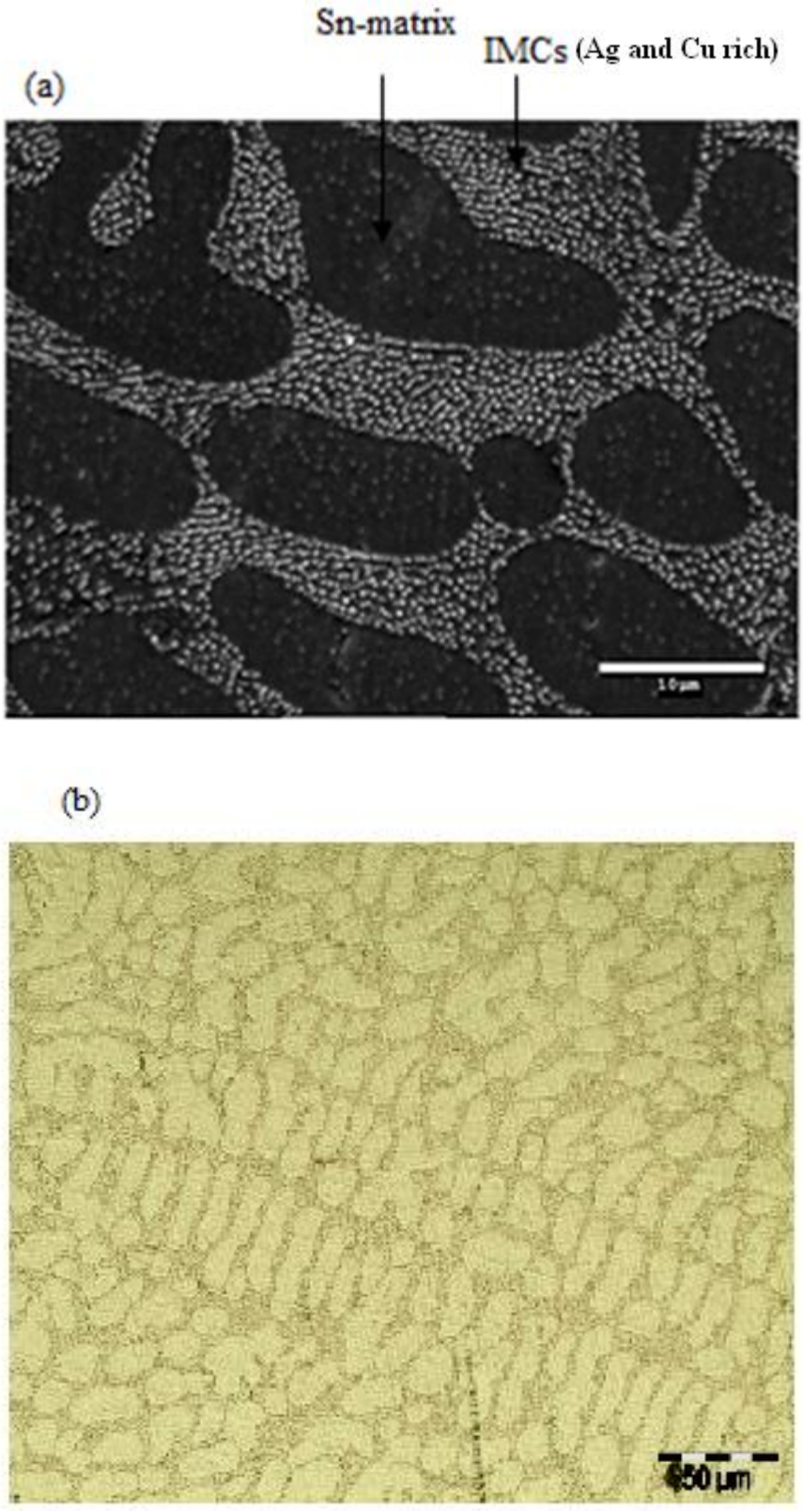

Figure 4.3: (a) SEM and (b) Optical Microscope images

The size of these particles depends on many parameters such as alloy composition, cooling rate and environmental conditions. In order to constrain the size of these IMCs, many researchers attempted a change in the cooling rate during the solidification process [Lewis et al. 2002 and Kim et al. 2002]. A fast cooling rate can generate a fine microstructure but in many cases, it is not feasible because of the large thermal stresses in the substrates. Sn being the most important constituent (96.5 wt %) is very important to describe in detail and therefore the detailed crystal structure and other properties are given in Appendix A along with some characteristics of Ag and Cu.

As the core alloy is the same, SAC305 but the La composition varies so it is predicted that the size of these IMCs varies for all SAC-La compositions.

4.3 Intermetallic Compounds

As discussed above, SAC alloy has brittle IMCs and soft β-Sn matrix. This is of utmost importance to characterize these phases for as cast and thermally aged alloys.The shape, size and spacing of these particles depend on many parameters including cooling rate, alloy composition and thermal aging etc. Slow cooling can create the particles that vary from needles of an approximate size of 10 microns [Wiese et al. 2003] to about sub micrometer size with spherical shapes (fast cool). Thus the cooling rate provided during solidification can play a major role in controlling these IMCs. In some situations, the interfaces between the Ag_3Sn plate and β-Sn phase play an important role in providing a preferential crack propagation path [Henderson et al. 2002 and Kang et al. 2003].

Modern electronic devices are subjected to severe thermal conditions varying up to 200°C. Moreover, many assemblies are composed of different electronic materials with wide

range of thermal expansion coefficients which causes extra heat generation. Therefore, different compositions of the La are tested in this study to get an optimum SAC-La alloy and mechanical properties are found in varying environmental conditions.

The high temperatures selected for aging are 150°C and 200°C and aging times of 10h,25h, 50h, 100h and 200h are tested. Specimens are exposed to these conditions in a furnace after polishing and etching. They are analysed at the end of each aging time and are put back in the furnace after analysis. Elemental mapping and chemical composition of each phase are achieved using an SEM equipped with an EDS system. Gauge area is focused during the entire period of study.

4.3.1 EDS Mappings

As previously mentioned, IMCs consist of Ag-Sn and Cu-Sn. An Oxford EDS system placed in the SEM enabled to realize elemental mappings for every specimen. The spatial distribution of Ag, Cu and Sn could be visualized in the IMCs; it is shown in Figure 4.4.

In order to follow the growth of these IMCs, another SEM image and spatial distribution of these elements is provided in Figure 4.5 for 100 hours thermally aged specimen. The Cu based IMCs are much darker than Ag based IMCs, as also reported in [Allen, Notis, Chromik, Vinci, et al. 2004] and are therefore easily distinguished and confirmed by the EDS for two different zones as marked A and B in Figure 4.5. About 25 IMCs were analyzed and an average measurement for the atomic % is provided in Table 4.1. The EDS elemental peaks are provided in Figure 4.6 for two zones marked as A (Cu_6Sn_5) and B (Ag_3Sn). The atomic % may not confirm the exact ratio for Ag_3Sn and Cu_6Sn_5 IMCs due to the limitation of our experimental

setup. The tip takes in consideration more Sn along the depth upto few microns which may not be the actual depth of these IMCs.

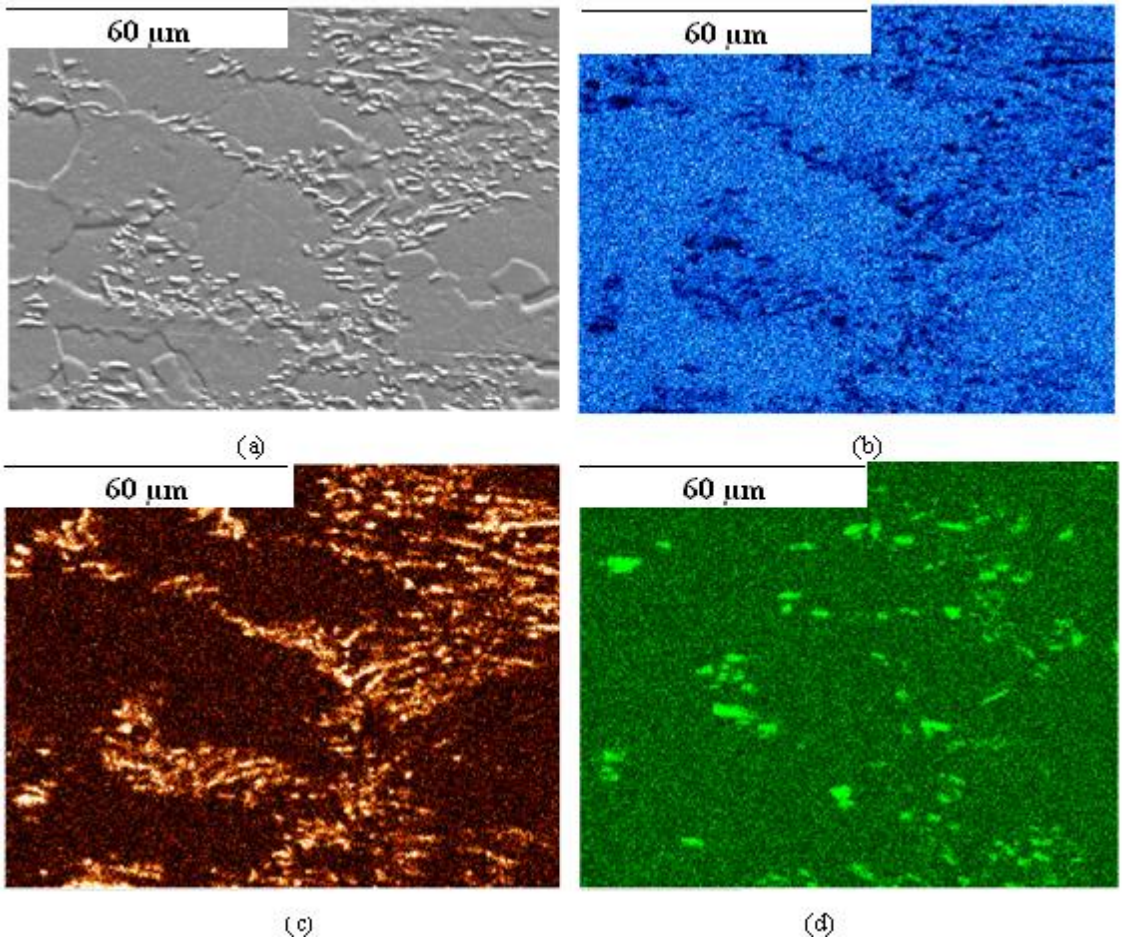

Figure 4.4: EDS elemental mappings of SAC (a) SEM image (b) Sn (c) Ag (d) Cu

Table 4.1: Atomic composition of IMCs

IMCs	**Atomic %**		
	Sn	Ag	Cu
Ag_3Sn	74 +/- 0.7	26 +/- 0.7	x
Cu_6Sn_5	52 +/- 0.4	x	48 +/- 0.4

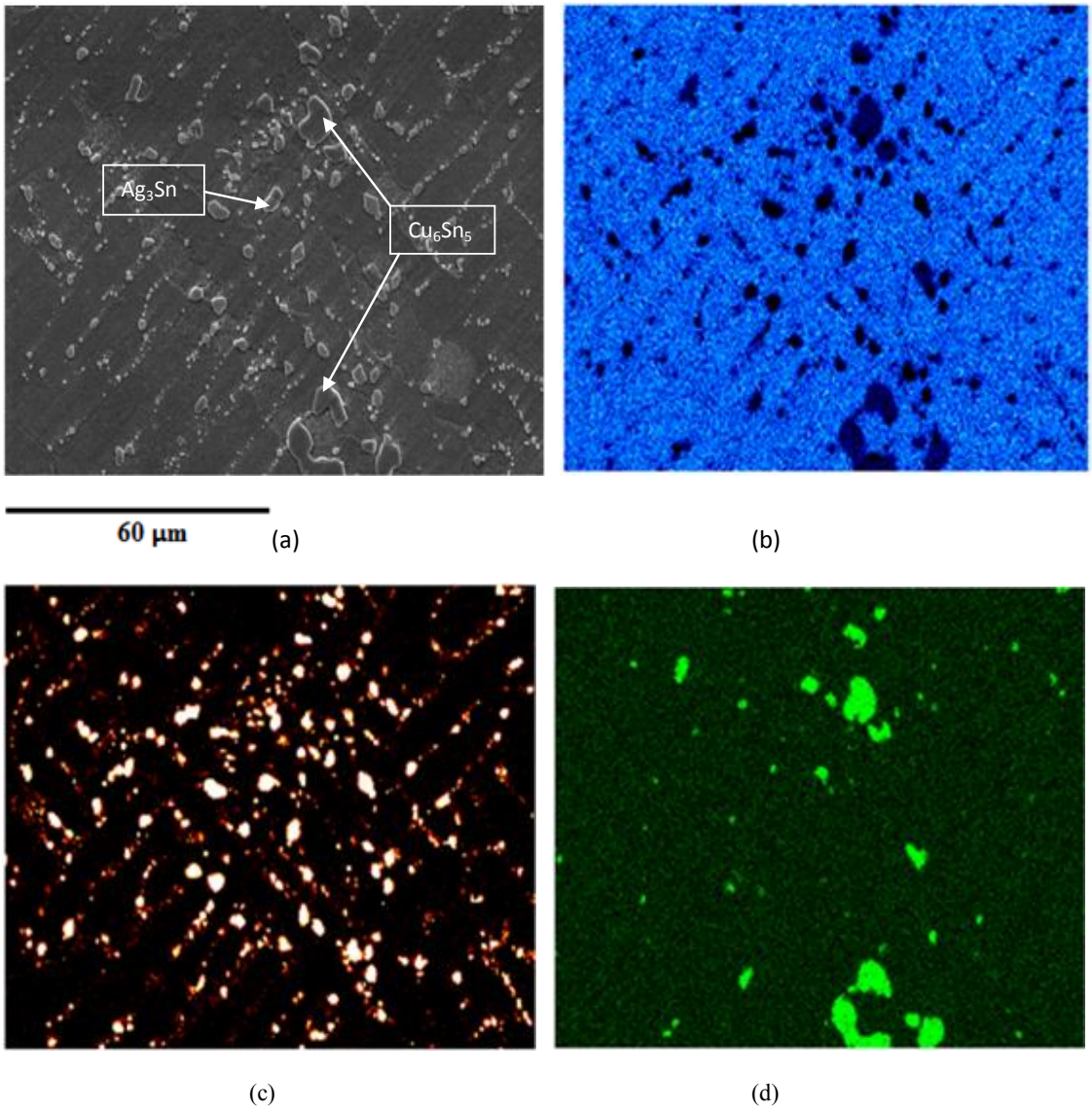

Figure 4.5: EDS elemental mapping of SAC-La after 100h thermal aging (a) SEM image (b) Sn (c) Ag and (d) Cu

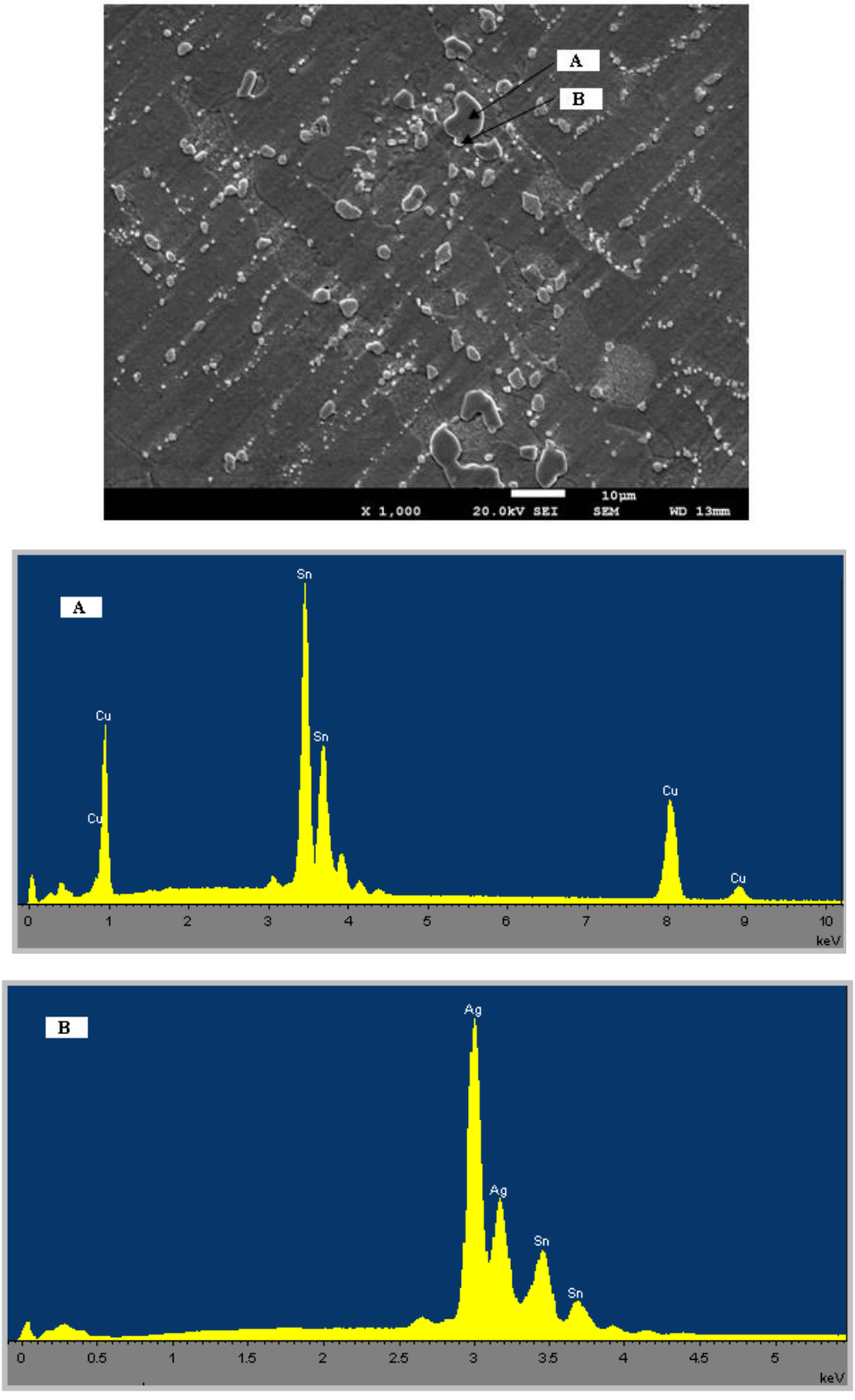

Figure 4.6: EDS peaks for the Cu_6Sn_5 IMCs (A) and Ag_3Sn IMCs (B)

4.3.2 Coarsening Process

Thermal aging causes the evolution of both Ag_3Sn and Cu_6Sn_5 IMCs and this process is governed by $r^3 \propto t$ where r is the average radii of the IMCs particles and t is the isothermal aging time [Allen, Notis, Chromik & Vinci 2004]. Both these two types of particles coarsen at different rates due to different rate-controlling mechanisms. The diffusion rate of Cu into Sn is higher than the diffusion rate of Ag into Sn [Allen, Notis, Chromik, Vinci, et al. 2004]. Therefore, with time, the coarsening of Cu_6Sn_5 is much higher than Ag_3Sn due to which Cu_6Sn_5 IMCs can be easily differentiated from Ag_3Sn IMCs. In [T. Chen & Dutta 2008], this has been reported that the size of Cu_6Sn_5 IMCs is much bigger than Ag_3Sn IMCs in SAC alloy.

The EDS mapping for SAC-La alloy after thermal aging was already presented in Figure 4.5. Contrary to Ag_3Sn particles, which have a normal increase with submicron size, the thermal evolution of Cu_6Sn_5 IMCs shows a significant growth up to few microns. This is consistent with [T. Chen & Dutta 2008]. The rapid growth starts after 50 hours of thermal aging at 150°C and 200°C. An SEM FEG Jeol 7001F is used to collect the images of each composition at different resolutions, in the initial state and after different aging times. The “as cast” and “thermally aged” SEM images for SAC and SAC-0.5La alloy are given in Figure 4.7. With thermal aging, coarsening of both Ag-Sn and Cu-Sn IMCs takes place with a rate depending on the temperature applied and aging time. It could be easily concluded from the micrographs that the coarsening rate for lanthanum doped alloy is much slower than the undoped alloy.

4.4 Particles Size Evaluation

Microstructure evolution is observed in terms of the IMCs average particle size, its volume fraction and interparticle spacing.

These measurements are evaluated as a function of aging time, aging temperature and lanthanum composition.

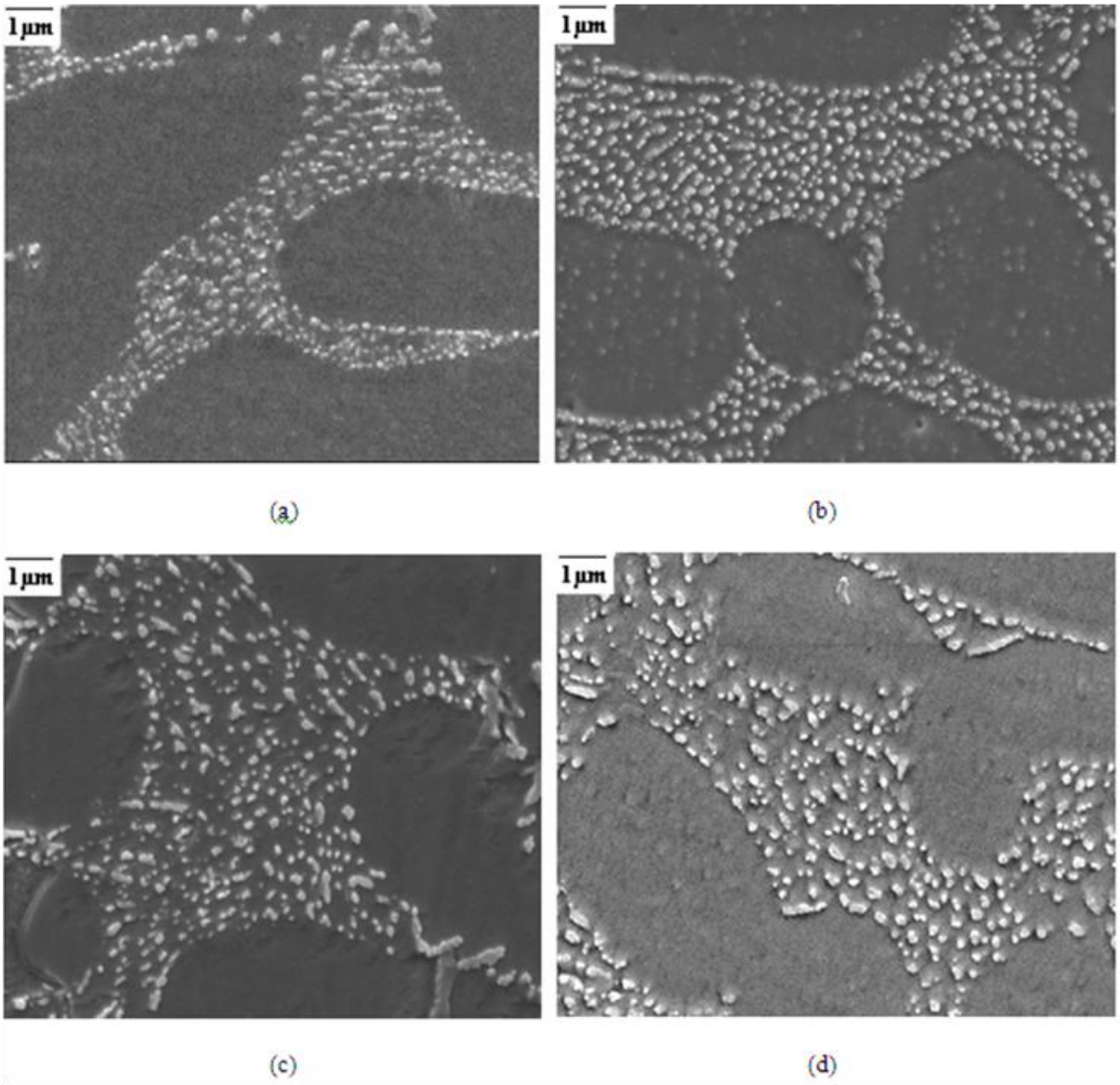

Figure 4.7: SEM images of (a) SAC (b) SAC-La before thermal aging and (c) SAC (d) SAC-La after thermal aging

ImageJ software (as given in Figure 4.8) is used to measure the average particle size at every aging interval. At least 3 images of every composition at different magnifications are provided for measurements, see Figure 4.9 (X represents La composition).

Manual means are also used to measure the average particles size in terms of average surface area using the [ASM handbook standards Vander Voort 2004]. It is plotted in Figure 4.10 as a function of lanthanum doping for the as cast and Figures 4.11-4.12 for the thermal aging at 150°C and 200°C respectively.

Further, in Figures 4.13-4.14, the average IMCs particles size is provided as a function of aging time at 150°C and 200°C respectively. An average measurement is done for the particles spacing and no significant difference is found for all compositions tested. This is consistent with [Pei M. and Qu J. 2007b]. Thus lanthanum doping did not change the average interparticles spacing for IMCs.

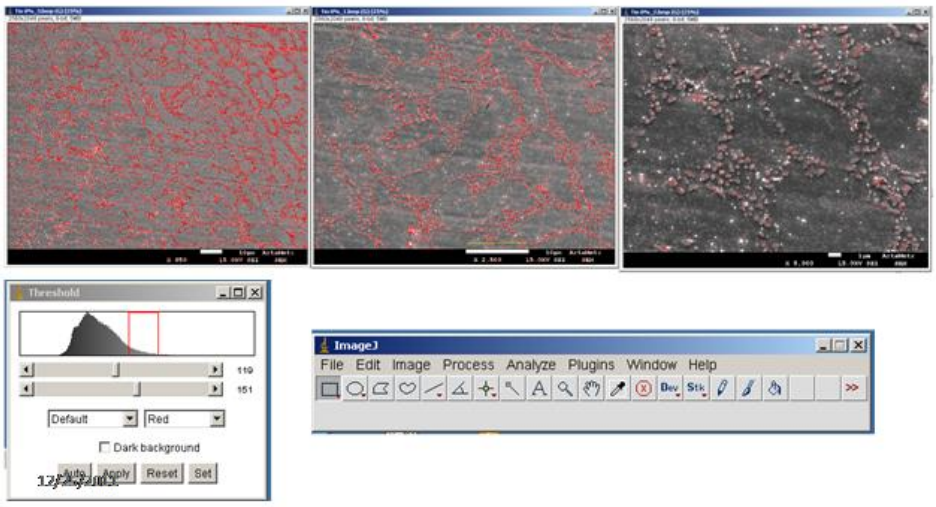

Figure 4.8: ImageJ particles size analysis

X=0

Image	Count	Total Area	Average Size	Perimeter	Circularity	Solidity
850x	56928	700312	12.3	11.6	0.865	0.881
2500x	24091	349925	14.2	12.9	0.851	0.874
5000x	6631	88480	13.4	16.9	0.715	0.781

X=0.01

Image	Count	Total Area	Average Size	Perimeter	Circularity	Solidity
850x	33790	364932	10.8	13.9	0.756	0.796
2500x	13651	165177	12.1	12.9	0.700	0.760
5000x	6631	75593	11.4	14.7	0.718	0.785

X=0.05

Image	Count	Total Area	Average Size	Perimeter	Circularity	Solidity
850x	28742	296042	10.3	12.8	0.789	0.812
2500x	11232	125798	11.2	11.1	0.723	0.765
5000x	4576	46217	10.1	12.9	0.810	0.763

X=0.5

Image	Count	Total Area	Average Size	Perimeter	Circularity	Solidity
850x	33790	202740	6.0	6.6	0.781	0.787
2500x	13651	103747	7.6	8.3	0.790	0.831
5000x	6631	41775	6.3	6.1	0.748	0.815

Figure 4.9: Particles size analysis at 850X, 2500X and 5000X

Figures 4.10-4.12 indicate a drastic decrease in the particle size due to lanthanum doping whereas Figures 4.13-4.14 show that the coarsening rate of these IMCs is smaller for the La doped alloys than the undoped alloys.

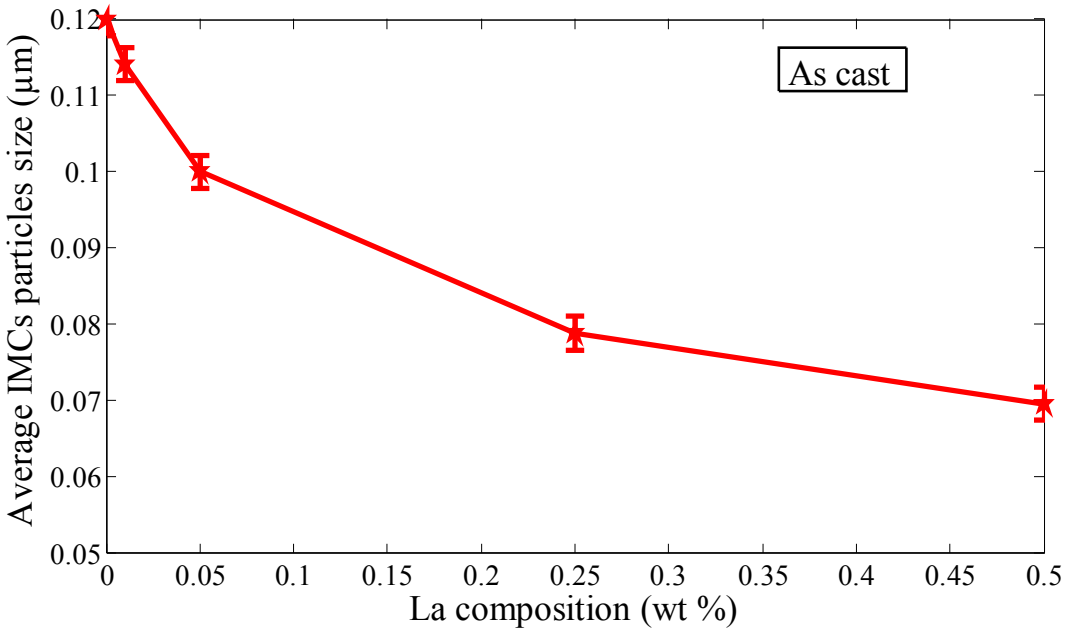

Figure 4.10: Average IMCs particles size vs. La composition (as cast)

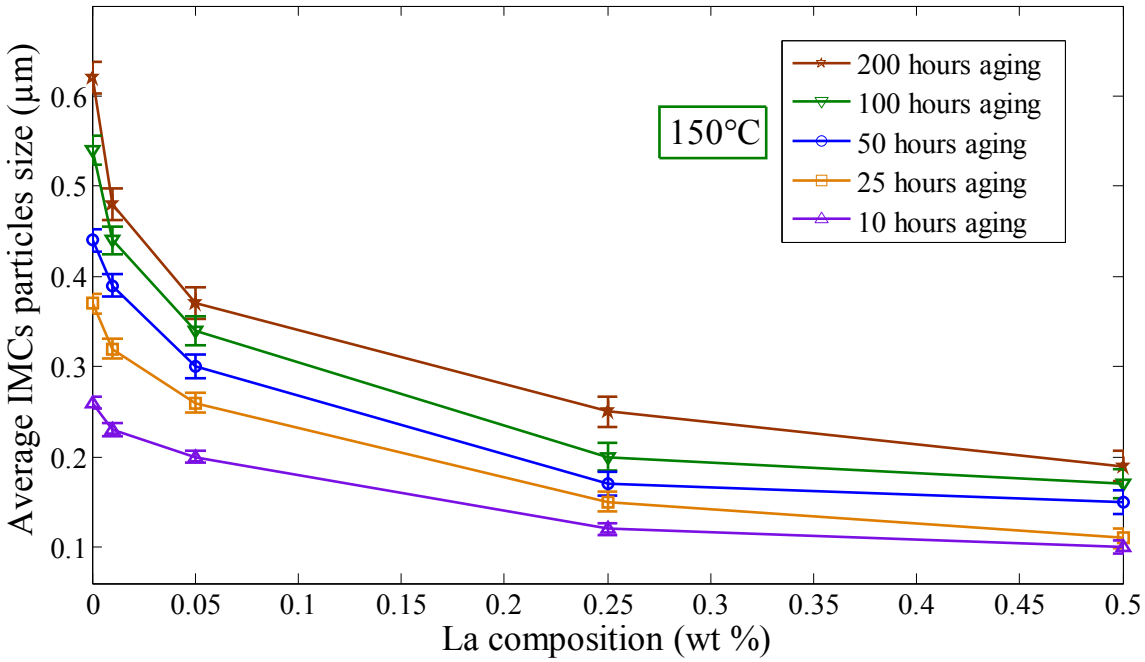

Figure 4.11: Average IMCs particles size vs. La composition (at 150°C thermal aging)

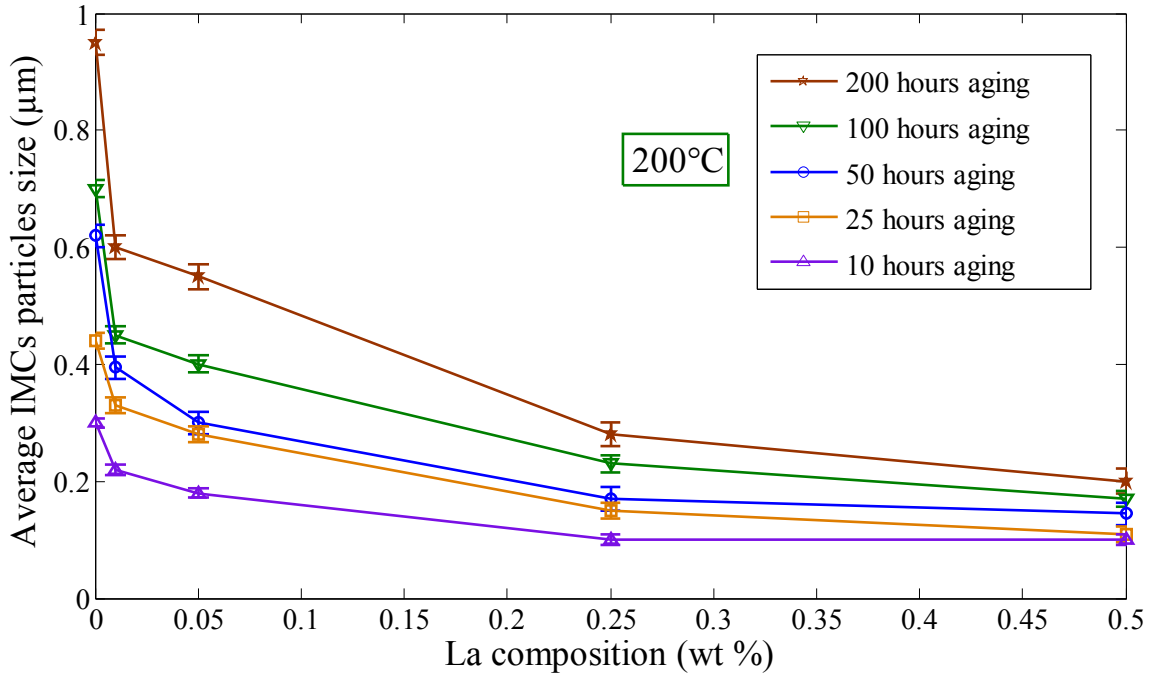

Figure 4.12: Average IMCs particles size vs. La composition (at 200°C thermal aging)

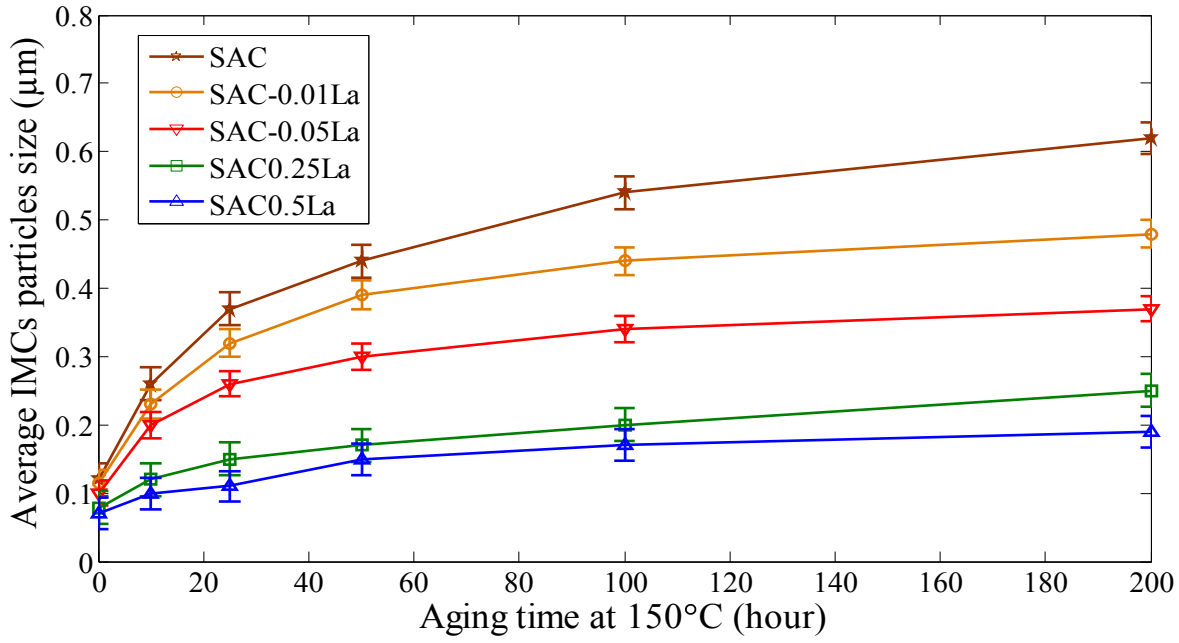

Figure 4.13: Average IMCs particles size vs. aging time at 150°C

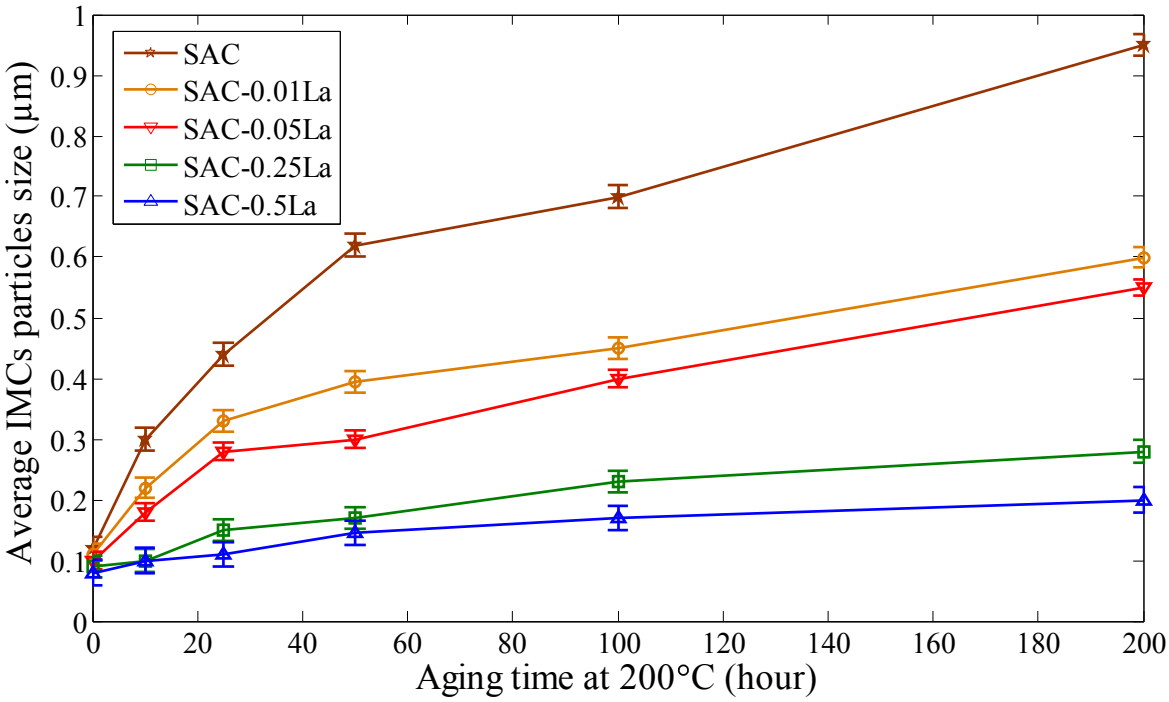

Figure 4.14: Average IMCs particles size vs. aging time at 200°C

4.5 Interparticle Spacing

In some situations the interparticle spacing can play a major role in affecting the dislocations movements in the materials. In [Han Y. D. et al. 2009], it has been studied that these interparticle spacing can play a major role in the back stress in lead-free solder alloys. There has been several stoichiometric studies which show that the volume fraction of IMCs in the eutectic Sn3.5Ag alloy composition is 0.07 [Dutta 2003]. In our study, the Ag and Cu amounts are kept constant for all compositions and also the La is limited to a maximum of 0.5 (wt%) , it is logical to assume that the IMCs volume fraction would be constant [Min Pei 2007]. Thus if the IMCs are considered to be spherical and also uniformly distributed in the matrix then the average interparticle spacing can be easily calculated from the volume fraction at the eutectic region.

These interparticle spacings are calculated and tabulated below (Table 4.2). The interparticle spacing, which is the side to side distance, is not changing with La composition. This is interesting as it was shown above that the La doping drastically reduces the IMCs size both for as-cast and thermally aged specimens. This could be described as; the high La doping causes reduction in size which increases the number of particles and keeping constant volume fraction provides almost constant interparticle spacing. This also leads to the fact that the high La doping would lead to higher volume fractions in the eutectic region [Min Pei 2007].

During the solidification process of the solder alloys, the IMCs are formed first [Min Pei 2007] because of their low undercooling requirements. Once these IMCs are formed, small amount of Sn covers them as a layer and then the Sn dendrites push them to form the eutectic region and the fact that the inter-particle spacing does not change with La doping seems to indicate that the thickness of this tin layer covering the particles is not affected by the La doping.

Table 4.2: Calculated interparticle spacing

RE doping (% wt)	0	0.05	0.25	0.5
Particle Spacing (μm)	0.05	0.06	0.05	0.05

4.6 Grain Size

Grain size is an important parameter in materials history. A fine grain material is expected to have higher mechanical properties including yield stress, tensile strength and creep behavior as compare to a coarse grain material. As the cooling rate during solidification play an

important role in controlling the grain size, therefore, a constant cooling rate was used for all alloy compositions as described in chapter 3 (Experimental Design).

4.6.1 Grain Size Evolution

Grain size is measured for the "as cast" samples and then continuously followed during thermal aging. Figure 4.15 shows the grain size images for SAC and SAC-0.05La as cast samples. Optical microscopy with cross polarized light is used for these images. With the help of cross polarized light, grains can be observed as different shade under the microscope. A significant decrease in the grain size, by the addition of lanthanum, can be seen.

Grain size, as a function of lanthanum composition, is plotted in Figure 4.16 for the as cast and in Figures 4.17-4.18 for the thermally aged specimens at 150°C and 200°C respectively. A huge refinement is observed from the plots.Figures 4.17-4.18 describe the grain size as function of aging time at 150°C and 200°C respectively. Since the number of grains are not too big, error bars are provided in both plots. Almost no change in grain size has been experienced due to thermal aging. For the Sn3.5Ag eutectic alloys, some studies have found that due to the pining effects of the Ag_3Sn particles, temperature aging does not affect the grain size in the un-doped case [AA Telang et al. 2002 and AU Telang et al. 2004]. It concludes that lanthanum doping not only refines it but also restricts its growth at high temperatures. This is consistent with [Pei & Qu 2008]. This refinement is due to the particular effect of lanthanum doping termed as lanthanum adsorption and is described in detail in Chapter 1 as introduction.

For the grain size measurements, there is almost one single grain in the width of the sample with no La doping. Therefore, the specimen width (8mm) is used as the grain size for un-

doped samples.Figures 4.19-4.20 show that the optimal La doping to minimize grain size is around 0.05%, which is consistent with many researchers [Pei M. and Qu J. 2007b and Wu et al. 2004].

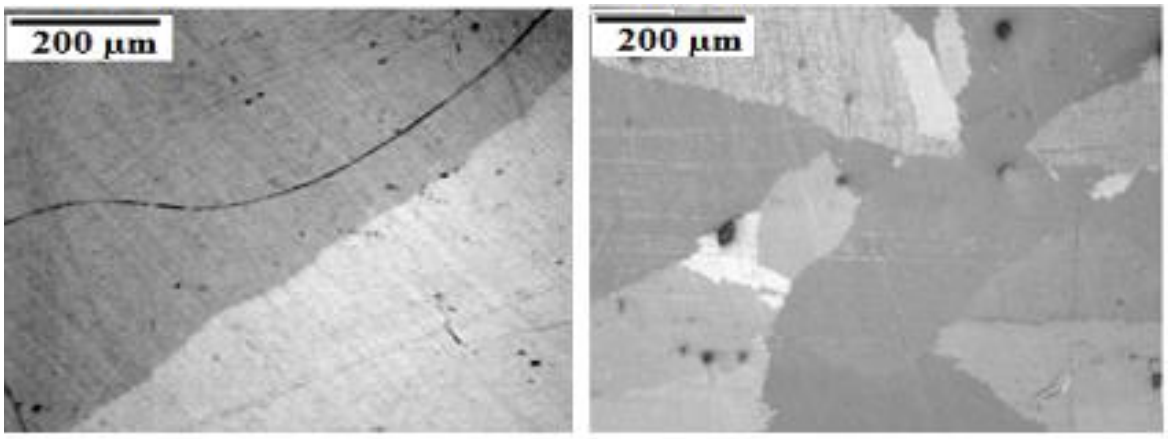

Figure 4.15: Optical microscope images of SAC (left) and SAC-La (right)

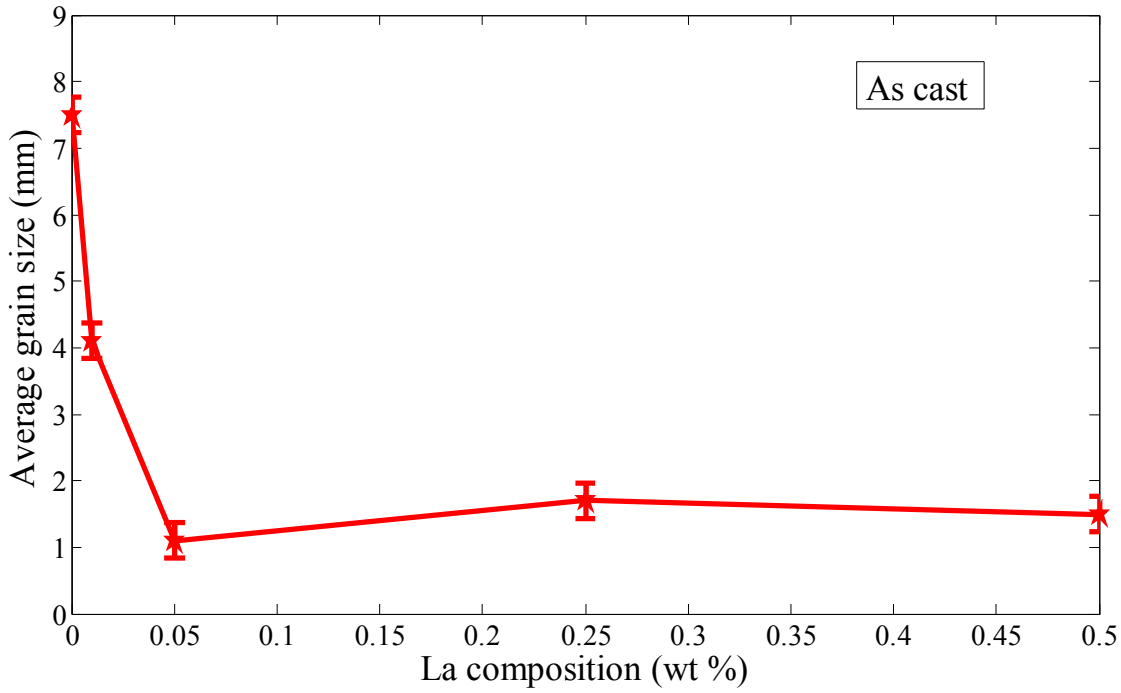

Figure 4.16: Average grain size vs. La composition (as cast)

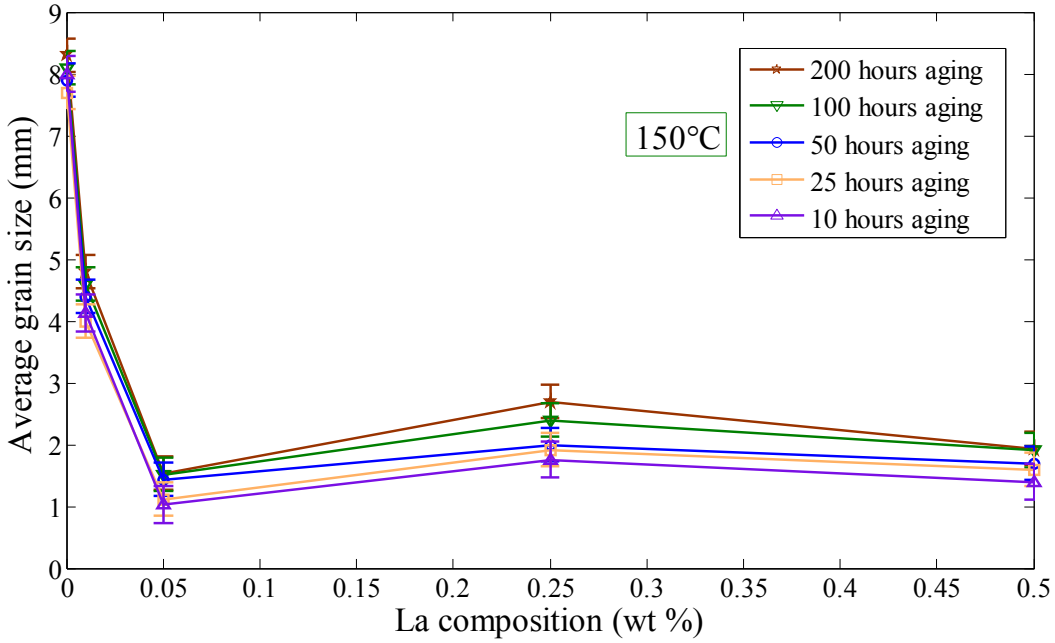

Figure 4.17: Average grain size vs. La composition (at 150°C thermal aging)

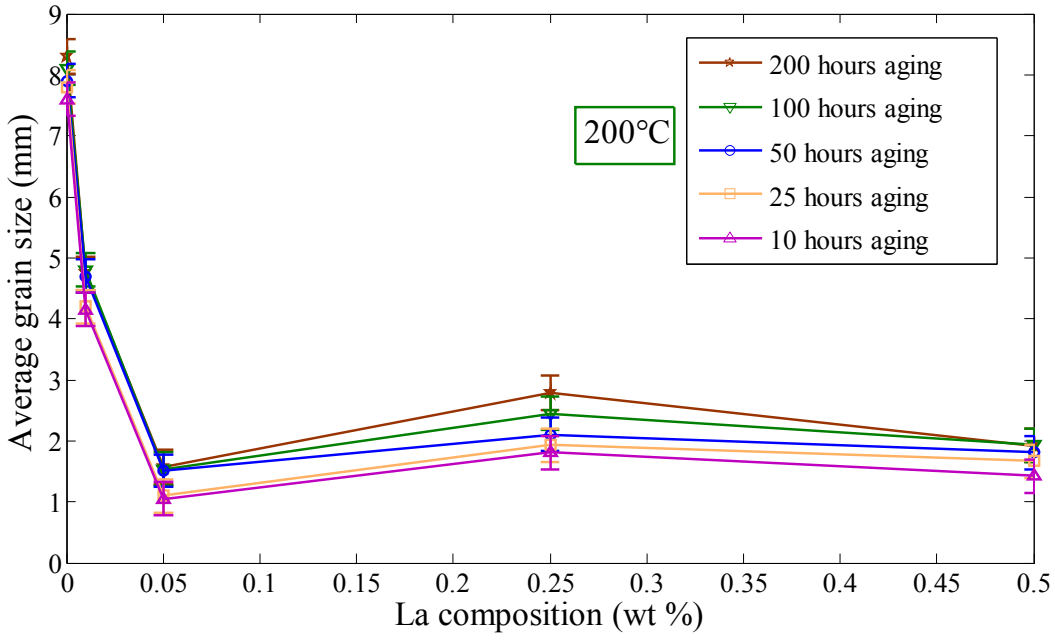

Figure 4.18: Average grain size vs. La composition (at 200°C thermal aging)

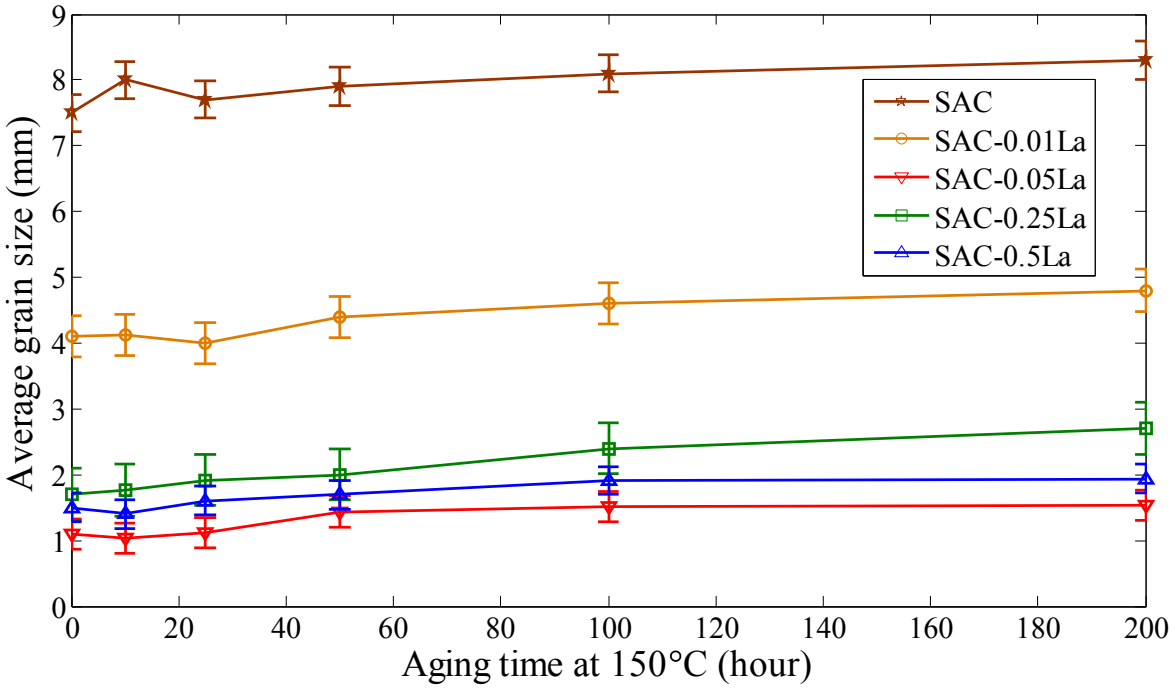

Figure 4.19: Average grain size vs. aging time at 150°C

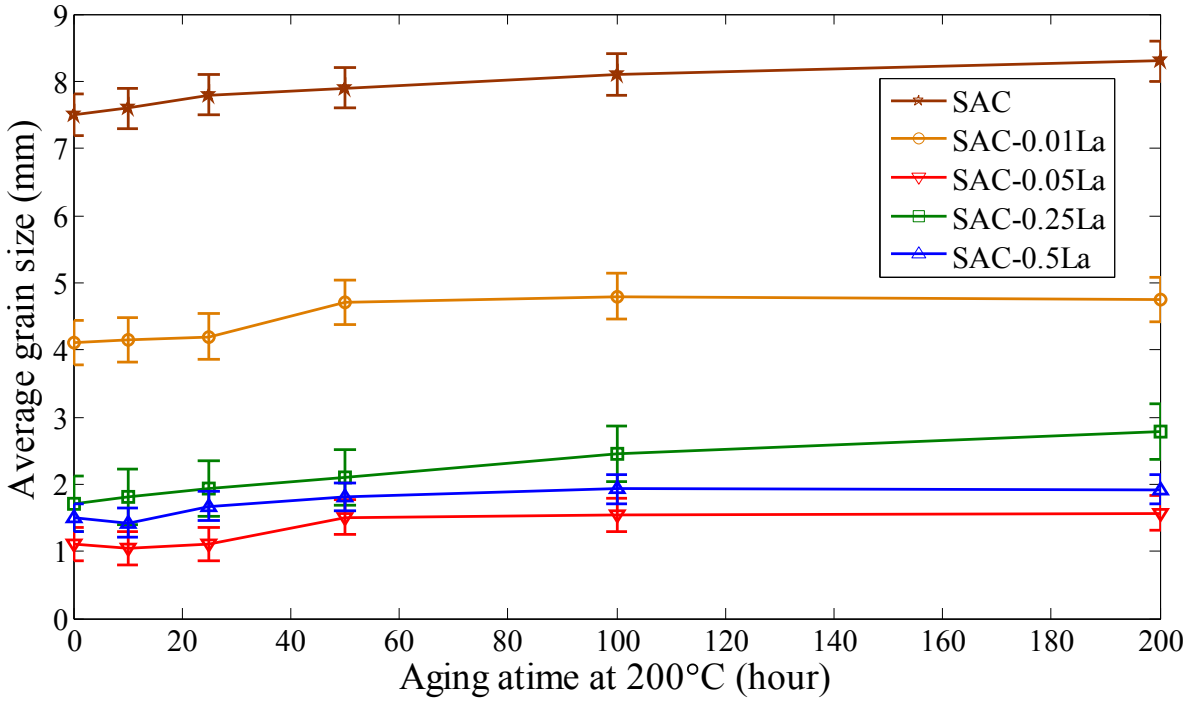

Figure 4.20: Average grain size vs. aging time at 200°C

4.6.2 Grain Size Measurements

Grain size measurement is complicated by a number of factors. First, the three-dimensional size of the grains is not constant and the sectioning plane will cut through the grains at random. Thus, on a cross-section, we will observe a range of sizes none larger than the cross section of the largest grain sampled. Grain shape also varies (particularly) as a function of grain size. Grain size measurement is also complicated by the different types of grains that can be present in metals, although their fundamental shapes are the same. For example, in body-centered cubic metals such as Fe, Mo, and Cr, we have ferrite grains; in face-centered cubic metals, such as Al, Ni, Cu, and certain stainless steels, we have austenite grains.

One of the difficulties was that there are not many grains in the SAC alloy specimens to take a good average measurement. ASM handbook 9 was used and international grain size measurements techniques were followed in this study which is provided in APPENDIX D for further reading.

4.7 Lanthanum Presence

EDX study has shown that La exists in lead-free solder materials on the natural surface or in the form of La-Sn Intermetallics [Min Pei 2007]. Moreover, it is reported in [Min Pei 2007] that La may be present in elemental form but they could not identify it due to the experimental limitations. In this work, La is confirmed to be present in the elemental form in the bulk alloy. The EDS elemental mapping for La is given in Figure 4.21. This elemental form is dispersed thoroughly in the bulk alloy and is mainly responsible for changing the overall microstructure of the alloy [Min Pei 2007].

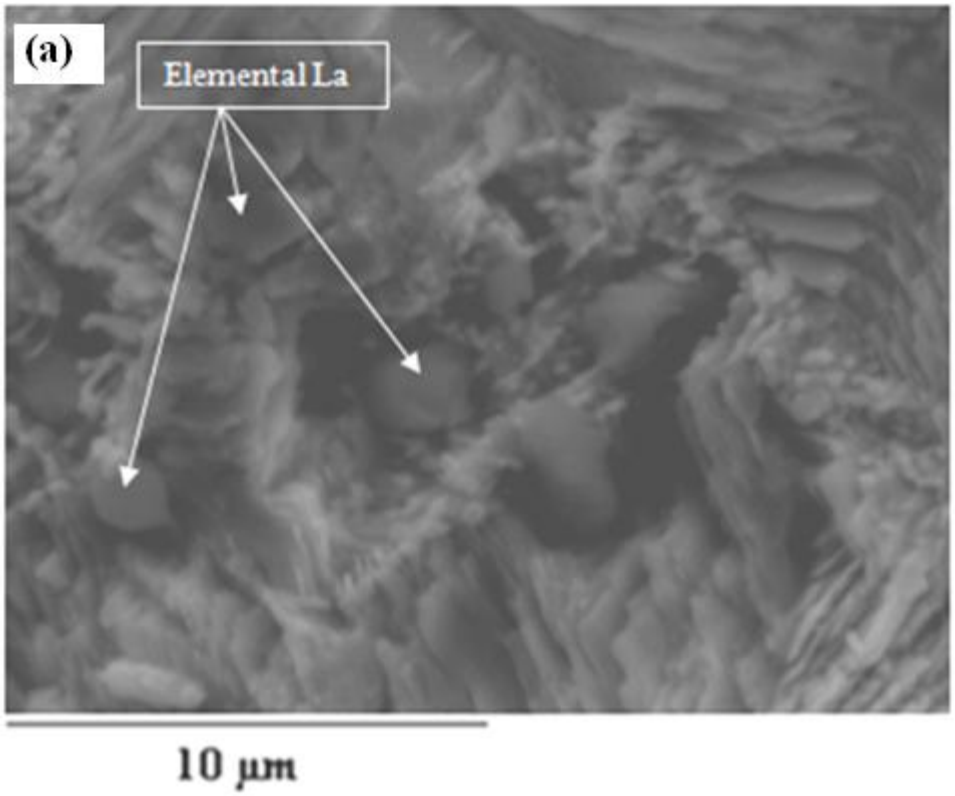
(a)
Elemental La
10 µm

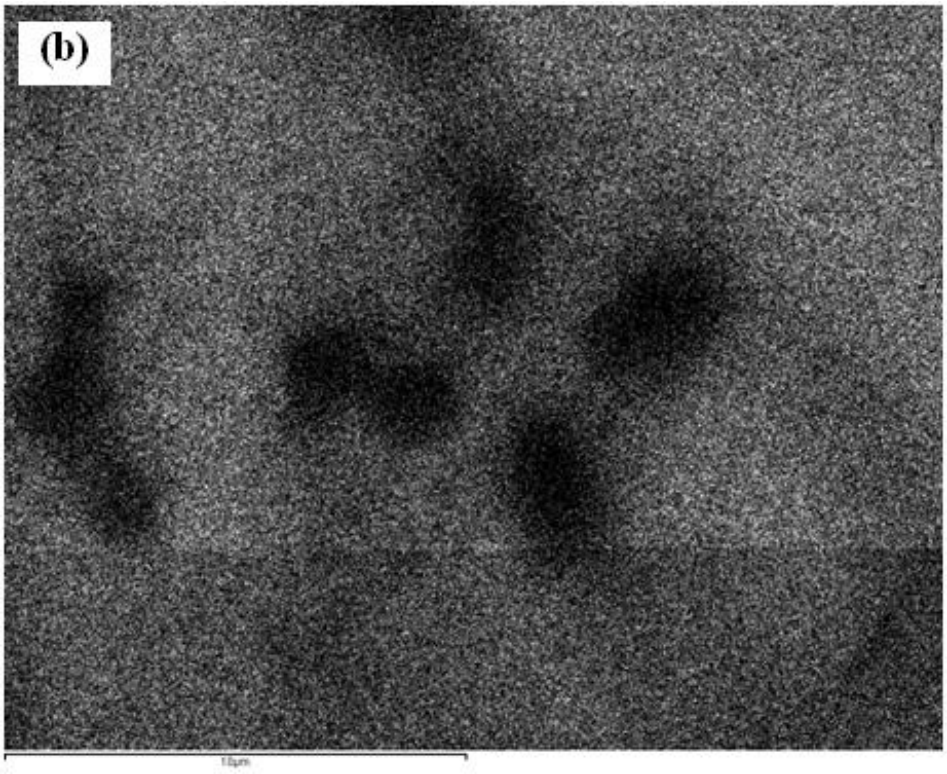
(b)

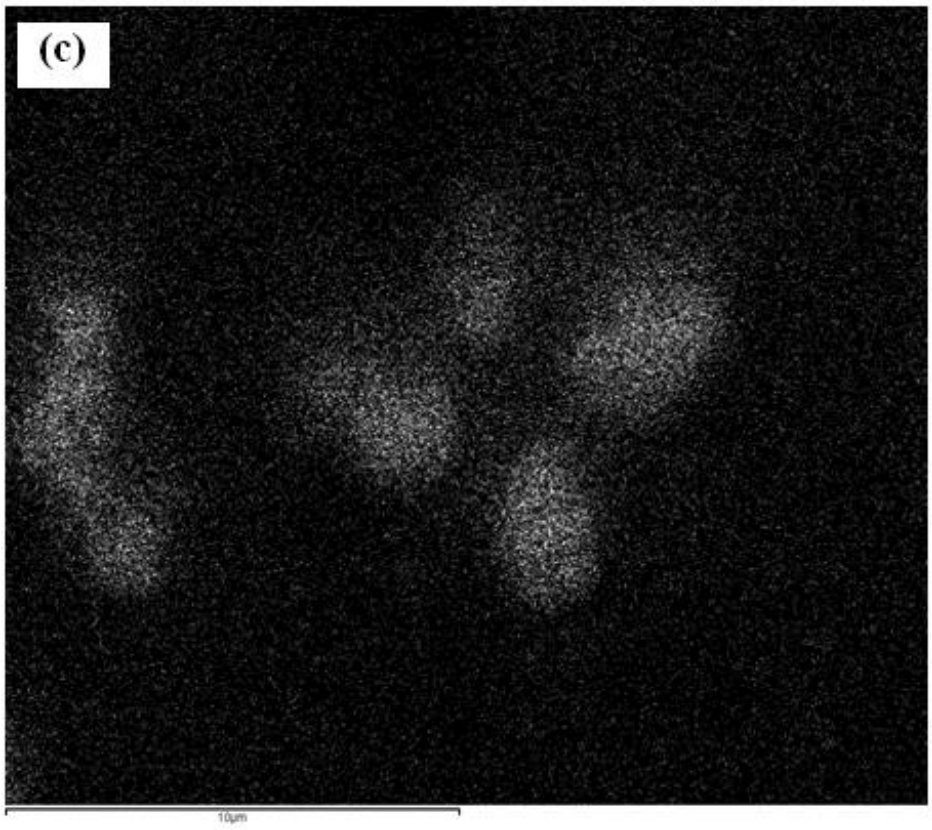

Figure 4.21: EDS elemental mapping of SAC-La (a) SEM image (b) Sn and (c) La

4.7.1 At Specimen Surface

RE elements in general are called the surface active elements. Therefore, during solidification, some of the La will move to the surface. Min Pei [Min Pei 2007] has shown that comparing with no doped condition, micron size pores are seen on the unpolished surface at doped sample. Similarly some EDX studies have been performed to trace the presence of La on the natural as-cast unpolished surface and a higher concentration is being identified. Several elemental mappings have been provided in different studies to confirm it. Moreover, a uniform distribution of La is present on the natural surface. This EDS mapping is given in Figure 4.22.

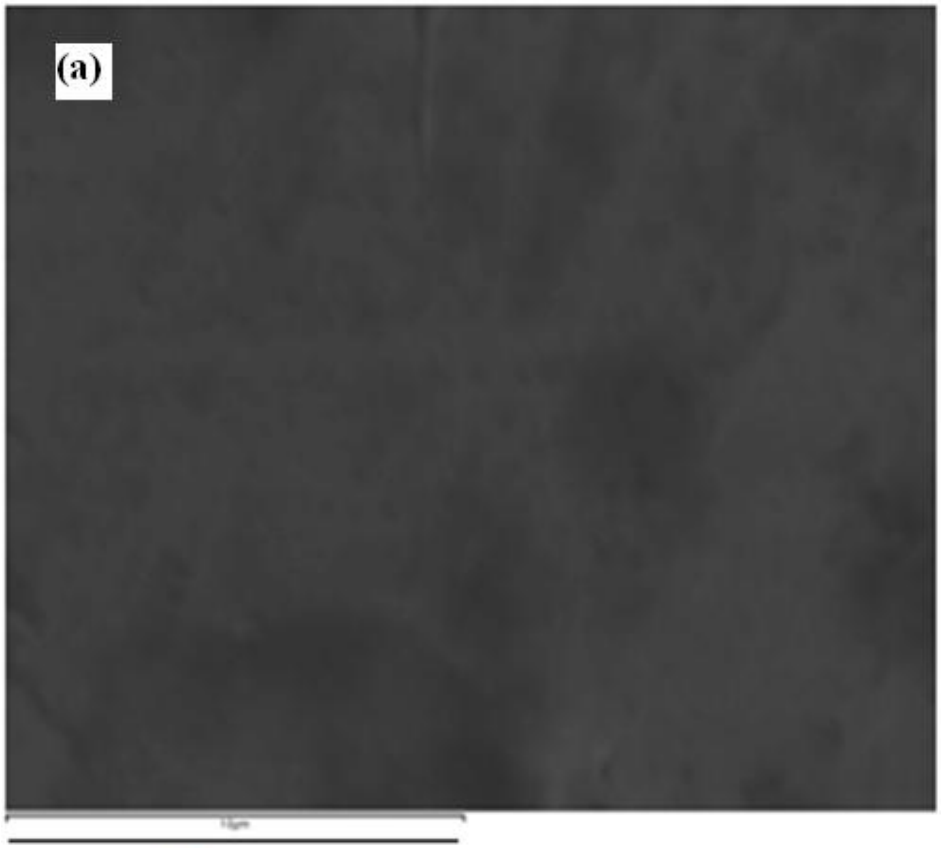
(a)
20 um

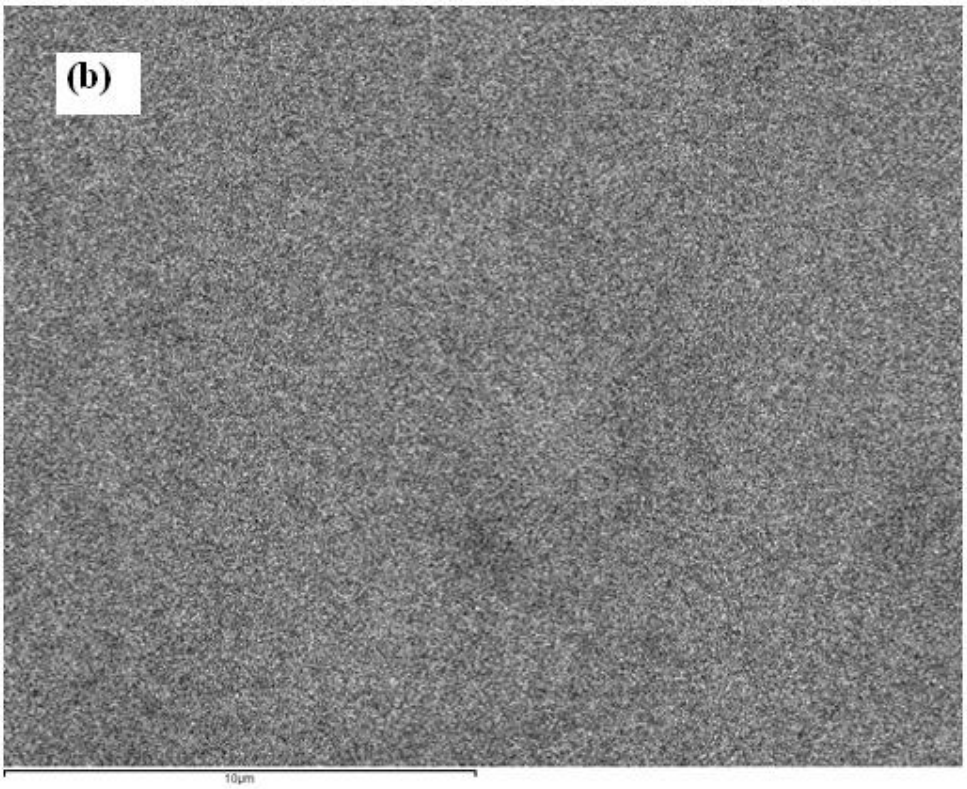
(b)

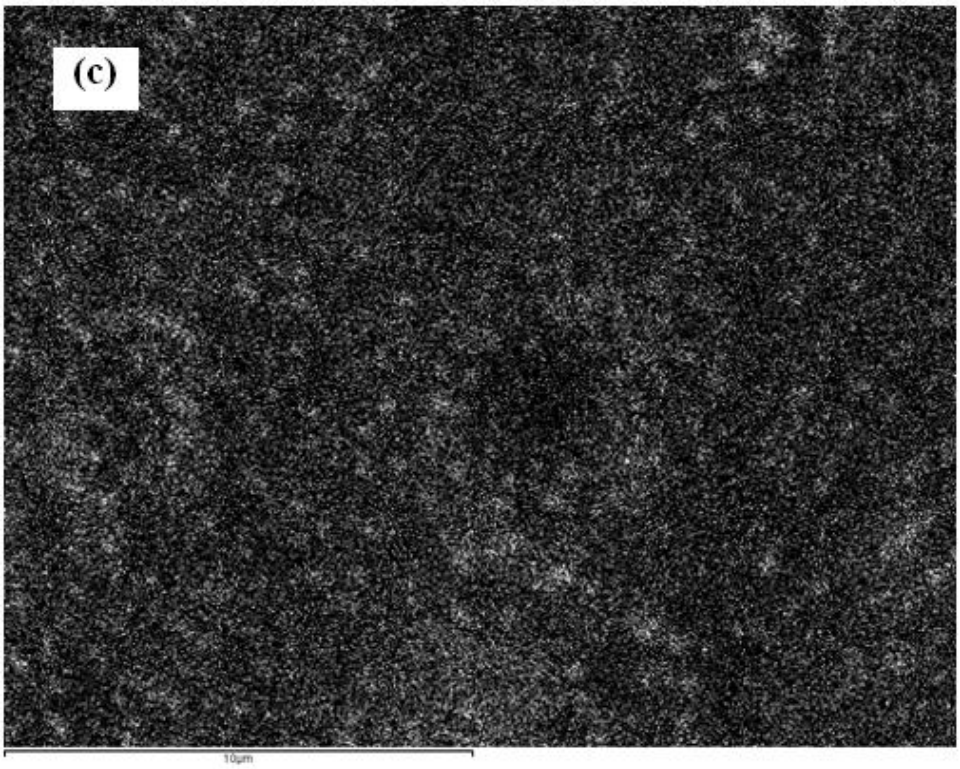
(c)
10µm

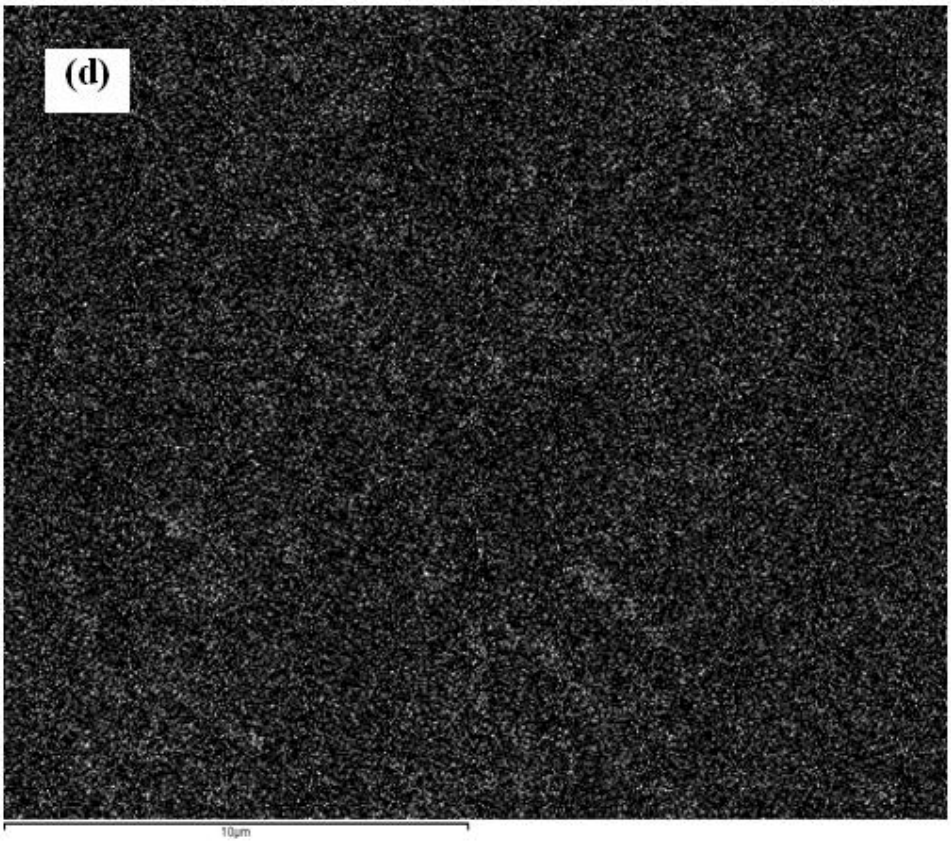
(d)
10µm

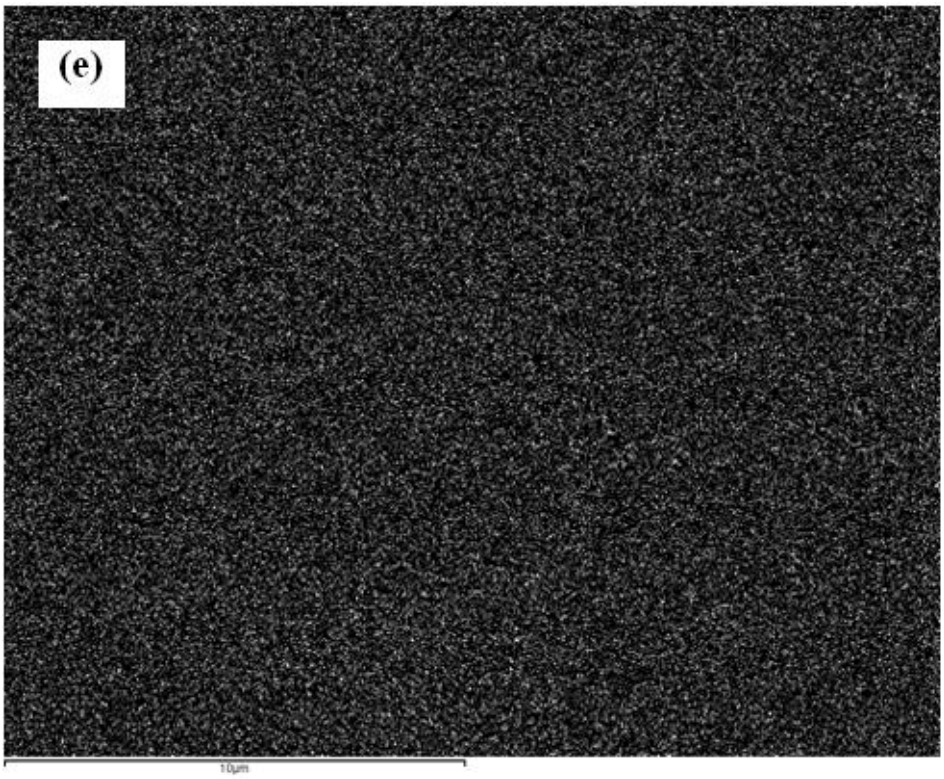

Figure 4.22: EDS mapping of SAC-La alloy (a) SEM image (b) Sn (c) Ag (d) Cu and (e) La

The higher concentrations of elemental La have two major effects on the natural surface. After making the solder joint, La present at the interface will make bonds with other materials and hence plays an important role in improving the solderability of solder alloys. On other hand, higher concentration on the surface means less La within the bulk.

4.7.2 In the Intermetallics

Other than the presence of La on the natural surface, La forms its own intermetallic compounds with Sn. As mentioned in [Dudek et al. 2006], La in SAC solder will form the La-Sn IMCs. The heat flow vs. temperature melting curves show that the melting temperature of this

IMC is ~335°C [Dudek et al. 2006]. The IMC has a complex 3D branch structure, which is usually shown as clusters of snowflakes [ZG Chen et al. 2002] in SEM images.

Previous research found that high doping of La will cause $LaSn_3$ IMC flakes to aggregate along grain boundaries and adversely affect the mechanical properties of solder alloy [Xia et al. 2002 and Z. Chen et al. 2003]. Following these results, 0.5wt% of La was set as the upper limit of this study. However this composition may change by changing the cooling rate which significantly controls the size of these $LaSn_3$ IMCs.

4.8 Summary

As described earlier, SAC and SAC-La alloys consists of soft Sn matrix and hard and brittle IMCs. These IMCs dictate the overall mechanical properties of solder alloys. This becomes more critical when solder joints are exposed to high temperature during service. Thermal coarsening (also known as thermal aging) takes place which increases the diffusion of Ag and Cu into Sn. This diffusion causes evolution of the IMCs which grow at high speed. A quantitative measure of this data is presented in terms of IMCs average size, interparticles spacing and volume fraction.

Lanthanum plays an important role in controlling the coarsening rate of IMCs at thermal aging of 150°C and 200°C. EDS elemental mapping was used to show schematically the chemical composition of each phase in the matrix and IMCs.

Grain size is the other parameter that plays a major role in overall mechanical properties of solder alloys. Lanthanum doping has important effects of refining the grains not only for as-cast case but also at elevated temperatures. ASM handbook 9 is used for measuring the average grain size and is presented for varying environmental conditions. Grain size was continuously

measured during thermal aging. Almost no coarsening of grain size was experienced both for SAC and SAC-La doped alloys. However, a huge refinement was noticed due to lanthanum doping for the as cast alloys. Grain size study was also carried out at 150°C and 200°C.

The refinement in IMCs during casting and decreased coarsening during thermal aging is described by many researchers. In the work performed by [Fu et al. 2009], they have stated two opinions for this refinement.One is the impact of RE doping on the driving force of Cu6Sn5 IMCs growth. The Cu atom diffuses through the IMC layer to Sn, which means the driving force of the Cu6Sn5 layer growing depends on the activity of Sn at the Cu6Sn5/Cu interface. Thermodynamic parameters of element affinity indicate that it is easy for RE to interact with Sn in the SAC alloys to form IMCs, resulting in increased resistance of Cu6Sn5 IMC layer growth.

The other aspect arises from the difference in Sn and RE atoms. The diameter of Sn atom is 0.141 nm whereas the diameters of Ce and La atoms are 0.183 nm and 0.181 nm, respectively. The radius of the RE atom is about 33% larger than the Sn atom which makes it difficult for RE atoms to replace Sn atoms in the matrix. As a result, it is easy for RE atoms to gather at crystal defects and resist the IMCs growth during coarsening. Moreover [Chen et al. 2002] showed that the interlocking of beta-Sn dendrite and Cu6Sn5 layer was present,where RE elements were enriched at the boundaries in the form of a web. This inserted structure can increase the resistance of grain growth, and hence, to some extent, repress grain coarsening.

CHAPTER 5

MICROSTRUCTURE COARSENING MODELS

5.1 Introduction to Modeling

The microstructure of SAC and SAC-La doped alloys has been described in detail in the earlier chapters. This microstructure consists of the hard and brittle IMCs and soft Sn matrix. In order to better understand the mechanical, electrical, thermal and chemical properties, it is very important to followup the microstructure evolution due to thermal aging in both isothermal and thermal cycling exposures. The experimental evaluation of the IMCs quantitative data and different plottings are presented in the earlier chapters. The purpose of this chapter is to provide the coarsening models to predict the average size of these IMCs and compare the results with the experimental values. These models consist of many experimental parameters including activation energy, aging time, aging temperature and coarsening constants.

5.2 Coarsening Mechanism

The increase in the average diameter of the IMCs due to high temperature aging is known as coarsening. This happens because of continuous diffusion of Ag and Cu into Sn due to which the as-cast particles size increases and for many polycrystalline materials, the particle size "d" varies with time "t" according to the following relationship [Callister 1985],

$$< d >^n - < d_0 >^n = K * t \quad \text{.....(5.1)}$$

where <d> is the average particle size at time t, <do> is the average initial particle size at the time when the particles start coarsening, and K and n are time-independent constants.

There are many coarsening mechanisms and therefore the particle size exponent "n" will have different values as provided in Table 5.1 [Allen et al. 2004]. In different studies over the SnAg solders, it has been noticed that for the particle coarsening, volume diffusion is the dominant process and 3 is used for the exponent "n" [Allen et al. 2004, Senkov et al. 1986, Dutta et al. 2004 and Gibson et al. 1997].

Table 5.1: Value of the particle size exponent n for coarsening processes with different rate-controlling mechanisms [Allen et al. 2004]

n	**Rate Controlling Mechanism**
2	Transfer of solute atoms across the interface between the particle and matrix
3	Volume diffusion
4	Diffusion along grain boundaries or interfaces
5	Diffusion along triple junctions or dislocations

5.3 Ostwald Ripening

Ostwald ripening is a thermodynamic driven process that takes place during the thermal aging of solder joints. Generally the larger IMCs particles are energetically more favored to this process as compare to the smaller IMCs particles [Ratke et al. 2002]. This happens with the fact that the molecules present at the surface of these IMCs particles are less stable (energetically) as compare to the molecules at the interior.

If a simple cubic crystal system is considered to understand this fact, then the atoms present at the interior are engaged/bonded to 6 other atoms but the atoms at the exterior or surface are connected to only 5 atoms and are hence less stable. Continuing to the same example,

larger particles are energetically more favorable as more atoms are bonded to 6 atoms at the interior and less atoms are bonded to the exterior and hence the unfavorable locations.

Thus if the process continues, the molecules at the surface of the smaller particles (and connected at the unfavorable locations to almost 4 or 5 atoms in their neighborhood) would detach form their respective IMCs particles and would diffuse into the solution following the Kelvin equation. This would be carried out for almost all smaller particles. It would cause an increase in the concentration of free atoms in the solution till a saturation of the free atoms is reached in the solution. It would cause the free atoms to condense on the surface of the larger particles [Ratke 2007]. Therefore, the larger particles would continue to grow at the cost of the smaller ones and hence the overall (average) size of the IMCs particles would grow. After a long time, all the particles would combine to form a big, ideally spherical shape, single particle to surround the entire surface area.

In case of diffusion of material during thermal coarsening, Lifshitz and Slyozove [Lifshitz and Slyozov 1961], performed a mathematical investigation of the ripening process. Their study explained how the shrinking of smaller particles continues and how the larger particles grow at almost a uniform rate till complete saturation. According to their work, the average size of the particles <R> grows as follows:

$$< R >^3 - < R >_0^3 = \frac{8\gamma c_\infty \upsilon^2 D}{9 R_g T} t \quad \text{.....(5.2)}$$

where <R>= Average radius of all the particles, γ = Surface tension or surface energy of the particles, c_∞= Solubility of the particle material, υ= Molar volume of the particle material, D =

Diffusion coefficient of the particle material, R_g = Ideal gas constant, T=Absolute temperature and t= Time. Thus, after simplifying the above equation,

$$< R >^3 - < R >_0^3 = \frac{K_0}{T} t \exp\left(-\frac{Q}{RT} \right) \quad \text{.....(5.3)}$$

where K_0 is a temperature and time independent constant, Q is the activation energy for the rate-controlling process. The activation energy is described as the least amount of energy needed for a chemical reaction to take place. Some elements and compounds react together naturally just by being close to each other and their activation energy is zero. Others will react together only after a certain amount of energy is added to them. Striking a match on the side of a matchbox, for example, provides the activation energy (in the form of heat produced by friction) necessary for the chemicals in the match to ignite. Activation energy is usually expressed in terms of joules per mole of reactants.

The activation energy was found to be between 45kJ/mol [Dutta et al. 2004 and Gibson et al. 1997] and 65kJ/mol [Min Pei 2007]. Dutta [Dutta 2003] also considered the effect of thermomechanical loading on coarsening. In his model, a strain rate dependent term was introduced into the constant K_0.

5.4 Model Fitting

Based on the discussion above, the coarsening model shown in equation (5.3) was used in La doped SnAg solder particle coarsening by Min Pei [Min Pei 2007]. Thus it is also applied here for the SAC and SAC-La doped alloys. The two important parameters for this model, K_0 and Q are evaluated experimentally with values in the range with other researchers. The coarsening activation energy for non-doped SAC solder was found to be about 35kJ/mol. This is

consistent with Dutta's result [Dutta et al. 2004]. The pre-exponential constant K_0 decreases drastically with increase of La addition [Min Pei 2007]. Because of the low pre-exponential constants, it will be easier for La doped solder alloys to reach the saturated particle size, and the saturated particle size is much smaller than that of the un-doped alloys.

The microstructural evolution is studied at 2 elevated temperatures; 150°C and 200°C. As the homologues temperature in this case is quite high, thus fast coarsening is experienced. The experimental results for intermetallic compounds average size, distribution, spacing and volume fraction are presented in Chapter 4. In this chapter, the model described above is used to fit to the experimental data. Good approximation is seen for all compositions. The thermal coarsening results are provided in Figure 5.1 for the SAC alloy at 150°C and in Figure 5.6 at 200°C. To account for the La doping effect, the coarsening model given by (5.3) can be modified to [Pei M. and Qu J. 2007],

$$< d >^3 - < d_0^{RE} >^3 = \frac{K_0^{RE}}{T} t \exp\left(-\frac{Q^{RE}}{RT} \right) \quad \text{.....(5.4)}$$

where

$$< d_0^{RE} >= d_0 \left(1 + 28.5RE\right)^{-0.2} \quad \text{.....(5.5)}$$

$$K_0^{RE} = K_0 \left(1 + 11.4RE\right)^{-7} \quad \text{.....(5.6)}$$

$$Q^{RE} = Q(1 + 0.71RE)^{-5.5} \quad \text{.....(5.7)}$$

with Q = 35 KJ/mol (taken from Figure 7.18 page 142) and Ko = 4.2.10^4 μm3/hour.

where RE is the La doping in wt %, d_0, K_0 and Q are the values of un-doped solder alloys. The results for SAC-0.05La, SAC-0.25La and SAC-0.5La alloys due to thermal coarsening at 150°C are provided in Figures 5.2-5.5 and at 200°C in Figures 5.7-5.10 respectively.

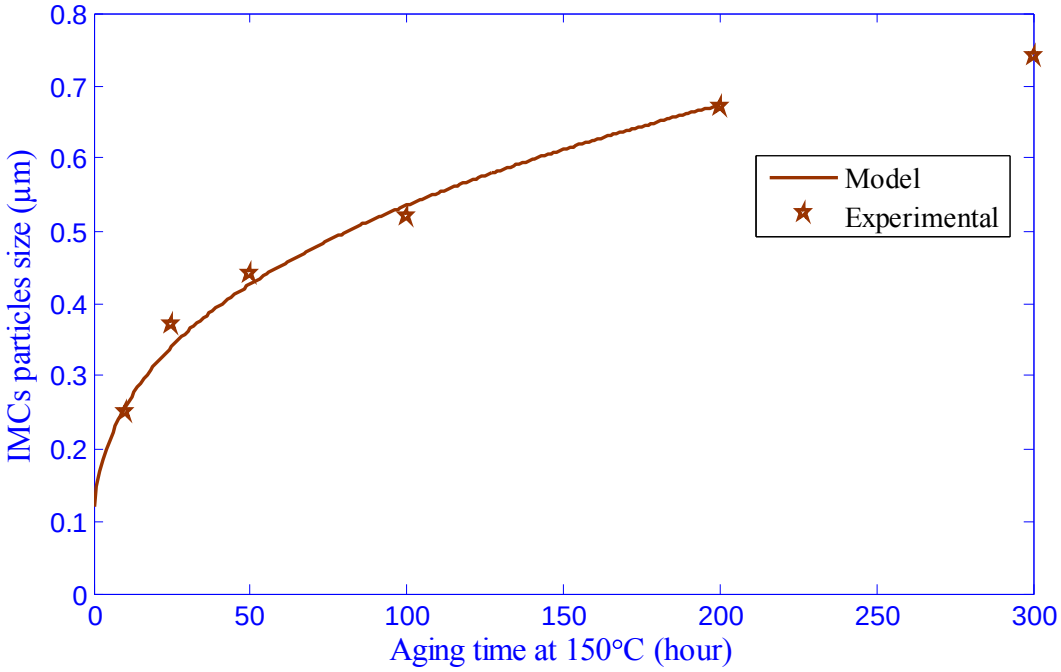

Figure 5.1: SAC coarsening at 150°C

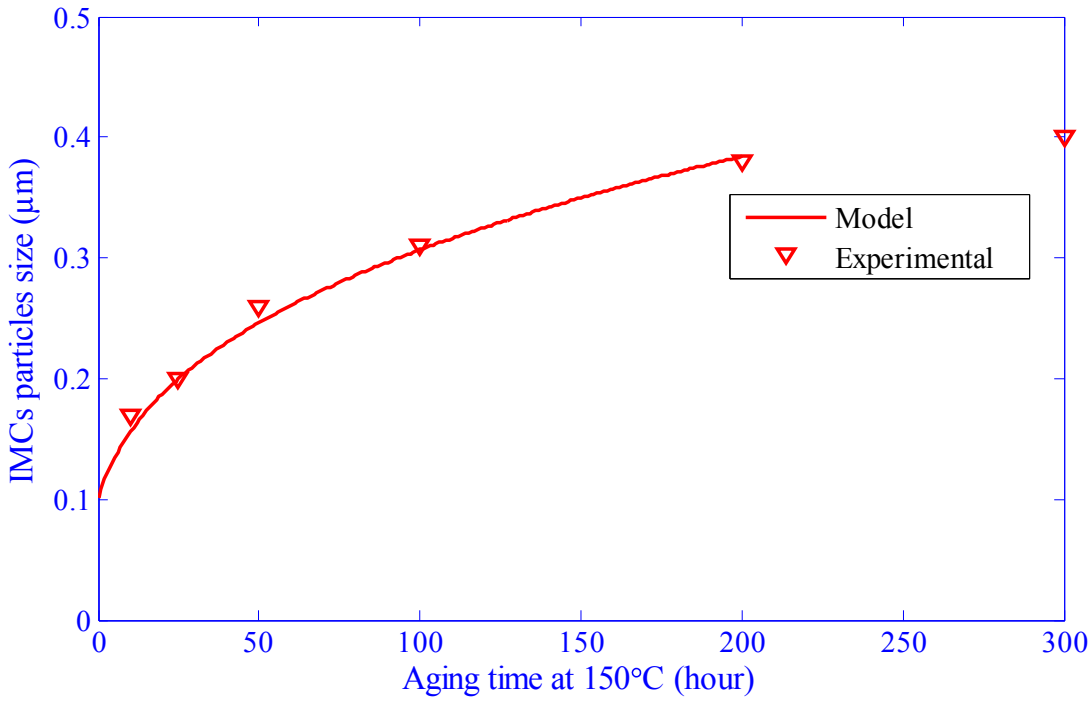

Figure 5.2: SAC-0.05La coarsening at 150°C

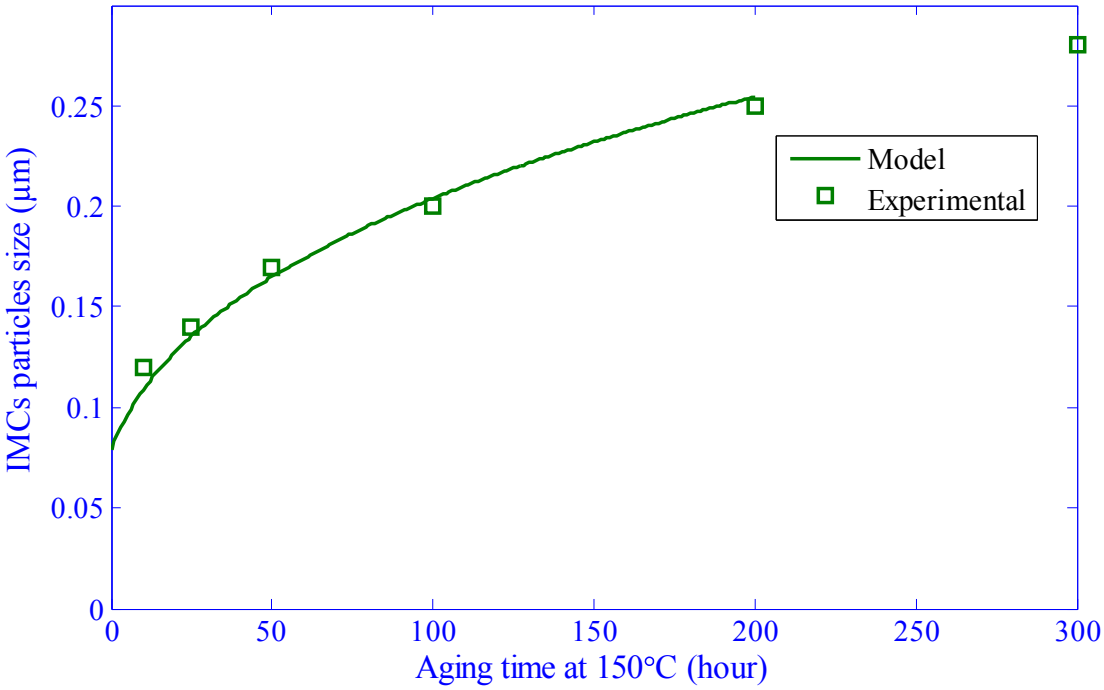

Figure 5.3: SAC-0.25La coarsening at 150°C

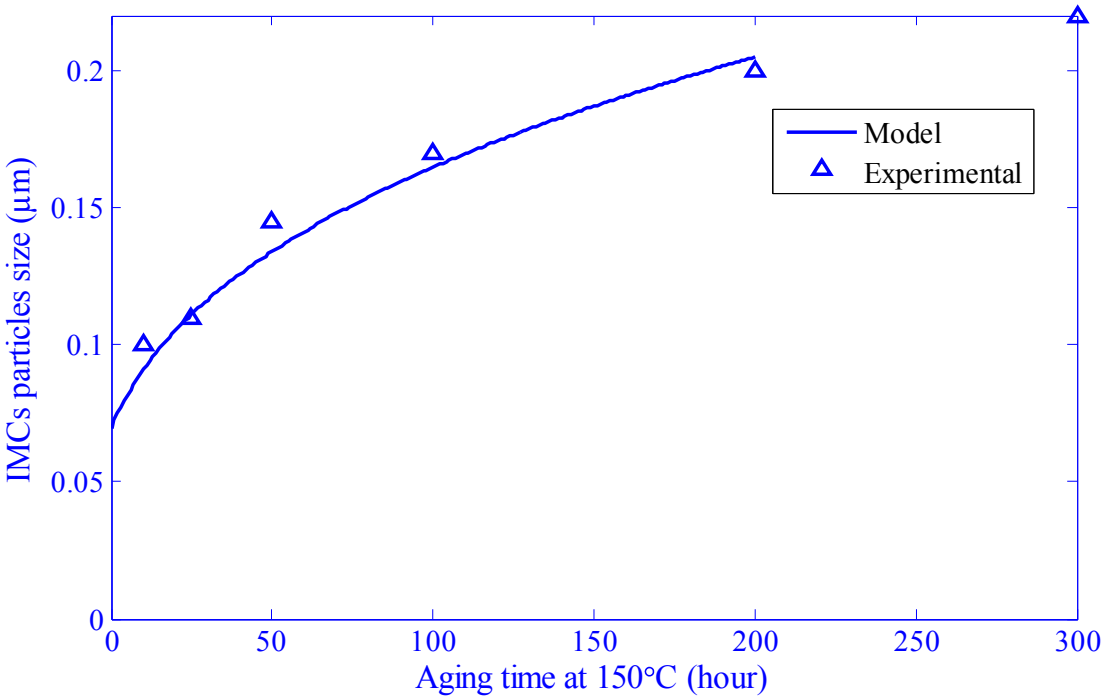

Figure 5.4: SAC-0.5La coarsening at 150°C

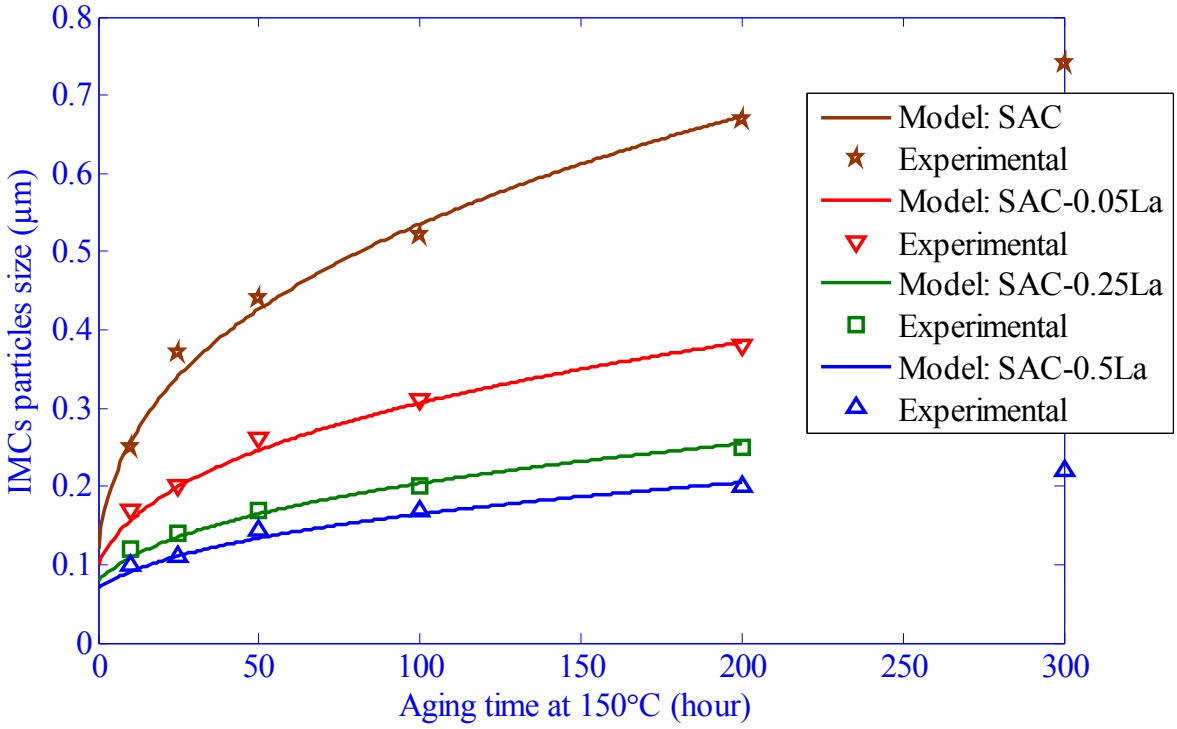

Figure 5.5: SAC and SAC-La coarsening at 150°C

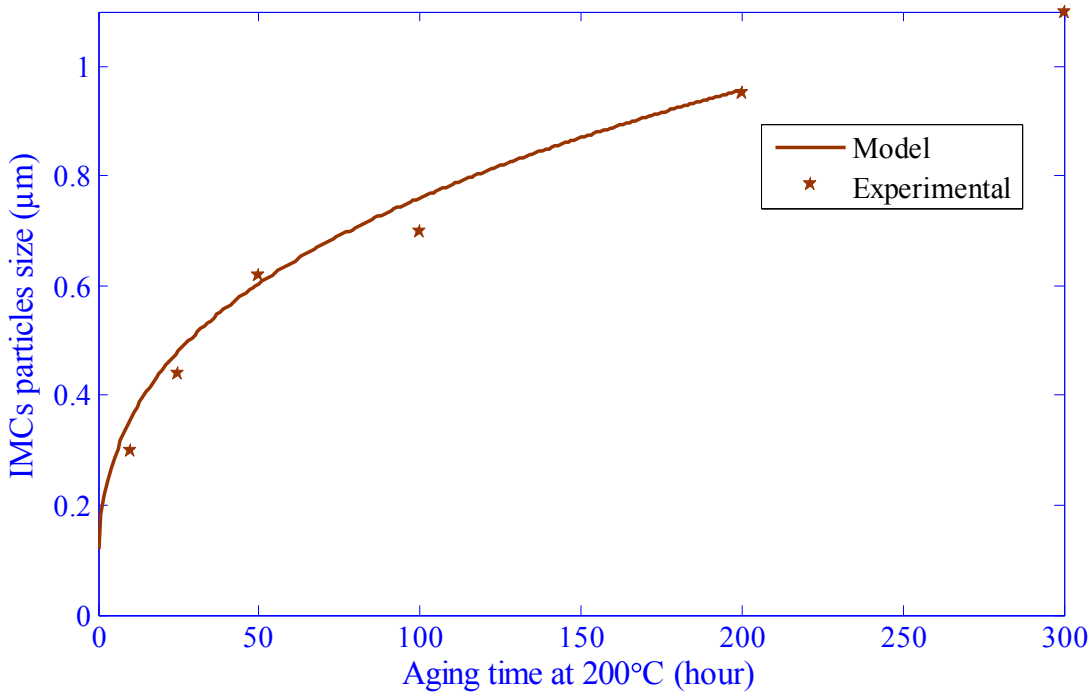

Figure 5.6: SAC coarsening at 200°C

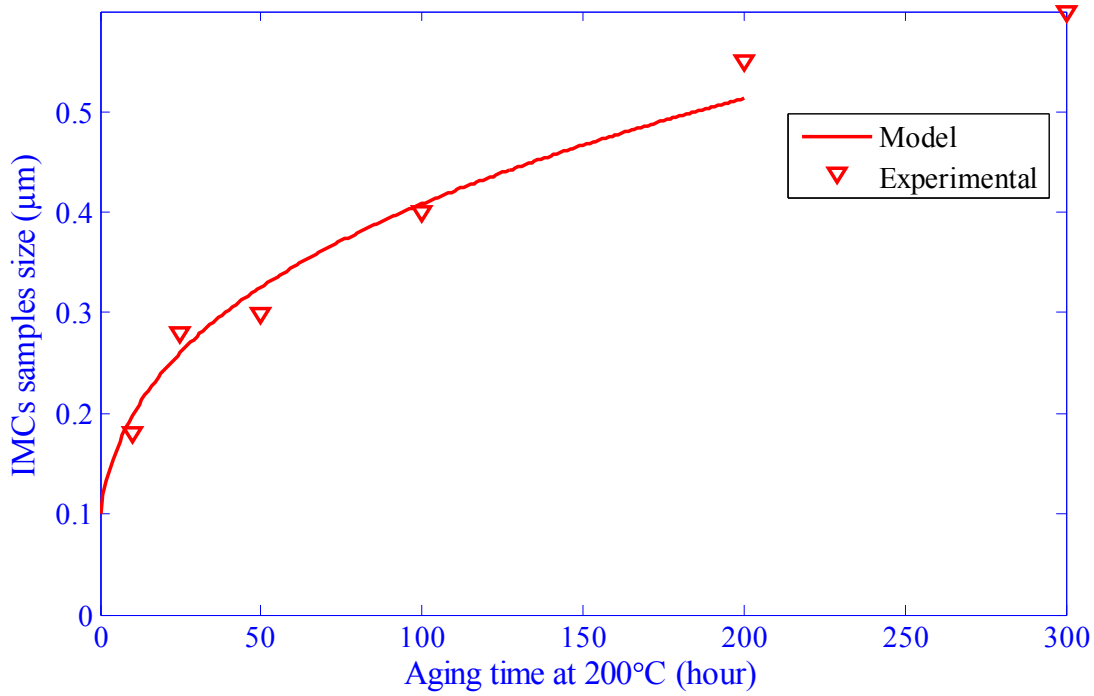

Figure 5.7: SAC-0.05La coarsening at 200°C

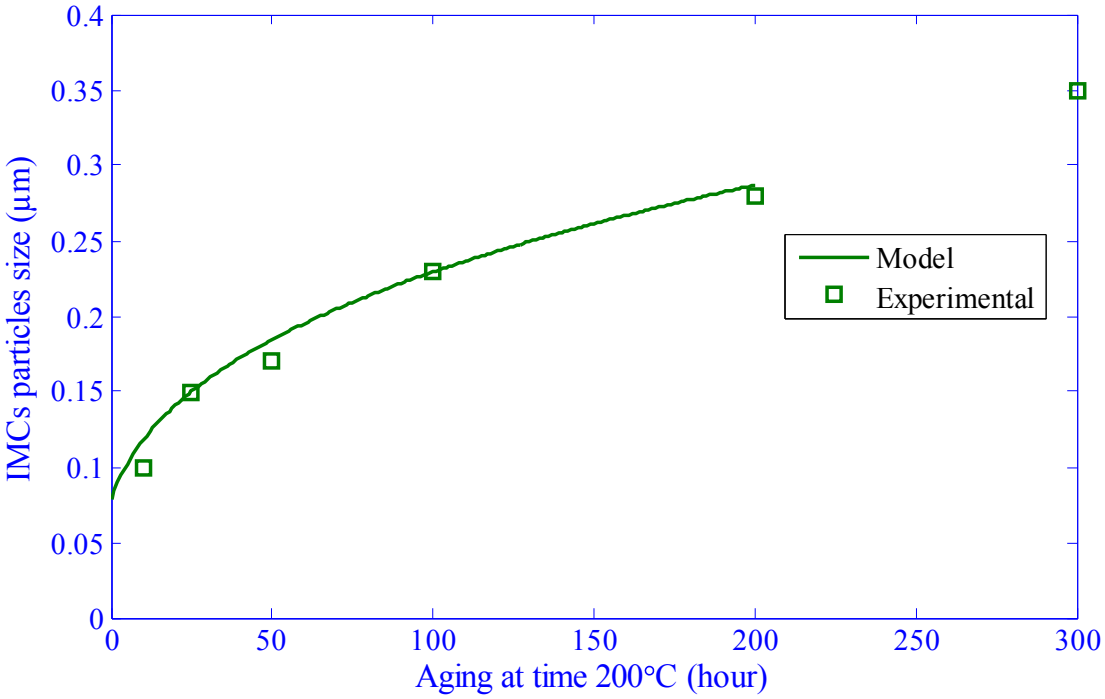

Figure 5.8: SAC-0.25La coarsening at 200°C

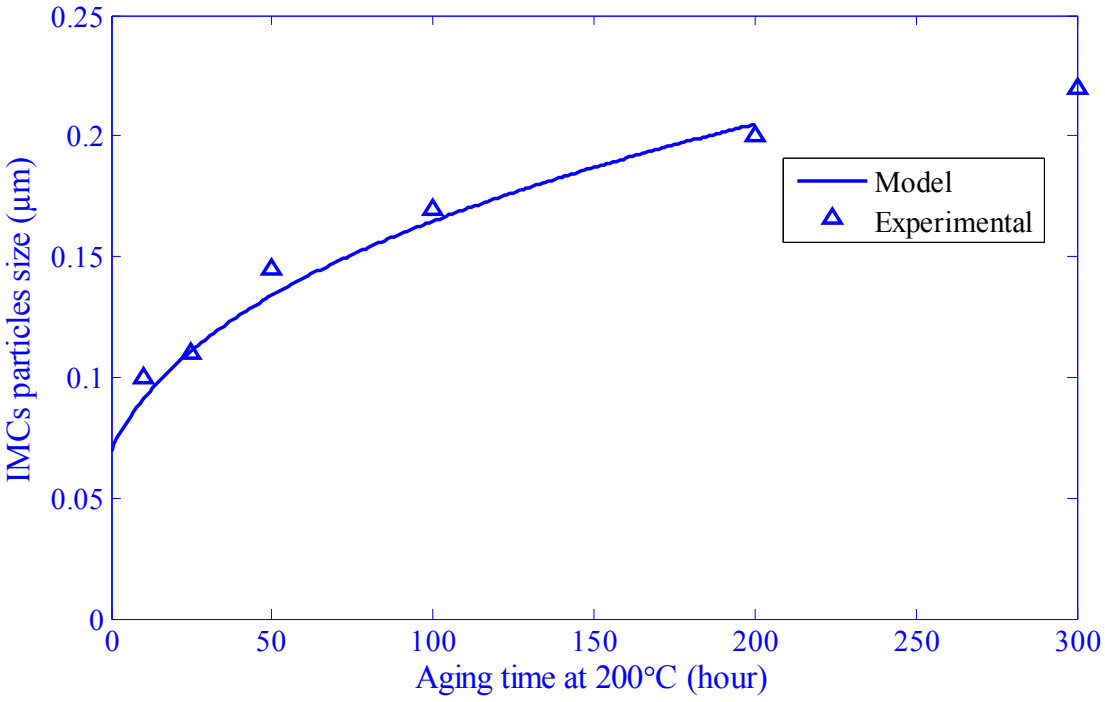

Figure 5.9: SAC-0.5La coarsening at 200°C

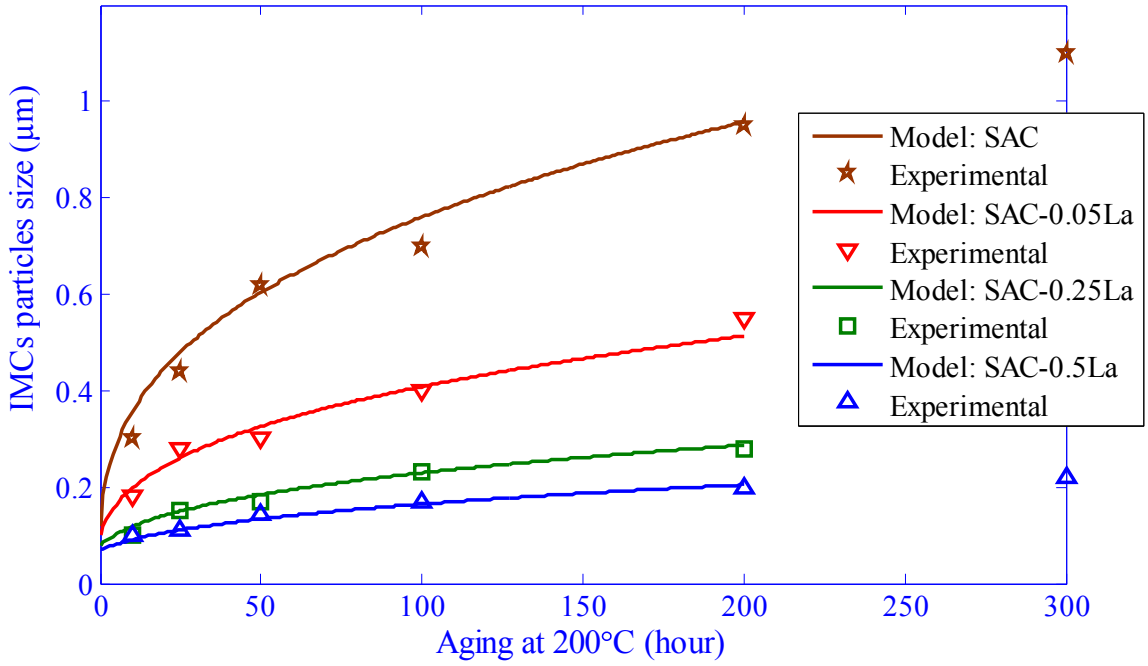

Figure 5.10: SAC and SAC-La coarsening at 200°C

5.5 Summary

As presented in the earlier chapters, a quantitative measure is done for the IMCs average size. For this study, extensive SEM images were collected after polishing and chemical ecthing the Specimens. These images should be of good quality to have clear contrast between different phases. Later on, ImageJ software was used to develop a good data base with a 3D matrix having thermal aging, aging temperature and lanthanum composition as its 3 axes. Since this process is quite lengthy and expensive if repeated all the times, thus the thermal coarsening models are used here to predict the average size of IMCs at 150°C and 200°C. There are many parameters that needs some experimental results such as activation energy (Q) tests, as-cast IMCs size (d_0), aging temperature (T),aging time (t) and an important time-independent constant (K_0). Good fitting is observed with measurements taken at 10 hours, 25 hours, 50 hours, 100 hours and 200 hours of thermal aging.

Quantitative models are developed with La wt % as a governing term to predict the average size of these IMCs at different aging temperatures and times. These models are predicting the results in an acceptable range of 5% with that of the experimental data collected from the SEM micrographs.

CHAPTER 6

MECHANICAL PROPERTIES

6.1 STRESS-STRAIN RELATIONS

Solder assemblies once exposed to high temperatures during service are subjected to tensile loading. In some cases, due to flexing down the substrate, excessive deformation takes place in the solder joints as shown in Figure 6.1 [Abtew & Selvaduray 2000 and Zhang 2010]. In such cases, the mechanical properties like yield stress, tensile strength, elastic modulus and ductility becomes very important in determining the extent of maximum tensile deformation which the solder joint can sustain prior to failure.

The strength of any material is an important parameter that limits its ability to which the material can be exposed before undue deformation or failure. This strength is determined by tensile test and is therefore called tensile strength and is evaluated from the typical stress-strain diagram as shown in Figure 6.2. In this Figure 6.2, two types of stress-strain diagrams are shown, the engineering (A) and true (B). The main difference appears in the zone of strain hardening in which case the magnitude of the stain becomes significant. The engineering stress-strain diagram has a significant advantage such that it provides quite useful information without taking in consideration the physical size or shape of the material (specimen) [Hertzberg 1996].

In some cases, the engineering designs are carried out in the elastic zone without sufficient distortion and hence the errors in using engineering stress-strain diagrams over the true

stress-strain diagrams are neglected. This makes the engineering stress-strain diagrams more convenient to use and employ.

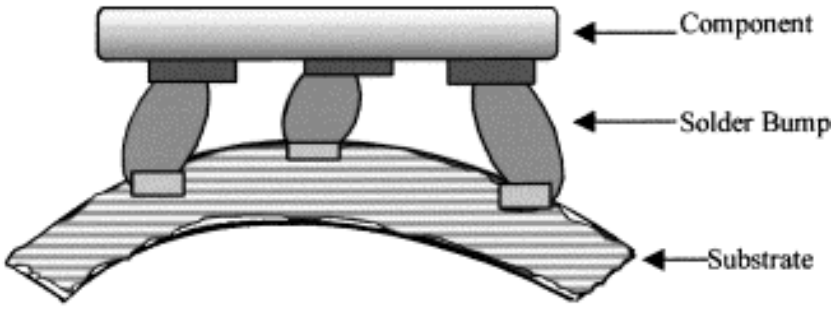

Figure 6.1: Solder joints subjected to tensile loading due to substrate flexing

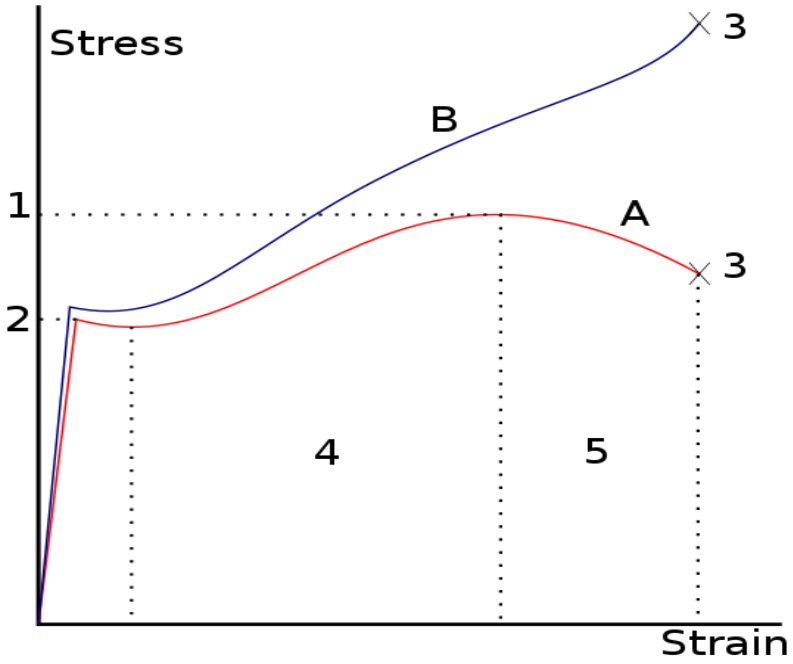

Figure 6.2: Typical Stress-Strain curve of Pb-free alloys

A. Engineering Stress-Strain Curve; B. True Stress-Strain Curve
1. Ultimate tensile strength (UTS), 2. Yield strength,
3. Rupture, 4. Elastic region
5. Strain hardening (plastic) region
6. Necking (plastic) region

6.2 SPECIMEN PREPARATION

The detailed procedure for tensile test specimens is explained in chapter 3 (Experimental Design). Most importantly, the procedures described are proved to prepare high quality specimens with oxidation free surfaces, notch free edges and uniform dimensions with excellent repeatability. Uniform cooling using partial water quenching was used to control the solidification rate and hence the overall microstructure of the specimens. Any flaws and voids were eliminated that could affect the overall behavior during mechanical testing. All stress-concentration effects were also avoided using circular edges at the gauge section of the tensile dog-bone shape specimens. As rectangular specimens were used in this study, any samples with shorter gripping length or sharp edges etc. were replaced with fresh specimens using the die casting process. All samples were carefully polished and etched and analyzed using SEM at different length scales to assure good quality samples before testing.

The final dog bone shape tensile test specimen is given in Figure 6.3 with all dimensions in mm. In the first attempt, the samples were casted and prepared for a width and thickness of 1 mm. In that case, it was quite difficult to polish and handle them as they were fragile due to which they used to get local defects before tensile testing which can affect the final behavior of the solder alloys. Therefore, the width of these new specimens was particularly selected to be 4 mm wide and 2 mm thick which made the specimens stronger and thus polishing quite easy.

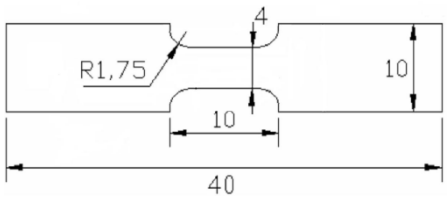

Figure 6.3: Dog-bone shape tensile specimen (all dimensions in mm)

6.3 TENSILE TESTING

Quasi-static tensile tests with 3 different strain rates of 2.10^{-4} s^{-1}, 2.10^{-3} s^{-1}, and 2.10^{-2} s^{-1} were carried out with an MTS tensile machine equipped with a 5kN load cell to determine the mechanical properties as a function of lanthanum doping for all compositions. At least 2 samples were used for every composition. All alloy compositions were used in the bulk form. A custom fixture was used to grip the specimen during loading.

In the uniaxial tension tests, forces and displacements were measured and corresponding axial stress and axial strain were calculated from the applied force and measured cross-head displacement using the following equations 6.1 and 6.2,

$$\sigma = \frac{F}{A} \quad \text{.....(6.1)}$$

$$\varepsilon = \frac{L}{L} = \frac{\delta}{L} \quad \text{.....(6.2)}$$

where σ is the uniaxial engineering stress, ε is the uniaxial engineering strain, F is the uniaxial measured force, A is the original cross section area, δ is the measured cross-head displacement and L is the gauge length of the specimen. The true stress and true strains were evaluated using the following relations,

True stress (MPa): $\sigma_{tr} = \sigma(1 + \frac{\varepsilon}{100})$ True strain (%): $\varepsilon_{tr} = \ln(1 + \frac{\varepsilon}{100}) * 100$

In the stress-strain relations, the Young's modulus used is the initial slope of the stress-strain curve. Most of the solder alloys have the viscoplastic nature and therefore this effective modulus would be rate dependent and would be closest to the true values when the strain rate

approaches to infinity. The yield stress, as explained already, would be taken as the standard 0.2% yield stress. After unloading, the permanent strain (δ) becomes 0.002 and the ultimate tensile strength (σ_u) is taken as the maximum stress recorded in the entire stress-strain diagram.

As the test continues after yielding, the strain already accumulated increases significantly and the narrowing down of the specimen takes place. This phenomenon is called necking which causes the stress level to drop and failure happens which ends up the stress-strain curve.

6.3.1 AS-CAST SPECIMENS TESTING

In this part, the as-cast specimens were tested with the experimental conditions as discussed above. Figures 6.4-6.6 show true and engineering stress-strain curves for SAC and SAC-La doped (as-cast alloys). These curves were treated to extract the yield stress and tensile strength which are plotted in Figures 6.7-6.8. Similarly, Figure 6.9 shows the average values for yield stress and tensile strength with 5 % error bars.

A significant increase in both yield stress and tensile strength is observed. This is consistent with [C. M. L. Wu & Wong 2007], in which an increase in tensile strength is investigated on Sn-0.7Cu, Sn-3.5Ag and Sn-9Zn alloys due to RE elements (mainly Ce and La). Since creep mechanism is mostly affected by the yield stress of the material, an increase in yield stress corresponds to an increase in the creep resistance of these alloys. On the other hand, an increase in La doping also leads to a decrease in elongation to failure. This may be due to the increase in the quantity of the hard RE-bearing particles [Chen et al. 2003]. In [Baker & Okamoto 1992], it is shown that lanthanum makes $LaSn_3$ compounds. The average microhardness of this phase, in a slow cooled alloy, has a high value of 48HV as compared to the average microhardness of the matrix of 13.5HV [C. Wu et al. 2002].

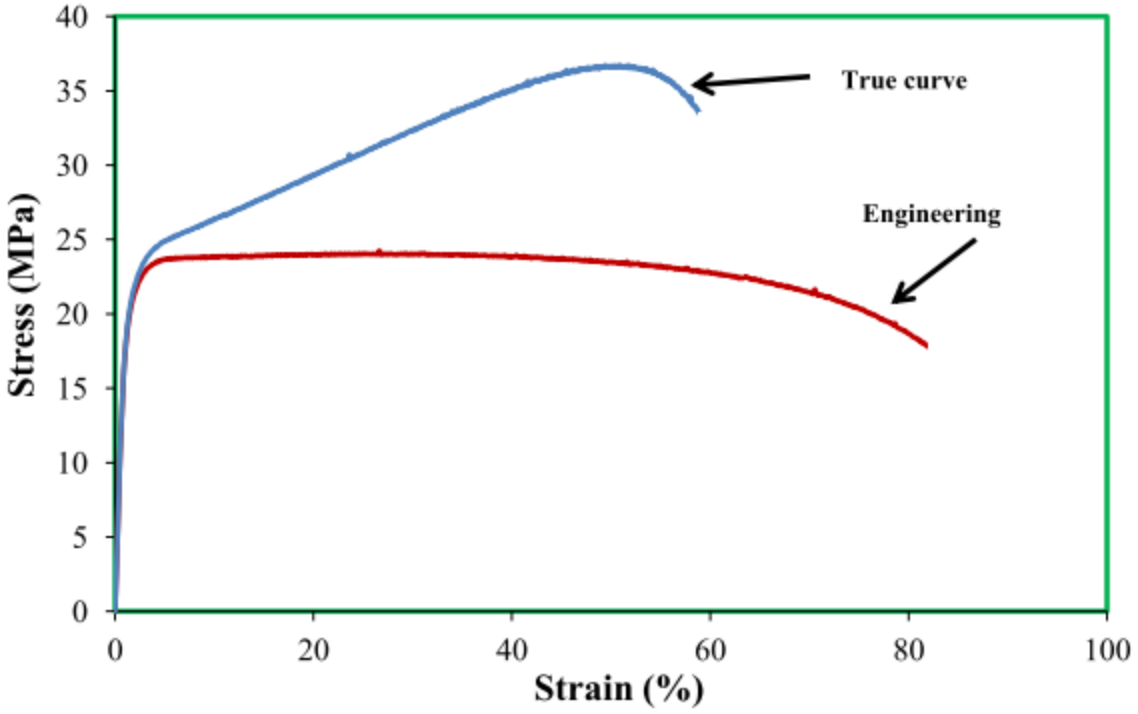

Figure 6.4: SAC "as cast" Engineering and True stress-strain curves

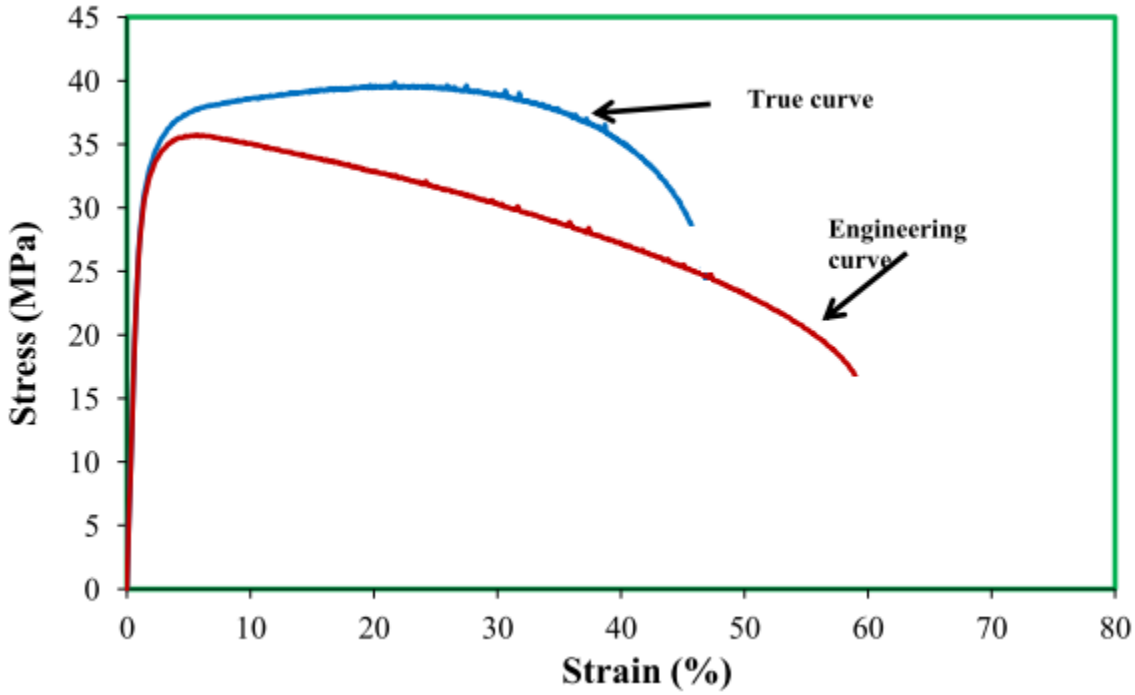

Figure 6.5: SAC-0.05La "as cast" Engineering and True stress-strain curves

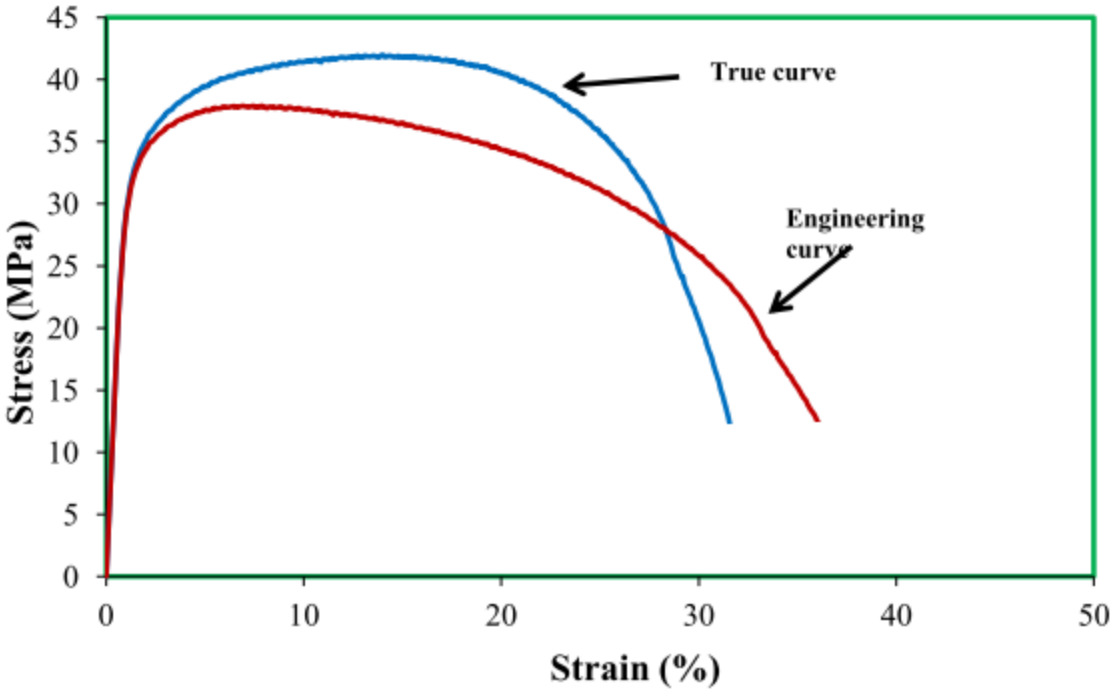

Figure 6.6: SAC-0.25La "as cast" Engineering and True stress-strain curves

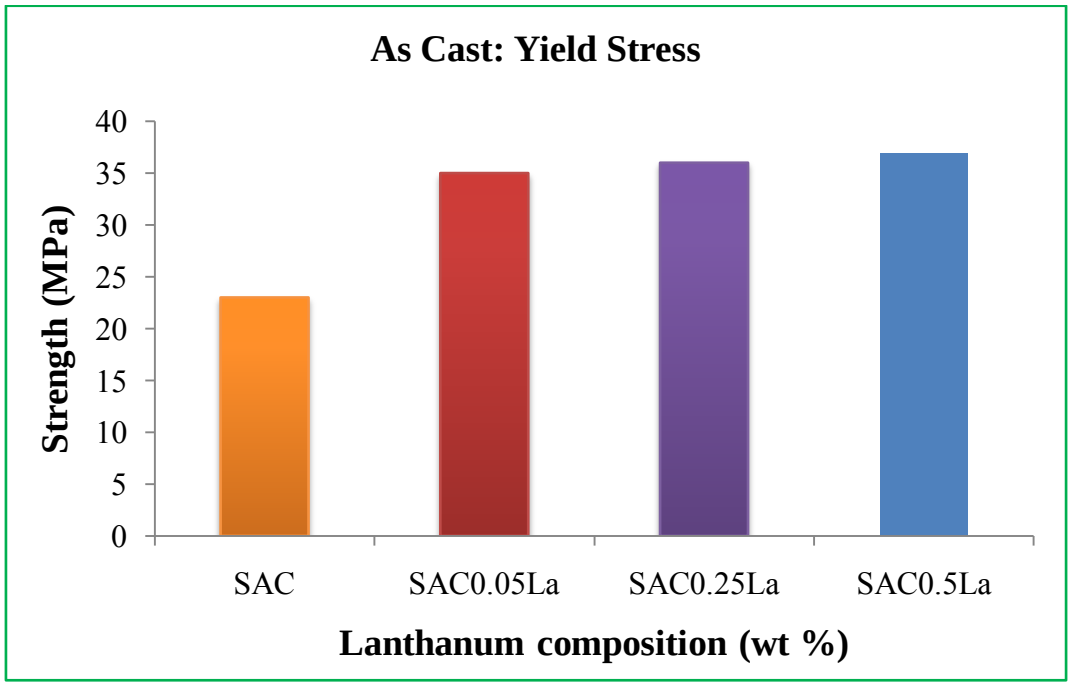

Figure 6.7: Yield Stress for SAC and SAC-La alloys (as cast)

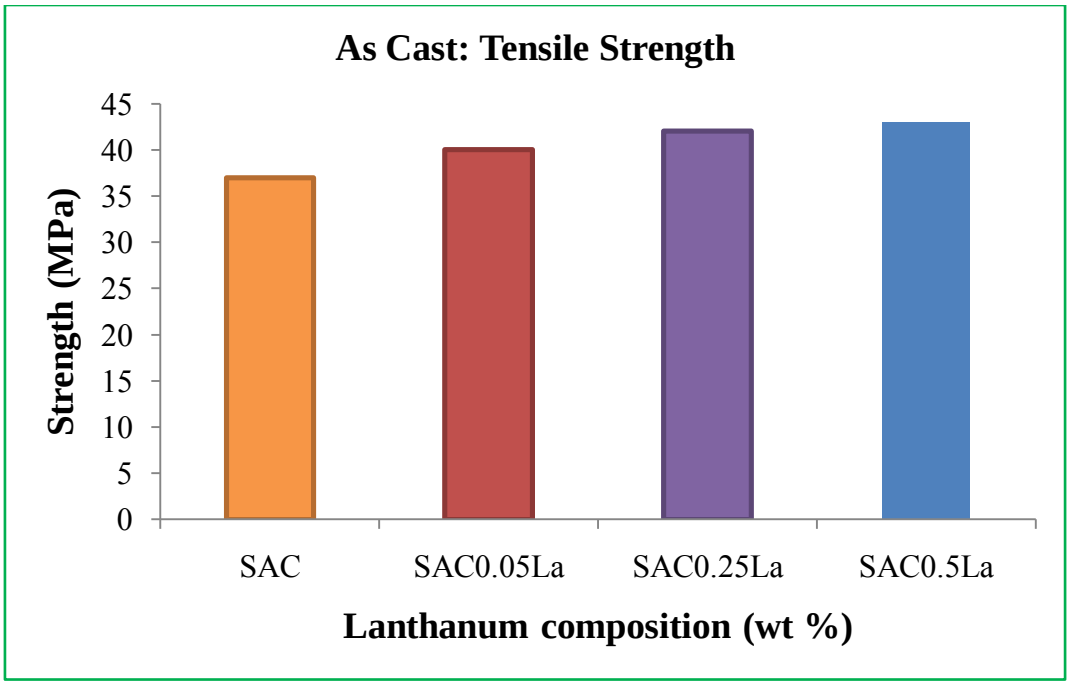

Figure 6.8: Tensile Strength for SAC and SAC-La alloys (as cast)

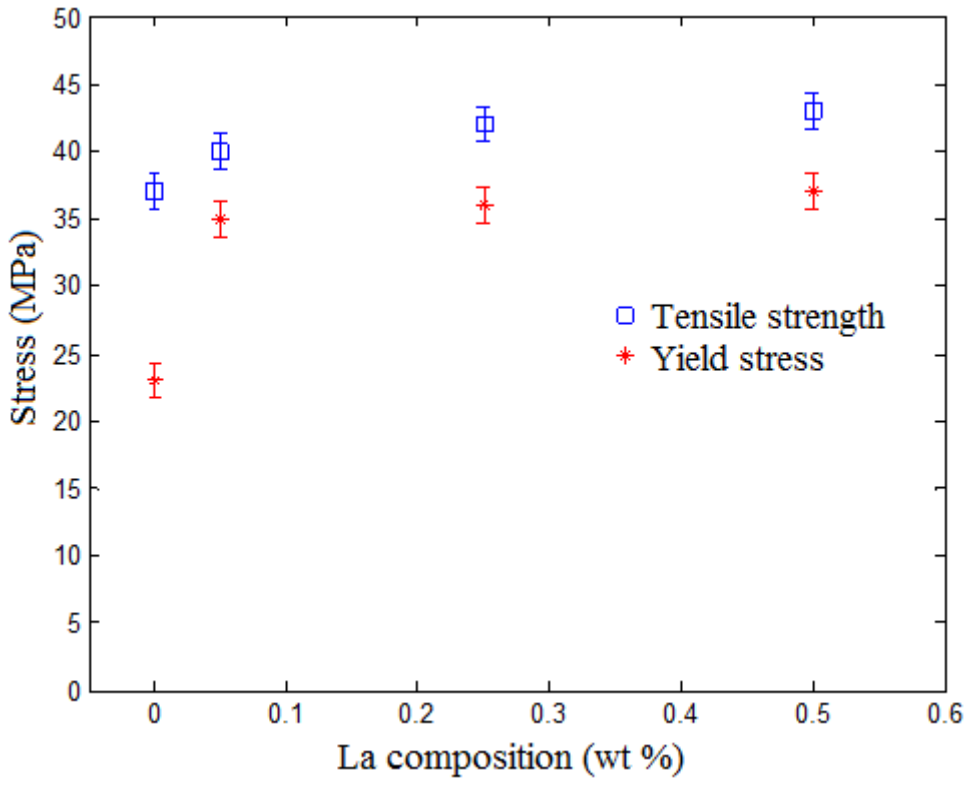

Figure 6.9: Yield stress and tensile strength as a function of La composition (as cast)

6.3.2 THERMALLY-TREATED SPECIMENS TESTING

Similar samples as used for "as cast testing" were prepared and placed in a heating chamber for isothermal aging at 150°C for 100 hours and 200 hours. The samples were placed at room temperature for 24 hours after thermal aging to release all stresses. The samples, after thermal aging, were analyzed in SEM before mechanical testing. Considerable coarsening of IMCs was seen due to high temperature aging. The size of IMCs rose from 1 micron to a few microns for both 100 hours and 200 hours thermal aging.

Thermal coarsening has largely affected the microstructure of SAC alloys. We can see a significant decrease in both yield stress and tensile strength from the as cast alloys to thermally aged alloys. This is because of the IMCs growth which causes an early failure and reduces the solder joint reliability. In all three cases, mechanical properties of doped solders are significantly higher than those of the undoped alloys. Even an increase of 2MPa could be appreciable since it corresponds to a 10% increase in the yield stress of 20MPa.

The evolution of yield stress and tensile strength for 100 hours aging at 150°C are given in Figures 6.10-6.11 respectively. Similarly, for 200 hours aging at 150°C, the yield stress and tensile strength are given in Figures 6.12-6.13 respectively. The increase in yield stress and tensile strength due to RE doping in tin based alloys is quite consistent with other studies [Wu et al. 2004]. Figure 6.14 (a) and Figure 6.14 (b) presents the average values for yield stress and tensile strengths for all compositions for 100 hours aging and 200 hours aging at 150°C respectively. Table 6.1 summarizes all these results.

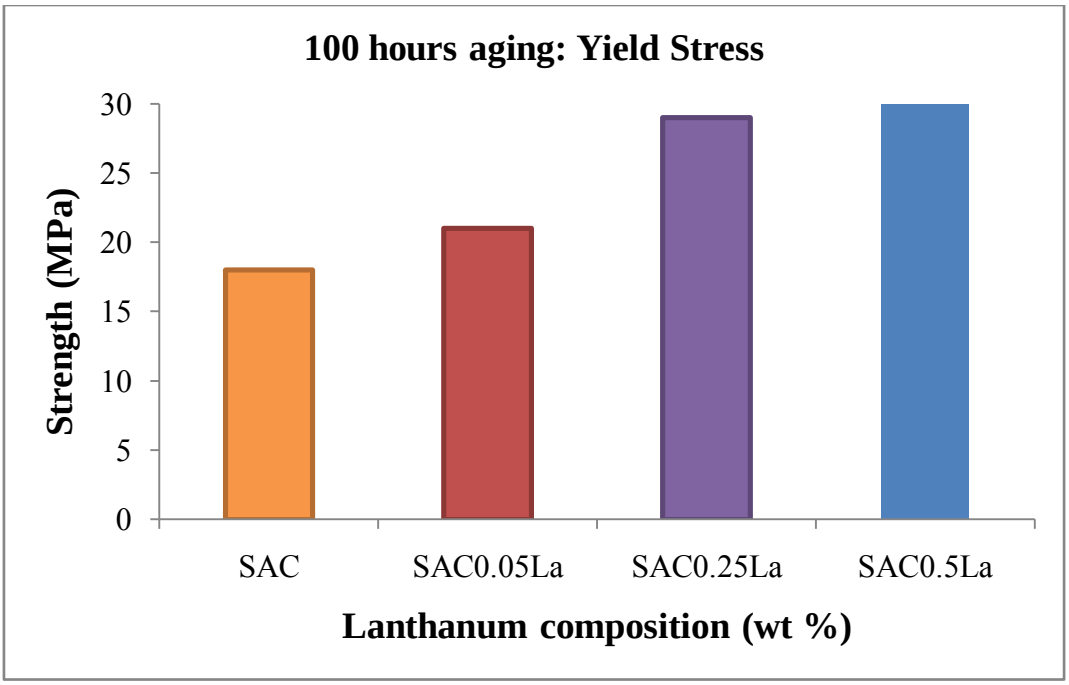

Figure 6.10: Yield Stress for SAC and SAC-La alloys (100 hours aging)

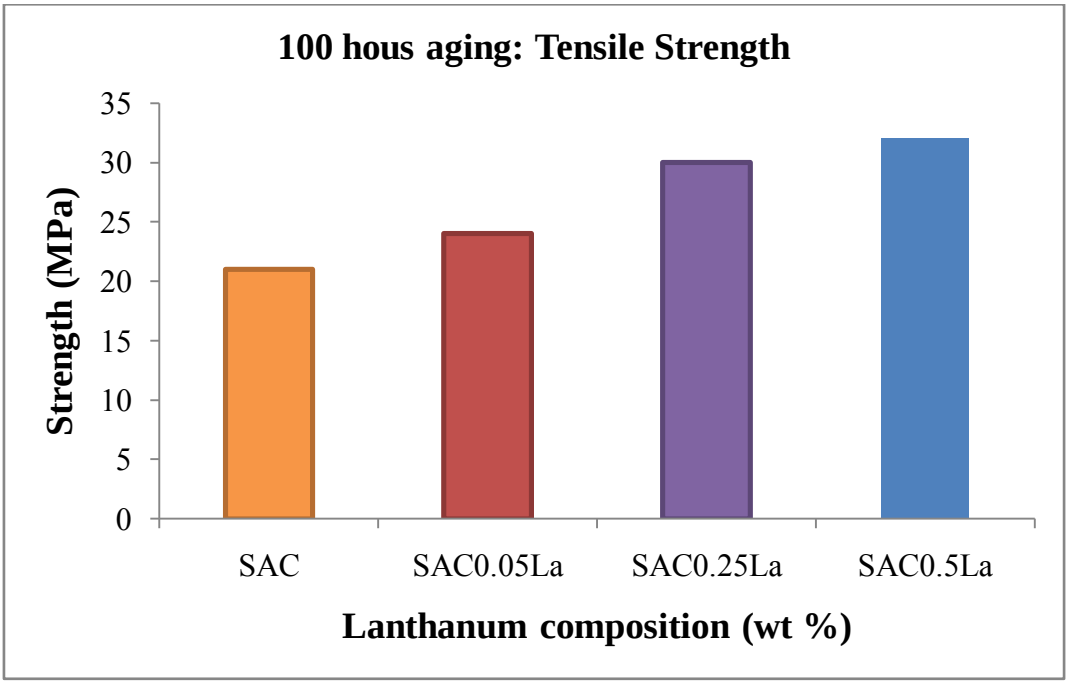

Figure 6.11: Tensile Strength for SAC and SAC-La alloys (100 hours aging)

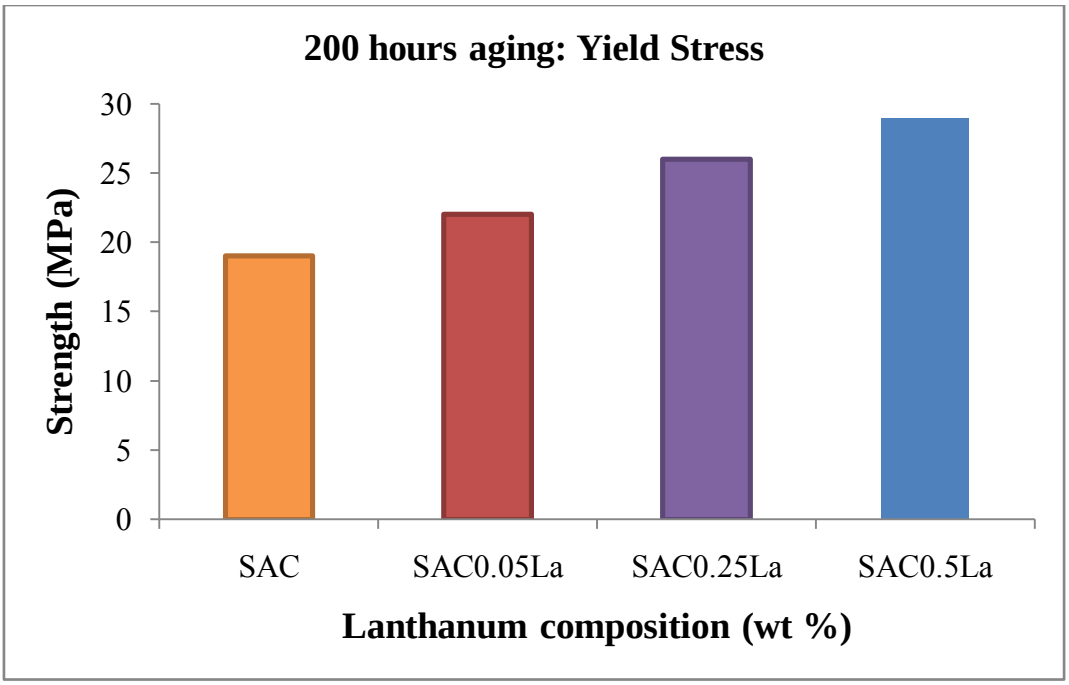

Figure 6.12: Yield Stress for SAC and SAC-La alloys (200 hours aging)

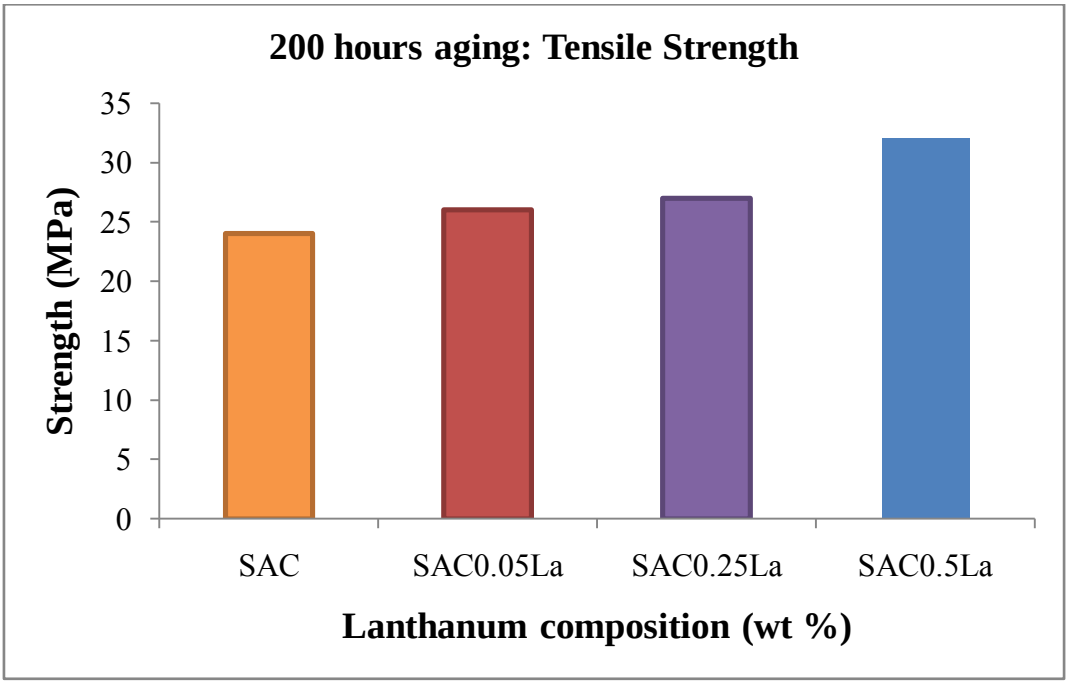

Figure 6.13: Tensile Strength for SAC and SAC-La alloys (200 hours aging)

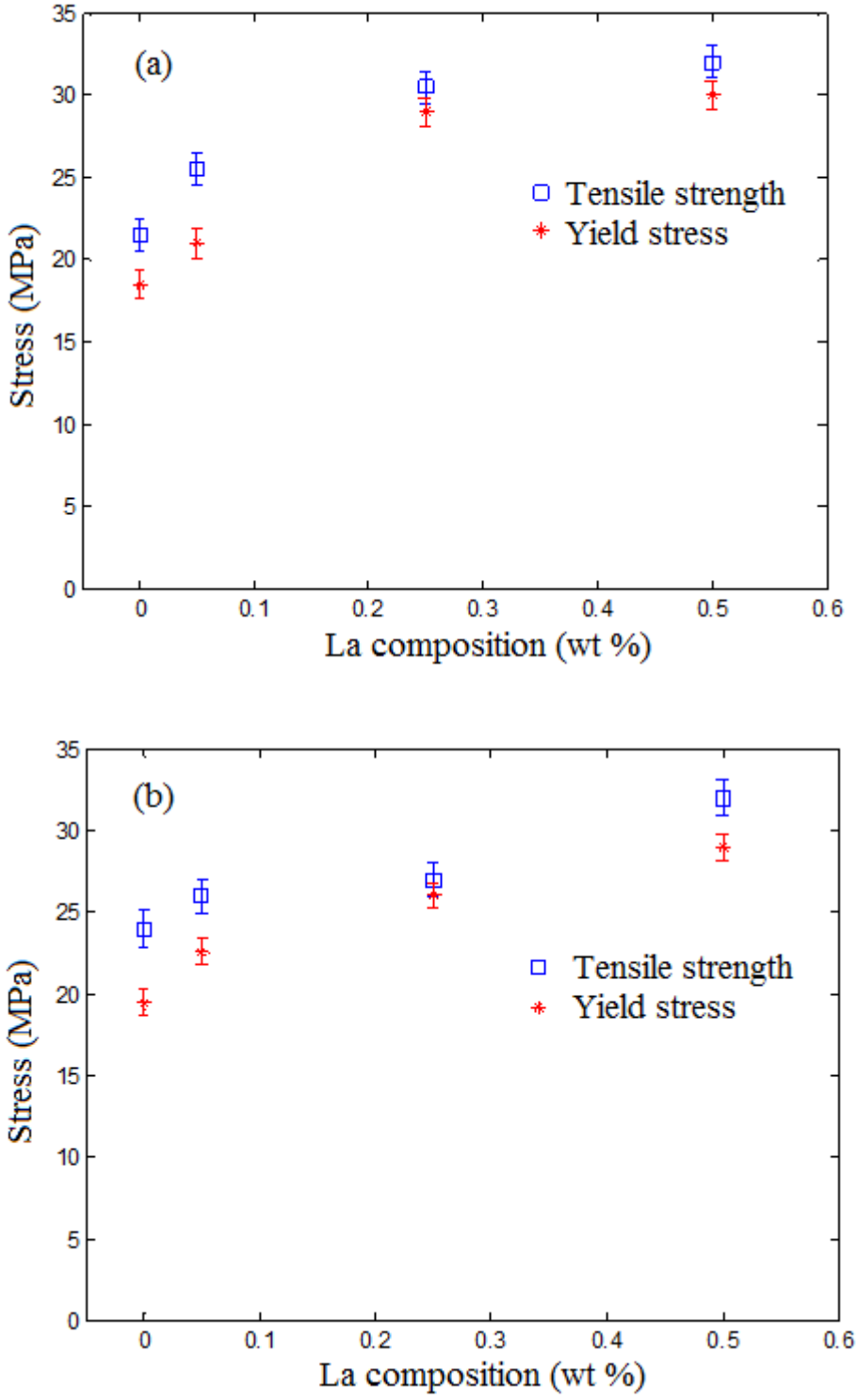

Figure 6.14: Yield stress and Tensile strength as a function of La composition for (a) 100h aged at 150°C and (b) 200h aged at 150°C

Table 6.1: Yield stress and tensile strength for SAC and SAC-La alloys in varying environmental conditions

Alloy	Condition	Yield stress (MPa)	Tensile strength (MPa)
SAC	As cast	23	37
	100 h aged at 150°C	18.5	21.5
	200 h aged at 150°C	19.5	24
SAC-0.05La	As cast	35	40
	100 h aged at 150°C	21	24.5
	200 h aged at 150°C	22.6	26
SAC-0.25La	As cast	36	42
	100 h aged at 150°C	29	30.5
	200 h aged at 150°C	26	27
SAC-0.5La	As cast	37	43
	100 h aged at 150°C	30	32
	200 h aged at 150°C	29	32

6.4 THERMAL CYCLE MECHANICAL TESTING

In most cases, electrical components pass through severe thermal cycling in which case the solder joints become the weakest and therefore the most critical points of the entire assembly. Thus, the solder joints controls the structural integrity of the whole component. This becomes most important when their microstructure becomes coarse due to thermal coarsening at high temperatures during service.

Several studies have been performed on investigating the effects of thermal cycling on the mechanical properties of many lead free solders including SAC and SnPb solders. In [Clech 2005], the strain-energy based model is used to study the effect of different thermal cycle parameters including ramp rates, mean temperature, dwell times and temperature profile on SAC solder joint life. Moreover, in [Jean Paul Clech 2005], a detailed study of dwell time and ramp rate effects shows how accelerated thermal cycling profiles can be optimized to improve test efficiency.

In [Subramanian & Lee 2004] the SAC alloys were studied for individual phases as eutectic and β-Sn and it was concluded that the β-Sn in the eutectic phase exhibits anisotropy in its elastic and thermal expansion properties. This may induce a significant amount of stress at Sn-grain boundaries during thermal cycling. Damage can initiate at boundaries with maximum induced normal/shear stress [Subramanian & Lee 2004]. Therefore, detailed investigation of failure in solder joints under thermal cycling has a paramount importance for the reliability concern of microelectronics devices.

The thermal cycles to which the solder joints are exposed varies for different applications. The thermal cycle in automotive is different than the pipelines and that of the aerospace for example. The thermal cycle used for the thermal treatment of both SAC and SAC-La doped samples is given in Figure 6.15 and is used according to the guidelines provided by the pipelines applications in the oil and gas industries.

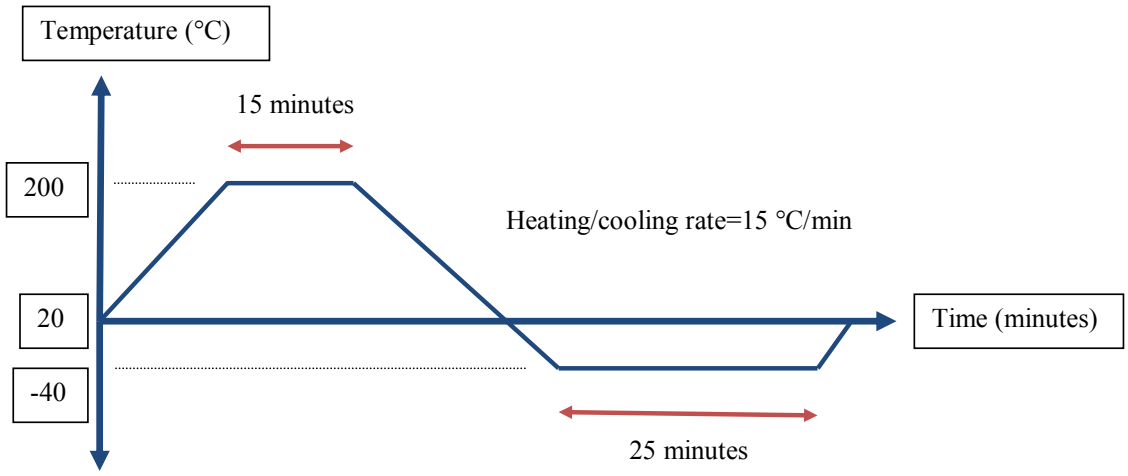

Figure 6.15: Thermal cycle diagram

6.4.1 THERMAL PROFILE

There are 4 important points in the thermal cycling which are summarized in the Table 6.2. These parameters can have a major influence on the final properties of solder joints.

In [Bartelo et al. 2001], they conducted experiments to compare the fatigue life of SAC and eutectic solders at temperature ranges of 0 to 100°C and -40 to 125°C. They concluded different results according to the ranges of the thermal cycles they used. They found that the fatigue life of SAC solders was better than the eutectic solders in the 0 to 100°C temperature range. However in [Setty et al. 2005], they found that in -40 to 125°C ranges, the eutectic solders had a better fatigue life than the SAC solders. They also studied the effects of the hot and cold dwell times on the similar behavior of SAC and eutectic alloys. They found that the cold dwell temperature has little effect on the relative fatigue life. It was concluded that the change in the fatigue life was due to either hot dwell peak temperature or due to the differences in the strain range imposed by the respective temperature ranges or due to both.

Table 6.2: Thermal cycle parameters

Maximum temperature	200°C
Minimum temperature	-40°C
Hot Dwell time	15 minutes
Cold Dwell time	25 minutes
Heating rate	15°C/min
Cooling rate	15°C/min

In the microelectronics industry, most of the damage accumulation in the solder joints is caused by the hot dwell time [Setty et al. 2005]. The accelerated heating or cooling may also play an important role in controlling the overall impact of thermal cycles. For the accelerated testing, it is highly recommended to relax the solders sufficiently during hot dwell times. Thus a shorter dwell time, during accelerated testing, would lead to a longer creep life which is mainly due to less fatigue damage per cycles. On the other hand, a longer hot dwell time results in an almost complete creep stress relaxation during each cycle and consequently a shorter fatigue life.

Further, in [Bartelo et al. 2001 and Sahasrabudhe et al. 2003], it was observed that the increase in the dwell time dramatically reduces the number of cycles to failure for solder. They also observed that it causes a rapid saturation of the cycles towards failure. Therefore, it is very important to allow sufficient relaxation to the solders during test conditions. This would allow one to accurately relate the life under test conditions to the life in the majority of the field

conditions. Furthermore, to understand the effects of dwell times on the fatigue life of SAC solders, [Sahasrabudhe et al. 2003] conducted thermal shock tests. They found that the fatigue life was most sensitive to hot dwell times in the range of 5 to 10 minutes. However it may change by changing the peak temperatures.

6.4.2 THERMAL CYCLES RESULTS

Dog-bone shape tensile specimens as presented in chapters 3 are used in this study. At least 3 samples for each composition were placed in the heating chamber with the thermal cycle as shown earlier in Figure 6.15. In our study, we focused on the number of thermal cycles. The results for 100 thermal cycles in the true and engineering stress-strain diagrams are given in Figures 6.16-6.19. After treating these results, the yield stress and tensile strengths are presented in Figures 6.20-6.21 respectively. A significant improvement is observed.

Similarly, in Figures 6.22-6.24, the true and engineering stress-strain curves are presented for 200 thermal cycles. These results are treated to extract the yield stress and tensile strengths and are given in Figure 6.25-6.26 respectively.

Figures 6.27-6.28 represent the true and engineering stress-strain curves at -60°C. Figures 6.29-6.31 show the true and engineering stress-strain curves at 140°C whereas these results are combinely plotted for engineering and true stress-strain curves in Figures 6.32-6.33 respectively. The yield stress and tensile strengths at 140°C are plotted in Figures 6.34-6.35 respectively.

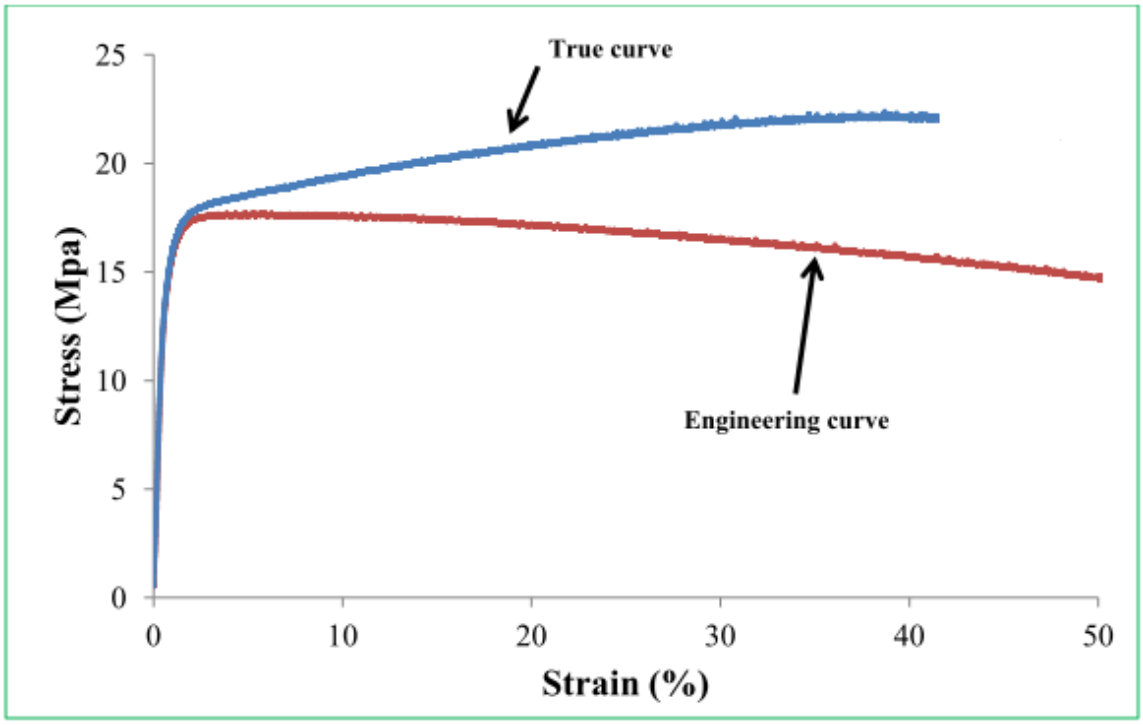

Figure 6.16: SAC "100 thermal cycles" True and Engineering stress-strain curves

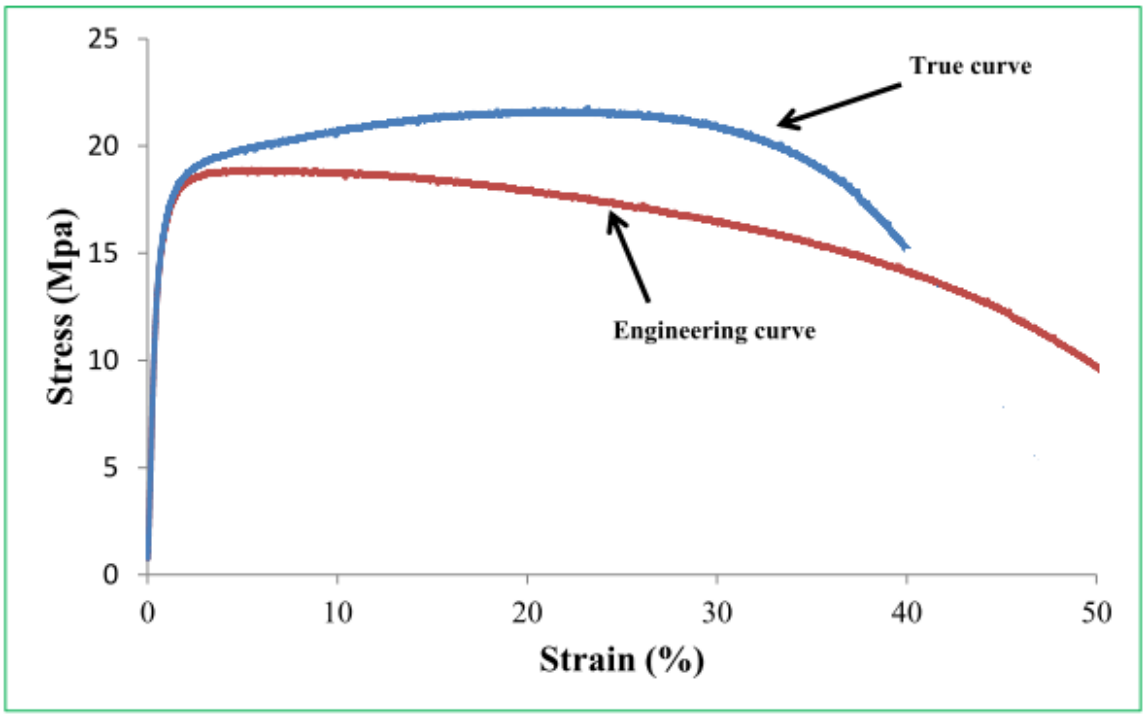

Figure 6.17: SAC-0.01La "100 thermal cycles" True and Engineering stress-strain curves

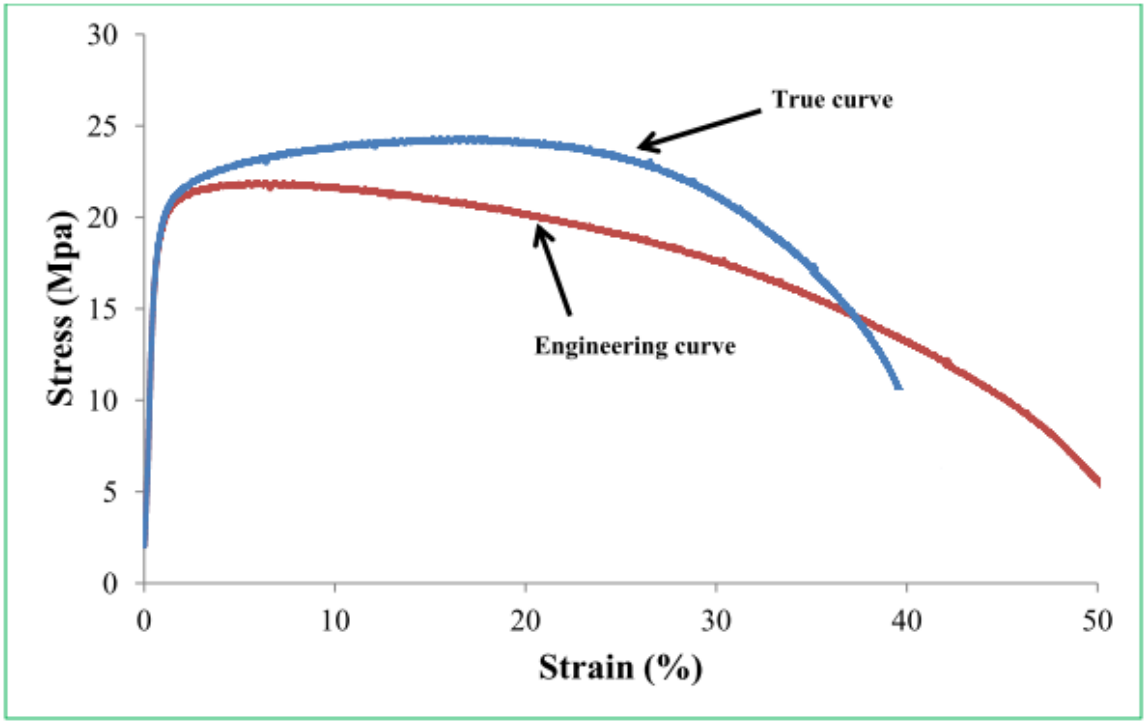

Figure 6.18: SAC-0.05La “100 thermal cycles” True and Engineering stress-strain curves

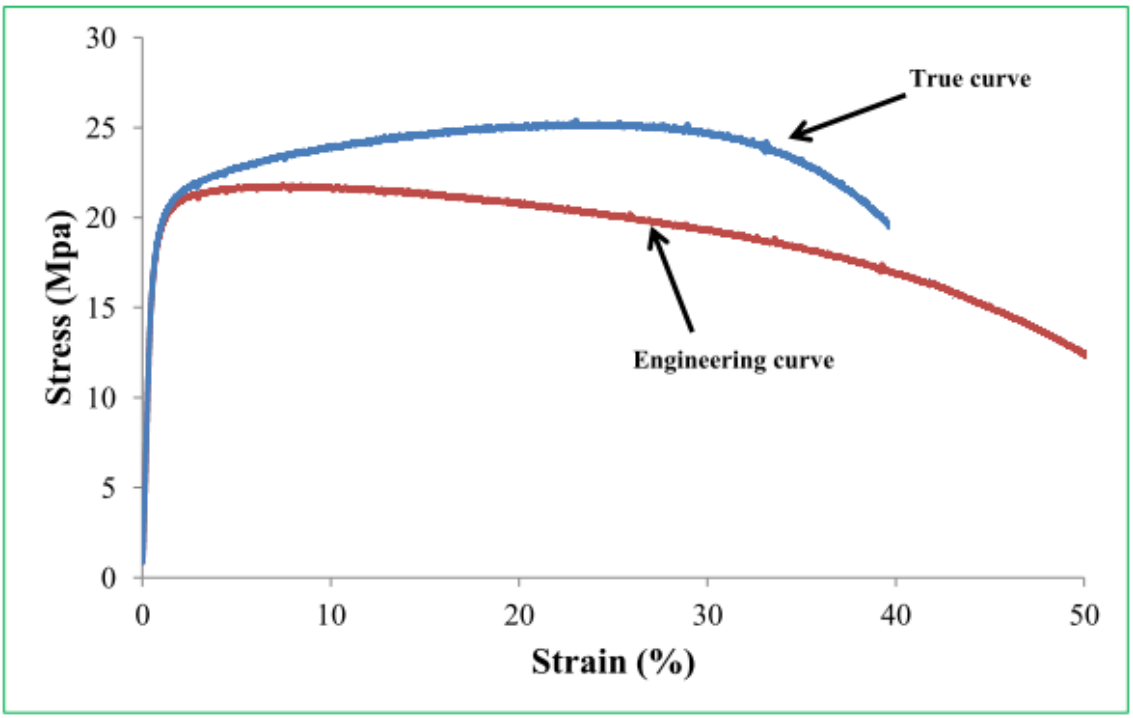

Figure 6.19: SAC-0.5La “100 thermal cycles” True and Engineering stress-strain curves

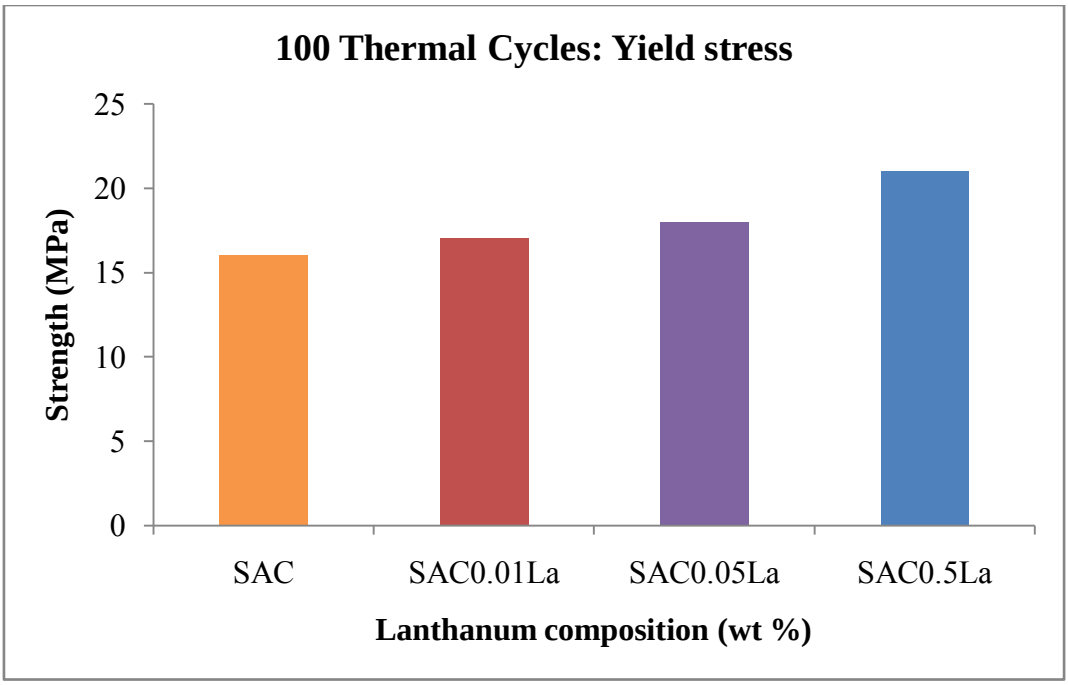

Figure 6.20: Yield stress for SAC and SAC-La alloys (100 thermal cycles)

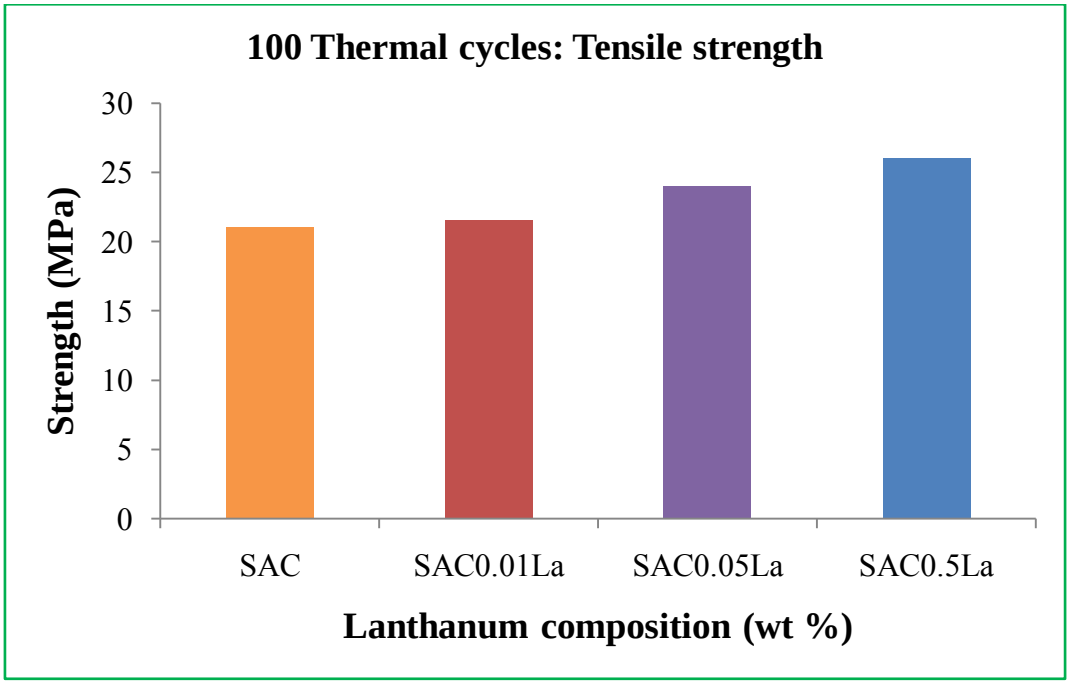

Figure 6.21: Tensile strength for SAC and SAC-La alloys (100 thermal cycles)

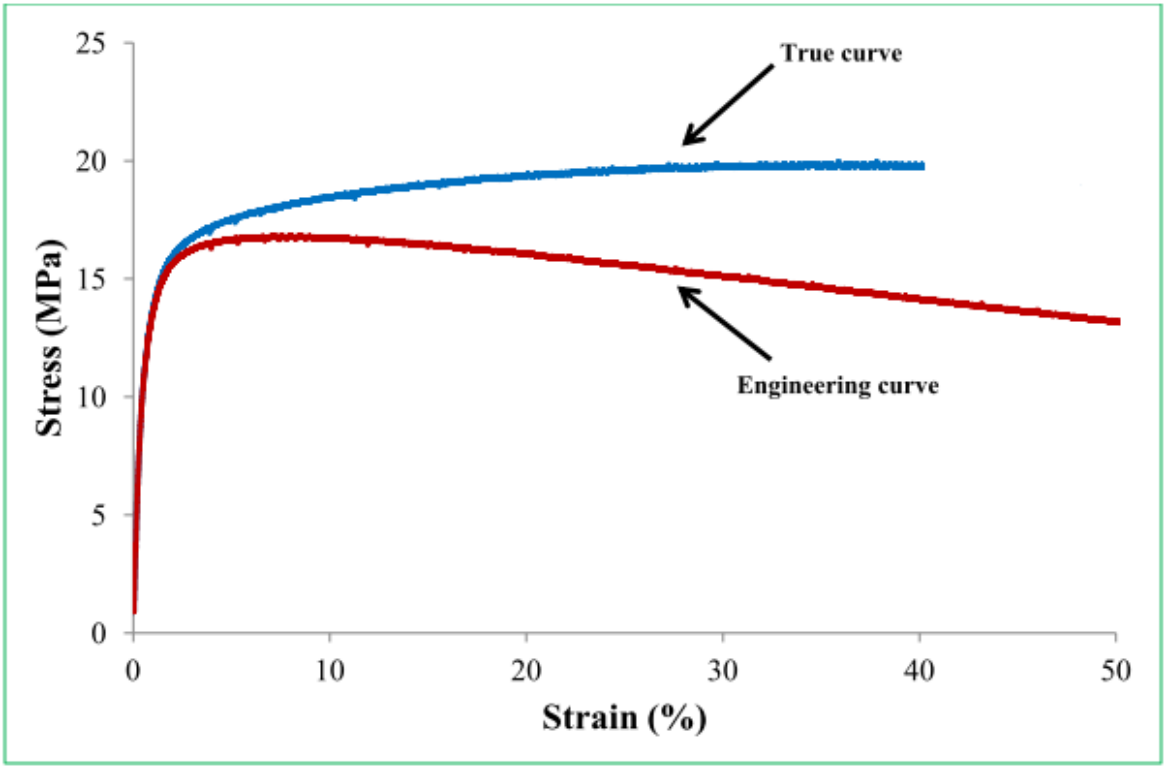

Figure 6.22: SAC "200 thermal cycles" True and Engineering stress-strain curves

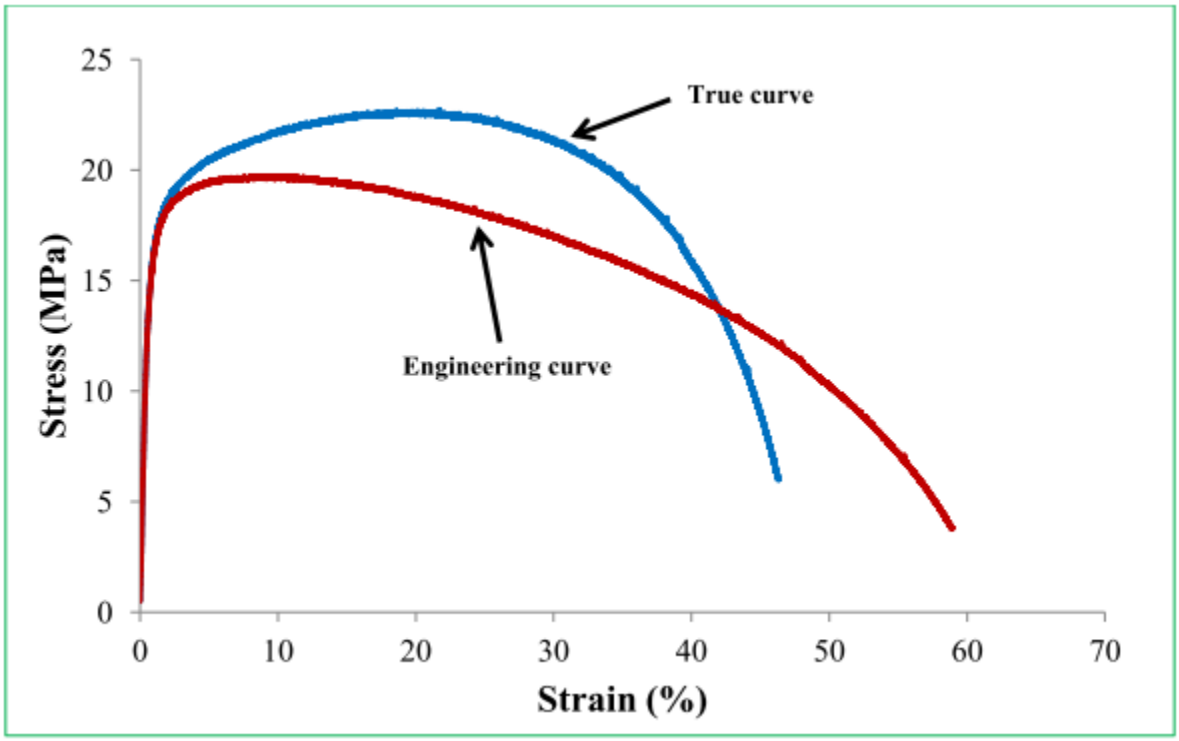

Figure 6.23: SAC-0.05La "200 thermal cycles" True and Engineering stress-strain curves

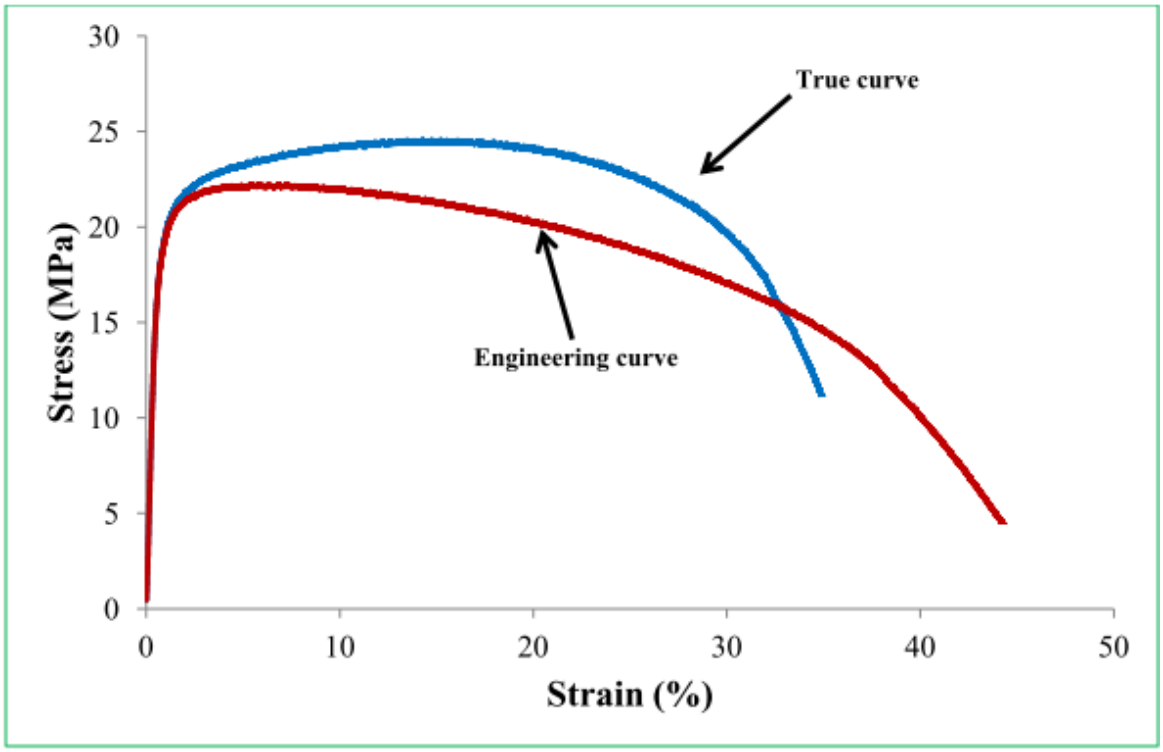

Figure 6.24: SAC-0.5La "200 thermal cycles" True and Engineering stress-strain curves

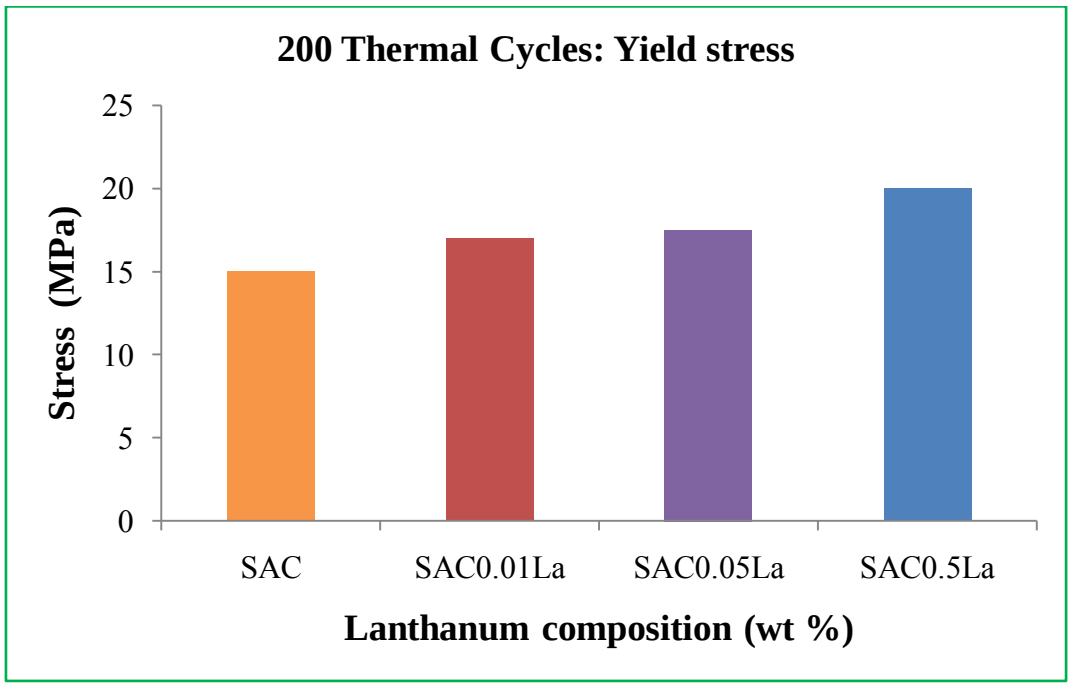

Figure 6.25: Yield stress for SAC and SAC-La alloys (200 thermal cycles)

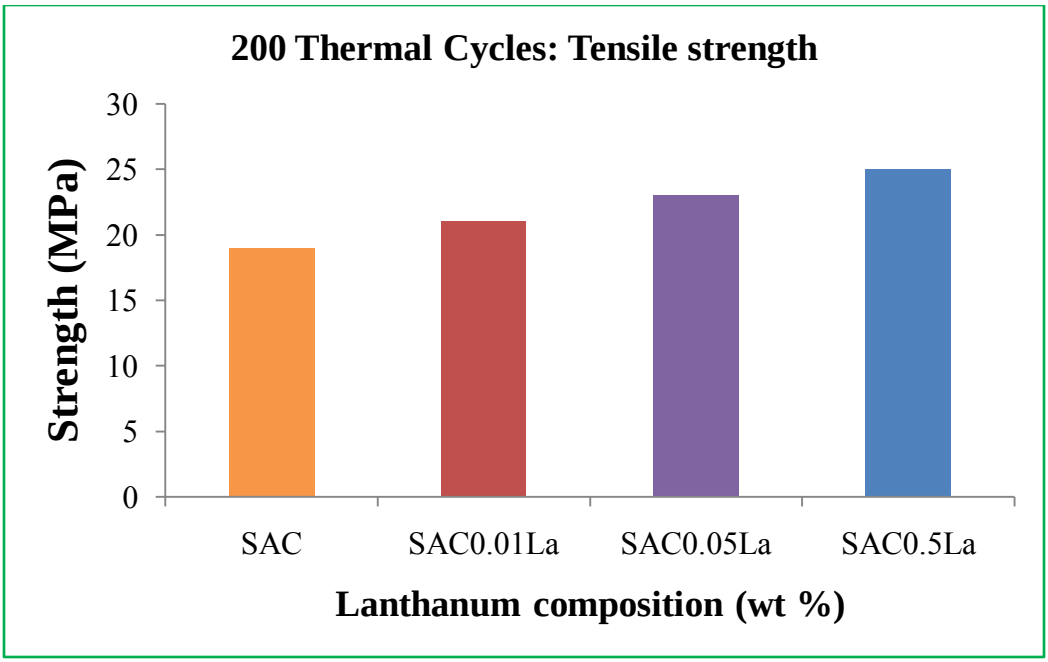

Figure 6.26: Tensile strength for SAC and SAC-La alloys (200 thermal cycles)

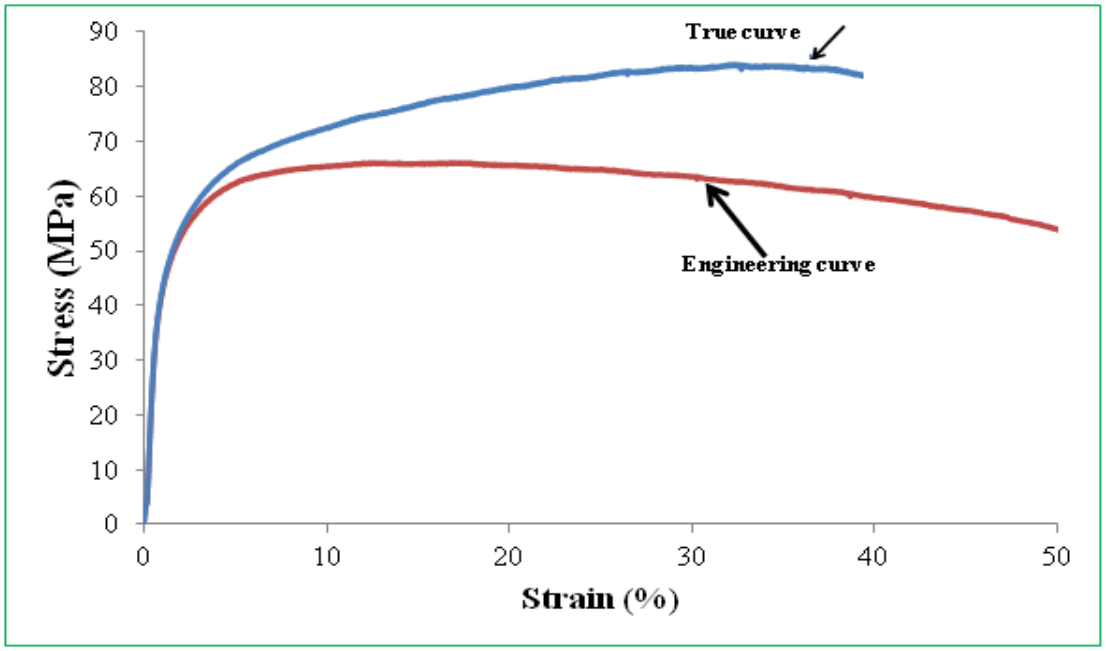

Figure 6.27: SAC "at -60°C" True and Engineering stress-strain curves

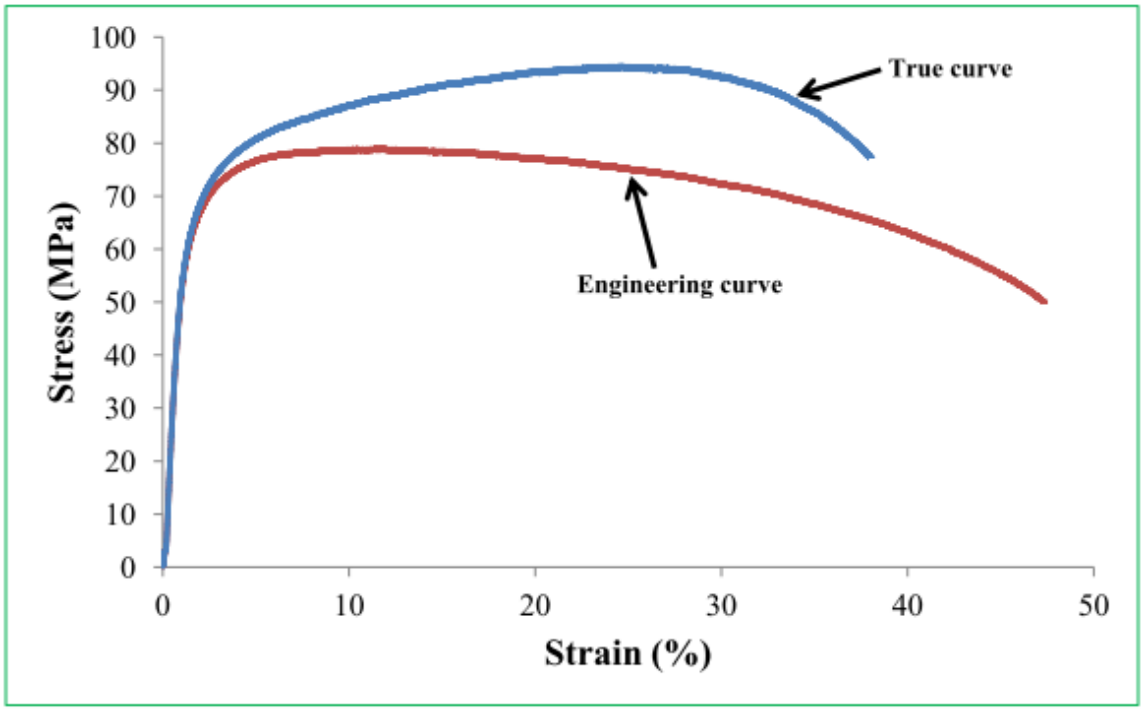

Figure 6.28: SAC-0.25La “at -60°C” True and Engineering stress-strain curves

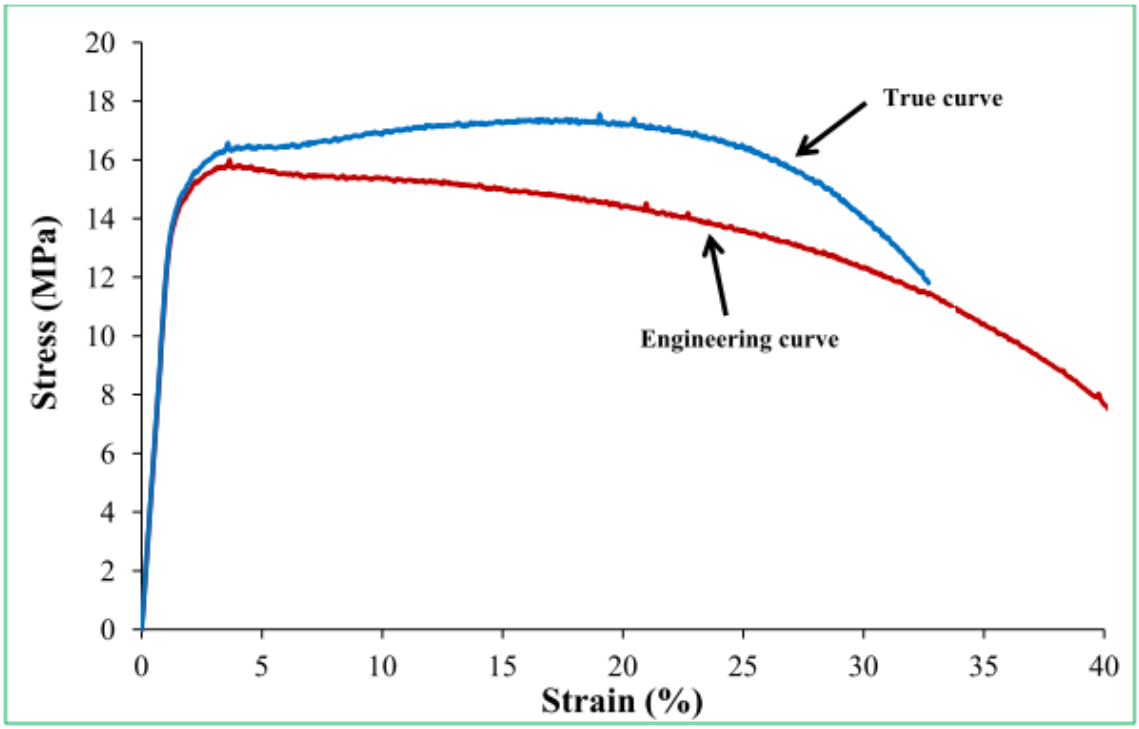

Figure 6.29: SAC “at 140°C” True and Engineering stress-strain curves

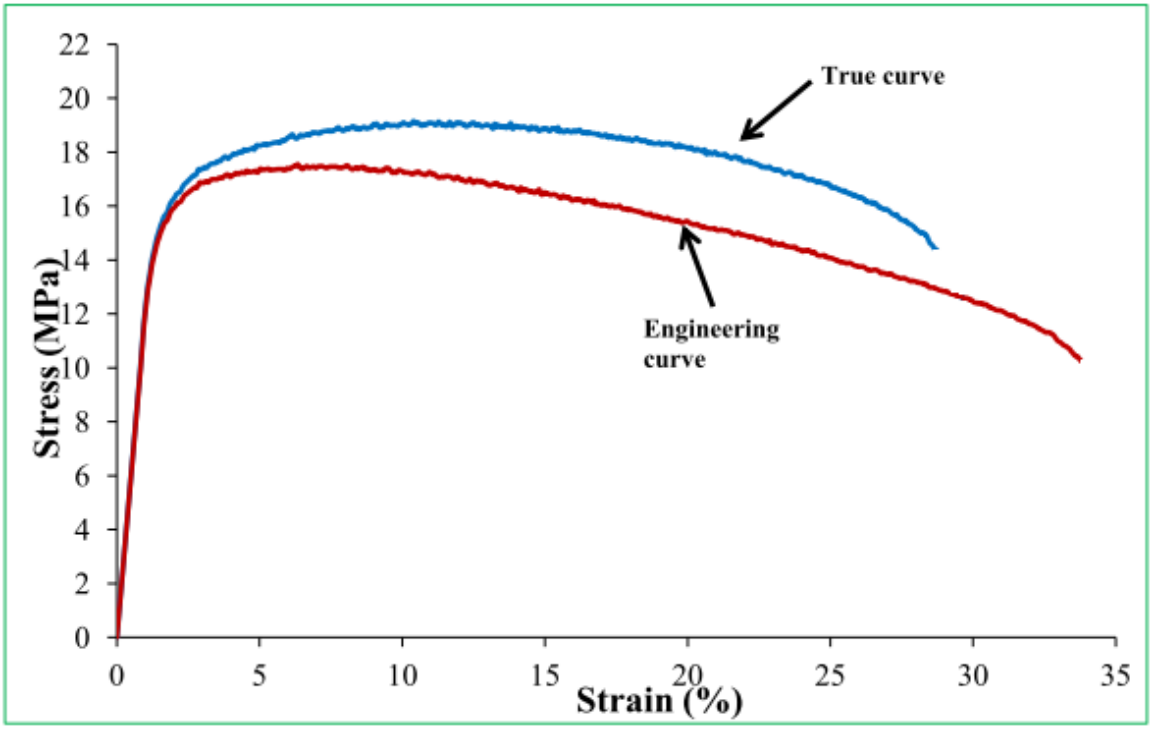

Figure 6.30: SAC-0.05La “at 140°C” True and Engineering stress-strain curves

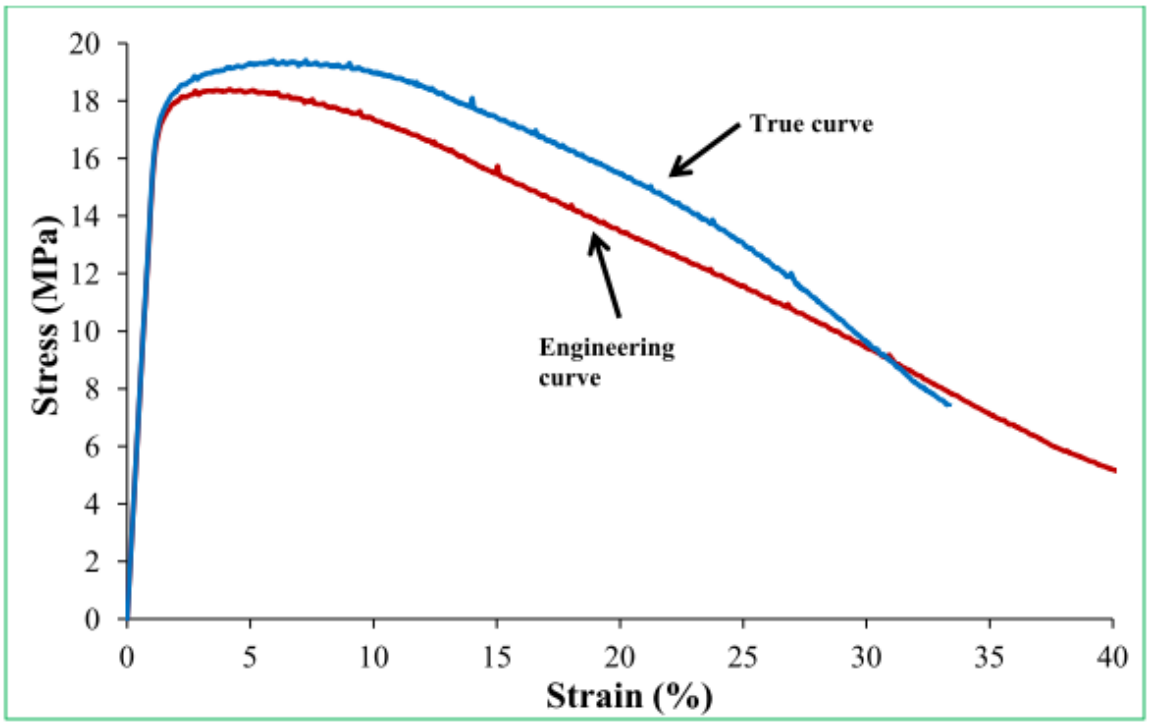

Figure 6.31: SAC-0.5La “at 140°C” True and Engineering stress-strain curves

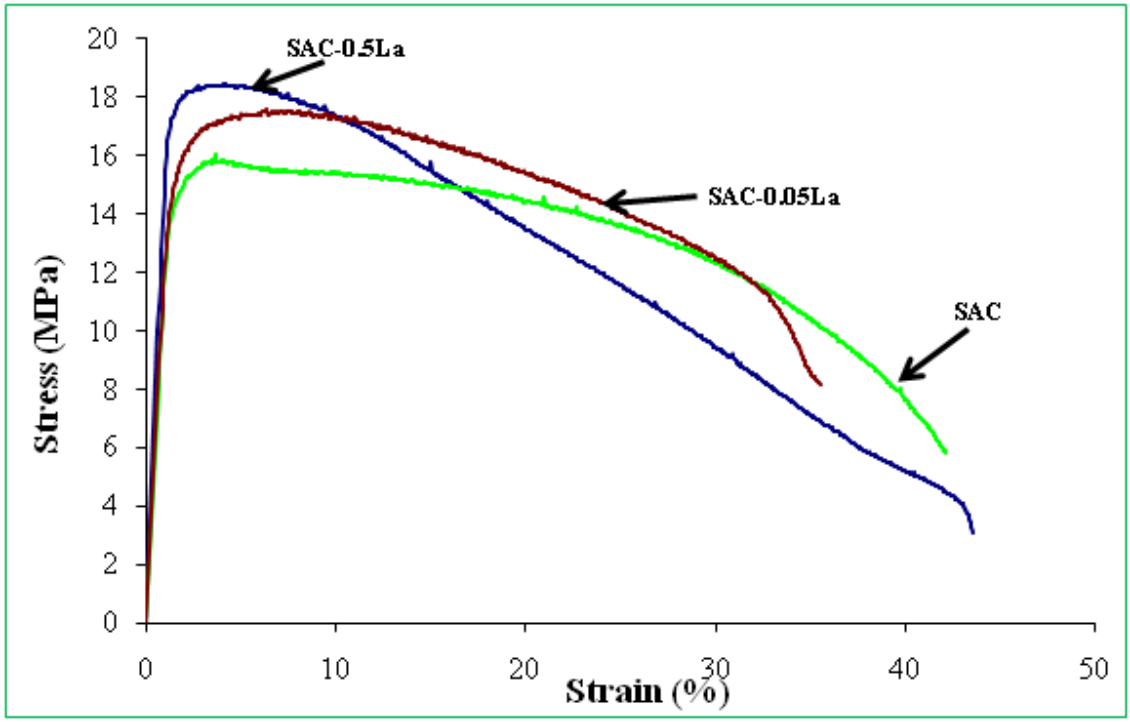

Figure 6.32: Engineering Stress-Strain curves at 140°C

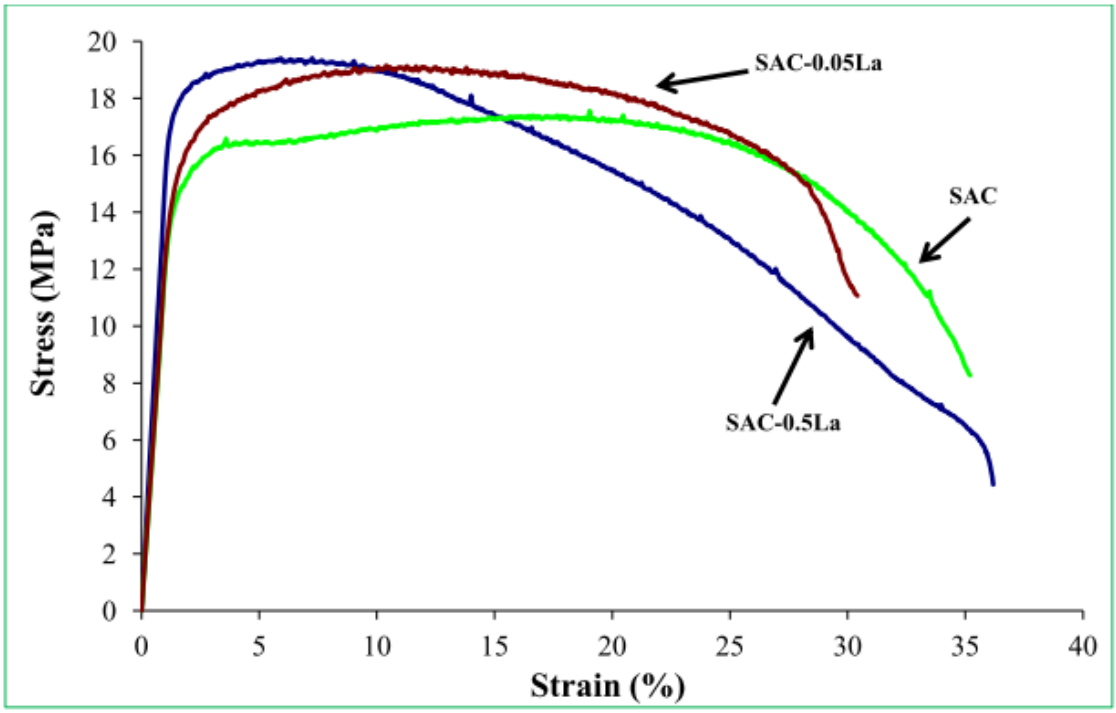

Figure 6.33: True Stress-Strain curves at 140°C

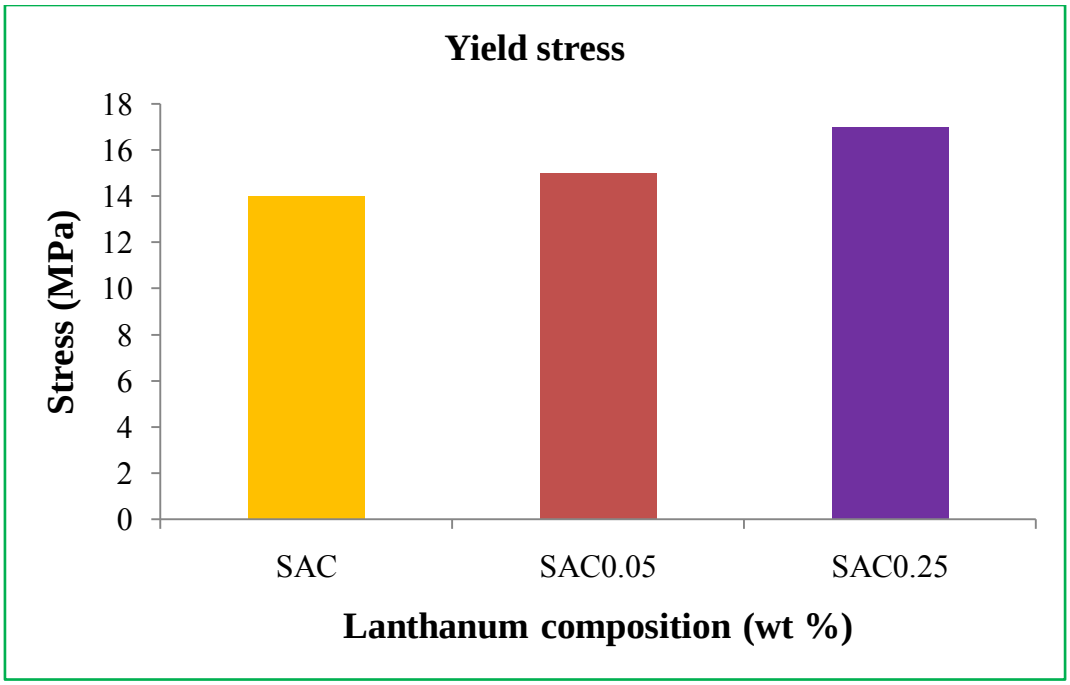

Figure 6.34: Yield stress for SAC and SAC-La alloys (at 140°C)

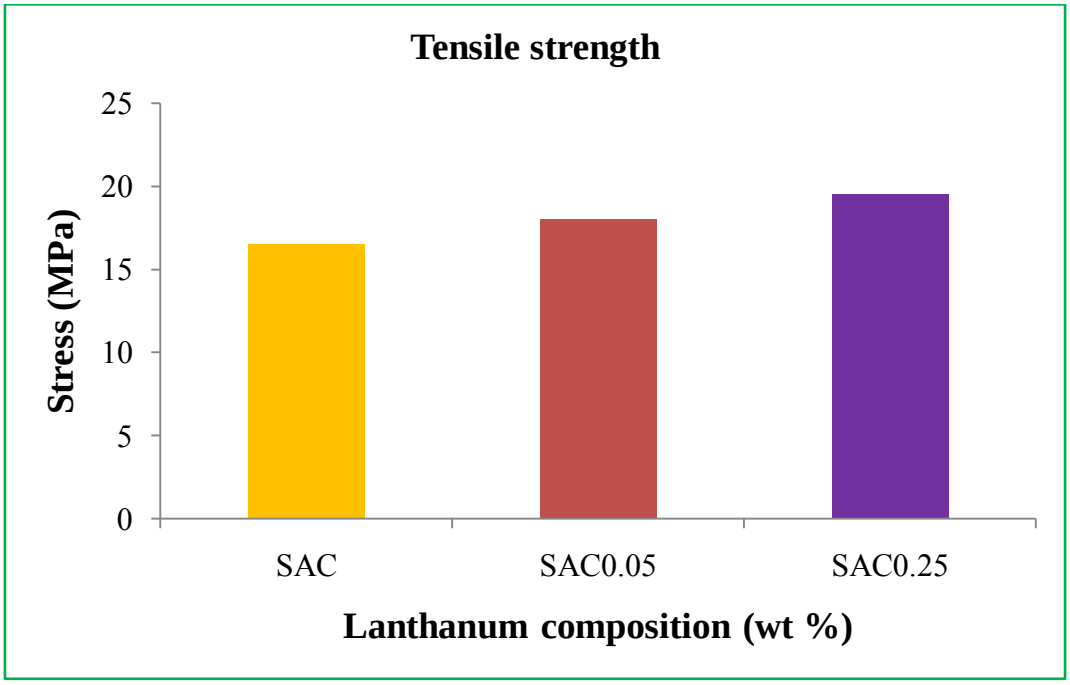

Figure 6.35: Tensile strength for SAC and SAC-La alloys (at 140°C)

6.5 COMPARISON WITH TIN-LEAD SOLDER ALLOYS

Due to long time usage of SnPb solders, good understanding and well established studies are available for them. Their mechanical properties are compared with both SAC and SAC-La doped alloys with similar domains of environmental and mechanical conditions applied during service/experiments. It has been shown that both yield stress and tensile strength for SAC-La doped alloys are higher than the conventional Sn-Pb solders as provided in Figures 6.36-6.37 respectively. It would be described in chapter 9 (wettability testing) that however the wettability characteristics of SnPb solders are much better than the SAC and SAC-La doped alloys. Mechanical properties are not the only parameter that classifies a solder to be the best. Infact, other characteristics such as wettability (solderability) over copper substrates should also be considered beyond the mechanical properties evaluation for highly reliable microelectronics applications.

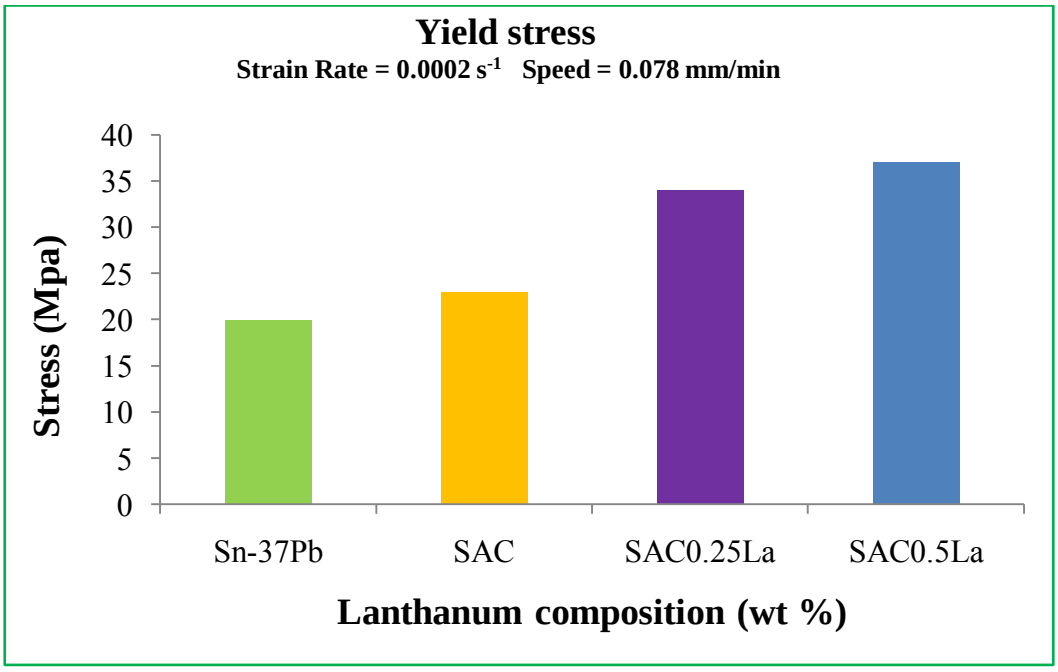

Figure 6.36: Yield stress for SnPb, SAC and SAC-La alloys

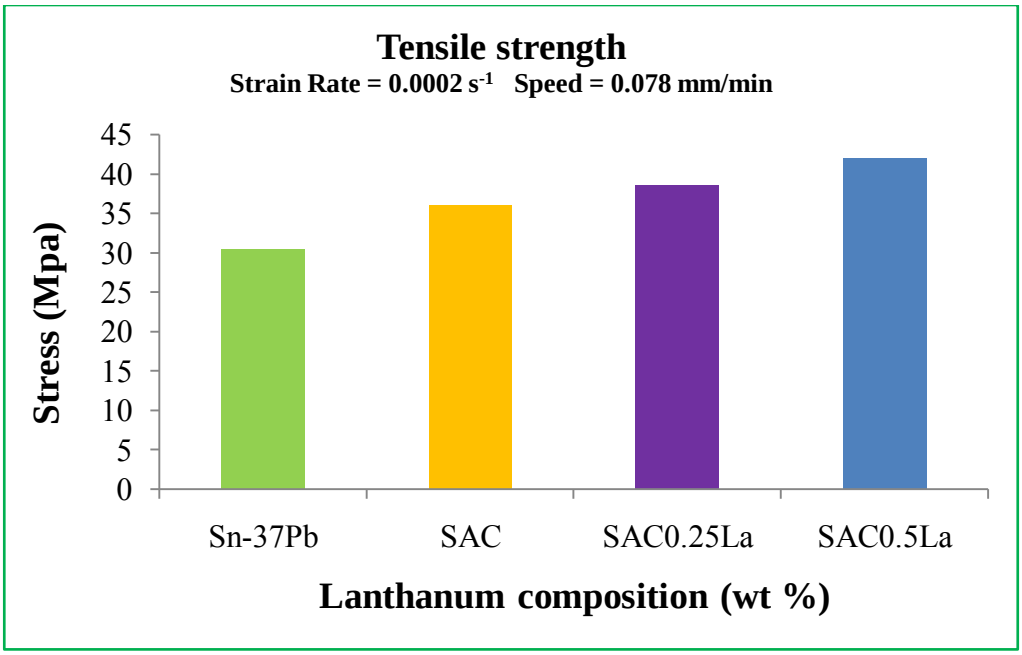

Figure 6.37: Tensile strength for SnPb, SAC and SAC-La alloys

6.6 SUMMARY

This chapter is dedicated to analyze the mechanical properties of SAC and SAC-La doped alloys. Yield stress, tensile strength and ductility are evaluated in varying environmental conditions.

The study is expanded from as-cast samples to isothermally aged samples at an elevated temperature of 150°C. Quasi uni-axial tensile testing is used at practically possible small strain rates of $2*10^{-4}$ s^{-1}, $2*10^{-3}$ s^{-1} and $2*10^{-2}$ s^{-1}, which are quite close to which the solder joints [Schlumberger] are exposed in the real time. Engineering stress-strain diagrams are used to plot the true stress-strain diagrams and are then treated using 0.2% offset technique to extract the interested values.

Other than the room temperatures testing, in some situations, the solder joints are exposed to quite low and quite high temperatures during service. The lowest temperature used in this study is -60°C whereas the highest temperature used is 140°C. Similar values are extracted as mentioned above.

In many applications, like consumable electronics and automotives, the solder joints are exposed to different environmental conditions that consist of high temperature isothermal aging and thermal cycles. The thermal cycles used in this study have the minimum temperature of -40°C and the maximum temperature of 200°C. Different number of cycles is used for at least 3 samples of each composition. A good enough heating/cooling rates are used up to 15°C/min. Different cold and hot dwell times are applied.

It has been concluded that lanthanum doping has significant effects on the improvement of mechanical properties for both as-cast and thermally treated alloys in almost all environmental conditions.

CHAPTER 7

CREEP EXPERIMENTS AND MODELING

7.1 Introduction to Creep

In general, many material properties vary with increasing or decreasing temperatures. Solder joints are exposed to severe conditions from -60°C up to 200°C (depending upon the alloy used). The high temperatures can increase some material properties like ductility but some properties can decrease dramatically as yield stress and tensile strength. Fick's Law, as given below in equation (7.1), provides useful information about the atomic mobility related to diffusion during high temperatures,

$$D = Do\ exp\left\{-\frac{Q}{RT}\right\} \quad (7.1)$$

where D is the diffusion rate, Do is a constant, Q is the activation energy for atomic motion, R is the universal gas constant (8.314J/mole K) and T is the absolute temperature. The diffusion controlled mechanisms significantly affect the mechanical properties and hence the performance of solder alloys at elevated temperatures during service. They include new slip systems, grain boundary sliding and concentration of vacancies etc. Other than that, the diffusion rate dependant process such as corrosion and oxidation would affect the creep life of solder alloys at high homologues temperatures.

Creep is not an intrinsic materials response and is therefore performance based behavior for almost all solder alloys (binary and tertiary). Moreover, creep is mostly dependent on the homologues temperatures to which the solder joints are exposed (where homologues temperature is the ratio of the absolute service temperature to the absolute melting temperature of the alloy). Creep can be defined as time-dependent deformation at absolute temperatures greater than one half of the absolute melting. In some cases, the temperature may not be very high but the creep phenomenon can still take place, as at room temperature for the SAC alloys.

In order to perform a creep test, a force is applied at a relatively high temperature and the changes in dimensions (mostly length) are measured (for example) with the help of an extensometer. In some cases, the sample can be loaded till it breaks, in that case the test is called a rupture test as show in Figure 7.1.

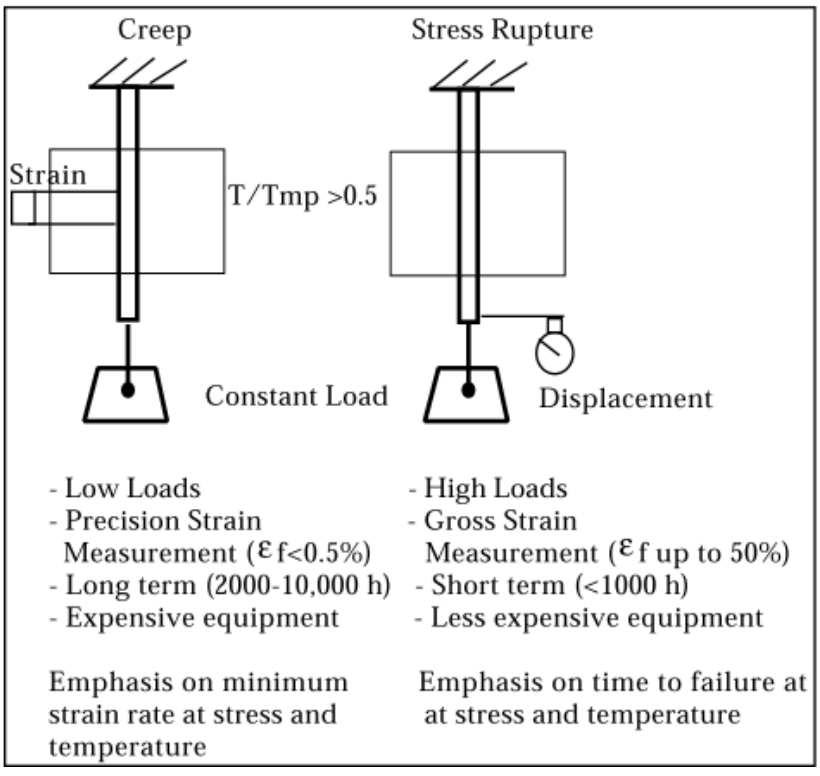

Figure 7.1: Comparison of creep and stress rupture tests

It may look easy to conduct the creep tests but in practice it is quite difficult as temperature control is critical and a big fluctuation can have a significant impact on the final results. Good resolution and well stable extensometers are an important concern as the strain rate is calculated from the % deformation stored by them. Environmental conditions can also influence the results and thus make the creep tests more complicated. In some cases, if a premature failure occurs, the creep tests are repeated with a fresh specimen. Uniformity of the applied stress is critical if the creep tests are to be interpreted.

The overall creep tests/results give the plots of strain vs. time, as schematically shown in Figure 7.2 [Zhang 2010]. The initial strain, $\varepsilon i = \sigma i/E$, is simply the elastic response to the applied load (stress). The strain itself is usually calculated as the engineering strain, $\varepsilon = \Delta L/Lo$.

The 3 major creep zones are shown in Figure 7.2. The primary region (I) is the transient creep with decreasing strain rate. This is due to the creep resistance offered by materials deformation. The secondary region (II) is called the steady state creep and is the most important parameter of creep curve. This steady state creep is used thoroughly in model fitting and classifying the solder alloys for the creep resistance.

In the tertiary region (III), the creep strain rate is significantly increased. This is due to the long time loading and necking phenomenon, generally happenes in tensile loadings. The load is continuously kept constant until fracture of the specimens happens. In some special cases, the quaternary regions are also included in the creep analysis of alloys but are very short and needs special attention for the data extraction.

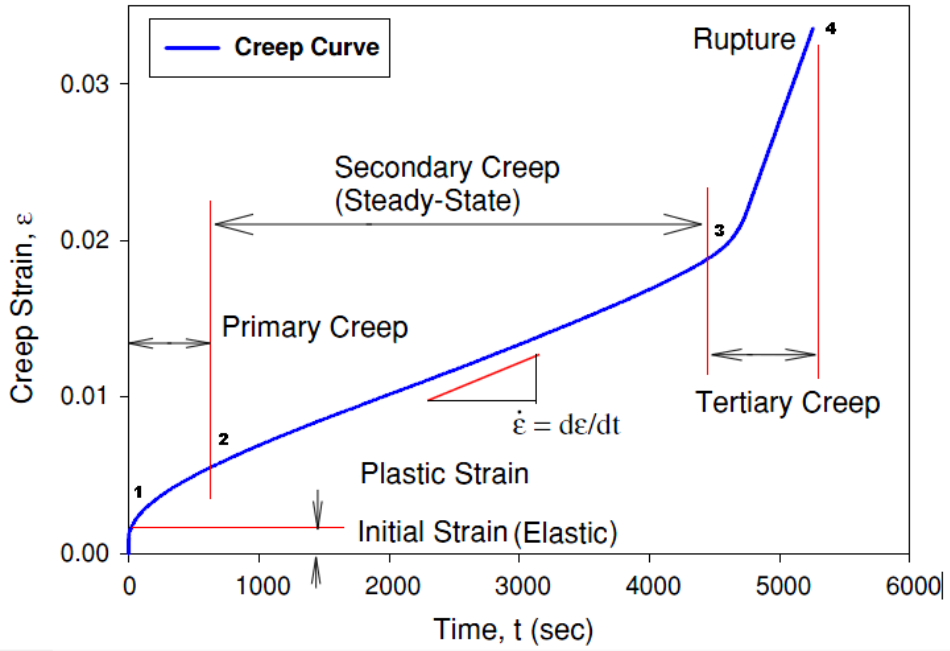

Figure 7.2: Typical creep zones [Zhang 2010]

As described earlier, the creep tests need to be linked to the applied stress (generally constant). During the elongation of the specimen, the cross sectional area decreases which compels one to decrease the applied loading in order to obtain constant stress. The effects of constant load and constant stress are shown in Figure 7.3.

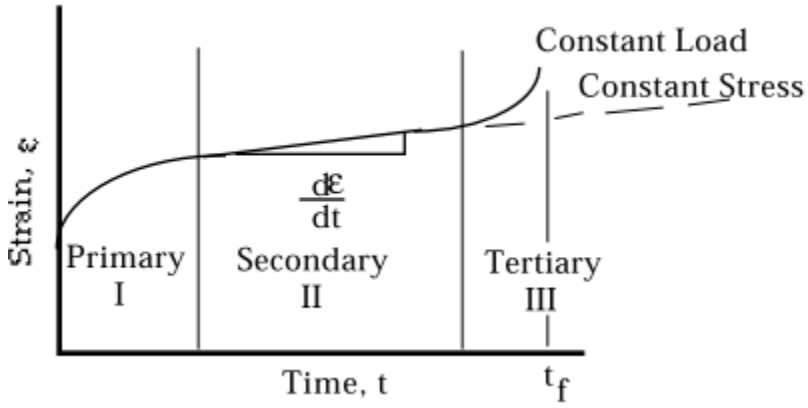

Figure 7.3: Strain time curve for a creep test

Generally, this effect (dashed line for constant stress in Figure 7.2) only manifests itself in the tertiary region, which is outside the region of interest from the secondary region. The effects of increasing temperature or increasing stress are to raise the levels and shapes of the strain time curves as shown in Figure 7.4. In isothermal tests, the shapes of the curves for increasing stress may change from dominant steady state to sigmoid with little steady state to dominant primary state. Similar trends are seen for iso-stress tests and increasing temperature (see Figure 7.4).

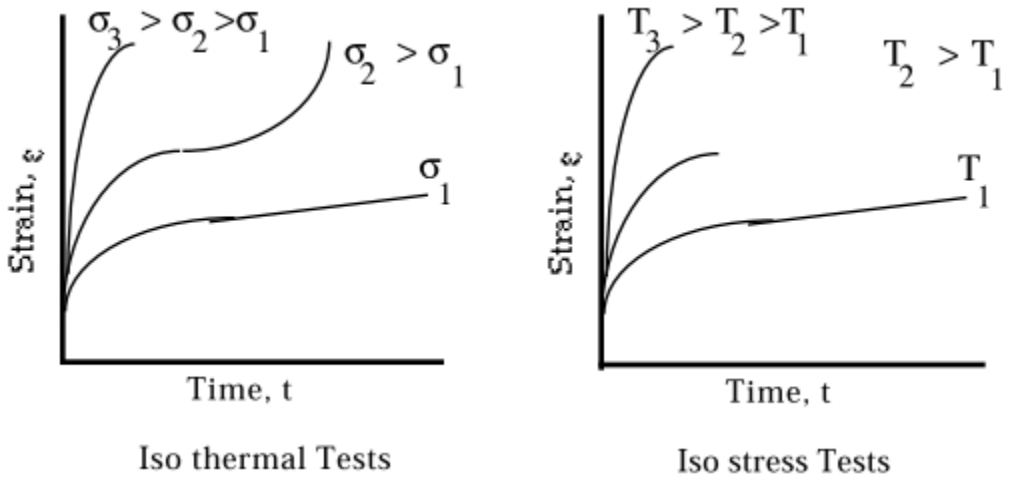

Figure 7.4: Effect of stress and temperature on strain-time creep curves

7.2 Creep Behavior of Tin Based Alloys

Figure 7.5 shows different zones in which the mechanical properties of a metal like strength and hardness change with temperatures (in Kelvin scale). If the curves are properly scaled and correctly referenced to the melting temperature of the materials, most of the metals follow the same trend with a reducing trend to zero at the melting point.

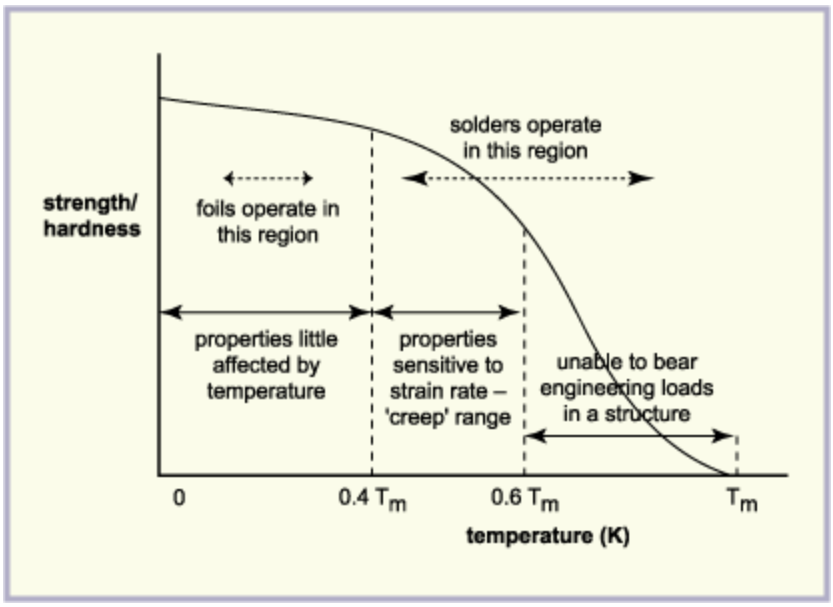

Figure 7.5: Strength/hardness of a metal related to its melting temperature
[Martin Tarr Reflow Soldering]

Many researchers refer to the idea of a "homologous temperature", where the actual service temperature of a material is expressed as a fraction of its melting temperature, in Kelvin. Solder (m.pt 183°C = 456K) at $0.85T_m$ or 115ºC (= 388K), would thus be expected to have comparable properties to copper (m.pt 1085°C = 1358K) at $0.85T_m$ or 881ºC (= 1154K). In electronics applications, where circuits typically operate over a –55ºC to +125ºC range, SAC solder (m. pt=217 ºC) is working at $0.48T_m$ to $0.57T_m$. From this, it can be deduced that the solder will have limited mechanical strength (as a bulk material) and be within the "creep range". This is mainly because of its comparatively low values for tensile strength, shear strength and modulus of elasticity as described in chapter 6 (Mechanical Properties).

Copper, on the other hand, has a much higher melting point, so foils are working at only $0.16T_m$ to $0.29T_m$, and their properties are little affected by temperature.

The creep behavior, as described earlier, is dependent on the service temperature. Of course high temperature would increase the creep strain rate and strongly impact the overall creep behavior of almost all solder alloys. RE doping is used to refine the overall microstructure and control the coarsening rate of IMCs. They increase the yield stress and tensile strength and therefore increase the solder joint reliability by increasing the creep resistance at high temperatures. Figure 7.6 shows how a typical creep curve is modified by adding RE elements (Ce) to SnAg alloy [C. Wu et al. 2004 and C. Wu, Yu, et al. 2002]. The creep curve is improved in both time and strain before failure. Moreover, the steady state creep strain is significantly decreased with RE dopings. This form of life-time improvement applies mainly to low creep temperatures, e.g. 30°C (303 K) and 75°C (348 K).

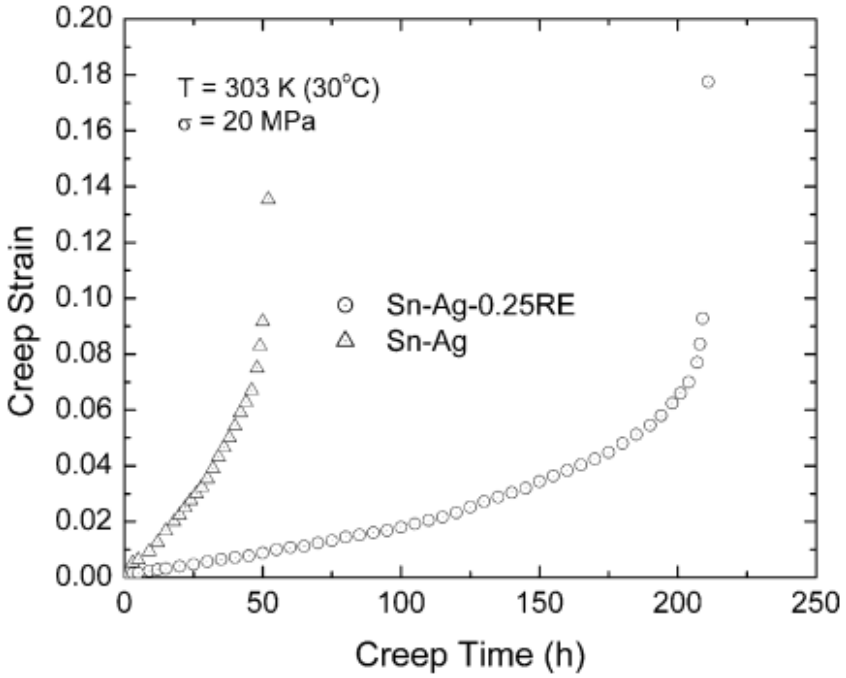

Figure 7.6: Typical creep curves of Sn–3.5Ag and Sn–3.5Ag–0.25RE [Wu et al. 2004]

Igoshev et al. also investigated the creep behavior of SnAg alloy. They found the nucleation of the microcracks mainly because of decohesion along the matrix/particle boundaries

[Igoshev et al. 1998, Igoshev & Kleiman 2000 and Igoshev et al. 2000]. The IMCs, specially Ag_3Sn intermetallics particles,play two different roles. They may strengthen the alloy matrix and prevent the formation of large dislocation pile-ups at grain boundaries. On the other hand, the higher the number of particles in a given matrix, the more matrix/intermetallics interfaces it contains, leading to a higher likelihood of micro-crack nucleation that can speed up the failure process [Wu et al. 2004]. In [Huang et al. 2002], the eutectic SnAg alloy was investigated for its creep behavior at three temperatures ranging from 30°C to 120°C (393 K), under the tensile stress range of $\sigma/E=10^{-4}$ to 10^{-3}. One of the major results is confirming that the steady-state creep rate of SnAg is controlled by the dislocation-pipe diffusion in the Sn matrix [Wu et al. 2004].

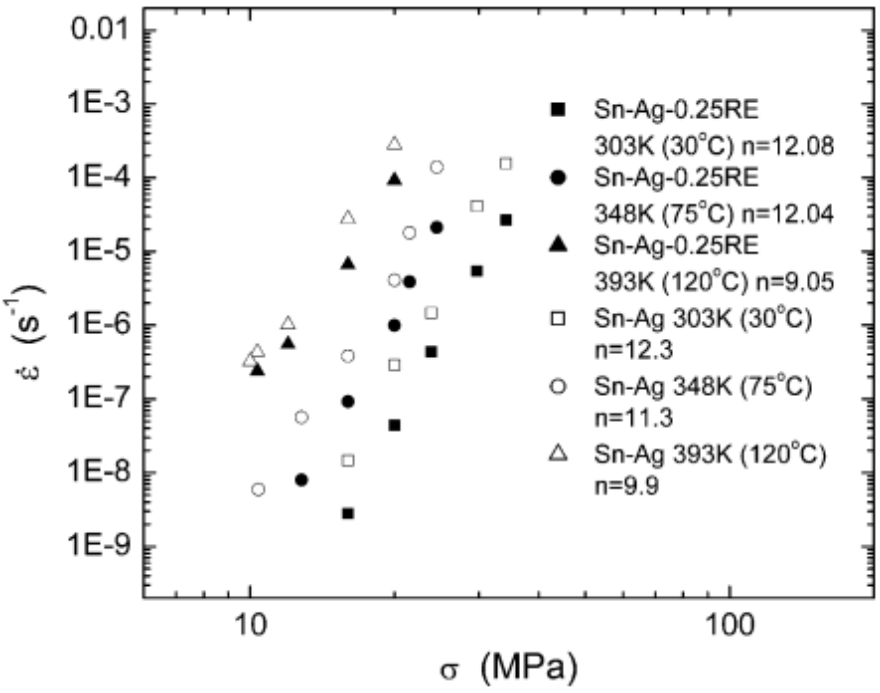

Figure 7.7: Comparison steady-state creep strain with creep time for Sn–3.5Ag and Sn–3.5Ag–0.25RE [Wu et al. 2004]

Similary, at different stress levels and temperatures, the experimental data for SnAg and SnAg–0.25RE are presented in Figure 7.7 above [C. Wu, Yu, et al. 2002]. With the addition of RE elements, mainly Ce and La, the creep strain decreased substantially.

The creep rate, $\dot{\gamma}$, that relates to the microstructure in alloys with precipitates can be expressed as equation (7.2) [Oliver & Nix 1982],

$$\dot{\gamma} = \frac{b\rho\lambda^2}{\Lambda\Delta t} \quad \text{.....(7.2)}$$

where ρ is the dislocation density, Λ the spacing of obstacles along an arrested dislocation under stress, Δt is the time required to by-pass an obstacle, and λ^2 is the average area per particle on the slip plane and is approximately the average area slipped per activated event.

With the addition of RE elements, the number of IMCs particles would increase. As discussed earlier, with 0.25% RE addition, a significant refinement of particles is seen, which would sharply decrease λ. As the creep rate is directly proportional to λ^2, therefore, the addition of small amounts of RE elements would provide an alloy with higher creep resistance.At the same time, it is essential to minimize particles coarsening, with the RE addition, during prolonged exposure at elevated temperatures. It would ensure that the finely dispersed IMCs particles are still stable at higher temperature, so as to control the creep rate [C. Wu, Yu, et al. 2002].

The improvement in creep behavior is also found in the SnCu alloy by adding Ce and La RE elements. As shown in Figure 7.8, the creep resistance of SnCu–0.5RE is superior to that of SnCu with a much longer creep lifetime [C. M. L. Wu, Yu, et al. 2004, C. M. L. Wu & Huang 2002].

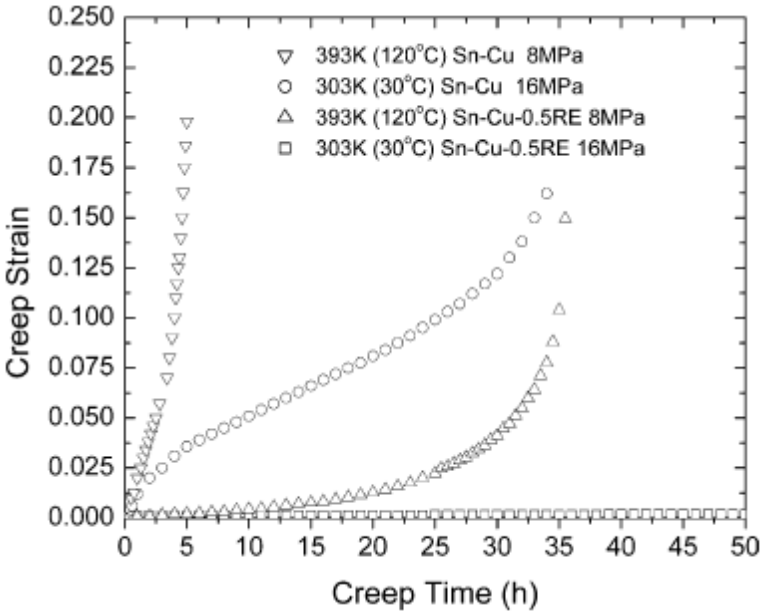

Figure 7.8: Comparison of creep resistance between Sn–0.7Cu and Sn–0.7Cu–0.5RE alloys [Wu et al. 2004]

Other than the binary alloy systems, the Sn–3.8Ag–0.7Cu tertiary alloy was doped with 1% RE elements in [Z. Chen et al. 2003]. As a result, the creeps rupture life of the solder joint at room temperature increased by about seven times.

7.3 Creep Experiments

To perform this study, the samples were prepared with a casting process avoiding oxidation and microstructure variations which are thermally activated phenomenon. A water quenching process has been used to cool down the samples just after casting as described in detail in chapter 3 (Experimental Design). The dog-bone shape specimens are used with gauge length of 6.5 mm, width of 3.98 mm and a thickness 1.98 mm as final dimenssions. 5kN load cell for the tensile testing machine is used. Heating chamber was connected to acquire the desired environmental conditions.

A special fixture was designed to provide enough space for the extensometer, used to extract the useful deformation (strain) history during testing. A digital thermocouple was connected to the specimens to ensure correct temperature readings.

Three different loadings were tested; 10Mpa, 14Mpa and 16Mpa on each alloy with SAC, SAC-0.05La and SAC-0.5La compositions at three different temperatures of 120°C, 80°C and 40°C with a displacement of the moving grip of 0.078mm/min. Different temperatures were necessary to calculate the activation energy of the materials during creep analysis for each alloy.

During the experiment, it is important to allow the temperature to reach to the desired peak limit. During this process, the material expands (during heating) and the grips of the machine need to be continuously adjusted (expanded) to avoid the excessive compression of the specimen. Following Figures 7.9-7.14 are the creep plots at 120°C and different stress ranges for SAC, SAC-0.05La and SAC-0.5La compositions. They are used to extract the creep strain and hence relate the respective creep resistance of different compositions.

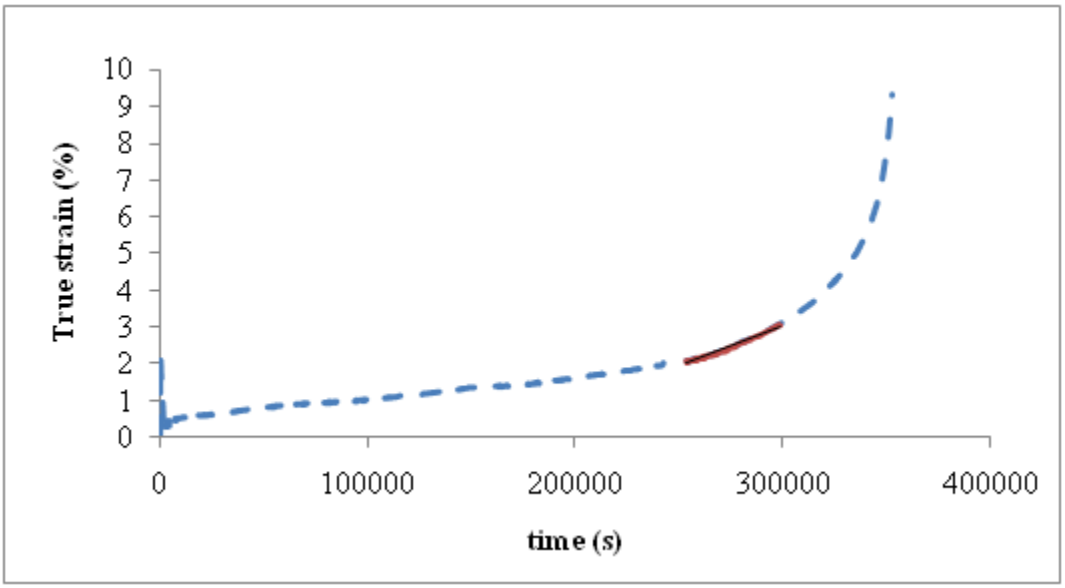

Figure 7.9: Creep curve for SAC at 10Mpa and 120°C

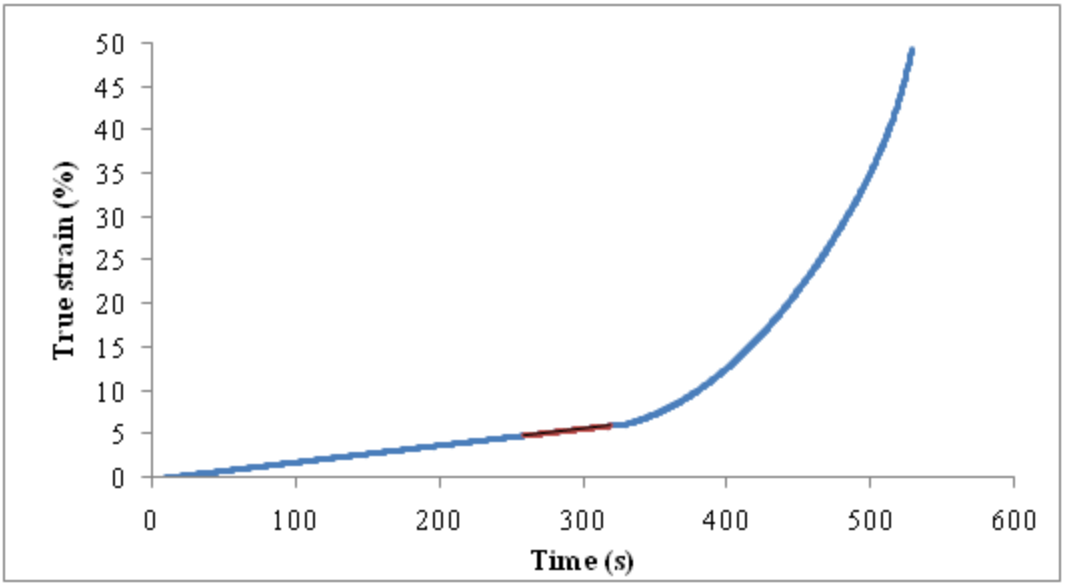

Figure 7.10: Creep curve for SAC at 16 Mpa and 120°C

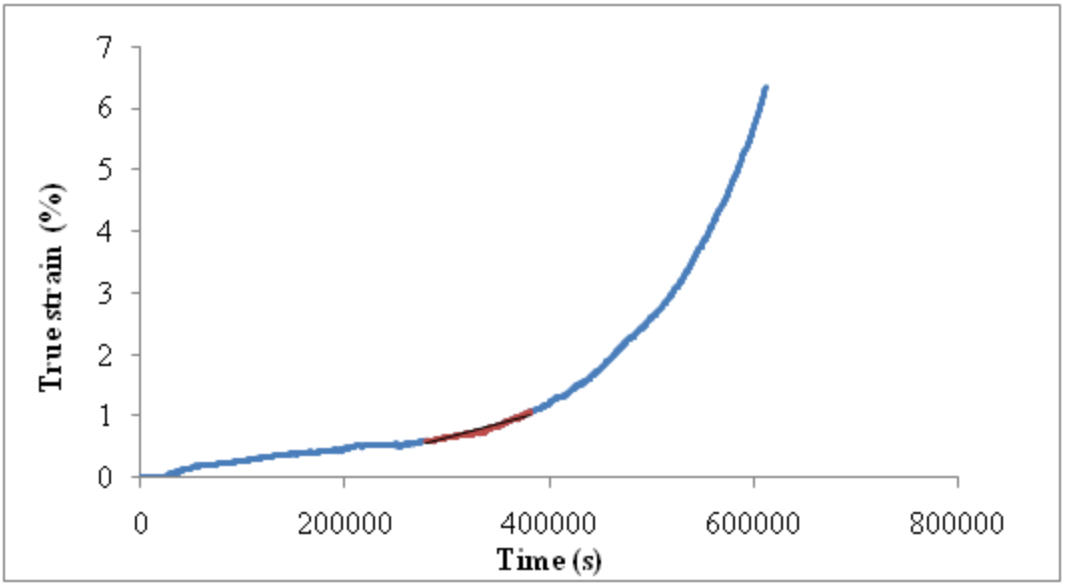

Figure 7.11: Creep curve for SAC-0.05La at 10 Mpa and 120°C

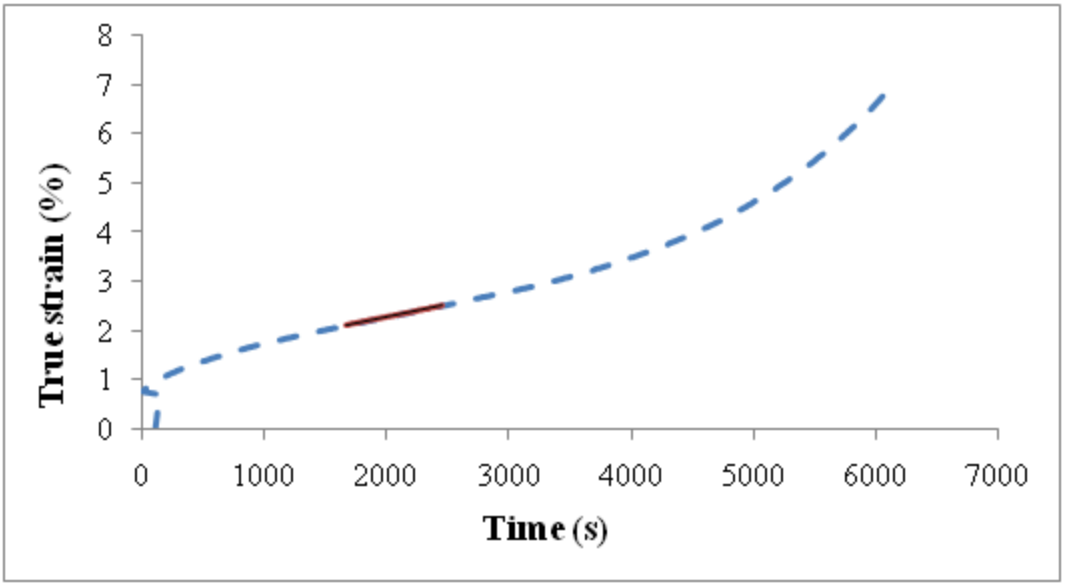

Figure 7.12: Creep curve for SAC-0.05 at 16 Mpa and 120°C

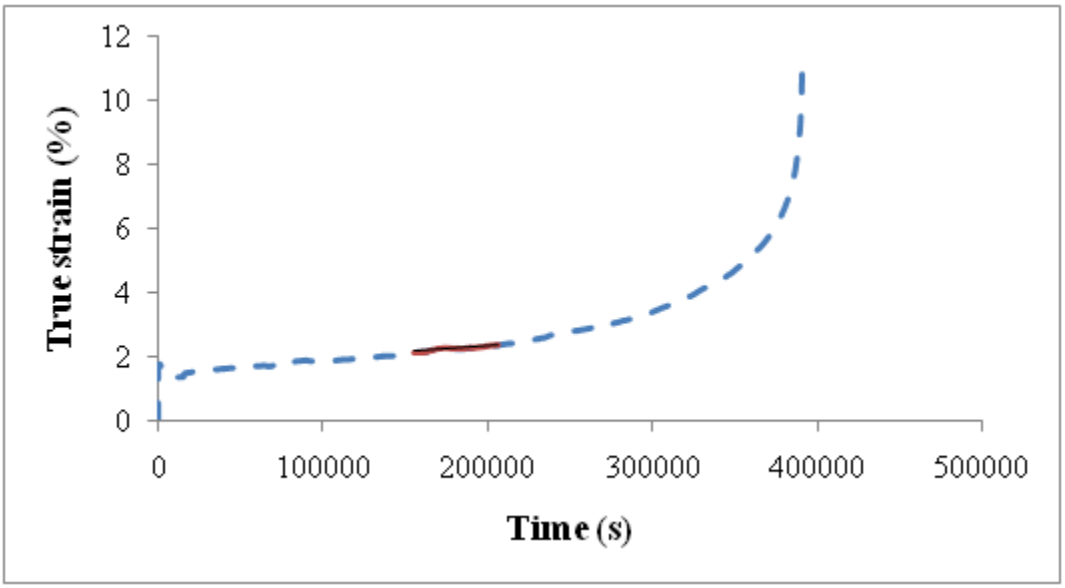

Figure 7.13: Creep curve for SAC-0.5La at 10 Mpa and 120°C

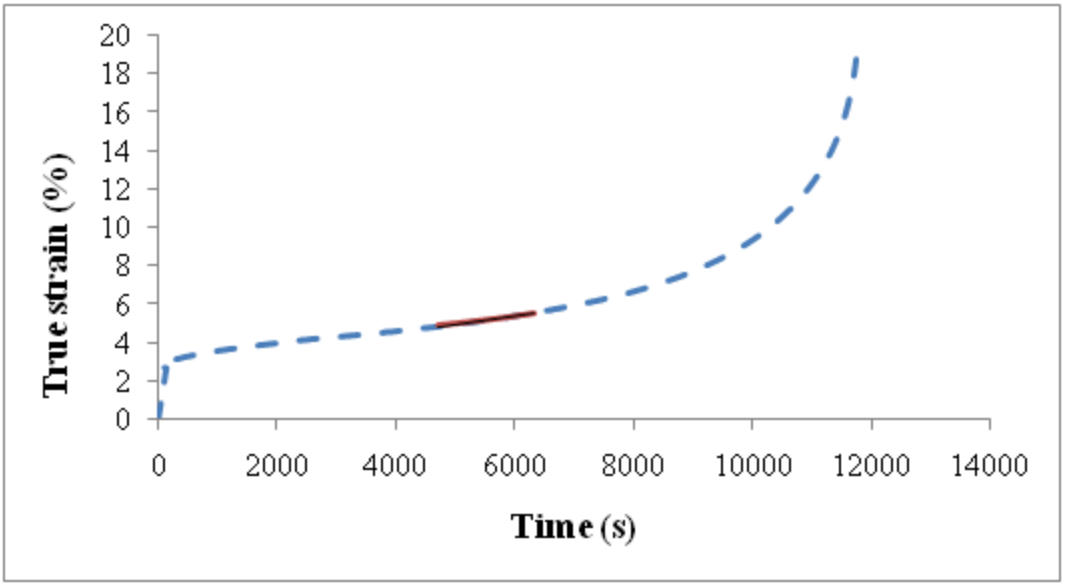

Figure 7.14: Creep curve for SAC-0.5La at 16 Mpa and 120°C

Many of the alloys were subjected till rupture whereas some of them were stopped when they reached the tertiary zones as the secondary zone strain rate (creep strain) was already measured.

7.4 Creep Mechanisms

All creep strain–time curves include three zones which are primary, steady-state (secondary) and tertiary. Out of these three, secondary creep being the most important. In many creep analysis techniques, the secondary creep is given most of the attention as it covers the largest portion of entire rupture life of solders [Shi et al. 2002].

To date, many creep models have been presented and used in different studies for describing the secondary creep of lead-free solders. Arrhenius power law model is one of the creep models

widely used. Moreover, Wen et al., Shi et al. [Shi et al. 2002] and Xiao et al. [Xiao 2004] have developed their models for predicting the creep behavior. During creep analysis, different stress regimes are applied, low stress regime (LSR) and high stress regime (HSR) and the models described earlier mostly break down in the HSR. As a result, the hyperbolic creep model [Yang et al. 2004] is used to avoid the power-law breakdown. But, these hyperbolic models are also mostly empirical equations and fail to describe the physical mechanism during creep. During creep testing, the microstructure does not remain the same due to high temperature thermal coarsening and the Arrhenius power law model and hyperbolic models do not consider these microstructural changes during creep deformation. These microstructural changes such as dislocation structures and crystallographic texture in materials strongly affect the inelastic deformation of the samples [Mayama et al. 2007] . Therefore, it is essential that a creep deformation behavior model must consider both the macroscopic deformation behaviou and also the presence of microstructural features.

As described in the earlier chapters, SAC solders consist of soft Sn matrix and hard and brittle Ag-Sn and Cu-Sn IMCs. These IMCs act as second phase and create obstacles against the motion of dislocations during creep. This generates back stress in the entire matrix and therefore should not be neglected when describing the creep behavior of solder alloys. Therefore, to describe the creep behavior in a better way, it is essential to incorporate this back stress into the existing creep models. Many investigators have already incorporated the back stress into the original creep models [Rist et al. 2006 , C. M. L. Wu & Huang 2002 and R. McCabe & Fine 2002]. A common method they used for determining the back stress from creep data was plotting the 1/n power of $\dot{\varepsilon}$ versus the stress for a given temperature on a linear plot and

extrapolating to zero strain rate [Han Y. D. et al. 2009]. However, the values of back stress obtained from this method were doubtful and did not take the microstructure into account [Han Y. D. et al. 2009]. Therefore, it is essential to calculate the back stress based on the physical mechanism.

A wide range of creep tests are performed at different stresses and temperatures on specially designed tensile dog-bone specimens prepared according to the experimental conditions explained in Chapter 3.

7.5 Dorn Creep Model

Creep data are generally analyzed by relating the steady-state strain rate to the stress through a power-law relation. The stress exponent "n" and the activation energy (Q) for creep can be calculated from the Dorn equation as given in equation (7.3) [McCabe 2000],

$$\dot{\varepsilon} = \frac{AGb}{RT}\left(\frac{\sigma}{G}\right)^{n} \exp\left(-\frac{Q}{RT}\right) \quad \text{(7.3)}$$

where Q represents the activation energy for creep, n is the power-law stress exponent, G is the temperature-dependent shear modulus, b is the Burgers vector, A is a material-dependent constant, R is the universal gas constant and T is the temperature.The values of n and Q are representative of the dominant creep mechanism. The simplified form of the Dorn creep model, used in many studies, is given as follows,

$$\dot{\varepsilon} = A\,\sigma^{n} \exp\left(\frac{-Q}{RT}\right) \quad \text{(7.4)}$$

where “A” is the pre-exponential factor which depends on the material microstructure, the temperature and the stress. We consider A as a constant here at first glance since the temperature and stress are fixed. Q is also a constant value because it is dependent on alloy composition, microstructure, applied stress, temperature and the shape of sample. The activation energies are also evaluated in this work at different temperatures.

7.5.1 Extraction of Parameters

The Dorn model takes into account three important parameters to describe the creep mechanism, “n” the stress exponent relative to the applied stress; “A” relative to the material microstructure and “Q”, the activation energy. They are the main concerns for in-depth modeling of lead-free solder creep behavior. We can use a natural logarithm to see the linear evolution of the creep and extract parameter’s values from the test results as provided in equation (7.5),

$$\mathrm{Ln}(\dot{\varepsilon}) = \mathrm{n}\,\mathrm{Ln}(\sigma) + \mathrm{Ln}(\mathrm{A}) - \frac{\mathrm{Q}}{\mathrm{RT}} \quad \ldots\ldots(7.5)$$

The stress exponent n can be derived from this function and the curves provided in Figures 7.15-7.17.

$$\mathrm{n} = \frac{\partial \mathrm{Ln}(\dot{\varepsilon})}{\partial \mathrm{Ln}(\sigma)}$$

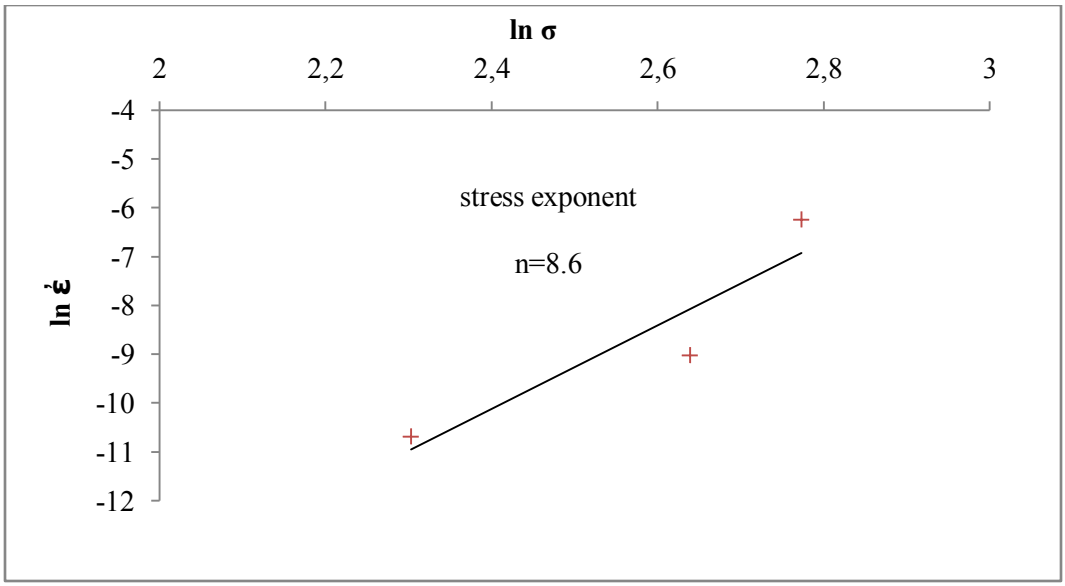

Figure 7.15: SAC stress exponent at 120°C

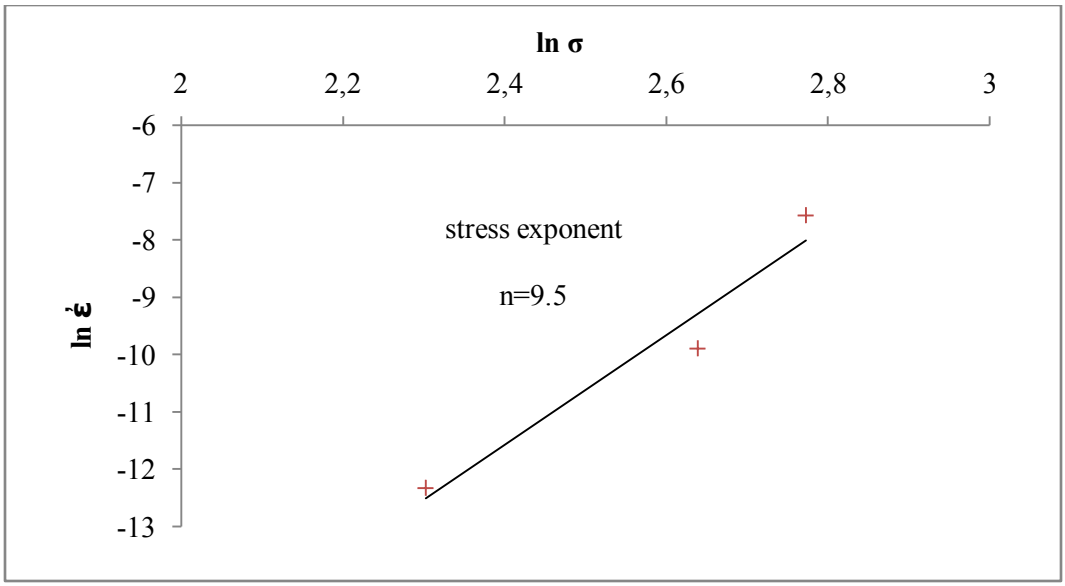

Figure 7.16: SAC-0.05La stress exponent at 120°C

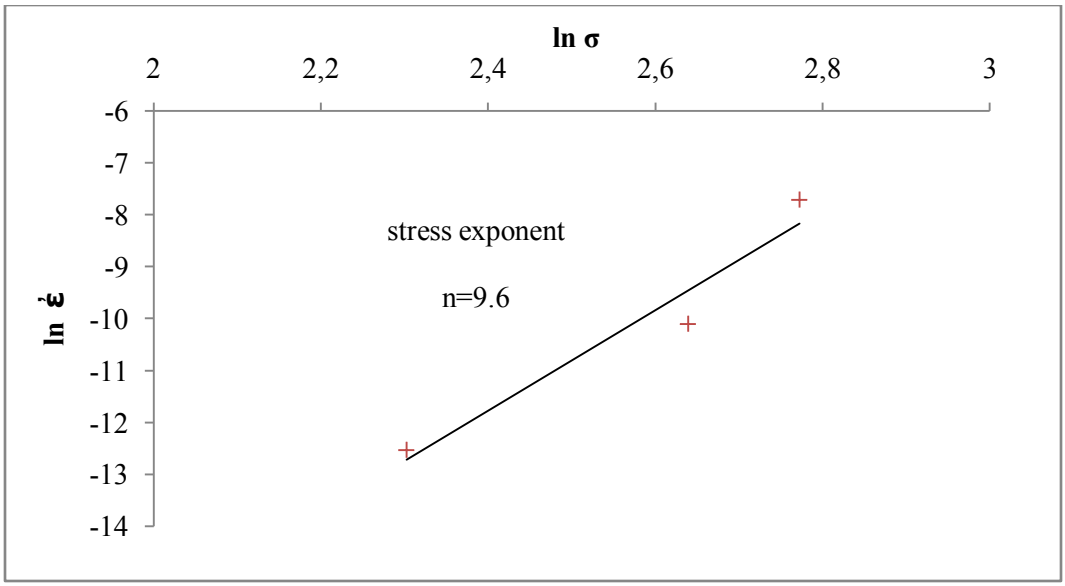

Figure 7.17: SAC-0.5La stress exponent at 120°C

Activation energy analysis can also be calculated from the experimental results by transforming as follows,

$$\mathrm{Ln}(\dot{\varepsilon}) = -\frac{\mathrm{Q}}{\mathrm{R}} \times \frac{1}{\mathrm{T}} + \mathrm{n}\ \mathrm{Ln}(\sigma) + \mathrm{Ln}(\mathrm{A}) \quad (7.6)$$

Then $\mathrm{Ln}(\dot{\varepsilon})$ is plotted as a function of 1/T in Figures 7.18-7.20 and calculate Q easily from equation (7.7). These measurements were carried out at 14 MPa and at 40°C, 80°C and 120°C.

$$\frac{\mathrm{Q}}{\mathrm{R}} = \left(\frac{\partial \mathrm{Ln}(\dot{\varepsilon})}{\partial 1/\mathrm{T}}\right) \quad (7.7)$$

with R=8.314 J/mol K

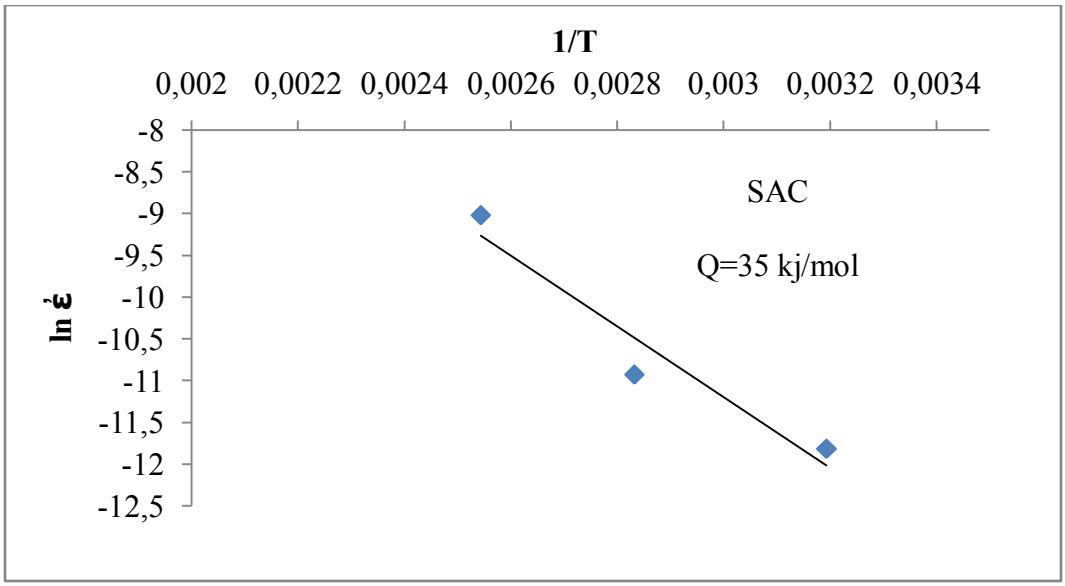

Figure 7.18: Activation energy calculation for SAC

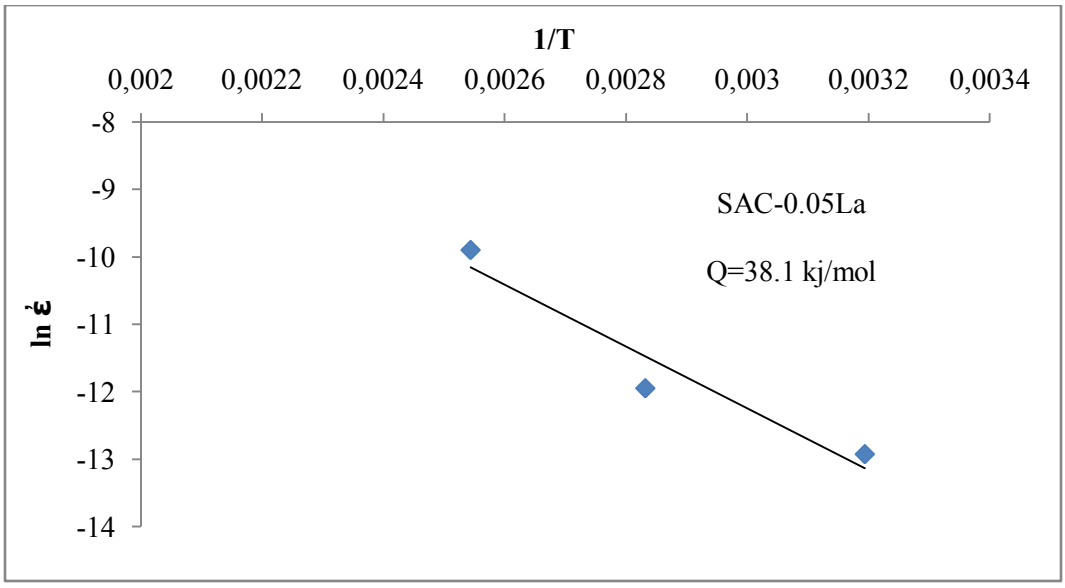

Figure 7.19: Activation energy calculation for SAC-0.05La

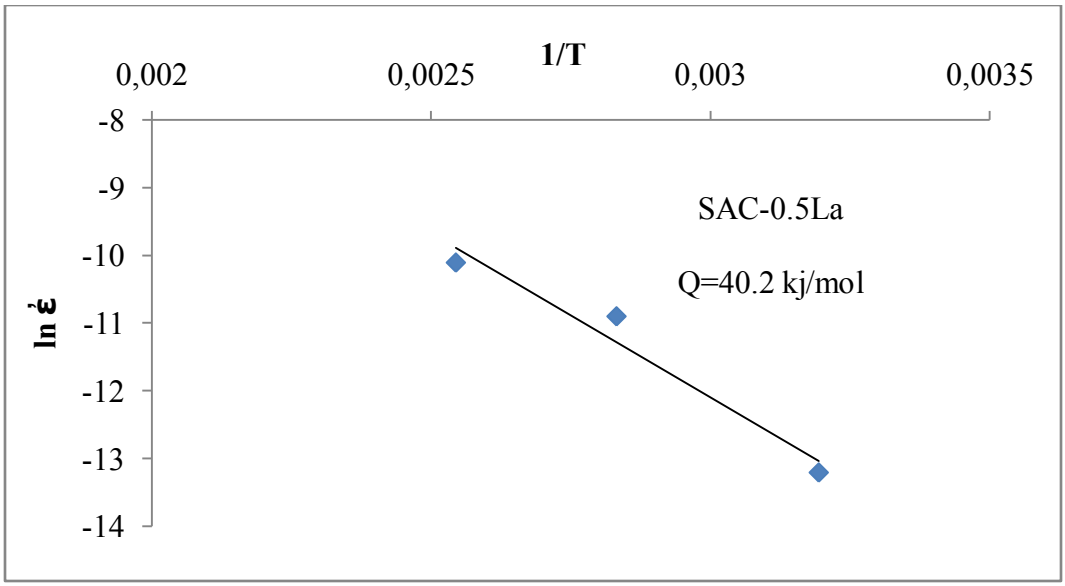

Figure 7.20: Activation energy calculation for SAC-0.5La

Those values for the activation energy are in a small range which is in agreement with other studies [Han Y. D. et al. 2009] and should not be too high for the solder materials as presented in [Zhigang Chen et al. 2004, Shi et al. 2002]. At this point, it was possible to calculate the best approximation (parameter for A with the modification of the equation (7.5) to the following equation (7.8),

$$\mathrm{Ln}(A) = n\,\mathrm{Ln}(\sigma) - \mathrm{Ln}\left(\dot{\varepsilon}\exp\left(-\frac{Q}{RT}\right)\right) \quad (7.8)$$

Assuming a constant Q value for all range of temperatures, the values collected at 120°C for three alloys are given in Table 7.1 with the best fit values for A and n.

Table 7.1: Dorn creep model parameters for SAC and SAC-La doped alloys at 120°C

Extracted parameters	SAC	SAC-0.05La	SAC-0.5La
Q (kj/mol)	35.1	38.1	40.2
ln A	-19,96	-22,87	-22,66
A	2,13E-09	1,16E-10	1,43E-10
n	8.5	9.5	9.7

7.5.2 Back Stress Creep Model

The back stress developed due to the second phase (IMCs) is already explained. In order to consider this back stress, the model presented in equation (7.9) needs to be modified. Different researchers have already attempted it. The activation energy for deformation is constant at high temperature and it decreases linearly starting at a transition temperature (T_t) [Henshall & Miller 1990]. Henshall and Miller [Henshall & Miller 1990] have attempted to simplify and rewrite the term exp (-Q/RT) as D and is given below along with the modified form of the creep model,

$$\dot{\varepsilon} = A\left(\frac{\sigma-\sigma_b}{G}\right)^{n_0} D$$

$$D = \exp\left[\left(-\frac{Q^*}{RT}\right)\left[\ln\left(\frac{T_t}{T}\right)+1\right]\right], T < T_t \quad \text{..... (7.9)}$$

$$D = \exp\left(-\frac{Q^*}{RT}\right), T \geq T_t$$

where σ_b is the back stress, n_0 is the stress exponent after incorporating back stress and Q is the activation energy at high temperature.

The term $(\sigma/G)^n$ describes the dependence of stress on the creep strain rate while the term $\exp(-Q/RT)$ describes the impact of temperature during creep. The shear modulus G can be computed from the following equation [Nai et al. 2008 and Henshall & Miller 1990]:

$$G = 16\,302 - 40.5(T - 273) \text{ where T is the absolute temperature}$$

Analysis for Creep Mechanisms and Back Stress Calculations

The creation of the back stress depends upon the stress regime, HSR or LSR. In SAC alloys, the dislocations can pass easily through the soft Sn matrix but when they arrive to the IMCs between the Sn matrix, they will either be pinned or arrested at these IMCs [Dutta et al. 2004]. In this situation, only a few of the dislocations can go through the particles by climbing over the IMCs. As the applied stress increases, more dislocations will be accumulated at the IMCs and when the applied stress crosses the threshold value, the dislocations between the IMCs and the matrix will get enough energy to detach themselves and thus glide over these IMCs and would finally result in some deformation. Figure 7.21 shows the schematic illustration of the dislocation motion during the creep process.

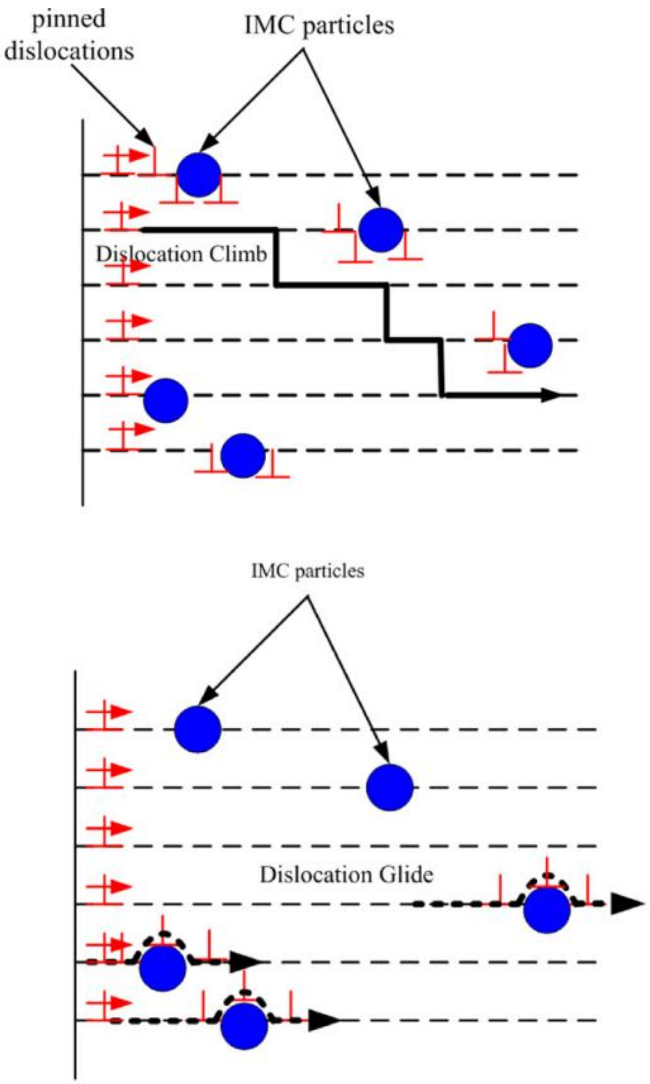

Figure 7.21: Dislocation climb and glide mechanisms [(Han Y. D. et al. 2009)]

Dislocation climb is the creep mechanism during LSR [Han Y. D. et al. 2009]. It was cleary demonstrated by Zhu et el. [Zhu et al. 1998] in in-situ TEM study. In this stress regime, the back stress was insensitive of the IMCs size [Kerr & Chawla 2004], distribution and volume fraction and was mainly dependent on the applied stress. If the samples are considered as well annealed then the back stress (σ_b) with creep strain will oppose the applied stress as given below,

$\sigma_b = a.\sigma$ and therefore $\sigma_e = \sigma - \sigma_b$ ..... (7.10)

where a is a constant and σ_e is the effective stress. Equation (7.9) can be rewritten by combining equation (7.10) and we have,

$$\dot{\varepsilon} = A\left(\frac{(1-a)\sigma}{G}\right)^{n_0} D \quad \text{..... (7.11)}$$

In the high stress regime (HSR), the creep mechanism is dislocation glide [Kerr & Chawla 2004]. As already described that the IMCs are quite hard in comparison to the soft Sn matrix and therefore the dislocations cannot cut or glide these IMCs. In this case, the Orowan Bowing of dislocations is the best mechanism to describe the creep behavior [Steen et al. 1985] as shown in Figure 7.22 [Dieter 1986]. Once the stress is applied, the dislocation actually bows around the IMCs and hence an additional stress is required to overcome the increase in energy arising from the elongation of the dislocation line [Han Y. D. et al. 2009].

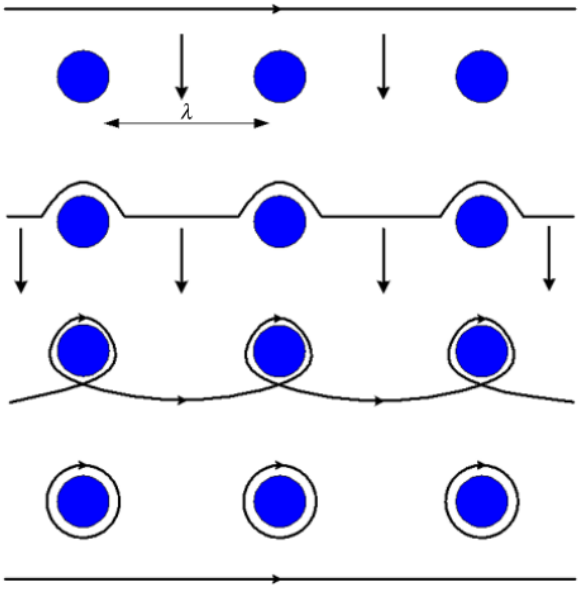

Figure 7.22: Orowan Bowing mechanism [Dieter 1986]

This Orowan stress can be used to calculate the back stress in the HSR. Many researchers like Kerr and Chawla [Kerr & Chawla 2004] have confirmed it with the help of TEM study on Sn-3.5Ag solder joint and Zhu et el. Have done it for NiAl precipitation strengthened ferritic alloy [Zhu et al. 1998]. Both of them reported that the dislocations appeared to be pinned by the second phase (IMCs) that causes the dislocations to bow. Hence, the back stress has a close relationship with the intermetallic particles size and the spacing. In the HSR, the back stress from particles for precipitation hardened materials can be derived by using the approach of the Orowan stress (σ_{or}) [Han Y. D. et al. 2009],

$$\sigma_{or} = \frac{0.84MGb}{\lambda - 2r} \quad \text{..... (7.12)}$$

where M is the Taylor factor, r is the mean radius of IMCs, λ is the interparticles spacing and b is Burger's vector. The interparticles spacing (λ) is determined using the following relation [Kerr & Chawla 2004],

$$\lambda = 2r\left(\frac{\pi}{6f}\right)^{1/2} \quad \text{..... (7.13)}$$

where f is the volume fraction of Ag_3Sn and Cu_6Sn_5 particles. The back stress (σ_b) is expressed as [Kerr & Chawla 2004, Dutta et al. 2004 and Zhu et al. 1998],

$$\sigma_b = \sigma_{or}\sqrt{1 - k_r^{\,2}} \quad \text{..... (7.14)}$$

where k_r is the intensity of the attraction between the IMCs and dislocations, and is usually in the range of 0–1. During exposure to high homologues service temperatures, the IMCs grow which is called thermal coarsening. The Lifshitz–Slyozov–Wagner (LSW) model provides a first-order prediction of the normal homogeneous coarsening [Han Y. D. et al. 2009] and it has been

employed by many investigators [Steen et al. 1985] for the description of the microstructural coarsening during creep. This coarsening mechanism and the quantitative measure have been described in detail in chapter 4 (Microstructure Evolution).

7.5.3 Model Validation

An adaptive and iterative fitting process was used to find out the best parameters values, in agreement with different works already performed. The following results give the model best fit to the experimental values. Based on the parameters already extracted and the experimental points, the model is plotted in Figures 7.23-7.25 for SAC, SAC-0.05La and SAC-0.5La respectively.

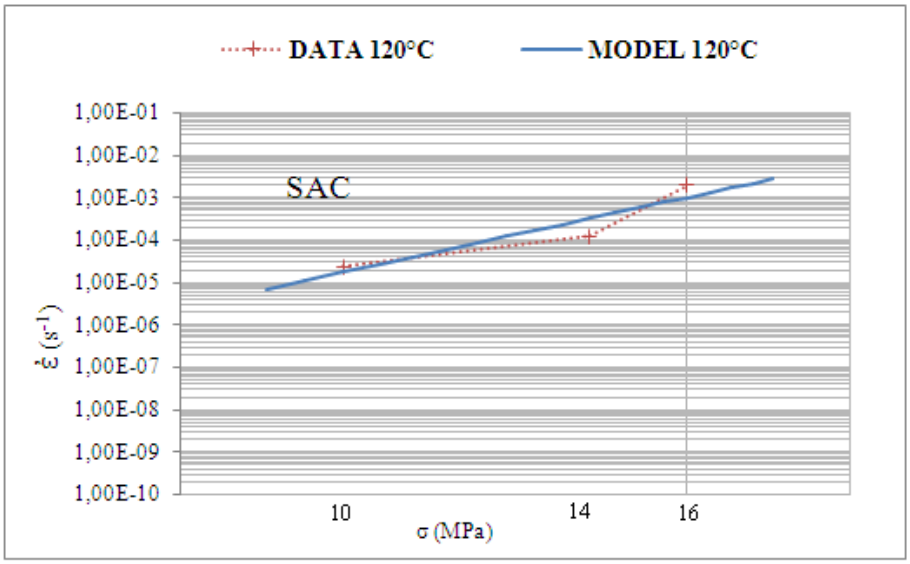

Figure 7.23: Dorn creep model validation with experimental results for SAC at 120°C

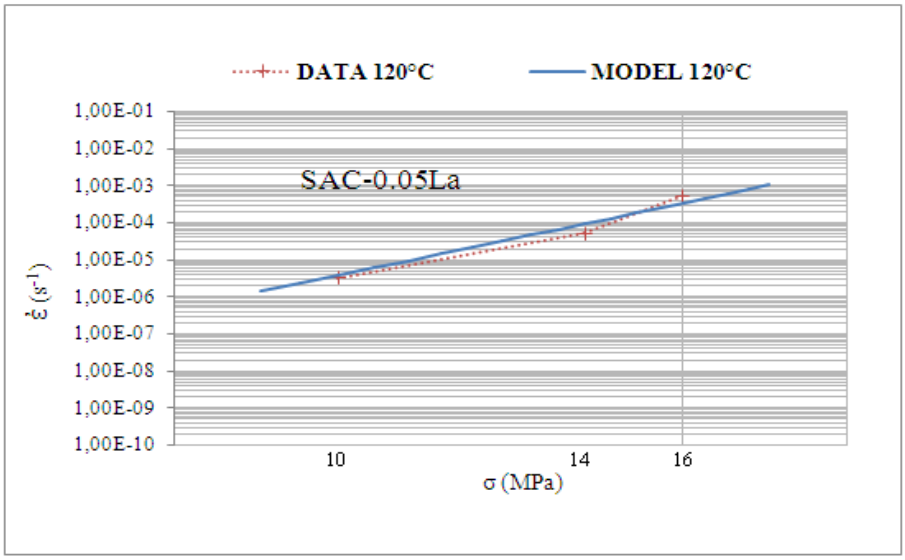

Figure 7.24: Dorn creep model validation with experimental results for SAC-0.05La at 120°C

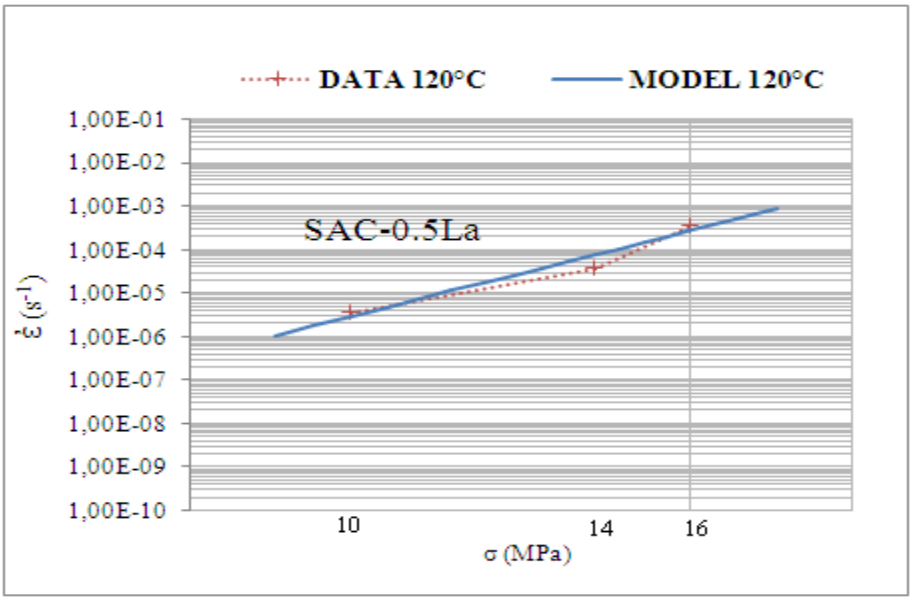

Figure 7.25: Dorn creep model validation with experimental results for SAC-0.5Laat 120°C

7.6 Summary

An extensive experimental work was performed to explore the creep resistance of the SAC and SAC-La doped alloys in different environmental conditions. Stress exponents and

activation energy measurements were done for all compositions. Strain rate measurements were provided for a comparative study.

The results indicate that, at different stress levels, the activation energy increases with RE addition. There is a strong indication that the improvement of creep behavior of SAC with different RE doping is due to an increase in activation energy for creep.

It is well known that RE elements are active and they like to agglomerate at the grain boundaries and at the interfaces of different phases. The energy of surface or grain boundary will decrease after the addition of RE. Thus, the RE elements would play an important role on preventing the movement of dislocations and the nucleation of microcracks. Consequently the fine dispersive particles and the active properties of RE improves the creep behavior of the SnAg [C. Wu, Yu, et al. 2004] and SAC alloys.

Creep experiments are time consuming and high accuracy is required to capture the true behavior of any alloy with extreme care to temperature and load fluctuations. Thus all the experimental work in this study was performed with acceptable variations in these parameters. The temperature was controlled by using a digital thermocouple attached to the sample during experiments whereas the load cell of only 5 KN was used for high accuracy.

In order to avoid the experimental work involved in the creep behavior, robust models are needed. These models should be validated by experiments and developped to predict the results in an acceptable range. The models presented in this chapter are predicting the creep strain in a close relation to experimental work and are also considering the back stress effects produced in almost all lead-free solders due to finely dispersed IMCs within a soft Sn matrix.

It was concluded, after models validation, that an overall improvement in the creep behavior due to minute La doping can play a major role in controlling the solder joints performance and hence enhance the overall solders reliability. In that sense, the life of solder in electronic packaging under high stress and high temperature conditions is really improved.

CHAPTER 8

NANOINDENTATION

8.1 Introduction to Nanoindentation

Nanoindentation is a recently developed technique to explore the near surface mechanical properties of different materials, including special multilayer materials on the substrates, at very small length scales [Oliver & G. M. Pharr 1992, Saha and Nix 2002,Nix D. William 1997]. Nanoindentation, also known as depth-sensing indentation, instrumented indentation or ultra-low-load indentation, uses its special probe with highly controlled movements in all 3 axes. This technique has been highly developed in the last 2 decades with high resolution sensors and actuators to continuously control the load applied by an indenter on the work-part and simultaneously monitor the resulting displacement into the specimen. The famous load-depth curve is plotted at the end of indentation test that gives very useful information about the entire mechanical behavior of material.

Generally, the indentation depth (or displacement) into the specimen varies from few microns to nanometer range that is why the technique is called nanoindentation. The most important advantage of this technique is that quite accurate and wealthy information can be very easily extracted from the load-depth curves without any complicated post treatment of the data thus avoiding the need to image the impression depth after testing [Oliver & G. M. Pharr 1992].

As the indentation depth produced is very small and extremely localized (in case of fine loading), thus measurements can be made without removing the film from its substrate [Saha and Nix 2002] as in the case of small coatings over the hard disks. Hence, it simplifies the preparation of specimens and also provides an opportunity to extract the results which might not be possible with other conventional methods.

This technique is widely used for determining the Young's modulus and hardness of different materials with many models used for these values including Oliver and Pharr model [Oliver and Pharr 2004]. Other than that, it can also be applied to extract other mechanical properties like yield stress and strain hardening of metals [Chollacoop et al. 2003, Dao et al. 2001]; parameters of damping and internal friction in polymers, such as the storage and loss modulus [Asif et al. 2001, Park et al. 2004]; and the activation energy and stress exponent for creep [Syed Asif & Pethica 1997, Feng & Ngan 2002, Elmustafa & Stone 2002]. In some cases, nanoindentation has even been used to estimate the fracture toughness of brittle materials [Oliver and Pharr 2004].

8.2 Nanoindentation Setup

Figure 8.1 shows the nanoindentation working mechanism with nanoindenter, sample and the XY-table whereas Figure 8.2 represents the CSM nanoindentation setup used during this study. The indenter is controlled with the actuator (coil/magnet). The displacement sensor keeps control of the indentation depth during the process. The reference ring or fork is used to keep control of the overall flatness of the samples during testing. Any unevenness during nanoindentation can lead false results with strange load-displacement curves.

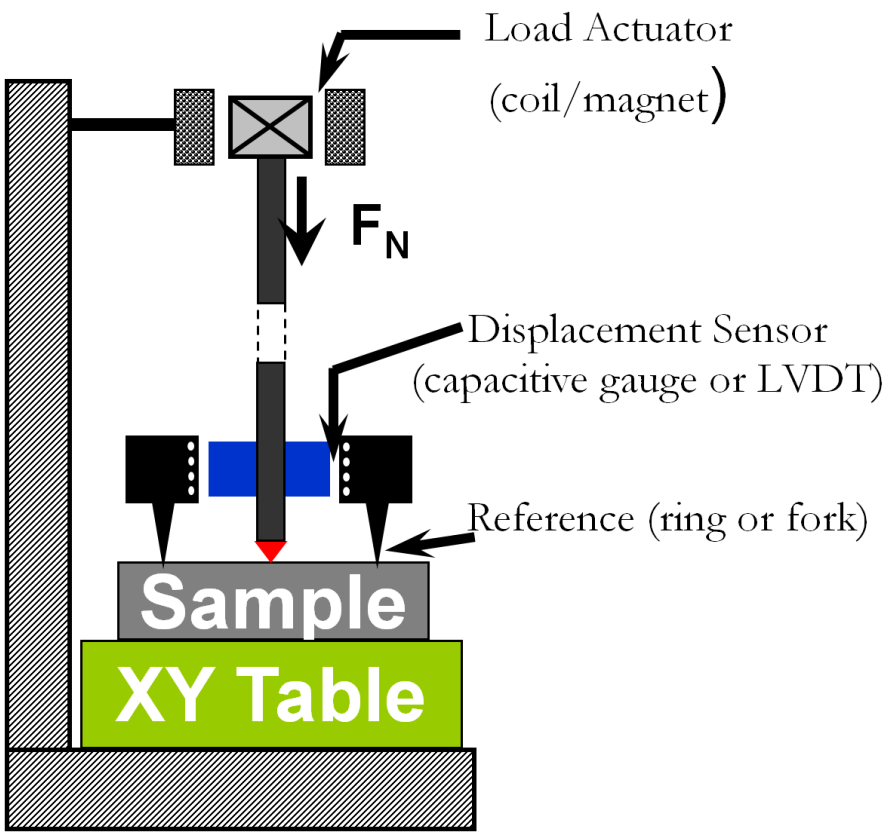

Figure 8.1: Nanoindentation working mechanism

Figure 8.3 describes the surface profiles produced during nanoindentation. At initial surface point, the first contact between the indenter and sample takes place with a theoretical height 'h'. With time, sinking effect causes to press the real surface and therefore an actual contact is developed at height 'hc'. This is called the real contact. An ideal load-unload curve is provided produced at the end of a good nanoindentation test. The same curve is used to extract most of the results and is explained in the remaining chapter.

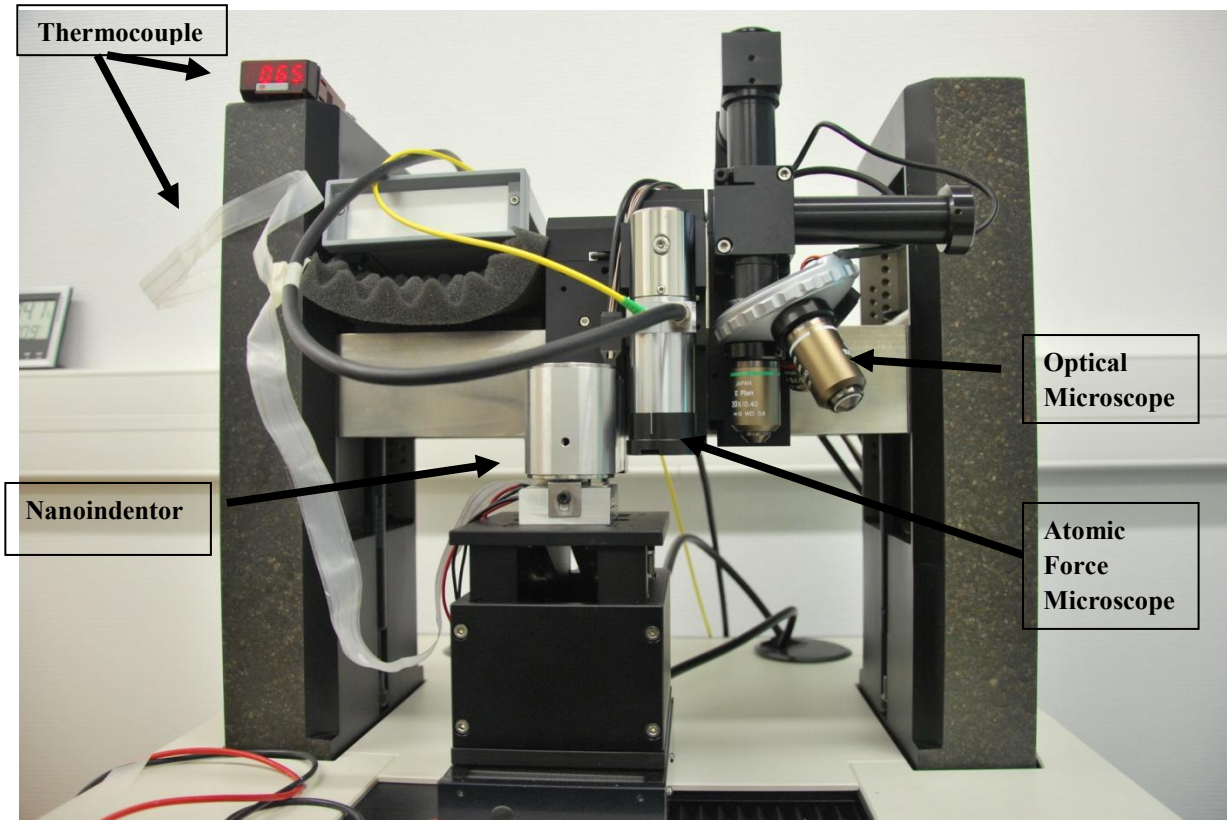

Figure 8.2: CSM nanoindentation setup

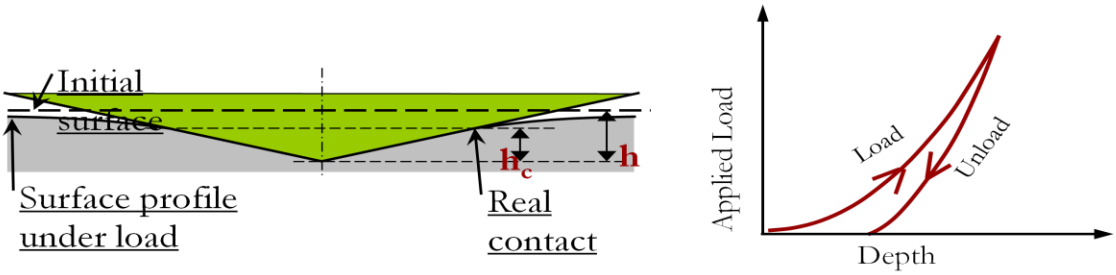

Figure 8.3: Nanoindentation surface profiles and curves

8.3 Experimental Conditions

The main focus of this chapter is to measure the individual phase properties like Young's modulus and hardness of SAC and SAC-La doped alloys for eutectic Sn and β-Sn phases with

the technique of nanoindentation as described briefly above. Many researchers have already attempted to determine the mechanical properties of Sn-Ag and SAC alloys [Deng et al. 2004 and Rhee et al. 2002]. The indenter causes piling up inside the soft Sn-matrix and eutectic phase. Many researchers have neglected this effect which makes the results unreliable. In this study, the piling up effect is considered for both phases and evaluated using semi-ellipse method and incorporated into results. Both results, before modification and after modification are provided for comparison.

Specimens of each composition were mechanical polished with silicon discs and 1 micron diamond paste. Chemical etching was performed for a few seconds using a 5% hydrochloric acid and 95% ethanol solution in order to distinguish before different phases.SEM and OM images are always collected before the nanoindentation. An Oxford EDS system, placed in the SEM, enables us to realize elemental mappings for every specimen.

Nanoindentation tests were carried out by using a nanoindenter XP equipped with a Berkovich-84 diamond indenter. The resolutions of the loading and displacement systems are 50 nano-newton and 0.01 nano-meter, respectively. The standard deviation errors of the measured hardness and reduced Young's modulus are well less than 1%. The hardness value and reduced modulus values were also extracted from the unloading part of load–depth curves by using Oliver and Pharr method [Oliver & G. M. Pharr 1992].

The acquisition frequency was 10 Hz and poison ratio, assumed, was 0.33, as consistent with other researchers. The load applied were 100 μN to 5000 μN with steps of 100 μN. The loading and unloading rates (mN/min) were two times that of load applied. An approach speed of

3000 μN/min was used. As the lead free solders exhibit severe creep deformation, even at room temperature [Gao & Takemoto 2006], the dwell time at the peak load is defined as 60 seconds in order to completely relieve the creep deformation and also avoid the famous "bulge" or "nose" effect during unloading [Y. T. Cheng & C. M. Cheng 2004].

The selection of position to indent was controlled under a high-resolution Optical Microscope (OM), by which various phases can be distinguished. OM was also used after indentation to confirm the indenter location and avoid the grain boundary effects. For each specimen, 9 points (3X3 arrays) were tested. Both phases, eutectic and β-Sn, were selectively indented by the visual matrix method. Same tested zones were studied after the indentation testing with Atomic Force Microscope (AFM).

Afterwards, Scanning Electron Microscope (SEM) and Energy Dispersive Spectroscopy (EDS) were applied to confirm the chemical composition of each phase. Further, because the Young's modules and hardness for each phase is different, curves for eutectic phase and β-Sn phase can be distinguished from the test array.

8.4 Nanoindentation Working

Figure 8.4 shows a typical load-displacement curve. At the beginning of the unloading portion of the curve the famous bulging out effect can be seen. As mentioned before, the SAC solder alloys are soft and vulnerable to creep which causes this bulge effect. Different loadings were used in order to relieve this effect but they were present as shown in Figure 8.4. This is the case when no holding time is used at the peak load. Since most of the nanoindentation calculations are based on the slope of the un-loading portion of the curve, it is important to have

no bulge effects at the beginning of the unloading curve; otherwise, the results could be wrong. Moreover, in order to investigate the creep effects on the mechanical properties, different holding times were used. In comparison to Sn matrix, the IMCs are expected to be resistant to the creep effect. In some cases, there is some bulge effect, but it can be concluded that this is because of the Sn matrix in which these particles are finally embedded.

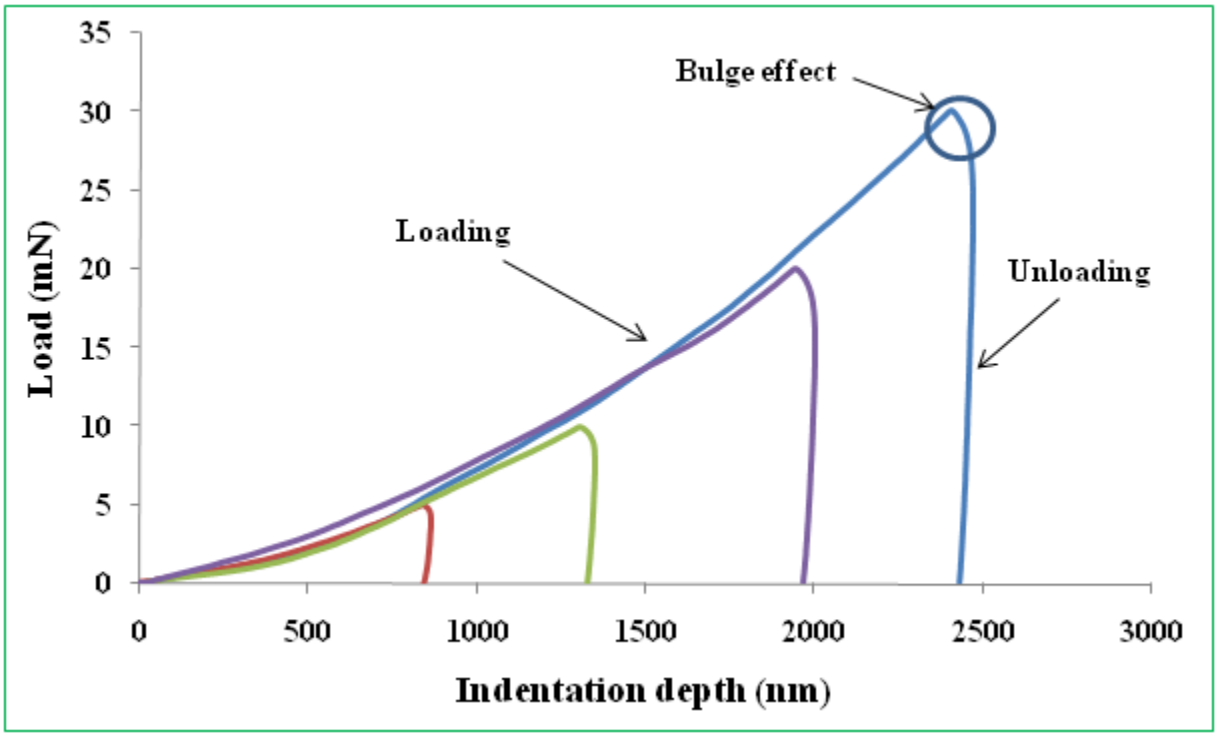

Figure 8.4: Load-displacement curves with no holding time

Indentation testing was carried out on both eutectic phase and β-Sn phase for all compositions. Figure 8.5 shows the nanoindentation with holding time and the bulge effect is negligible in this case. Much information can be extracted from these curves.

It can be seen (Fig. 8.5) that there is a significant plastic deformation in both phases. The elastic deformation is quite small and therefore the slope of the un-loading curve is almost

vertical. The indentation depth for eutectic-Sn phase is much smaller than that of the β-Sn phase. It was experienced for both SAC and SAC-La compositions. This effect was also confirmed when the hardness of both phases were compared, eutectic phase being harder than β -Sn phase. This could be the effect of diffusion of Ag and Cu in Sn in the eutectic zone.

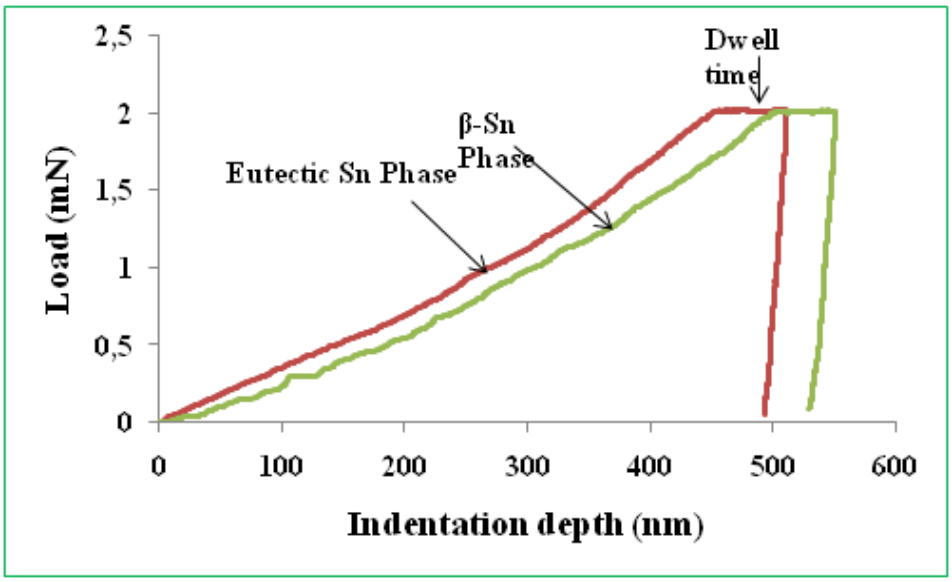

Figure 8.5: Load-displacement curves with holding time

8.5 OLIVER AND PHARR MODEL

The values of the reduced modulus E_r were acquired during the test through Oliver and Pharr method [Oliver & G. M. Pharr 1992]. The elastic modulus of the materials can be calculated using,

$$E_r = \frac{\sqrt{\pi}}{2\beta} \cdot \frac{S}{\sqrt{A_{op}}} \quad \text{.....(8.1)}$$

where E_r represents the reduced modulus, S is the contact stiffness, β is a constant related to the geometry of the indenter, and A_{op} is the oliver-pharr projected area by indentation. At the same time, the reduced Young's modulus could be formulated as

$$\frac{1}{E_r} = \frac{1-\nu^2}{E} + \frac{1-\nu_i^2}{E_i} \quad \text{.....(8.2)}$$

where E and υ are the Young's modulus and Poisson's ratio of the tested material and E_i, υ_i are the Young's modulus and Poisson's ratio for the diamond tip. The values of E_i and υ_i used in this study were 1140 GPa and 0.07 respectively as used in most of the studies[Gao et al. 2009] and the Poisson's ratio of each phase, i.e., β-Sn and eutectic Sn phase was approximated to be 0.33 which was consistent with the previous studies [Deng et al. 2004]. Hardness (H) of the material, on the other hand, can be determined by,

$$H = \frac{F_{\max}}{Aop} \quad \text{.....(8.3)}$$

where F_{max} is the peak indentation load and A_{op} is the projected contact area which is calculated,

$$A_{op} = 24.5h_c^2 + \sum_{i=1}^{8} C_i h_c^{\frac{1}{2i}} \quad \text{.....(8.4)}$$

where C is the constant depending on the indenter type and shape as given in Table 8.1 and h_c is the contact depth which is smaller than the theoretical depth due to the sinking effect of the specimen under indenter.

Table 8.1: Constant "C" values for berkovich-BK-06 tip

C_0	C_1	C_2	C_3	C_4	C_5
24.5	10.31	-16.03	24.45	-7.32	5.12

Both Young's modulus and hardness are determined and plotted for eutectic phase and β-Sn phase in Figure 8.6 (a) and 8.6 (b) respectively (before pileup effects). These values are summarized in Table 8.2. Almost no change was investigated with varying loadings (mN) and loading rates (mN/min). This is consistent with other studies [Gao & Takemoto 2006]. This study was performed for both SAC and SAC-0.25La compositions.

The AFM images with 3X3 indentation array are shown in Figure 8.7. For pure Sn, it is given in Figure 8.8. The images collected were analyzed in the Image-plus to characterize the indentation profiles. Figure 8.9 shows the AFM image of nanoindentation performed on eutectic zone. Different size of indentation represents different loadings applied during testing.

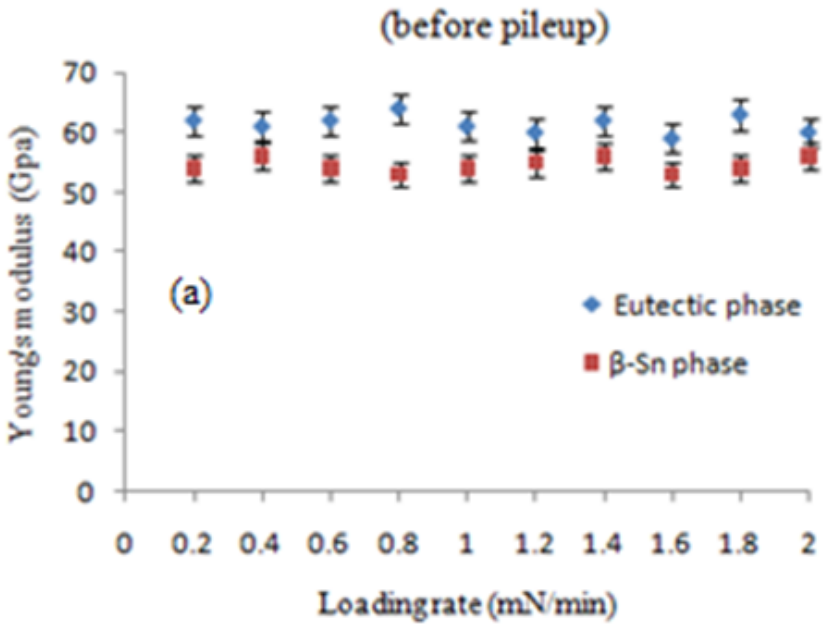

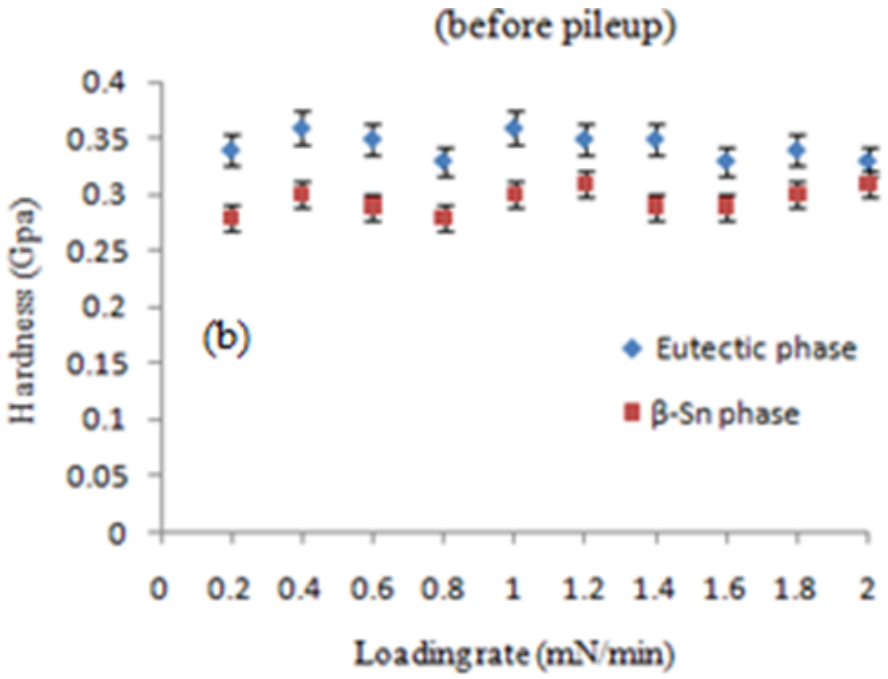

Figure 8.6: Young's modulus (a) and hardness (b) for eutectic and β-Sn phases before pileup effects

Table 8.2: Young's modulus and hardness (before pileup)

Loading rate (mN/min)	E (GPa)		H (GPa)	
	Eutectic phase	β-Sn phase	Eutectic phase	β-Sn phase
0.2	62	54	0.34	0.28
0.4	61	56	0.36	0.30
0.6	62	54	0.35	0.29
0.8	64	53	0.33	0.28
1	61	54	0.36	0.30
1.2	60	55	0.35	0.31
1.4	62	56	0.35	0.29
1.6	59	53	0.33	0.29
1.8	63	54	0.34	0.30
2	60	56	0.33	0.31

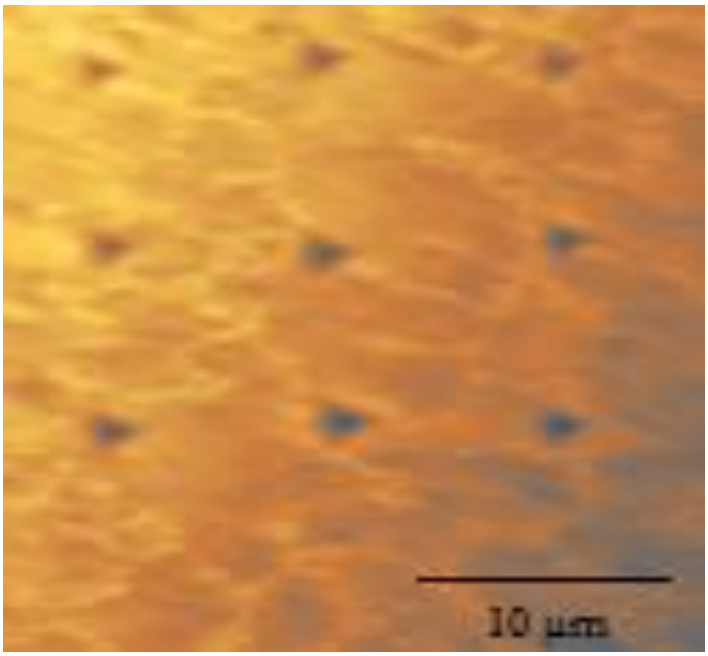

Figure 8.7: AFM micrograph of a 3x3 indentation array

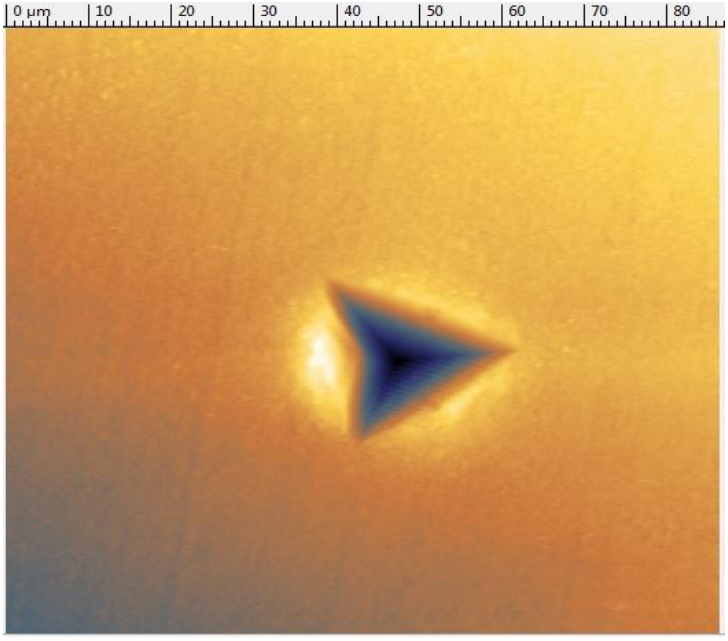

Figure 8.8: AFM micrograph for pure Sn

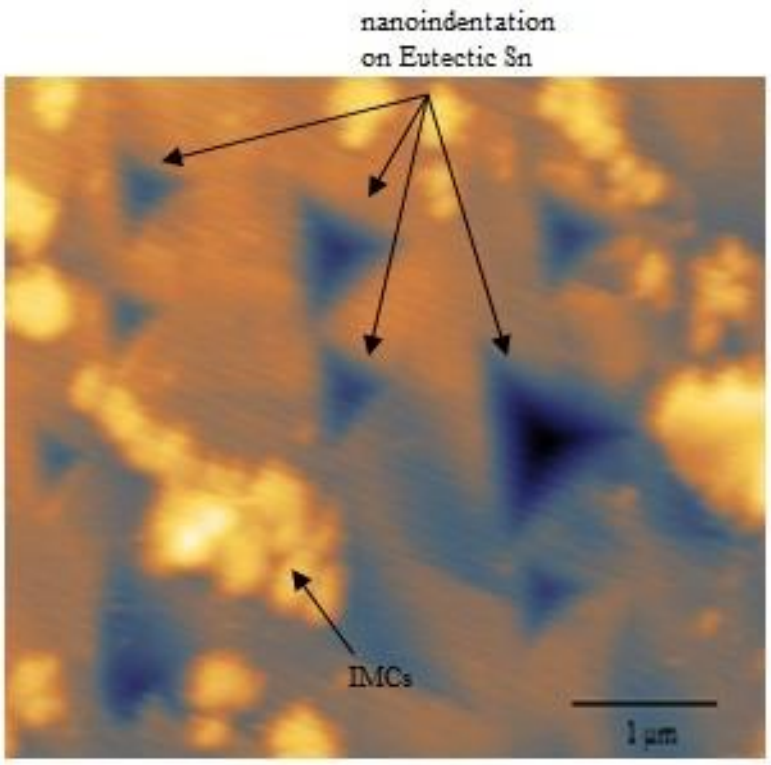

Figure 8.9: AFM micrograph of indenter testing at eutectic phase

Creep Characterization at Room Temperature

At peak loading, creep phenomenon is quite significant. This is due to the low creep resistance of SAC alloys. Lanthanum is added to refine the microstructure and improve the creep life. As shown earlier, indentation depth continues at the peak load. In order to extract the "rate" behavior and explore the creep phenomenon using nanoindentation, a dwell time was applied at the peak loads.

Figure 8.10 shows this indentation for both β-Sn and eutectic Sn at the peak load. This depth being much higher for β-Sn as compared to eutectic-Sn for the same loading that varies from 600 μN to 1000 μN. This effect was found both for SAC and SAC-0.25La compositions.

The differences between the eutectic and β-Sn may also be observed from AFM images of residual indents. As expected from the nanoindentation, residual indents in the β-Sn were much larger than in eutectic-Sn.

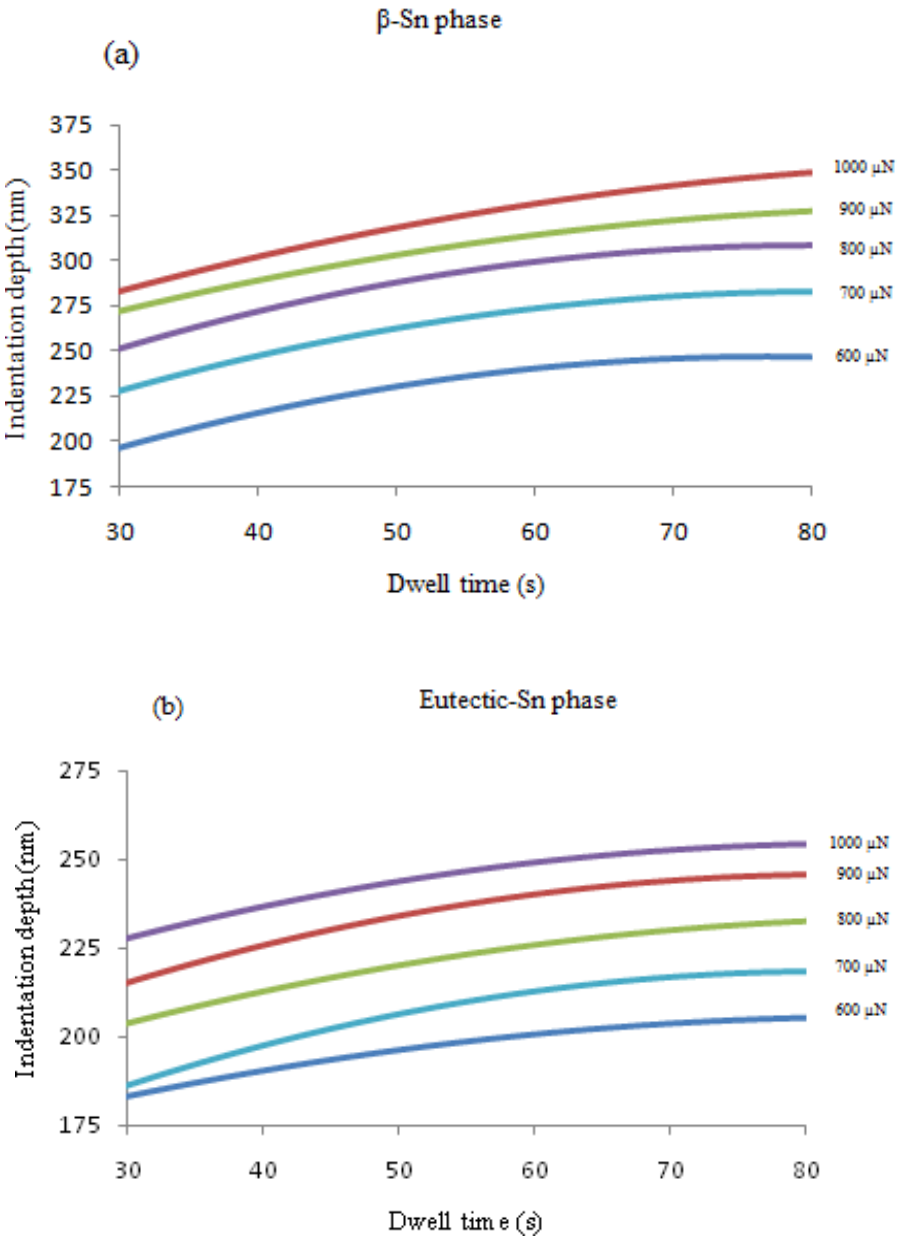

Figure 8.10: Displacement curves at holding time (a) β-Sn and (b) Eutectic Sn phase

8.5.1 Special Pileup Effects

For materials that are quite soft and plastic, as observed for SAC solder, pile-up behavior is expected [Bolshakov & G. Pharr 1998] and must be taken into account when calculating mechanical properties from the nanoindentation data. All of the residual indents observed for the eutectic-Sn exhibited relatively smooth profile with small detected pile-up or sink-in of material in comparison to β-Sn. These pileups are given in Figure 8.11 with AFM images and treated with Image-plus software.

The projected area (given below) is calculated in different ways for the indenter which consists of two portions. One is the indentation area given directly by the Oliver-Pharr model. The other being the pileup area which needs to be incorporated into the projected area which is calculated by the indenter, otherwise,the results would be unreliable because of underestimating the total projected area. The total area is noted as A which is the sum of pile-up area and projected area, as given below,

$$A=A_{op}+A_{pu}$$

Since both Hardness (H) and Young's modulus (E) are inversely related to the total area, it could be concluded that incorporating the pile-up area would reduce both H and E.

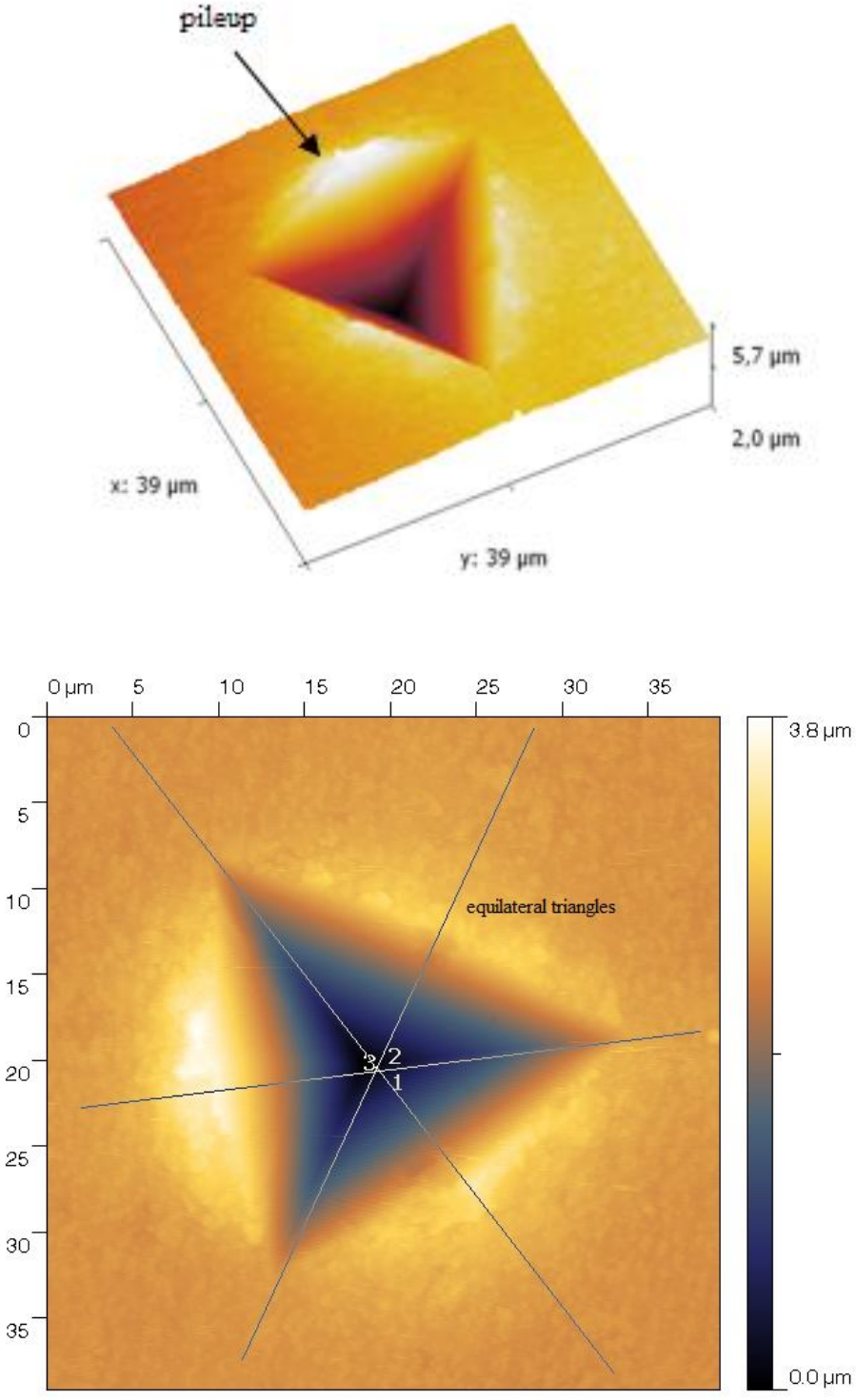

Figure 8.11: AFM images showing the pile-up phenomenon

8.5.2 PILE-UP AREA CALCULATIONS

Assuming that the projected contact area, A_c, determined at contact depth, hc, traces an equilateral triangle of side b, then for a perfect Berkovich tip,

$$A_c = 0.577b^2 = 24.56h_c^2 \quad (8.5)$$

The area of each semi-elliptical pile-up projected contact area is $\frac{\pi b}{4} a_i$ and the total pile-up contact area is, therefore,

$$A_{pu} = \frac{\pi b}{4} \sum a_i \quad (8.6)$$

where the summation is over three semi-elliptical projected pile-up lobes and a_i being the measurement of piling up width on three surface (sides) of the equilateral triangles [Sun et al. 2008]. The AFM images are analyzed in Image-plus to trace the surface profiles and are given in Figure 8.12. Knowing then the contact area from the Oliver–Pharr method, the total or true contact area for an indent can be obtained as,

$$A = 24.5h_c^2 + \sum_{i=1}^{8} C_i h_c^{\frac{1}{2i}} + \frac{\pi b}{4} \sum a_i \quad (8.7)$$

Thus the new calculations are done as following,

$$E_r = \frac{\sqrt{\pi}}{2\beta} \cdot \frac{S}{\sqrt{A_{op} + A_{pu}}} \quad (8.8)$$

$$H = \frac{F_{\max}}{A_{op} + A_{pu}} \quad (8.9)$$

The Young's modulus and hardness measured for eutectic and β-Sn phases are shown in Figure 8.13 (a) and 8.13 (b) respectively incorporating the pileup effects. These results are summarized in Table 8.3. These results are in a better agreement with the previous studies [Deng et al. 2004]. This collection of data allows for comparison of mechanical properties of alloys, where all samples were prepared and tested in the same manner.

The semi ellipse model of equilateral triangles is applied to both eutectic and β-Sn phases. This is quite obvious that increasing the loading and loading rate increases the indentation depth. Extreme care is required for results obtained at less than 100nm indentation depth due to uneven polishing or etching of the specimen.

Strain rate sensitivity constants were calculated for both phases with small difference being dedicated to the refinement of microstructure due to lanthanum doping. Both Young's modulus and hardness were also determined along the indentation depth with experiencing only small variations which is also consistent with [Deng et al. 2004]. The average values for the Young's modulus for eutectic phase, along the indentation depth, are determined to be 51 GPa whereas for β-Sn it is 48 GPa. Similarly, the average values for hardness, along the depth, for eutectic phase are determined to be 0.26 GPa whereas for β-Sn it is 0.22 GPa. The average values are taken from 100 nm to 500 nm depth. These values are taken after considering the pileup effects.

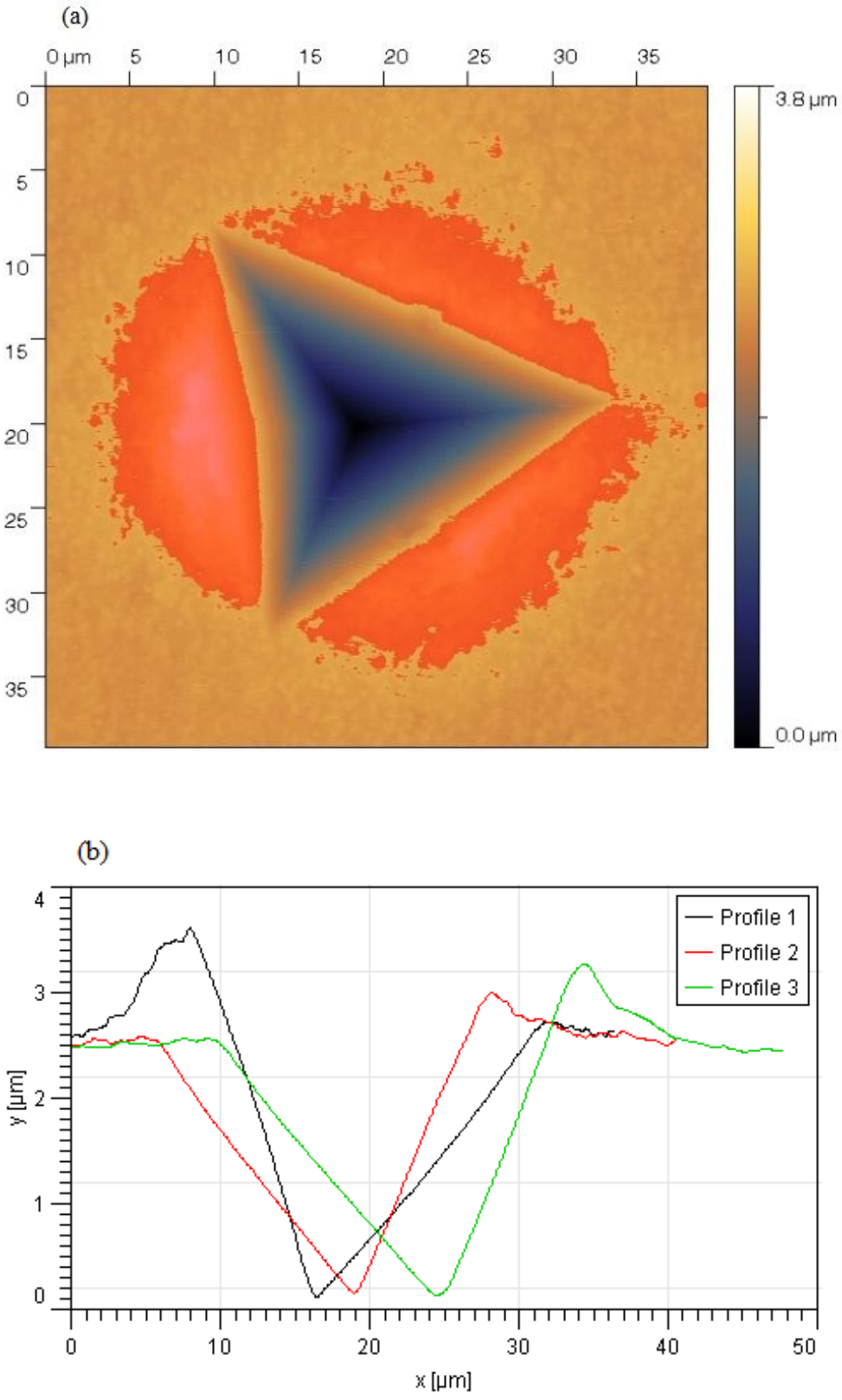

Figure 8.12: (a) Equilateral triangles and (b) Pile-up profiles

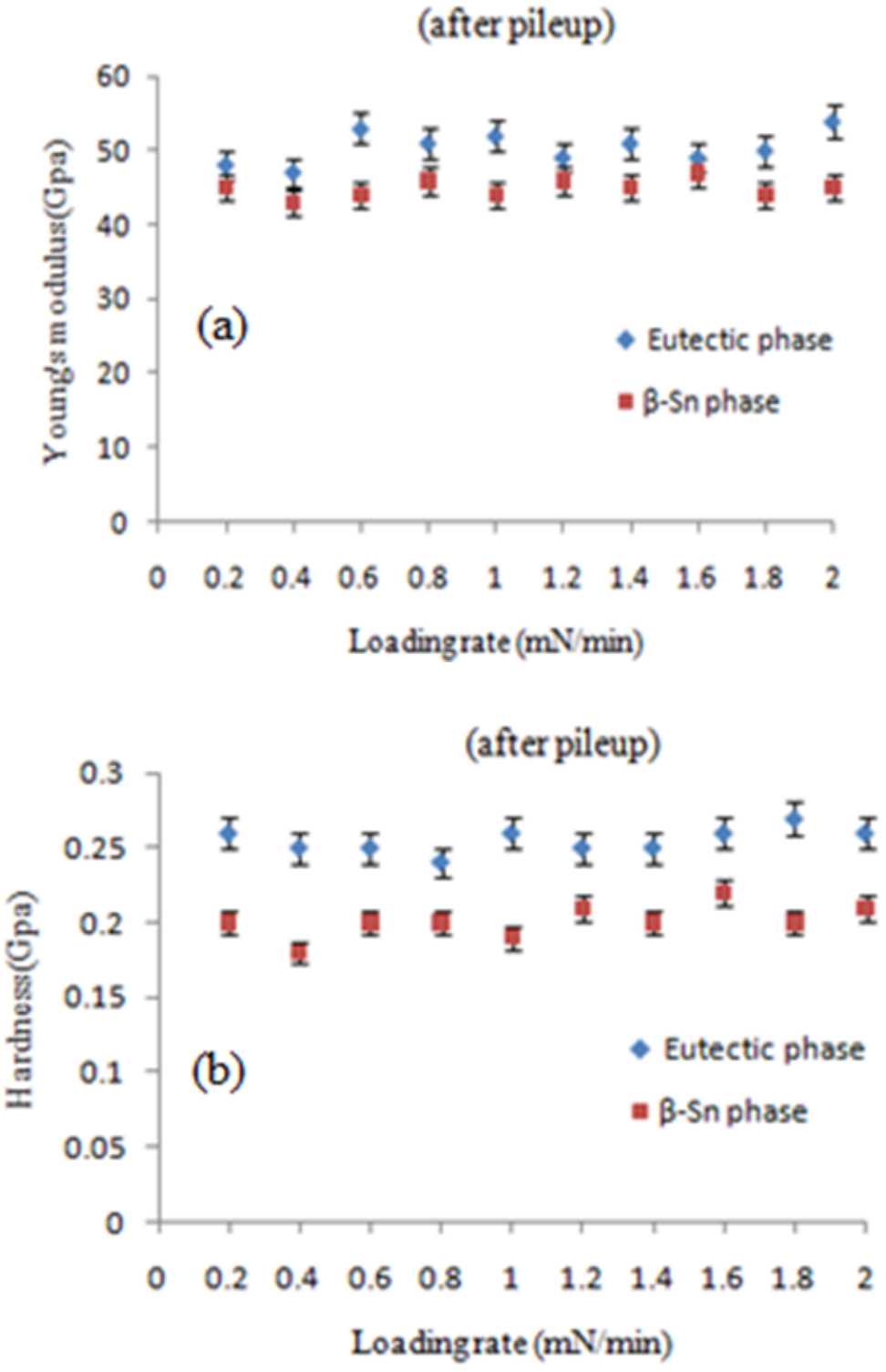

Figure 8.13: Young's modulus (a) and hardness (b) for eutectic and β-Sn phases after pileup effects

Table 8.3: Young's modulus and hardness (after pileup)

Loading rate (mN/min)	E (GPa)		H (GPa)	
	Eutectic phase	β-Sn phase	Eutectic phase	β-Sn phase
0.2	48	45	0.26	0.20
0.4	47	43	0.25	0.18
0.6	53	44	0.25	0.20
0.8	51	46	0.24	0.20
1	52	44	0.26	0.19
1.2	49	46	0.25	0.21
1.4	51	45	0.25	0.20
1.6	49	47	0.26	0.22
1.8	50	44	0.27	0.20
2	54	45	0.26	0.21

8.6 Nanoindentation for IMCs

Similar to the other phases of SAC alloys namely β-Sn, eutectic Sn and pure Sn, the nanoindentation setup is used for IMCs. These IMCs are hard and brittle as compare to the other phases in the same specimens. The EDS elemental mapping (as explained in chapter 4) is used to verify the compositions of these IMCs before implementing the nanoindentation.

The AFM micrograph is given in Figure 8.14 in which the indentation is used for IMCs. These images are collected just after the indentation process. The results for Young's modulus and hardness for both Ag_3Sn and Cu_6Sn_5 IMCs are provided in Table 8.4, with good comparison to the previous studies [Chromik et al. 2003, Sun et al. 2008, Xu and Pang 2006]. This is important to mention that the pileup effect is very small for these particles which is consistent with previous studies and therefore is neglected for IMCs.

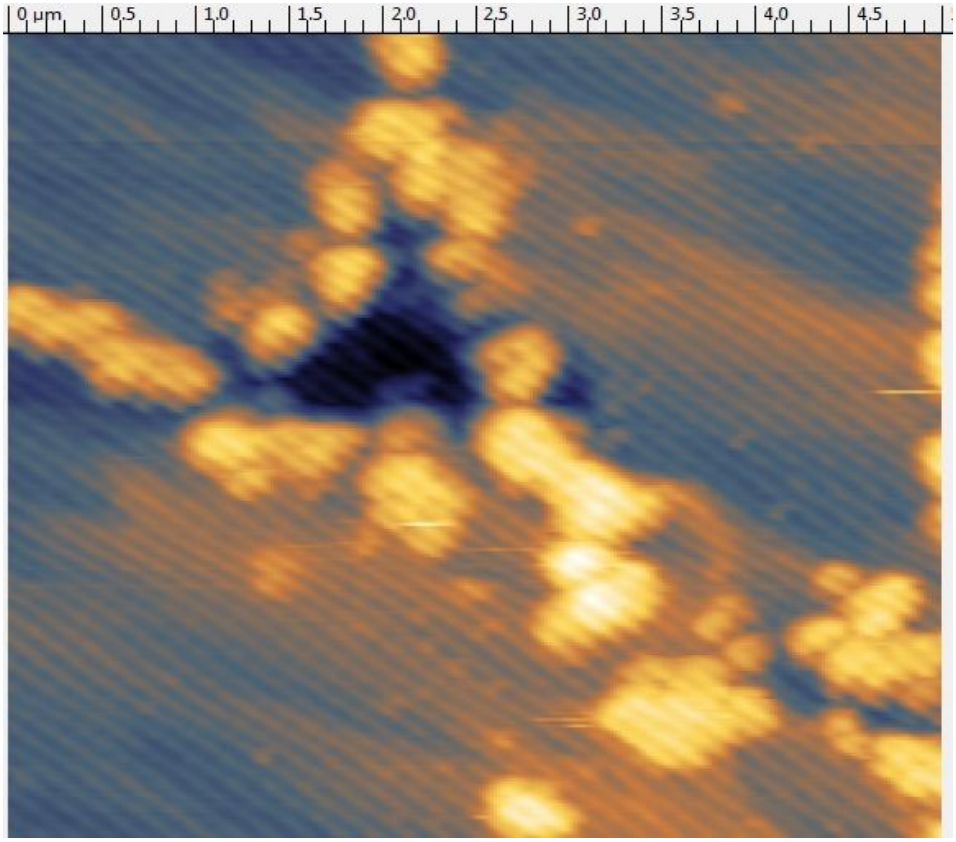

Figure 8.14: Nanoindentation performed on the IMCs

Table 8.4: IMCs Young's modulus and hardness

IMCs	Young's Modulus (GPa)	Hardness (GPa)
Ag_3Sn	74 ± 3	3.32 ± 0.2
Cu_6Sn_5	91 ± 5	5.8 ± 0.6

8.7 CREEP CHARACTERIZATIONS BY NANOINDENTATION

It is well known that due to the higher homologous temperature (>0.5 T_m , T_m is the absolute melting temperature), the solder alloy shows a remarkable creep deformation even at room temperature [Gao et al. 2009]. Other than that, many mechanical properties vary significantly at elevated temperatures. It was important to characterize the creep phenomenon and some other important mechanical properties like Young's modulus and hardness at higher temperatures. The different temperatures used to extract important thermal and mechanical properties like activation energies, strain rate sensitivity index and creep strain rate were 20°C, 45°C, 65°C and 85°C.

The creep deformation takes place at constant target load; consequently the hardness value will be a function of the creep displacement. Usually, a typical creep curve consists of three segments: primary, steady state and tertiary (as explained in the chapter 7 dedicated to creep behavior). The primary creep can be described by Andrade's law as,

$$\varepsilon = b.\sqrt[3]{t} \quad \text{.....(8.10)}$$

where ε denotes strain, t is the time, and b is a constant related to the material properties. Apparently, the strain rate sensitivity index will be determined by the steady-state creep

deformation, rather than the primary deformation. Actually, the steady creep deformation is well described by Dorn's equation [Gao et al. 2009] also presented in chapter 7 for the creep behavior modeling,

$$\dot{\varepsilon} = AD_0 \frac{Gb}{RT}\left(\frac{b}{d}\right)^P \left(\frac{\sigma}{G}\right)^n \exp\left(\frac{-Q}{RT}\right) \quad \text{(8.11)}$$

where σ represents stress, and $\dot{\varepsilon}$ is strain rate.The factor Q denotes the activation energy, R is the universal gas constant, T is the absolute temperature, b is the Burgers vector and d is the grain size of solder alloy. Assume that the shear modulus G is independent of temperature and n represents the stress exponent. Thus Eq. (8.11) can be simplified as the following expression, i.e., Norton power-law,

$$\sigma = a.\dot{\varepsilon}^m.\exp\left(\frac{-Q}{RT}\right) \quad \text{(8.12)}$$

where m is the strain rate sensitivity, which is the inverse of n for the indentation test. The strain rate can be derived from the large steady-state creep deformation portion occurred at the dwell time of target load based on Mayo–Nix theory [Mayo & Nix 1988 and Mayo et al. 1992]. That is given as,

$$\dot{\varepsilon} = \frac{dh}{dt}.\frac{1}{h} \quad \text{(8.13)}$$

The load-time curve for a loading of 5mN (5000 μN) is given in Figure 8.15. The dwell time implemented to extract the creep behavior is 60 seconds. The load against indentation

depth is plotted in Figures 8.16-8.18 for 20°C, 45°C and 85°C for β-Sn and Eutectic phases respectively. The indentation depth against entire time is traced and therefore the portion of indentation depth against dwell time is plotted in Figures 8.19-8.24 for both β-Sn and Eutectic phases at 20°C, 45°C and 85°C respectively. The *dh/dt* term as used in equation (8.13) is evaluated (where "h" is the indentation depth at the start of the dwell time). It was observed that the creep rate increases at increasing temperature which is clear as the material is less resistant at high temperatures. Moreover the creep resistance of eutectic phase was identified to be better than the β-Sn phase.

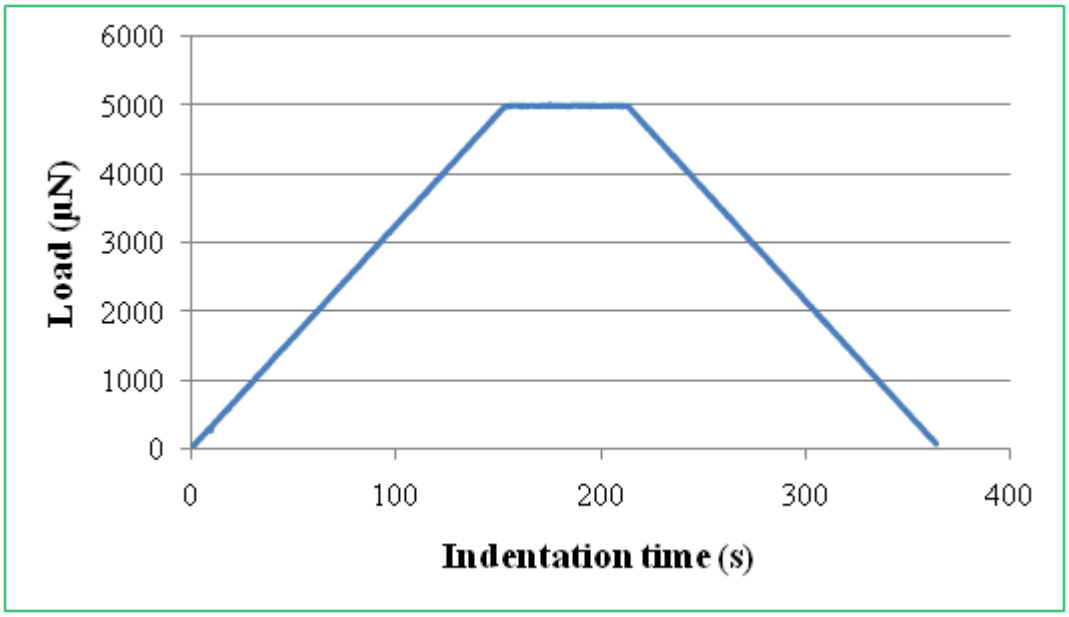

Figure 8.15: Load-time history with 60 seconds of dwell time

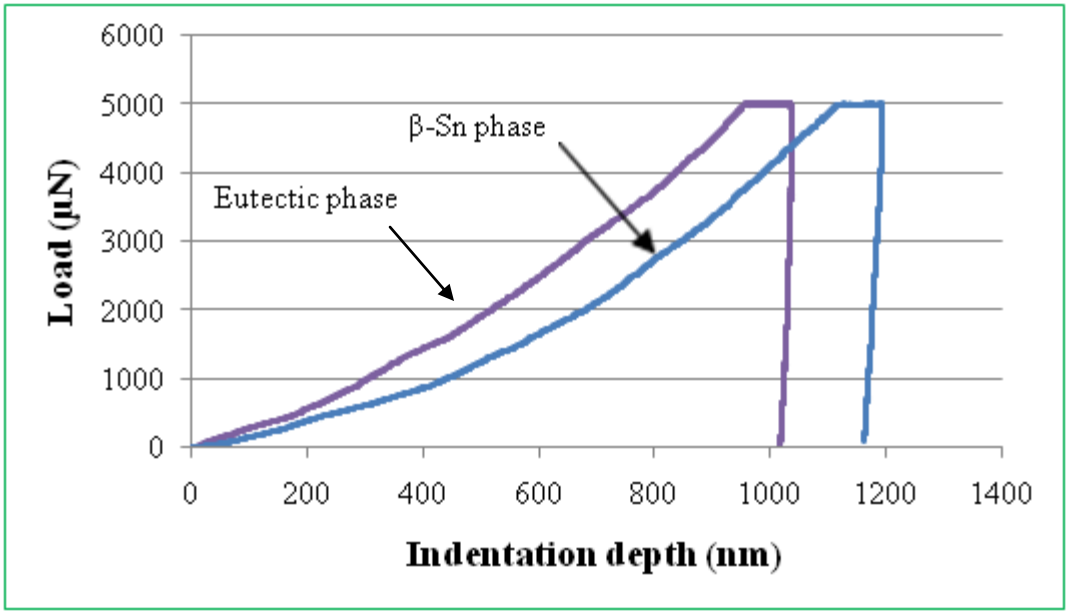

Figure 8.16: Load-displacement curves for Eutectic and β-Sn phases at 20°C

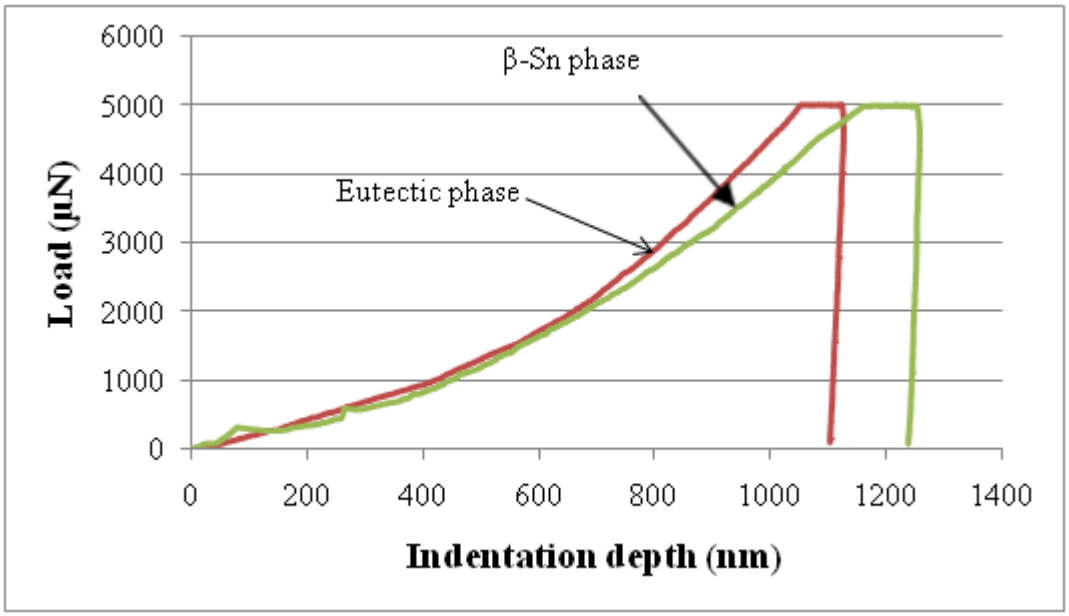

Figure 8.17: Load-displacement curves for Eutectic and β-Sn phases at 45°C

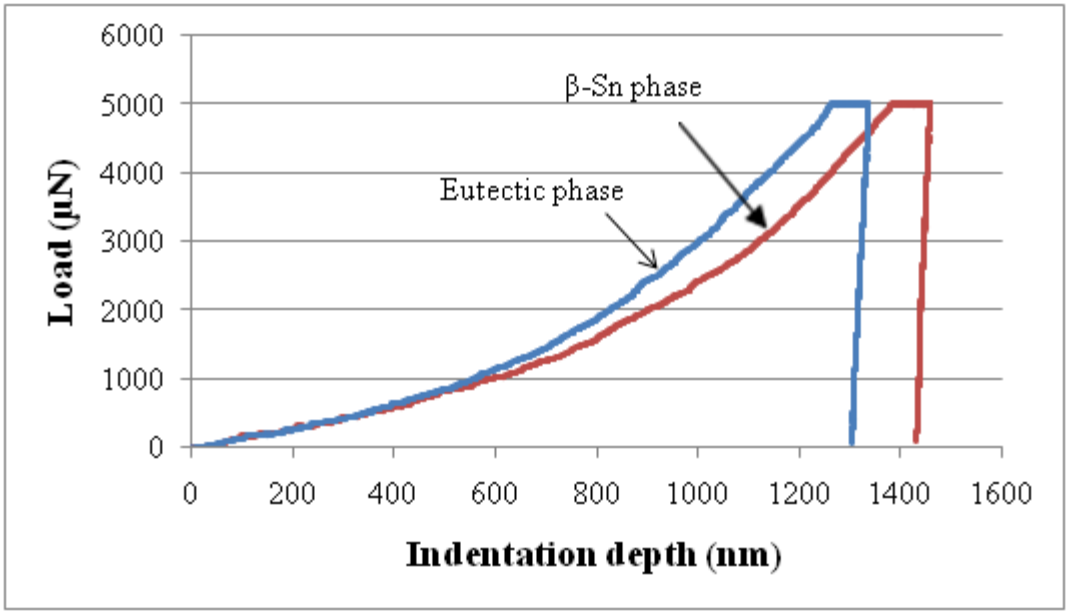

Figure 8.18: Load-displacement curves for Eutectic and β-Sn phases at 85°C

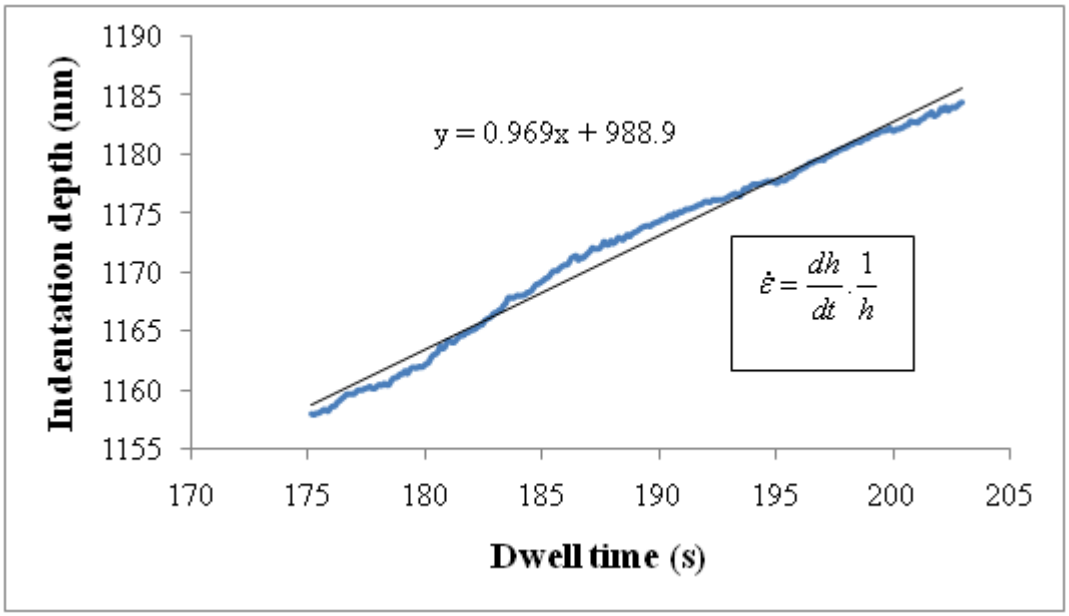

Figure 8.19: Indentation depth at dwell time for β-Sn phase at 20°C

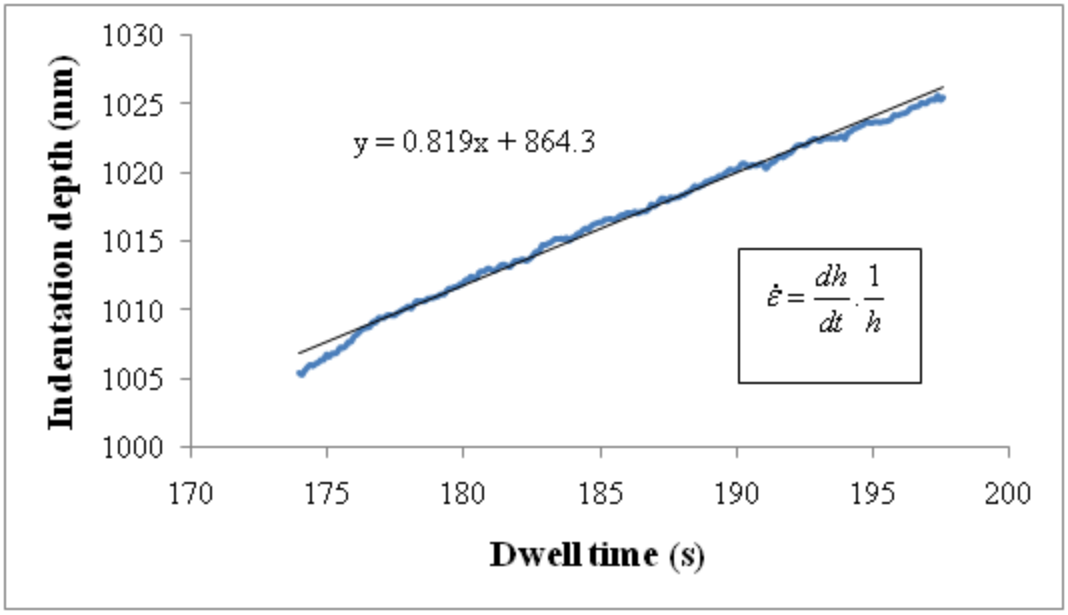

Figure 8.20: Indentation depth at dwell time for Eutectic-Sn phase at 20°C

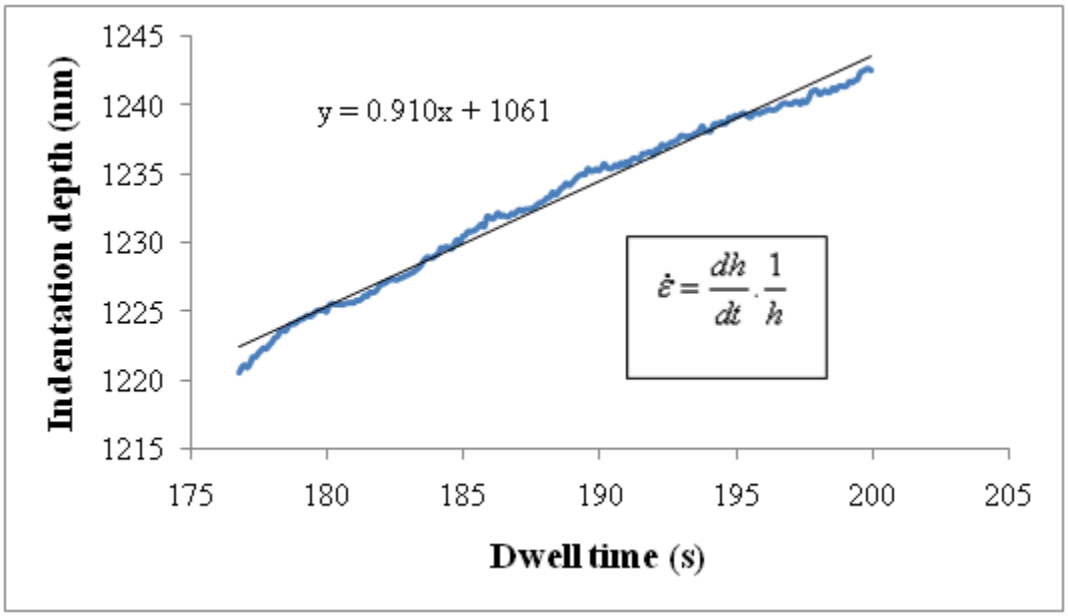

Figure 8.21: Indentation depth at dwell time for β-Sn phase at 45°C

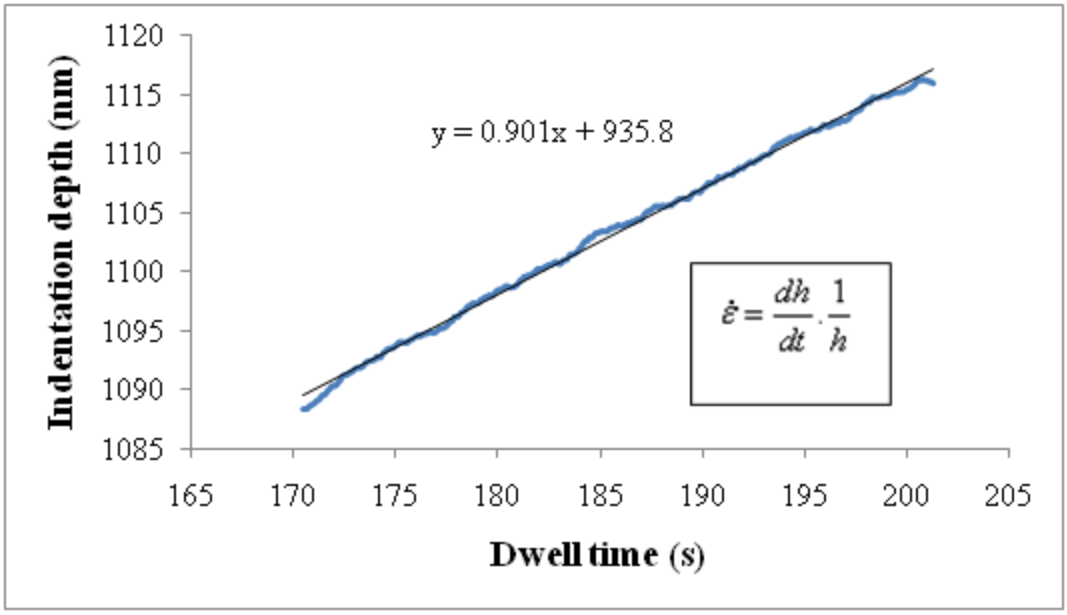

Figure 8.22: Indentation depth at dwell time for Eutectic-Sn phase at 45°C

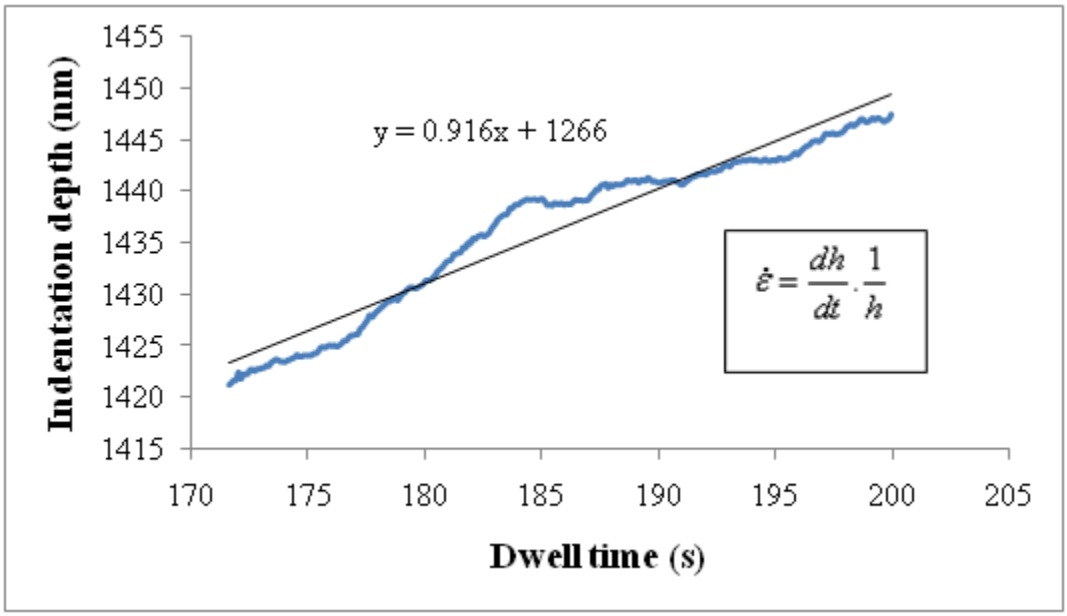

Figure 8.23: Indentation depth at dwell time for β-Sn phase at 85°C

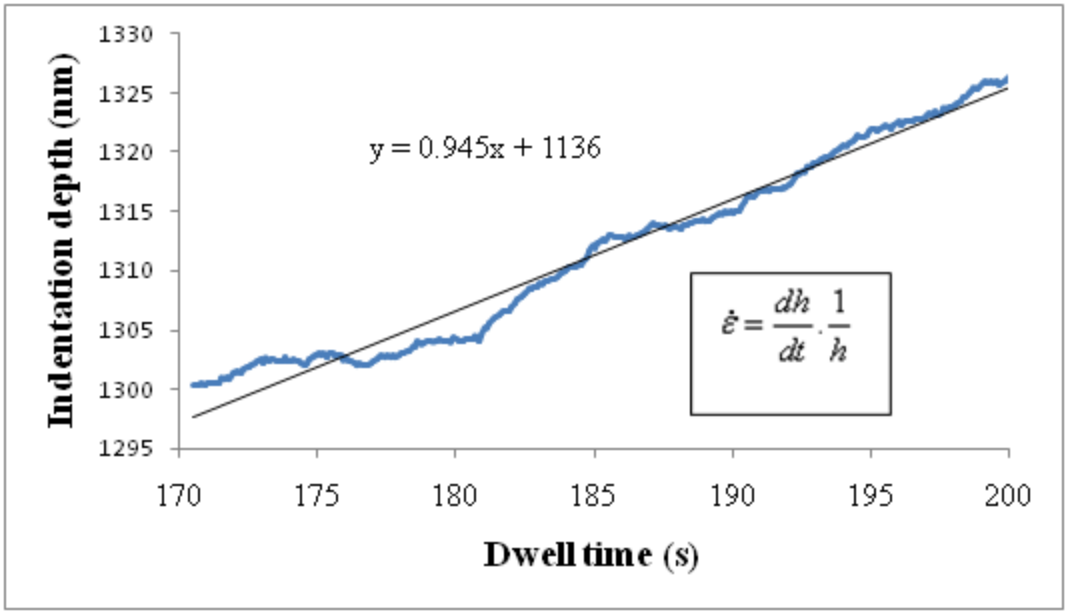

Figure 8.24: Indentation depth at dwell time for Eutectic-Sn phase at 85°C

The relation of the creep deformation vs. time at the target load can be fitted well by an exponential function h(t)=h(0) + Aln(Bt + 1) [Gao et al. 2009]. Here the factors A and B are all material constants. Thus the slope value (dh/dt) in Eq. (8) can be readily extracted from the indentation depth curves.

The values for creep strain rate for both eutectic and β-Sn phases at different temperatures are given in the Table 8.5.

Table 8.5 Creep strain rates for β-Sn and Eutectic phase at different temperatures

Temperature (°C)	**Creep strain rate (s^{-1})** **Eutectic phase**	**Creep strain rate (s^{-1})** **β-Sn phase**
20	$6.78*10^{-4}$	$6.94*10^{-4}$
45	$7.41*10^{-4}$	$7.46*10^{-4}$
85	$7.27*10^{-4}$	$7.93*10^{-4}$

According to the previous statements, the Mayer's hardness H is able to reflect the similar physical meaning of conventional stress σ, thus the strain rate sensitivity index "m" can be extracted from *lnH* versus $\ln \dot{\varepsilon}$ curve as given in equation (8.14),

$$m = \frac{\partial \ln \sigma}{\partial \ln \dot{\varepsilon}} = \frac{\partial \ln H}{\partial \ln \dot{\varepsilon}} \quad \text{..... (8.14)}$$

The different measures of strain rate sensitivity index are provided below in Tables 8.6 and 8.7 for the β-Sn and eutectic phases respectively.

Table 8.6: Mechanical properties for β-Sn phase at different temperatures

Temperature (°C)	**Young's modulus (GPa)**	**Hardness (GPa)**	**Strain rate sensitivity index (m)**
45	37.42 ±2.1	0.10 ±0.03	0.054
65	36.21 ±3.2	0.095 ± 0.025	0.068
85	34.85 ±3.5	0.087 ± 0.027	0.073

Table 8.7: Mechanical properties for Eutectic phase at different temperatures

Temperature (°C)	**Young's modulus (GPa)**	**Hardness (GPa)**	**Strain rate sensitivity index (m)**
45	47.83 ±2.7	0.19 ±0.040	0.18
65	44.72 ±2.2	0.17 ± 0.025	0.19
85	42.85 ±4.5	0.11 ± 0.027	0.16

8.8 Summary

Nanoindentation technique was used to perform a detailed study for the Sn-based lead-free solders. Young's modulus and hardness were calculated with varying loading rates for different phases. Almost no change was found due to the increasing loading rate for both phases. Because of their low creep resistance, bulge effect is very common in SAC solders, which are avoided by attempting different dwell times. Indentation causes piling up in soft SAC solders with appreciable pileup areas. These Pileup areas were calculated using AFM images after indentation. Image-plus was used for the surface profiles for all loading rates and both phases. It was concluded that this pileup area play a major role in calculating the real results particularly for the soft Sn phase which has more pileup than the eutectic phase. Young's modulus and hardness were also determined along the indentation depth and almost no change was observed which is consistent with [Deng et al. 2004].

High temperature Nanoindentation was performed to extract the "time rate" behavior like creep resistance and the strain rate sensitivity index. Creep strains were calculated using Dorn Model. Young's modulus and hardness were also evaluated and their decreasing nature with increasing temperature was explored. Once more, hot dwell times were used to extract most of these described parameters.

CHAPTER 9

WETTABILITY TESTING

9.1 Wettability of Solders

Wetting is the behavior of a liquid to wet a solid surface. This behavior is very important to the interconnection of electronic packages, especially in soldering, for making highly strong bonding between different solid components. In order to attain successful soldering, a certain degree of wetting of the molten solder on the solid substrate surface is required. So generally, a wetting or solderability test is used to measure,

- The initial wettability of the component termination materials
- The wetting properties of a newly developed solder

A proper metallurgical bond is always necessary to form before analyzing the wetting performance of any solder alloy. This bond, of course, varies for different substrates. An interfacial reaction takes place which forms certain amount of IMCs or in some cases an Inter Metallic Layer (IML) at the two interfaces. These IMCs or IML works as an adhesion layer between the substrate and the solder and hence keep them firmly together.

The wettability of any lead-free solder alloy varies with changing its chemical composition and the substrate. For SnPb, the wettability is good over many metallic substrates including copper. Thus, changing from SnPb to lead-free, wettability is an important concern. The substitute must have sufficient wettability under severe service conditions and for different soldering processes such as reflow and wave soldering.

9.2 Wettability Measurement Methods

There are mainly 2 methods for the wettability measurements; Spread-area test (good for reflow soldering) and the wetting balance test (good for the wave soldering). They are described below.

9.2.1 Spread-Area Test

A solder disc (e.g. 6 mm in diameter and 1 mm in thickness) is coated with flux and melted, and then allowed to solidify on a substrate (e.g. Cu). When a bond is formed, the free energy is reduced and hence the solder changes its shape [Wu et al. 2004]. This change in shape causes an increase in the contact area which indicates the wetting behavior of solder. In some cases, the ratio of the as-bonded area to this new area (after soldering) is taken as the wettability of solder. This wetting is given by wetting (or contact angle), θ_c, and is calculated using the Young Dupre's equations as 9.1 and 9.2 [Wu et al. 2004],

$$\gamma_{SF} = \gamma_{SL} + \gamma_{LF} Cos\theta_c \quad \text{.....(9.1)}$$

$$Cos\theta_c = \frac{\gamma_{SF} - \gamma_{SL}}{\gamma_{LF}} \quad \text{.....(9.2)}$$

where γ_{SF}, γ_{LF}, and γ_{SL} refer to the surface tensions of the substrate/flux, liquid (solder)/flux, and substrate/liquid (solder) interfaces, respectively, as shown in Figure 9.1 [Wu et al. 2004]. For a good wetting, the contact or wetting angle should be small (i.e. γ_{LF}, and γ_{SL} smaller and γ_{SF} larger). The spread area test is a good approximation for the reflow soldering process. The solder disc, in the spread area test, has a similar shape to the layer of solder paste by screen-printing or in similar process. Besides, the solder disc in the spread area test and the solder paste in reflow soldering undergo the same process of heating. They are heated above the melting point and are then allowed to solidify.

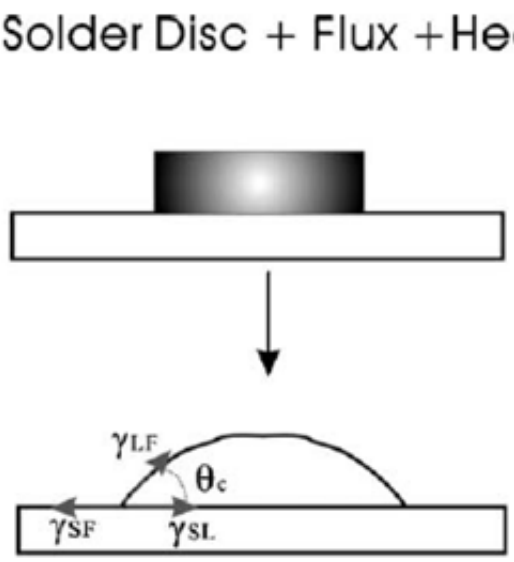

Figure 9.1: Schematic diagram of the spread area test

9.2.2 Wetting Balance Test

Wetting balance test is the second important technique to evaluate the solder wettability. In this method, the coupon (for example Cu) is dipped into the molten solder, present inside the crucible at a temperature more than its melting point. The molten solder climbs up the Cu coupon due to wetting force exerted on it as shown in Figure 9.2 [Wu et al. 2004]. As spread area

test was a good approximation of reflow soldering, this wetting balance test is a good approximation of the wave soldering in which the substrate is brought into contact with the molten solder. The height of the solder onto the Cu coupon depends on many parameters including the soldering temperature, alloy composition and wetting time. Generally, the wetting force is directly proportional to the height of the molten solder onto the Cu coupon. Different forces, due to buoyancy, come in action after partial dipping of the coupon into the solder bath, including the surface tensions which are quite high at the solder/flux interface. The measurement of the resultant force is representative of the meniscus and of the wetting angle and, consequently, of the solderability. The resultant force or wetting force, F_w, can be expressed as follows using equations (9.3 and 9.4),

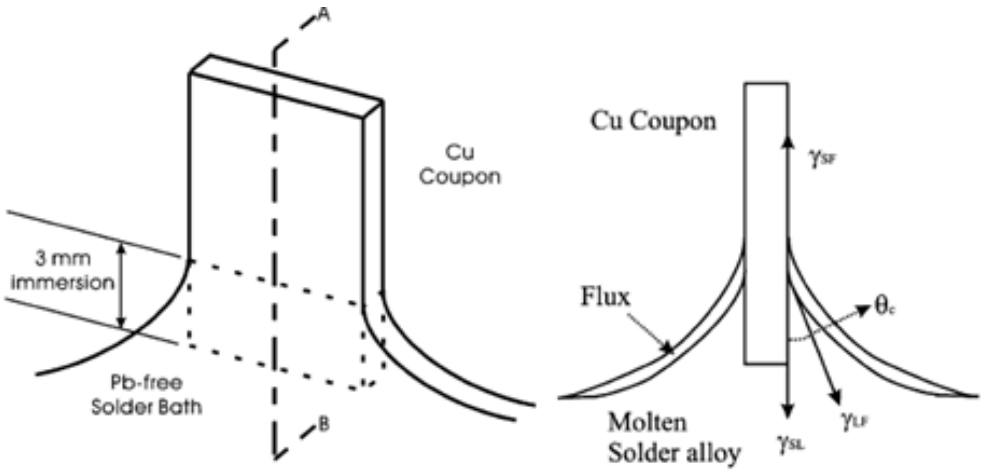

Figure 9.2: Coupon geometry for wetting balance test on molten solder alloy [Wu et al. 2004]

$$F_w = p\gamma_{LF}\cos\theta_c - \rho g V \quad \text{.....(9.3)}$$

$$\cos\theta_c = \frac{F_w + \rho V g}{\gamma_{LF} p} \quad \text{.....(9.4)}$$

Where p is the perimeter of the coupon, γ_{LF} the surface tension of the solder in contact with the flux, θ_c the contact angle, ρ the density of the solder, g the acceleration due to gravity, and V is the immersed volume. A typical wetting curve is shown in Figure 9.3 which represents different types of wettings for solders, in which the wetting time, t_w, is the time at which the solder contact angle to the coupon is 90°, as shown at point B. Wetting occurring in a short wetting time is considered to be good. Hence, the wetting force and time of each solder system are revealed by the wetting balance test.

The wettability of lead-free solders becomes crucial when high solder joint reliability is needed. As presented in equation 9.4, the contact angle is one of the most important parameter in characterizing the solderability (wettability) of any lead-free solder. A smaller contact angle, θ_c, and thus higher cos θ_c is representing good wettability. Ideally, cos θ_c can reach to 1 which makes θ_c to be 0° which is the best possible wettability. But, in practice, it is somewhere in the range of 40 to 50°, as shown in Figure 9.4, depending on the temperature applied, flux used and many other experimental parameters. On the other hand, a contact angle of more than 90° is not recommended for good joining. A schematic of contact angle more than 90° is provided in Figure 9.5.

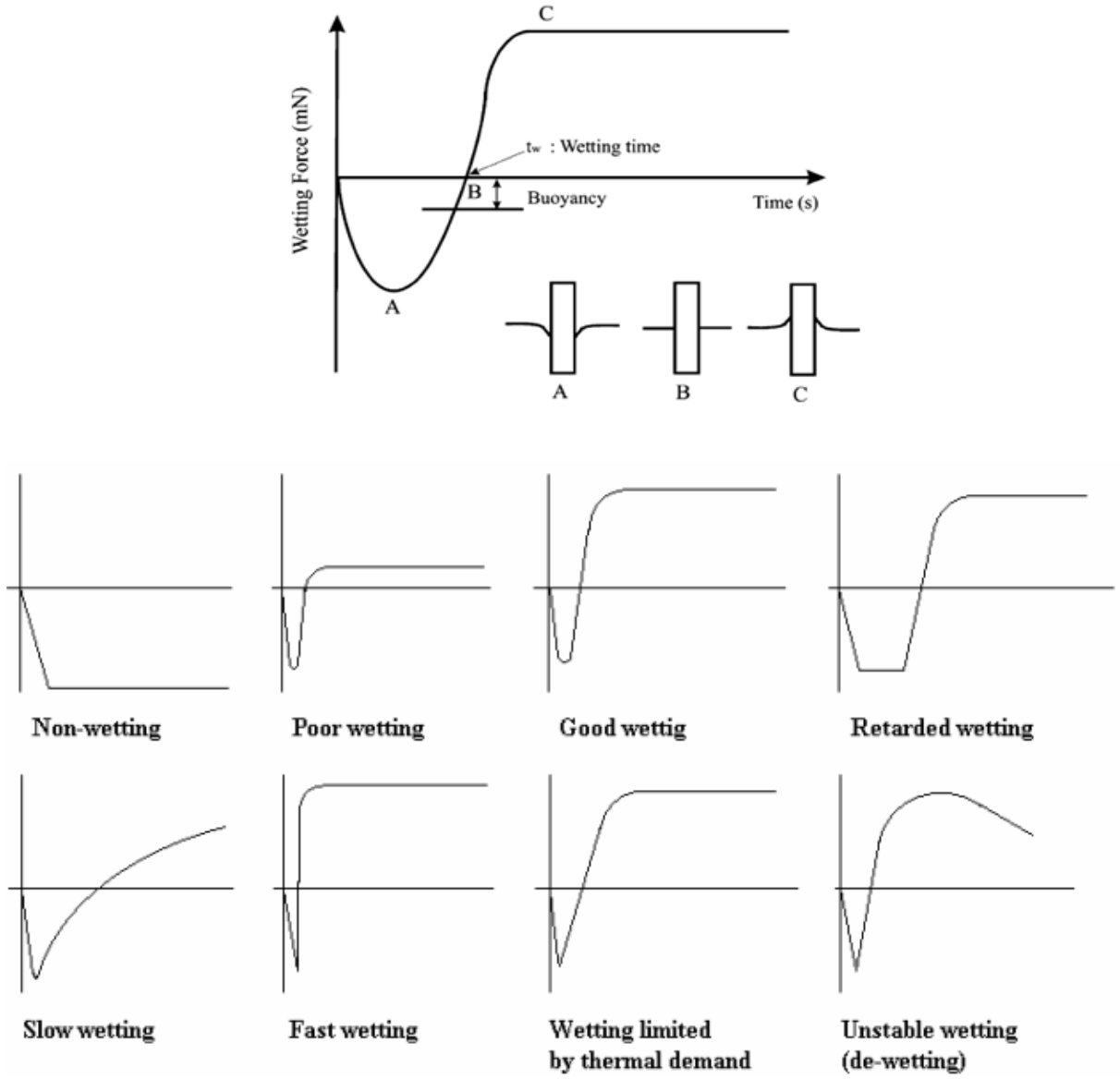

Figure 9.3: Variation of wetting force with time [METRONELEC]

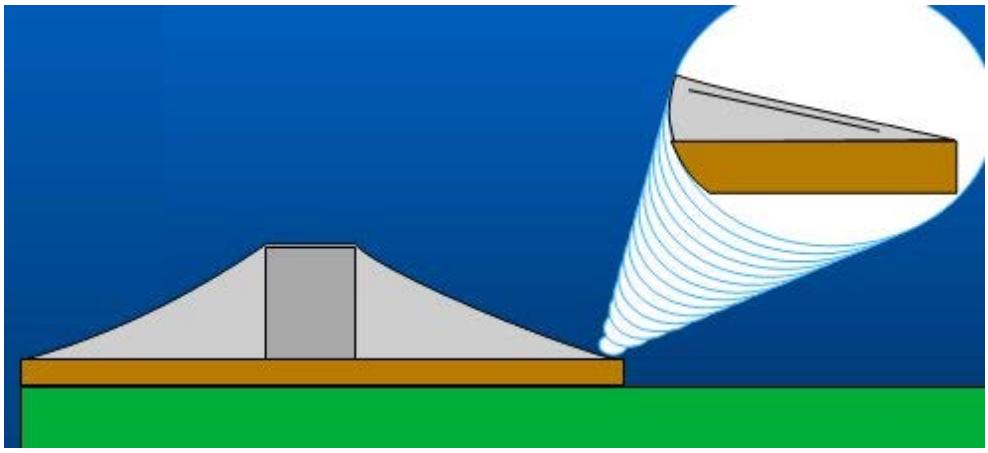

Figure 9.4: Wettability with smaller contact angle

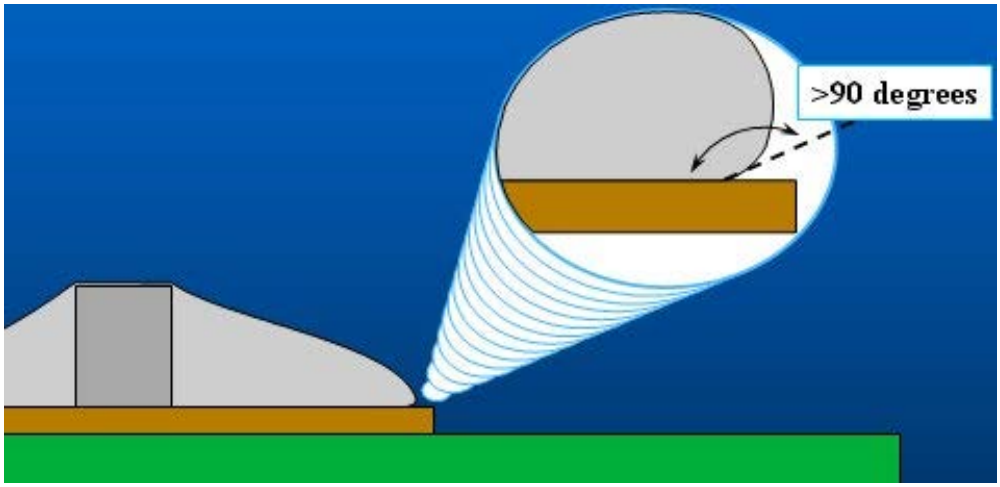

Figure 9.5: Wettability with higher contact angle

Different studies have been performed to trace the solder wettability for binary and tertiary Sn-based lead-free solder alloys including Sn-3.5Ag (eutectic) and SAC alloy compositions. In general, the wettability increases with increasing temperature keeping the same solder flux. In [Wu et al. 2004], the impact of RE elements, mainly Ce and La, has been studied for the wettability performance on SnPb, SnAg, SnCu and SAC. It has been reported that they can all be soldered successfully using the rosin mildly activated (RMA) flux.

The wettability of SnPb solder is quite good in comparison to SnAg, SnCu and SAC alloys. In any case, over the copper substrates, SAC alloys perform well whereas the RE dopings have shown significant improvements in the wetting performance of all SnAg, SnCu and SAC alloys [Wu et al. 2004]. In most of the cases, the addition of RE elements help to reduce the wetting angle. It can be seen that the amount of RE elements needs to be optimized for the best wetting performance, Figure 9.6.

An extensive experimental study on wettability study on Sn3.5Ag eutectic and Sn-3.5Ag-RE doped alloys was made by [Wu et al. 2004]. The wetting curves of SnAg, SnAg–0.25RE and SnAg–0.5RE are compared with that of SnPb in Figure 9.6. It can be seen that all four solders have roughly the same wetting time. However, the wetting force of SnPb is the highest among the four alloys. The effect of adding RE elements (mainly Ce and La) is clearly demonstrated by a significant increase in the wetting force of Sn3.5Ag-0.25RE alloy as getting closer to the SnPb solder. However, an excessive amount of RE addition can lower the wetting force. In the same study, this effect was also applicable to the wetting angle, such that SnAg–0.25RE has the lowest wetting angle among SnAg, SnAg–0.25RE and SnAg–0.5RE.

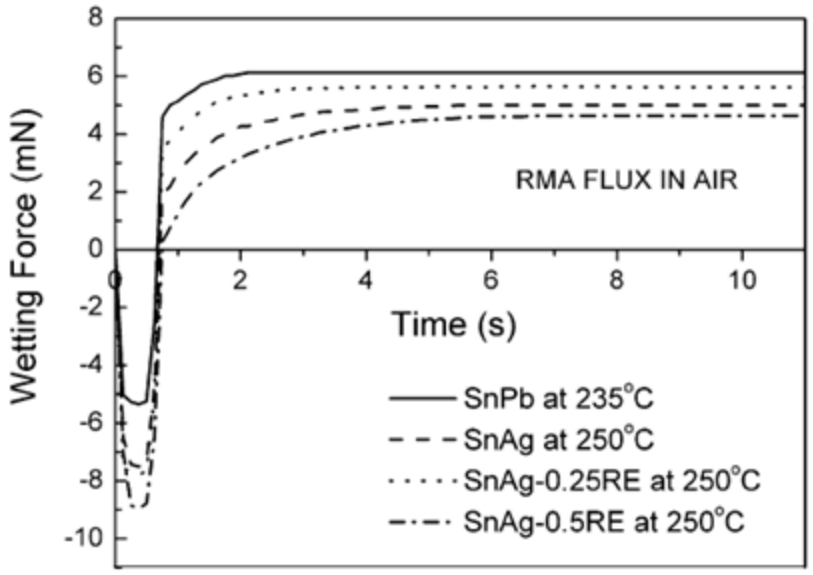

Figure 9.6: Wetting curves of Sn-3.5Ag-RE solders compared with Sn-Pb solder [Wu et al. 2004]

9.3 Sample Preparation And Experimental Conditions

The equipment used for the wetting balance test was METRONELEC as shown in Figure 9.7, a French manufacturer of soldering equipments. The copper foils used as substrates were 0.025mm thick and 12mm wide. They were purchased from the "Good Fellows", France, with a purity of 99.9%. The samples were cleaned with acetone and dried. Later on, they were dipped into 20 % HNO_3 solution for 20 seconds and then placed in the flux for about 1 second. The flux used was resin mildly activated (RMA) and was manufactured by "Metaux Blancs Ouvres" with fluxing code BC 310.15. The immersion depth into the crucibles, for the copper substrate, was 3mm as shown in Figure 9.8. The wetting time used was 10s and the wetting temperatures applied were 250°C and 260°C.

Figure 9.7: METRONELEC wettability setup

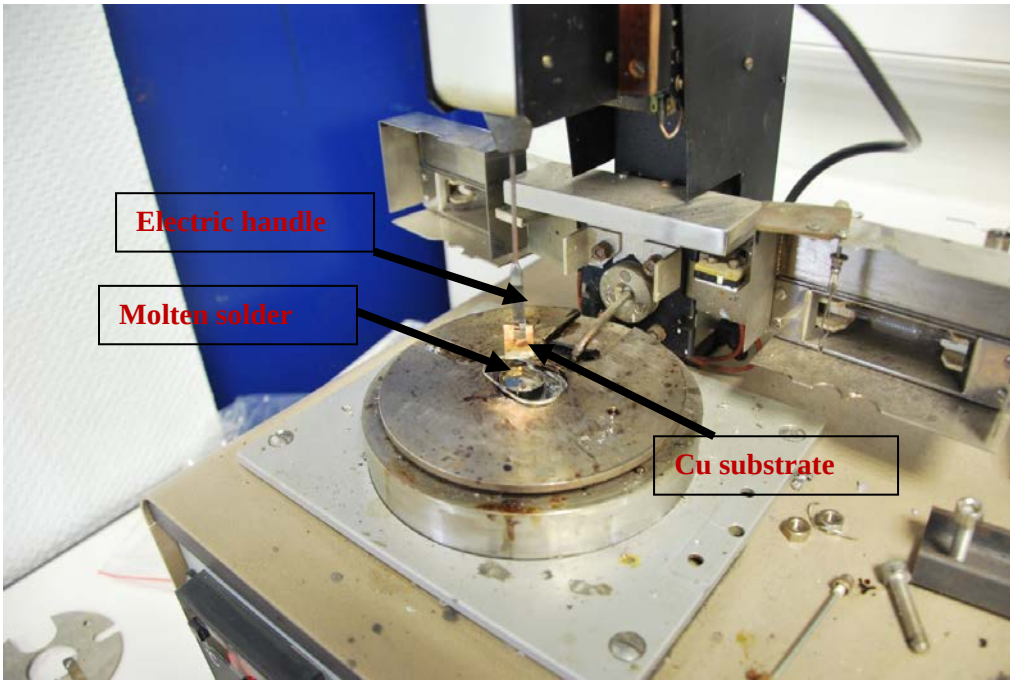

Figure 9.8: Wettability measuring method

9.4 Wetting Phenomena Principle

There are different kinds of soldering techniques as described in chapter 2 (Soldering background/methods/techniques). Mainly, in the reflow soldering process, three different phases are present namely;

- the solid phase (parts to be soldered),
- the liquid phase (molten solder alloy),
- the vapour phase (atmospheric air in most cases).

These 3 phases form a regular meniscus as shown in Figure 9.9. The molecular interactions of these three phases, taken in pairs, are surface tensions,

- $\vec{\gamma}_{SL}$: solid-liquid phase,
- $\vec{\gamma}_{SV}$: solid-vapour phase,
- $\vec{\gamma}_{LV}$: liquid-vapour phase.

The balance of those three forces is attained when the liquid, which wets the solid, forms a meniscus represented by the Young's formula,

$$\vec{\gamma}_{SV} + \vec{\gamma}_{SL} + \vec{\gamma}_{LV} \quad \text{.....(9.5)}$$

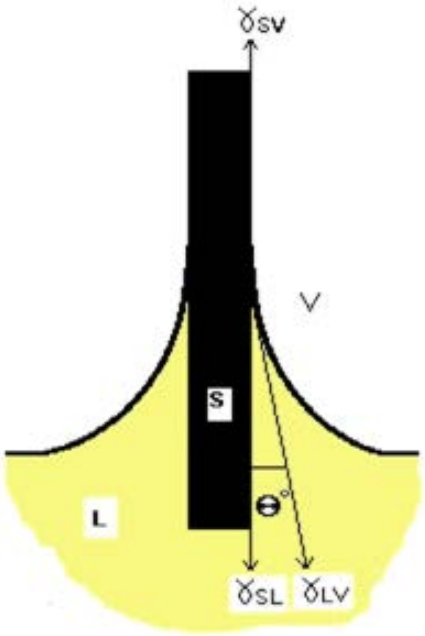

Figure 9.9: Meniscus formed during the wetting balance test [METRONELEC]

The angle θ is formed by the surface of the solid and the liquid at their extreme point of contact and is known as the wetting angle or the contact angle. Taking the sum of the forces along the vertical projection of the plane,

$$\gamma_{SV} - \gamma_{SL} - \gamma_{LV} Cos\theta = 0 \quad \text{.....(9.6)}$$

This gives equation 9.7,

$$Cos\theta = \frac{\gamma_{SV} - \gamma_{SL}}{\gamma_{LV}} \quad \text{.....(9.7)}$$

The angle θ as directly linked to surface tensions is thus representative of the wetting quality. For a smaller contact angle, and thus better wettability, γ_{LV} should be as small as

possible. This is the main function performed by adding the RE elements which decrease the surface tension and this reduces the contact angle as performed during the experiments. This is important to mention that the contact angle is only conceivable for the alloys in the molten state.

9.5 Meniscography Principle

As described earlier, after immersing the Cu coupon into the molten solder bath, the surface tensions are highest at the solder/flux interface. The measurement of the resultant force is representative of the meniscus and, consequently, of the wetting angle θ and of the solderability. The principle set forth above is described in equation 9.8,

$F=F_m-F_a$ …… (9.8)

Where F= resultant force; F_m= wetting force and F_a=force of buoyancy. Thus, after balancing,

$F= \gamma_{LV}$ P $\cos\theta$ - ρ v g……..……. (9.9)

and from here the contact angle becomes,

$$Cos\theta = \frac{F + \rho Vg}{\gamma_{LV} P} \quad \text{.....(9.10)}$$

Where ρ is the mass density of the solder alloys, which is provided in Table 9.1, P is the perimeter of the coupon immersed into the solder crucible and g is the acceleration due to gravity (9.81 m/s^2). Thus F is the measured force from which the contact angle is deduced.

Table 9.1: Densities for SAC and SAC-La alloys

Alloy	Density (mg/mm^3)
SAC	7.45
SAC-0.05	7.453
SAC0.25	7.46
SAC-0.5	7.48

9.6 Wettability Measuring Parameters

Generally, there are 3 important parameters for the wettability measurements. These are the surface tension, wetting force and the contact (or wetting) angle. These parameters with required description and evaluation are provided below.

9.6.1 Flux-Solder Surface Tension

In order to determine the wettability in terms of wetting force and contact angles, it is necessary to calculate the surface tension, γ_{LV}. The results for surface tension are given in Figures 9.10-9.16 for different compositions and at different temperatures. Good reproducibility was observed for all the cases. The sample preparation and the flux used was the same for all compositions.

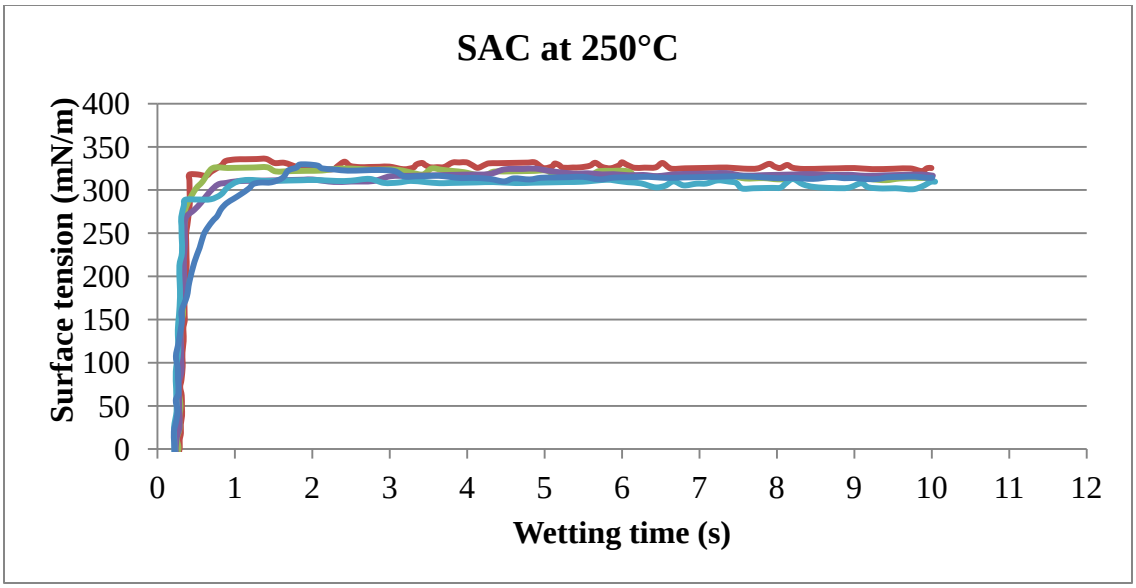

Figure 9.10: SAC surface tension vs. wetting time at 250°C

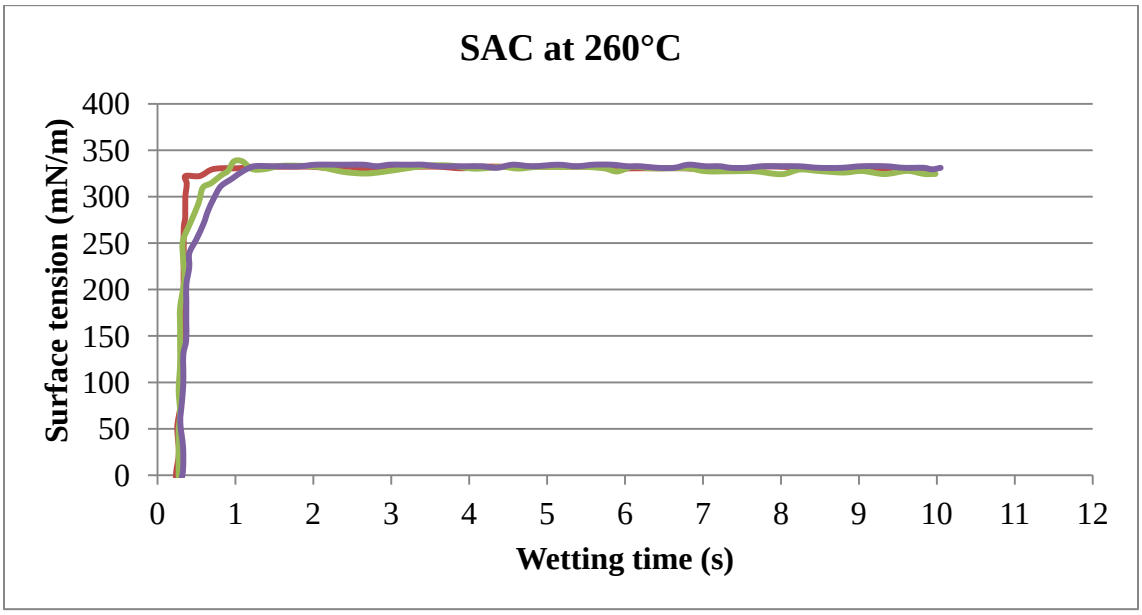

Figure 9.11: SAC surface tension vs. wetting time at 260°C

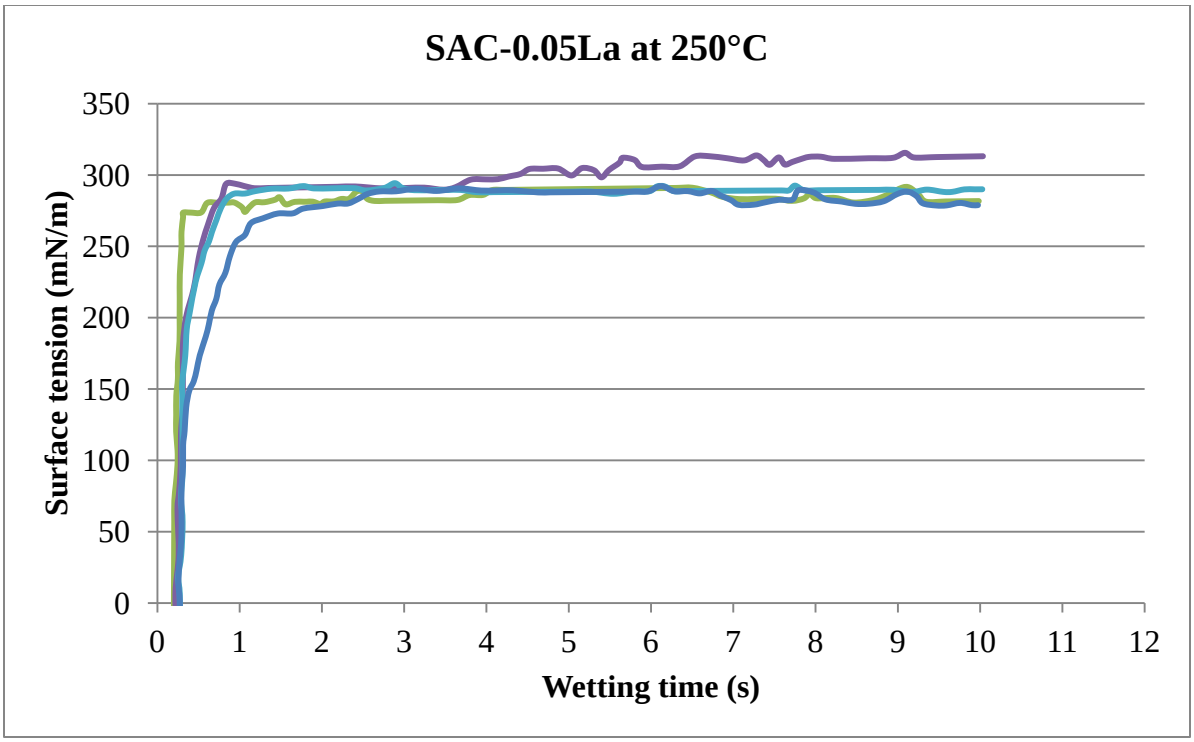

Figure 9.12: SAC-0.05La surface tension vs. wetting time at 250°C

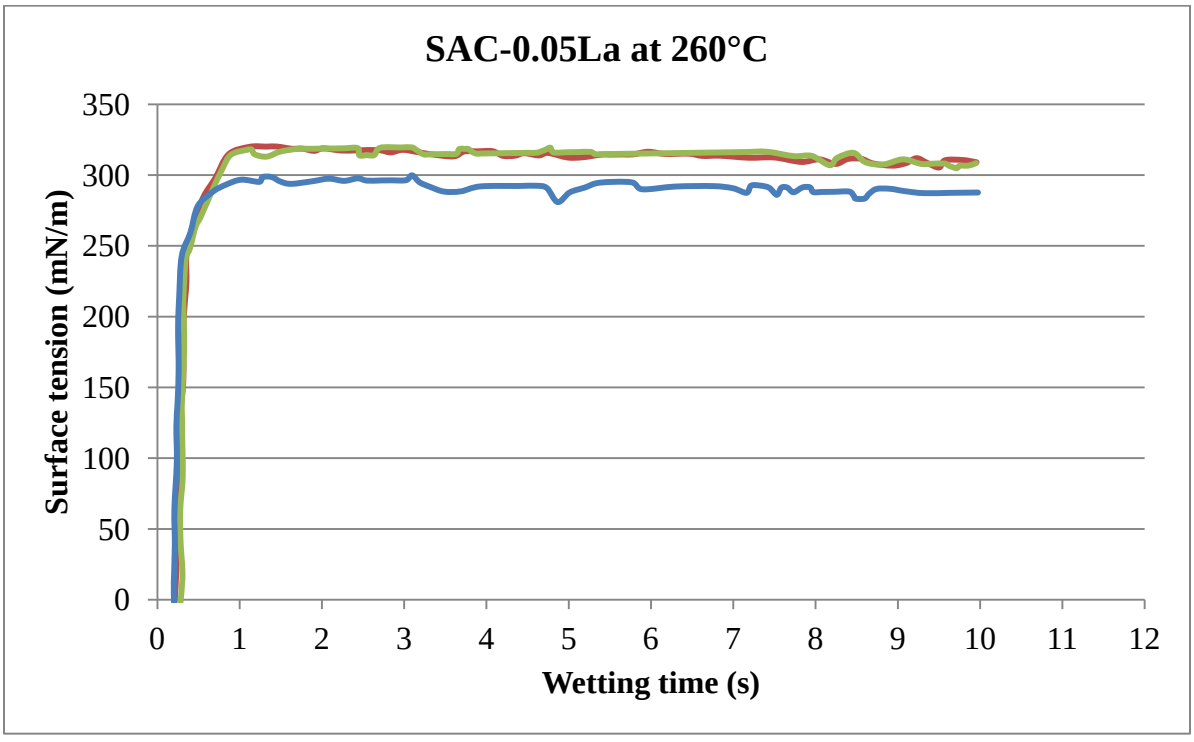

Figure 9.13: SAC-0.05La surface tension vs. wetting time at 260°C

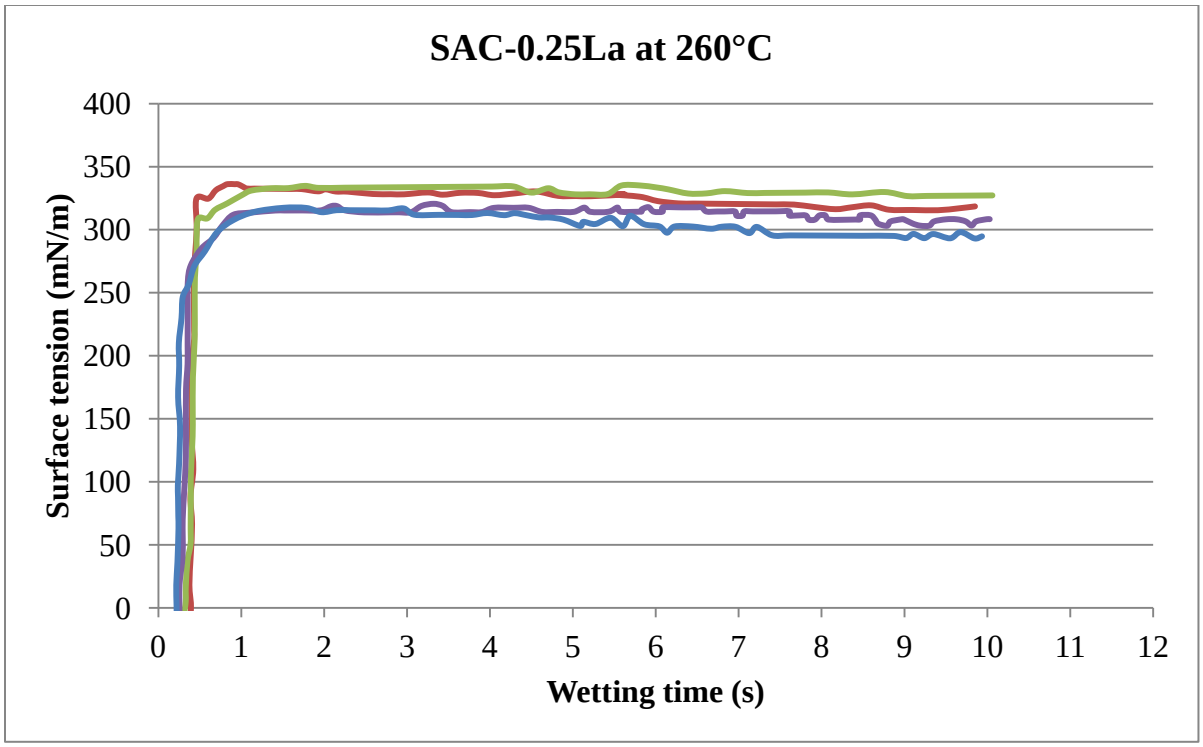

Figure 9.14: SAC-0.25La surface tension vs. wetting time at 260°C

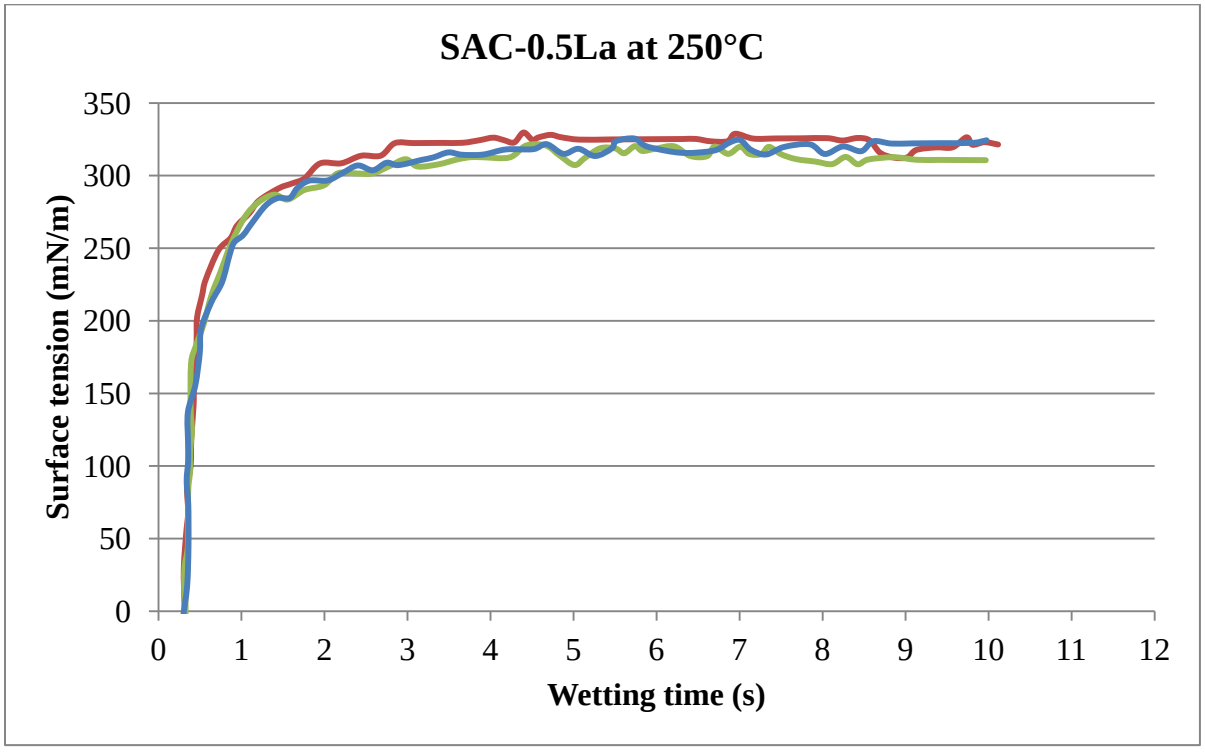

Figure 9.15: SAC-0.5La surface tension vs. wetting time at 250°C

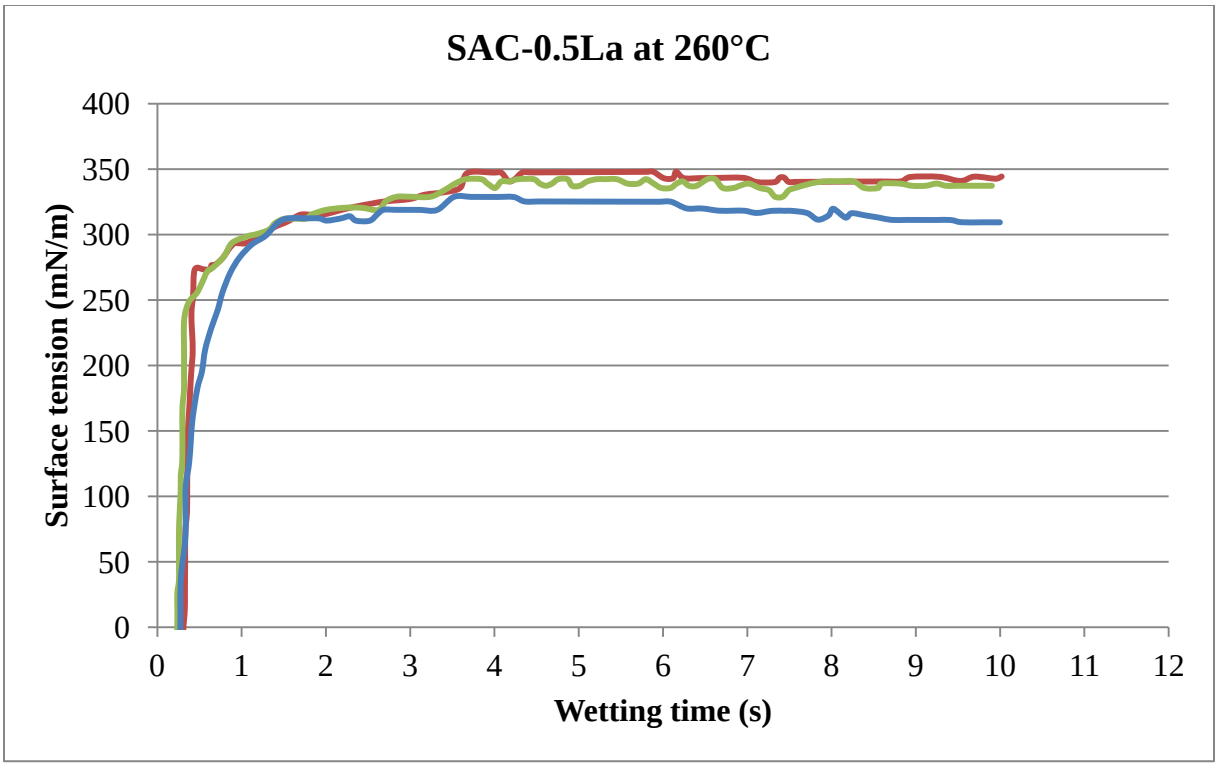

Figure 9.16: SAC-0.5La surface tension vs. wetting time at 260°C

9.6.2 Wetting Force

After measuring the surface tensions for SAC and SAC-La doped alloys, they were used to evaluate the other important wettability characteristic, called the wetting force. The wetting forces imposed by the molten solder on the test surface, as it is dipped into and held in the solder bath, are plotted as a function of time. These plots start with the negative wetting force which represents the non-wetting conditions, and rises until it crosses the zero axis of wetting force, indicating that wetting has occurred. The time taken to reach the zero value is an important parameter known as the wetting time and is used to assess the solderability. Wetting force mainly depends on the density and surface tension of the solder.

Similar conditions as used for the surface tension were kept again and the results for wetting forces for SAC and SAC-La doped alloys are presented in Figures 9.17-9.20. The average values with 5% error bars are given in Figure 9.21.

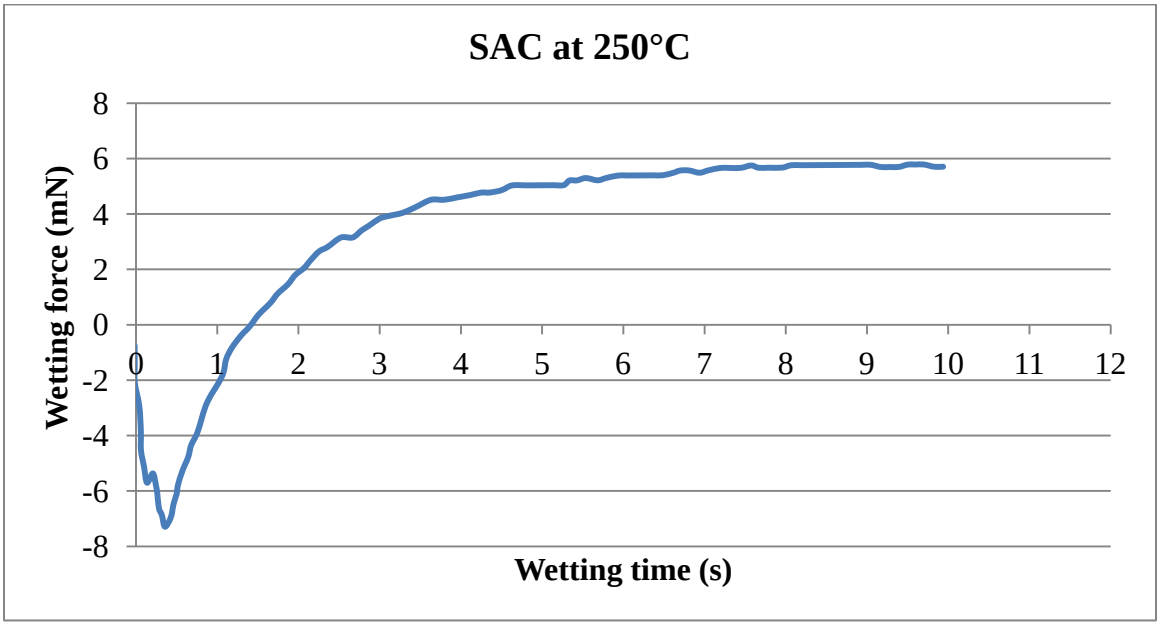

Figure 9.17: SAC wetting force vs. wetting time at 250°C

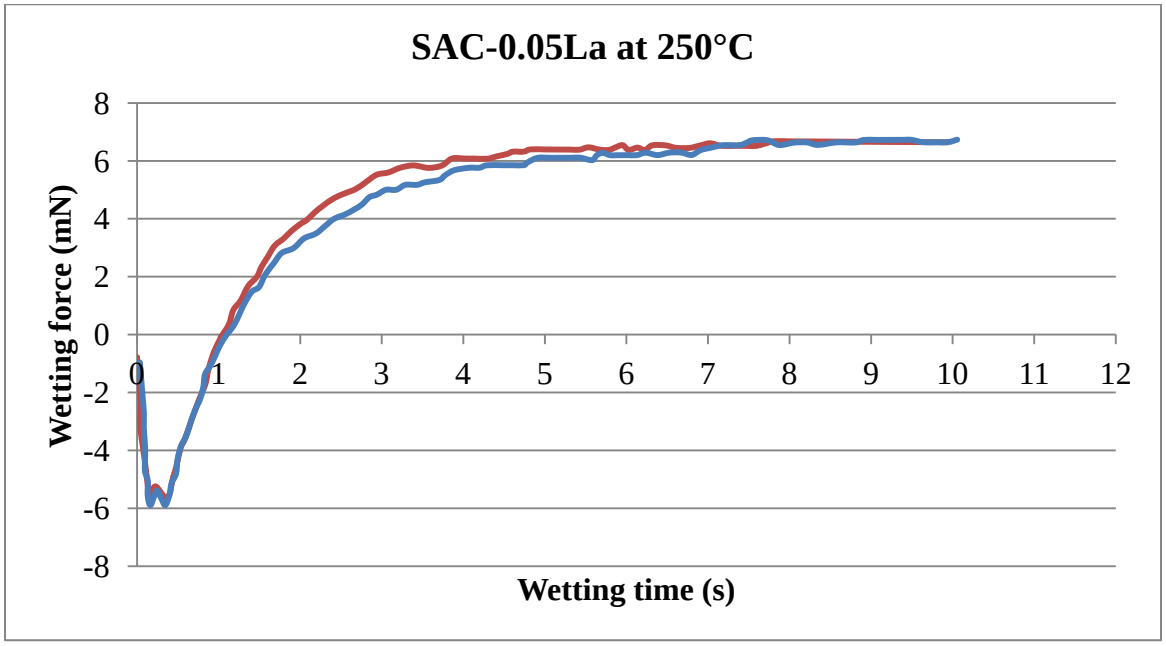

Figure 9.18: SAC-0.05La surface tension vs. wetting time at 250°C

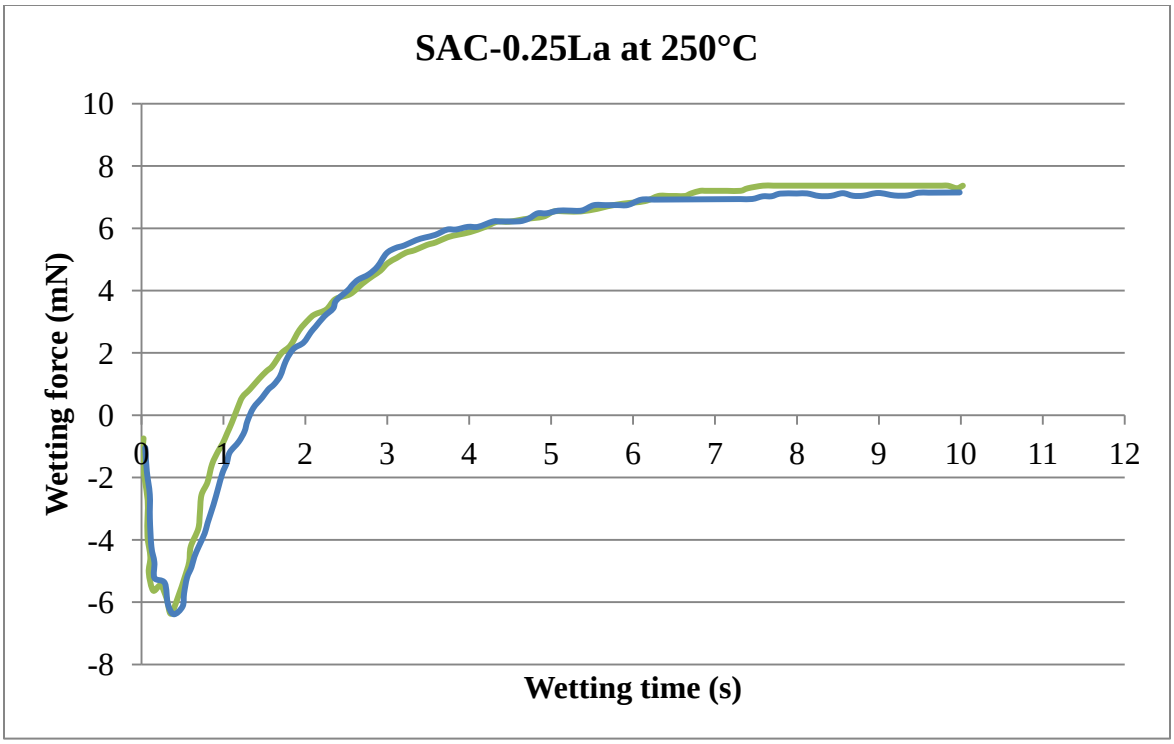

Figure 9.19: SAC-0.25La surface tension vs. wetting time at 250°C

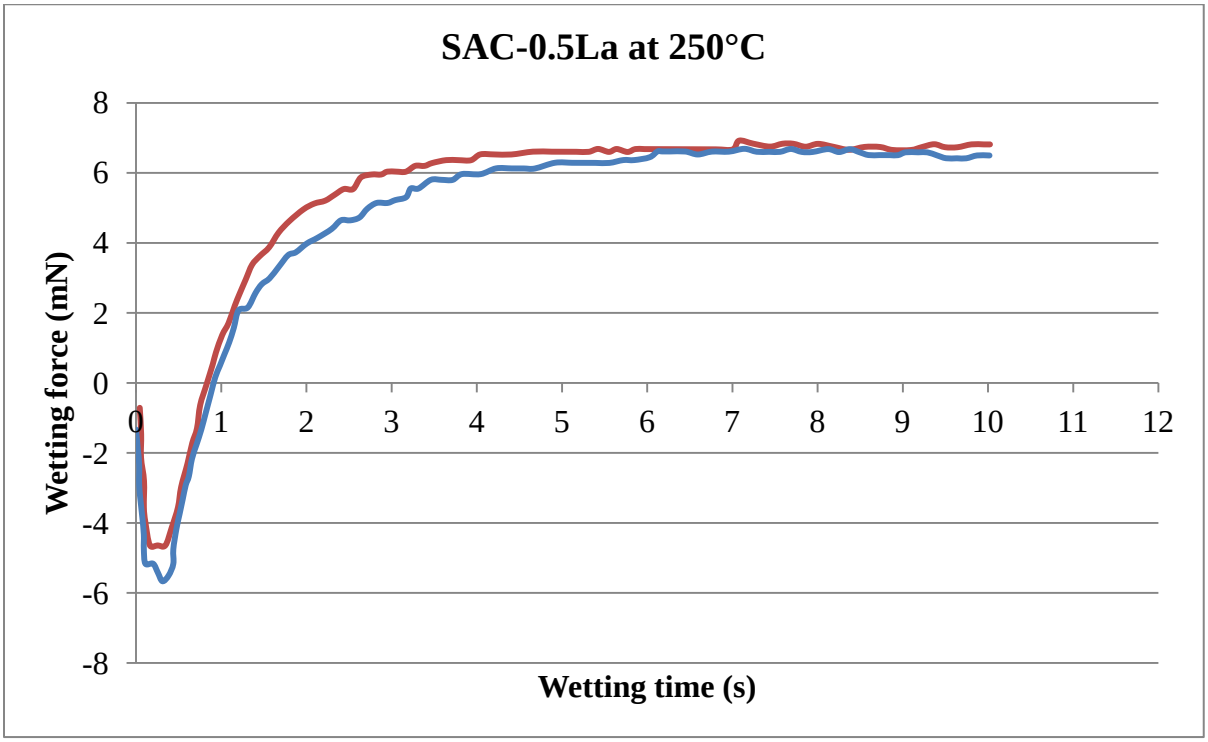

Figure 9.20: SAC-0.5La surface tension vs. wetting time at 250°C

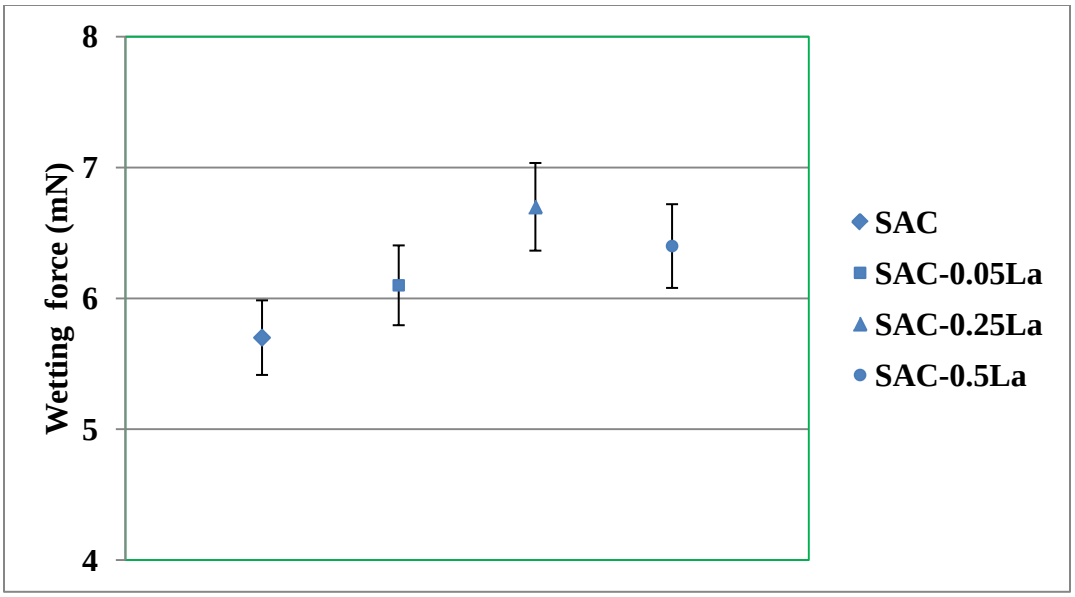

Figure 9.21: SAC and SAC-La wetting forces at 250°C

9.6.3 Wetting or Contact Angle

The contact angles were measured for SAC and SAC-La doped alloys in parallel to wetting forces. The results are presented in Figures 9.22-9.25. The average values with 5% error bars are also given in Figure 9.26. 205 The contact angles were measured for SAC and SAC-La doped alloys in parallel to wetting forces. The results are presented in Figures 9.22-9.25. The average values with 5% error bars are also given in Figure 9.26. This increase of wetting angle, if RE is in excess (>0.25%), is mainly because of the oxidation resistance during wetting due to the strong affinity of RE to oxidize. Oxidation at the solder surface inhibits the molten solder from contacting with the solid substrate, which usually causes non-wetting behavior. But when the oxide is massive, or the oxide quickly generates, the flux cannot perfectly remove the oxides, and the wettability will degrade. This has also been confirmed by the work performed by [Zhou et al. 2009]. They showed (after TGA analysis) that 0.1% of Nd is the optimum amount as the surface tension increases if Nd is more than 0.1% which finally increases the contact angle. Similarly [Shi et al. 2008] have suggested the maximum RE (Er) doping as 0.1-0.4% and [Wang el al. 2002] have demonstrated RE (Ce) as 0.25-0.5% in SnAg alloys. In the work performed by [Noh et al. 2010], they stated that RE is liable to oxidation [Huang et al. 2002] due to its strong affinity towards oxygen and have suggested 0.3 % of Ce as the optimum doping in SAC alloys. The

formation of RE oxides is also confirmed during our EDS mapping on the free surface of unpolished specimens.

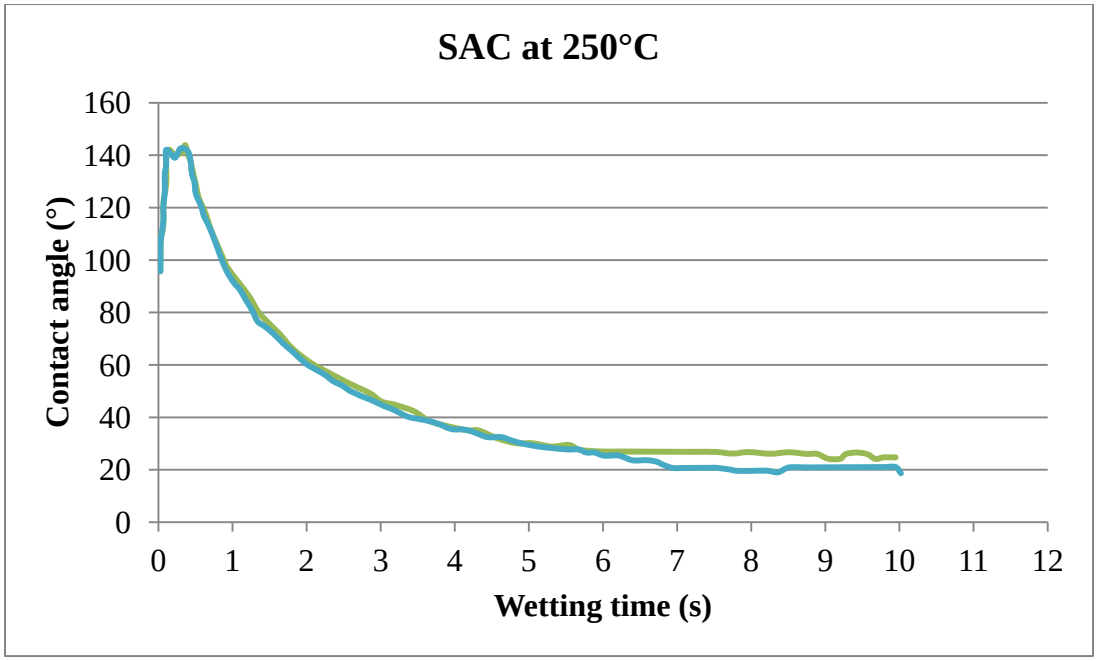

Figure 9.22: SAC contact angle vs. wetting time at 250°C

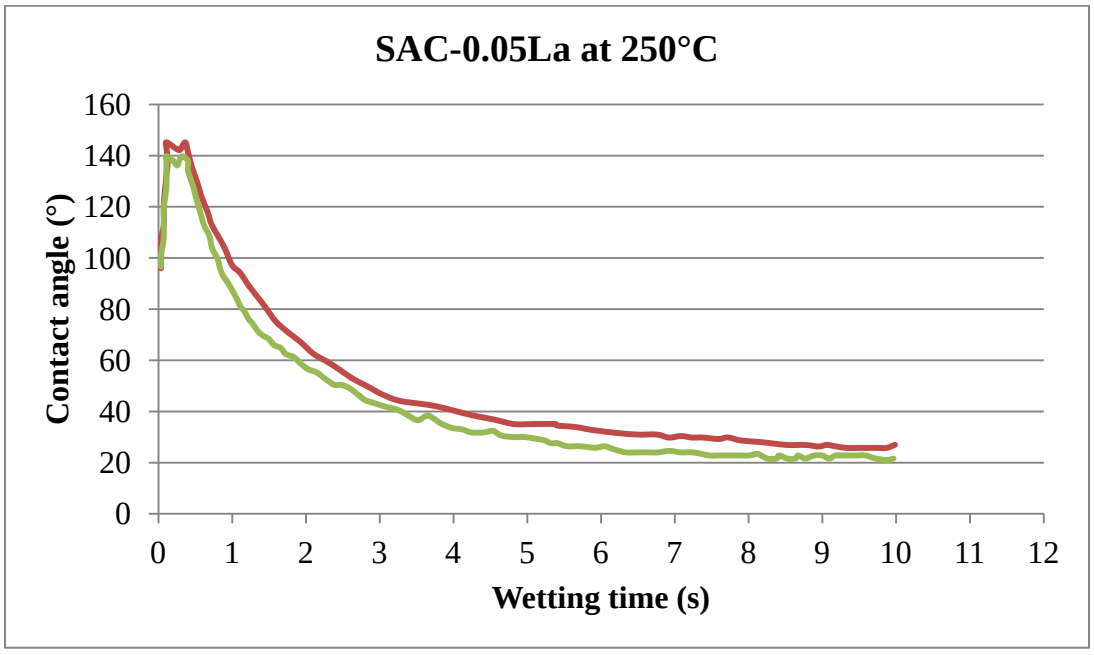

Figure 9.23: SAC-0.05La contact angle vs. wetting time at 250°C

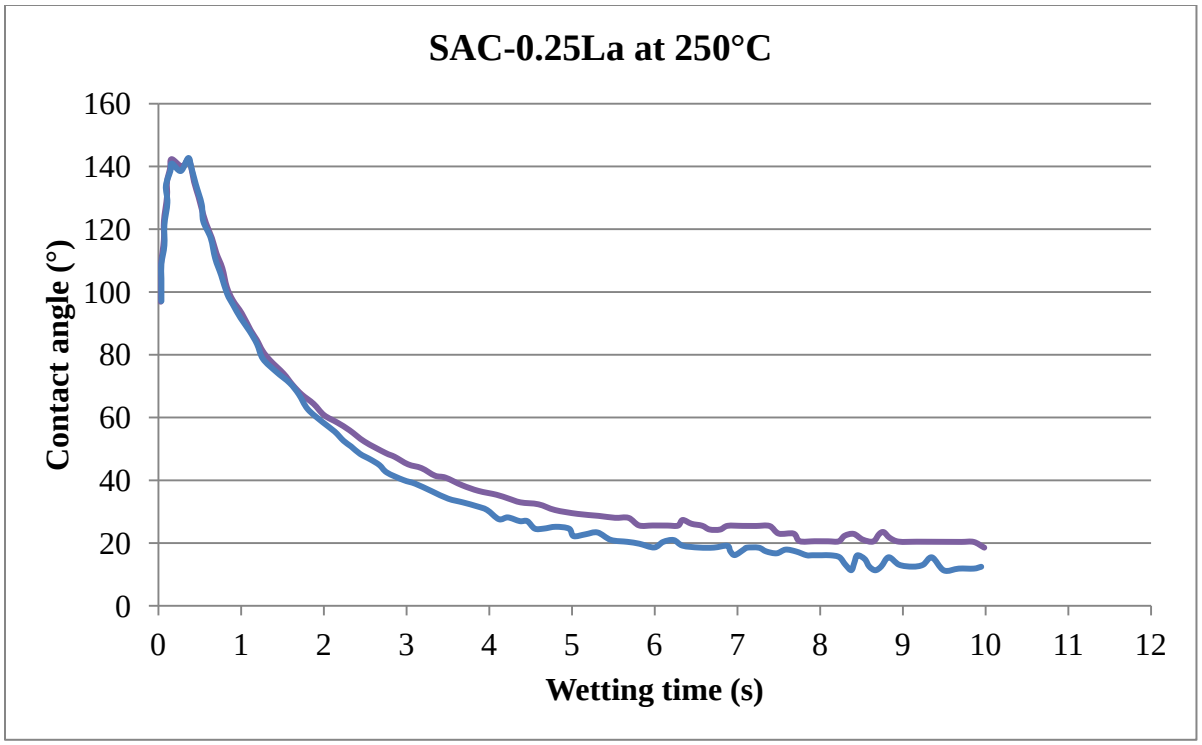

Figure 9.24: SAC-0.25La contact angle vs. wetting time at 250°C

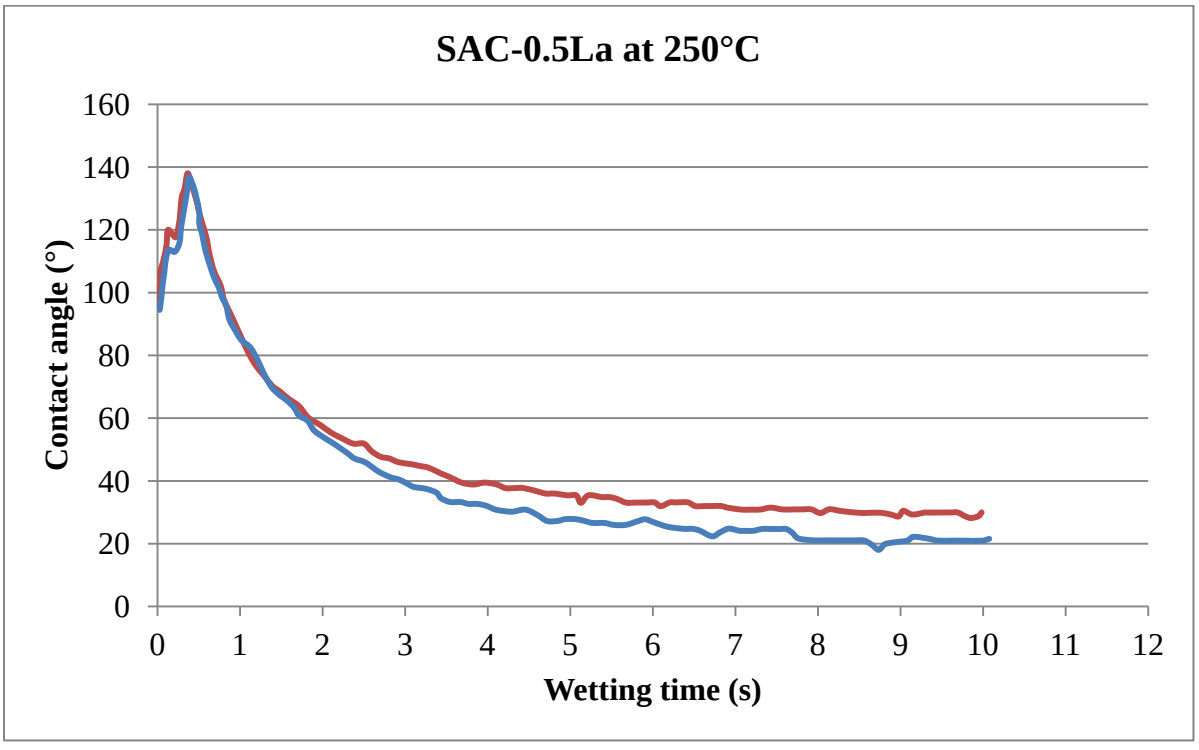

Figure 9.25: SAC-0.5La contact angle vs. wetting time at 250°C

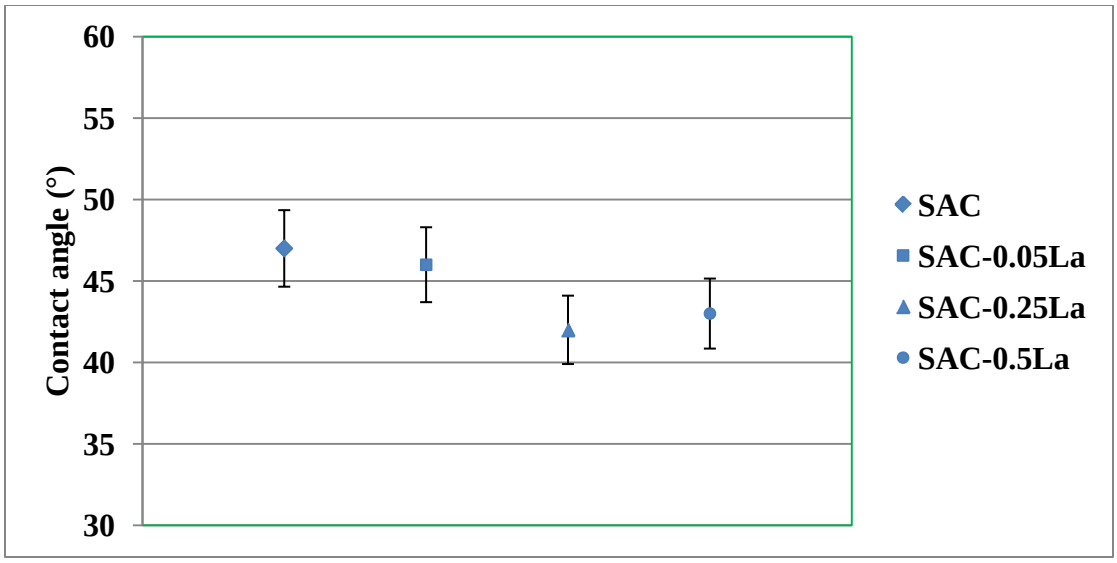

Figure 9.26: SAC and SAC-La contact angles at 250°C

9.7 Summary

Extensive work has been performed on the wettability testing of SAC and SAC-La doped alloys at 2 different temperatures of 250°C and 260°C. It was noticed that increasing temperatures make better wettability for the same composition. This is dedicated to the decreasing effects of surface tension at elevated temperatures.

For the SAC-La doped alloys, the surface tension decreased due to RE dopings at both 250°C and 260°C as compare to the SAC alloy. RE doping further increases the wetting forces from 5.7 mN (SAC) up to 6.7 mN (SAC-0.25La). SAC-0.5La has smaller wetting force than SAC-0.25La which means an optimization of RE elements is to be specified for better alloy compositions.

Wetting or contact angles measurements were made on the basis of the surface tensions already evaluated. An appreciable decrease in the contact angles was investigated and once again SAC-0.25La has a better (smaller) contact angle than SAC and SAC-0.5La alloys.

CHAPTER 10

SCIENTIFIC CONTRIBUTIONS, CONCLUSIONS AND FUTURE WORK

10.1 Scientific Contributions

This PhD thesis aims to investigate the impact of lanthanum doping on the microstructure evolution, bulk mechanical properties, creep behavior, individual phase mechanical properties and wettability of SAC and SAC-La doped alloys. The anticipated contribution is summarized as follows,

i. A detailed study for the novel lead-free solders with high melting point, fine microstructure, better mechanical properties and long creep life.

ii. Impact of thermal aging on the microstructure evolution of lanthanum doped SAC lead-free solders including IMCs coarsening rate, volume fraction, size, spacing, shape and grain size growth.

iii. Evaluation and evolution of mechanical properties like yield stress and tensile strength for as cast and thermally aged compositions in varying environmental conditions.

iv. Evaluation and evolution of Young's modulus, hardness, creep strain and strain rate sensitivity index for the SAC and SAC-La doped alloys for individual phases namely matrix, eutectic and β-Sn and IMCs using nanoindentation.

v. Exploring the creep behavior and studying the impact of lanthanum on the creep life of SAC and SAC-La doped solders with experiments and modeling.

vi. Exploring the wettability (or solderability) performance of lanthanum doped SAC alloys. Wetting balance test is used to measure the contact angle and wetting force. They are plotted against the lanthanum composition.

The goal is to provide an advanced experimental approach, supported by models, towards material-by-design of a novel lanthanum doped tin-based lead-free solder for the next generation of microelectronics applications in severe environment. This research would result in improving the solder joint reliability with an overall increase in the quality of electronics packaging.

10.2 Conclusions

In this thesis, quantitative microstructure study has been performed at various length scales to investigate the effects of La doping on SAC and SAC-La doped solder alloys. It is found that La doping (i) drastically reduces grain size, (ii) does not affect grain size coarsening, (iii) significantly reduces the Ag_3Sn and Cu_6Sn_5 particles size, (iv) does not change the inter-particle spacing, and (v) greatly reduces the particle coarsening rate.

Mechanical properties like yield stress, tensile strength and ductility of most of the materials are influenced by their microstructures.A fine microstructure is expected to provide good set of these properties. On the other hand, a coarse microstructure will provide smaller yield stress and tensile strength for the same alloys. The microstructure evolutions have been studied in detail. It was shown, both qualitatively and quantitatively, that the lanthanum doping refines the microstructure and controls, to a large extent, the formation of IMCs. Not only this, but lanthanum doping is also useful in controlling the growth of these IMCs at elevated temperatures during service.

Quasi uni-axial tensile tests are used at low strain rates of 2.10^{-4} s^{-1}, 2.10^{-3} s^{-1} and 2.10^{-2} s^{-1}. At least 3 samples are tested for every composition. The samples tested were both as-cast and thermally aged at 150°C for 100 hours and 200 hours.

Varying environmental conditions from -60°C up to 140°C are employed during testing. Engineering stress-strain curves are collected and true stress-strain curves are plotted later on. Offset 0.2% method is used to extract the yield stress for all compositions. Extensometers are used to collect the deformation (%) of the materials.

Good improvement in yield stress and tensile strength has been recorded. This is mainly due to the fine microstructure and controlled growth of the IMCs. A decrease in ductility is observed which may be due to hard particles of $LaSn_3$.

A wide range of experiments were conducted for the creep behavior. All three zones, primary, secondary and tertiary, were evaluated till the rupture of samples. A temperature of 120°C and a constant loading of 10Mpa, 14Mpa and 16Mpa were used during creep experiments. Activation energy measurements were carried out at 14Mpa and 120°C. Other important parameters to apply the Dorn and back-stress creep models were extracted from experiments. Good fitting for the models was observed with the experimental results.

Nanoindentation is used to provide the individual phase mechanical properties for SAC and SAC-La doped alloys. Different loadings that range from 100 μN to 5000 μN are used in this study. Young's modulus and hardness are plotted against varying loading rates (mN/min). These values are also provided against the indentation depth. Activation energy measurements are made at different temperatures. Creep strain rates are plotted against the dwell time. Special pile-up effects are incorporated that makes the results more reliable. Nanoindentation was also

applied at high temperatures to explore the "rate" behavior of SAC and SAC-La doped alloys using the hot dwell time technique.

Solderability or wettability is an important parameter to be evaluated in order to check the performance/behavior of solder alloys over the copper substrates. Different tests were performed to evaluate the surface tension at 2 different temperatures of 250°C and 260°C. The wetting forces and contact angles (or wetting angles) were also measured with significant improvements due to La doping.

10.3 Future Work

Lead-free solder alloys are used as multi-functional materials like mechanical support, current flow and thermal heat dissipation.Thus an alloy with a good set of these properties would be considered as the best substitute for the lead base alloy. Solder joints being the most critical points of the printed circuit boards (PCBs) when electronics assemblies are subjected to different environments. These conditions could be high cycle fatigue or elevated temperatures or both in many cases. β-Sn in eutectic SAC solder exhibits anisotropy in its elastic and thermal expansion properties that may induce a significant amount of stress at Sn-grain boundaries during thermal cycling. Damage can initiate at boundaries with maximum induced normal/shear stress.Therefore, detailed investigation of failure in solder joints under thermal cycling is required for the reliability concern of microelectronics devices.

In pipelines industries, the electronics are subjected to high temperatures for several years. Any early failure can be catastrophe and may cause high cost and delay the process. This high temperature is termed as "hot dwell time". Thus a longer "hot dwell time" study is important and should be fitted with some sort of reliability models for the variety of applications.

At present, life acceleration factors for SAC alloys between accelerated tests and field use conditions are not well understood. Further, the cycle time for accelerated testing of lead-free solders is currently an industry concern since the rate of damage accumulation due to thermomechanical loading in lead-free solders is different from the eutectic Sn-Pb solders. Thus a detailed research study is required to develop an understanding of the acceleration factors through a combination of temperature cycling tests, power cycling tests and validated damage modelling. Thermo-mechanical fatigue is also an important property to be investigated as a future work for the solder joints and its components, as solder joints are exposed to excessive mechanical shocks during service.

The current study has explored many directions towards lanthanum performance as elemental form, $LaSn_3$ IMCs and surface active element. Before industrialization of the RE doped alloys, different concerns related to cost, availability and environmental issues need to be resolved.

In the current work, Dorn creep models are used with fitting parameters to the experimental data. In some cases, the IMCs play an important role in developing the back stress mechanisms to the dislocations movements. This stress is calculated for the back-stress models. Microstructural parameters like IMCs size, spacing and volume fraction are incorporated into these models. However, more sphisticated back-stress models are necessary for in-depth analysis.

In the current work, copper substrates are used for the wettability testing. More substrates need to be used and different fluxes should be applied with the wettability testing to cover much broader area of electronics packaging

APPENDIX A

SUMMARIZED DATA OF Sn CYSTAL

Sn has the tetragonal crystal structure with X = Y = 5.8318Å and Z = 3.1819Å [webelements 2006]. Figure A.1 is provided for the crystal structure rendered with (VMD) Visual Molecular Dynamics [Humphrey et al. 1996]. The atoms are shown as yellow spheres, and the bonds between them are shown with dynamic bound method with cut off distance of 2.3 Å.

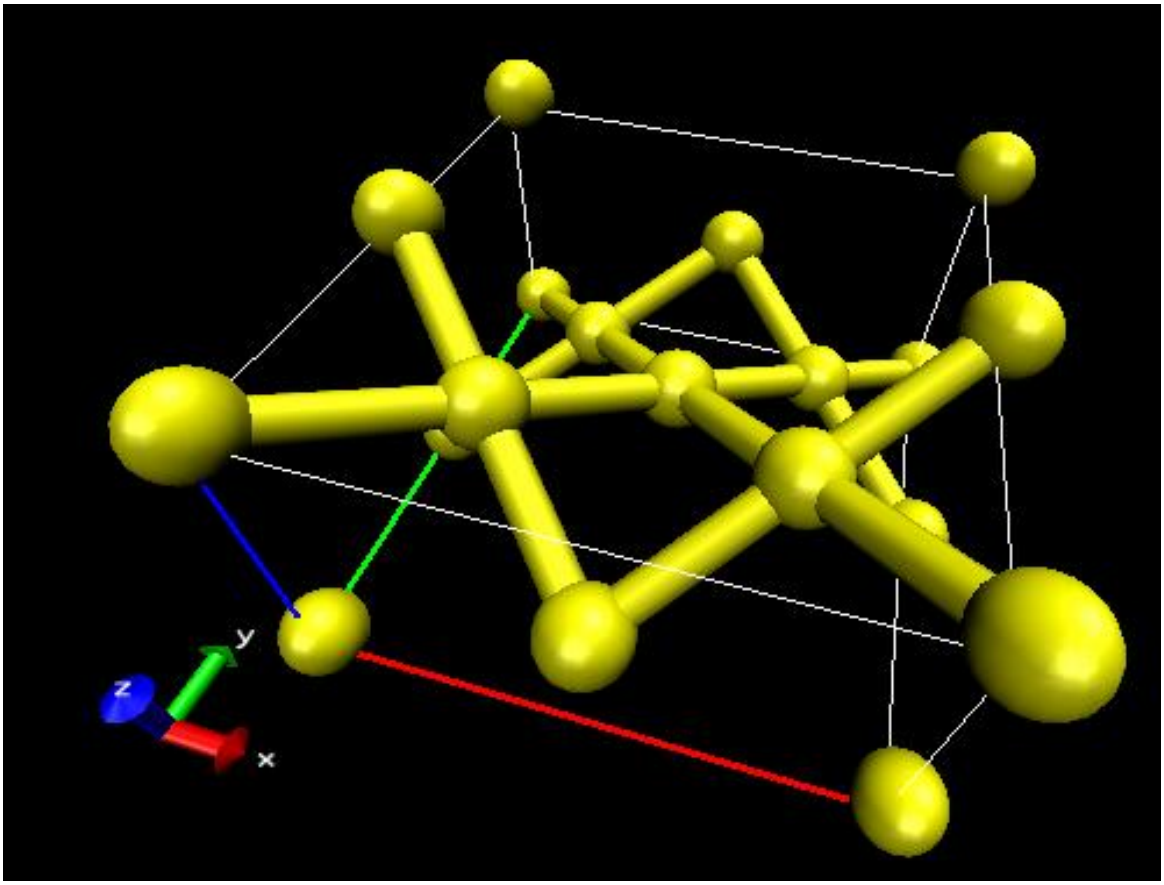

Figure A.1: Crystal structure for Sn

Table A.1: Thermal and mechanical properties of single-crystal Sn [Humphrey et al. 1996]

Direction	Coefficient of Thermal Expansion: CTE (ppm/°C)	Young's modulus (GPa)	Hardness (GPa)
X, Y	15.4	85	0.98
Z	30.5	54	

Table A.2: Calculated CTE and Young's modulus [Humphrey et al. 1996]

Direction	<100>	<101>	<103>	<001>	<113>	<112>	<111>	<110>
CTE (ppm/°C)	15.4	18.9	26.4	30.5	24.2	21.1	20.5	15.4
Young's modulus (GPa)	54.1	48.1	55.8	84.7	42.3	14.8	25.5	26.3

The elastic stiffness matrix for Sn at 300K [Lee et al. 2002]

$$C_{Sn} = \begin{bmatrix} 72.30 & 59.40 & 35.78 & 0 & 0 & 0 \\ 59.40 & 72.30 & 35.78 & 0 & 0 & 0 \\ 35.78 & 35.78 & 88.40 & 0 & 0 & 0 \\ 0 & 0 & 0 & 22.03 & 0 & 0 \\ 0 & 0 & 0 & 0 & 22.03 & 0 \\ 0 & 0 & 0 & 0 & 0 & 22.03 \end{bmatrix} \times 10^3 \text{MPa}$$

Silver (Ag) and copper (Cu) have the Face-Centered Cubic (FCC) crystal structure as shown in Figure A.2.

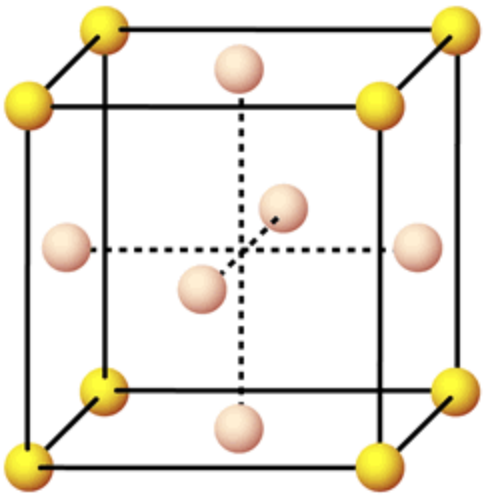

Figure A.2: FCC crystal structure for Silver (Ag) and Copper (Cu)

Lanthanum (La) has hexagonal crystal structure given in Figure A.3.

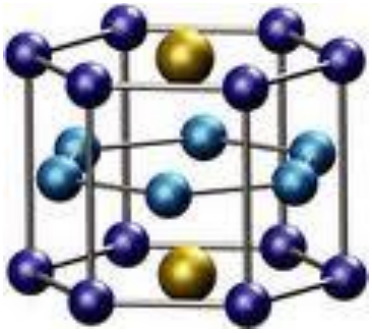

Figure A.3: Hexagonal crystal structure for Lanthanum (La)

Ag_3Sn has the orthorhombic crystal structure, where in crystallography the **orthorhombic** crystal system is one of the seven lattice point groups. Orthorhombic lattices result from stretching a cubic lattice along two of its orthogonal pairs by two different factors, resulting in a rectangular prism with a rectangular base (*a* by *b*) and height (*c*), such that *a*, *b*, and *c* are distinct. All three bases intersect at 90° angles. The three lattice vectors remain mutually orthogonal. **Cu_6Sn_5** has the **hexagonal** crystal structure.

APPENDIX B

PHASE DIAGRAMS

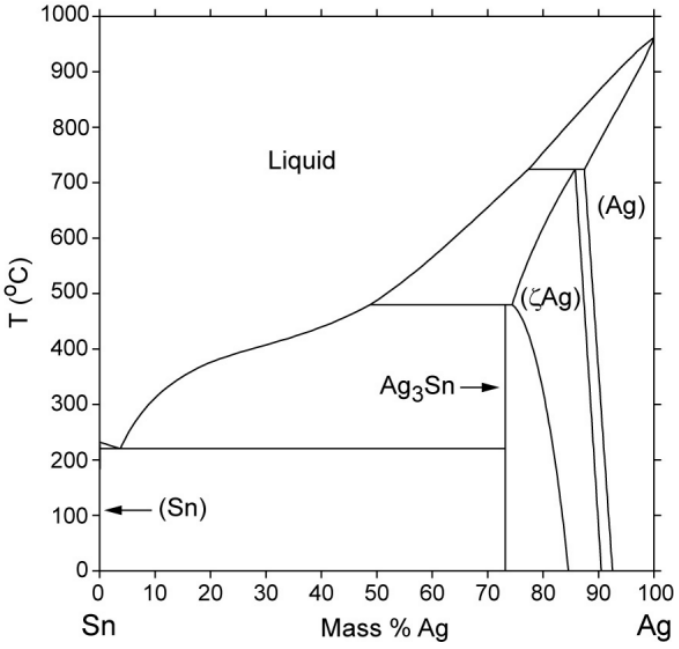

Figure B.1: Phase Diagram for Sn-Ag

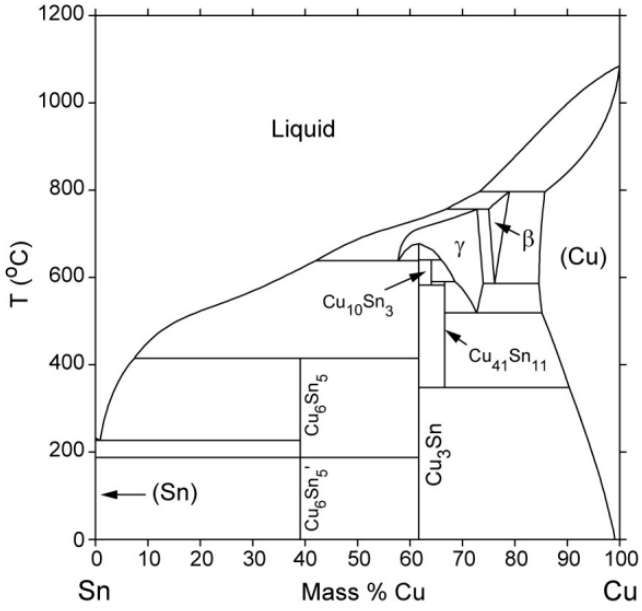

Figure B.2: Phase Diagram for Sn-Cu

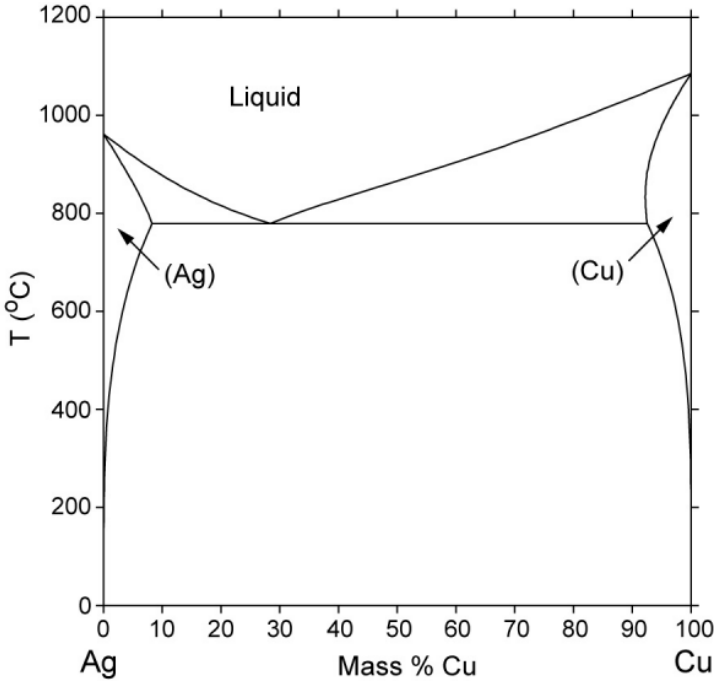

Figure B.3: Phase Diagram for Ag-Cu

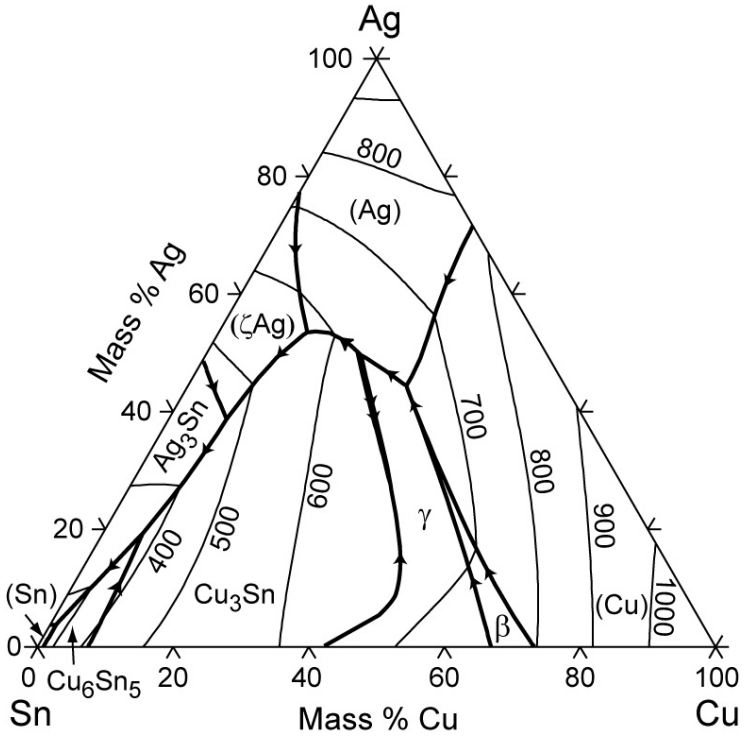

Figure B.4: Phase Diagram for Sn-Ag-Cu

APPENDIX C

MELTING BEHAVIOR

It is important to analyze the impact of lanthanum doping on the melting point of SAC and SAC-La doped alloys. DSC curves are used for this study. At least 3 tests are performed for each composition. The thermal profile used had 20°C and 300°C as two peaks with 5 minutes of hot dwell time and 5°C/min as heating/cooling rates.

About 2-3°C difference is identified between SAC and SAC-0.5La alloys thus concluding almost no impact of lanthanum doping on the melting points of SAC alloys. The results for SAC and SAC-0.5La are presented in Figures C.1 and C.2 respectively.

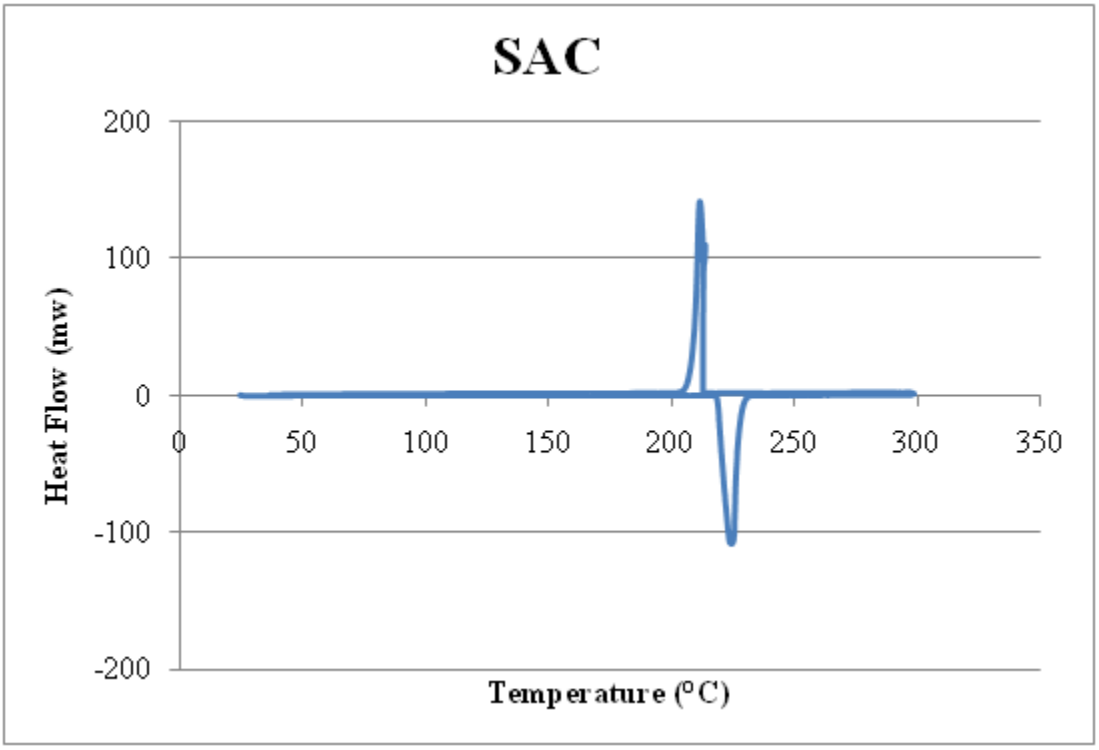

Figure C.1: SAC-0.05La DSC curve

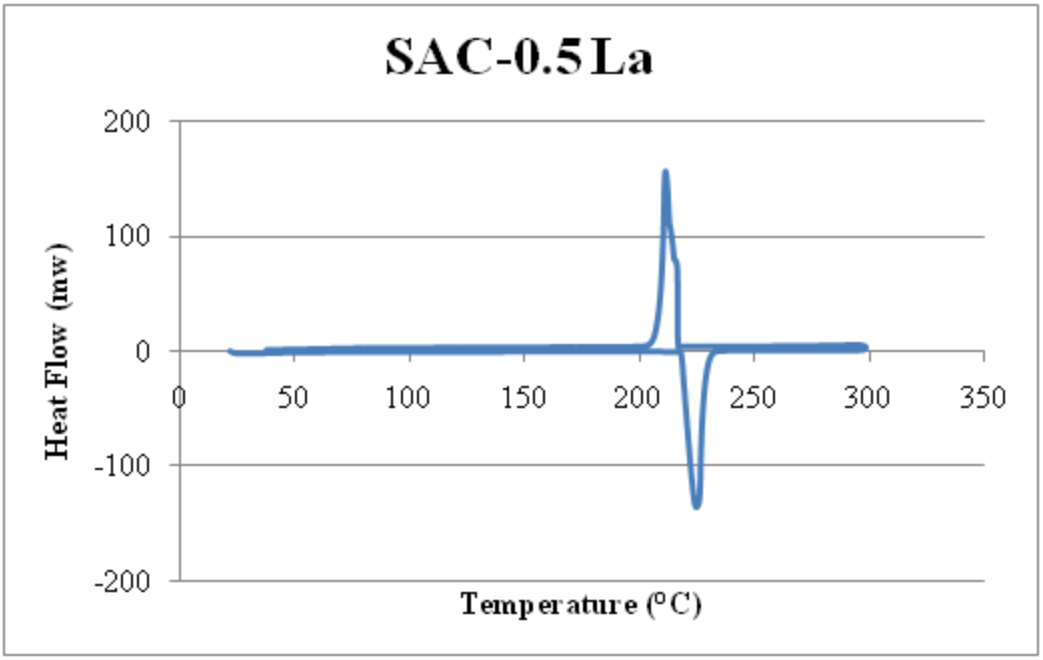

Figure C.2: SAC-0.5La DSC curve

APPENDIX D

GRAIN SIZE MEASUREMENTS

ASTM Committee E-4 and Grain Size Measurements

Metals, except in a few instances, are crystalline in nature and, except for single crystals; they contain internal boundaries known as grain boundaries. When a new grain is nucleated during processing (as in solidification or annealing after cold working), the atoms within each growing grain are lined up in a specific pattern that depends upon the crystal structure of the metal or alloy. With growth, each grain will eventually impinge on others and form an interface where the atomic orientations are different.

As early as the year 1900, it was well known that most mechanical properties were improved as the size of the grains decreased. A few notable exceptions exist where a coarse grain structure is desired. Alloy composition and processing must be controlled to achieve the desired grain size. Metallographers examine polished cross sections of specimens from appropriate locations to determine the grain size.

Complications--Grain Characteristics

Grain size measurement is complicated by a number of factors. First, the three-dimensional size of the grains is not constant and the sectioning plane will cut through the grains at random. Thus, on a cross-section we will observe a range of sizes, none larger than the cross

section of the largest grain sampled. Grain shape also varies, particularly as a function of grain size.

Grain size measurement is also complicated by the different types of grains that can be present in metals, although their fundamental shapes are the same. For example, in body-centered cubic metals, such as Fe, Mo, and Cr, we have ferrite grains; in face-centered cubic metals, such as Al, Ni, Cu, and certain stainless steels, we have austenite grains.

In heat-treated steels, it is recognized that the grain size of the product of the heat treatment, usually martensite, is not measured or cannot be measured. For low-carbon steel, the martensite forms in packets within the parent austenite grains. In high-carbon martensites, we do not observe any convenient structural shape that can be measured. In most cases, we try to measure the size of the parent austenite grains that were formed during the high temperature hold during the heat treatment. This is usually referred to as the "prior-austenite grain size" and it has been widely correlated to the properties of heat treated steels. The most difficult process here is the etching procedure needed to reveal these prior boundaries. Sometimes they cannot be revealed, particularly in low-carbon steels. In this case, it may be possible to measure the low-carbon lath martensite packet size, which is a function of the prior-austenite grain size.

Complications---Different Measures of Size

Another complicating factor is the different measures of grain size. The planimetric method, described below, yields the number of grains per square millimeter area, N_A, from which we can calculate the average grain area, A. It is common practice to take the square root of A and call this the grain diameter, *d*, although this assumes that the cross sectional shape of the

grains is a square, which it is not. The intercept method yields a mean intercept length, L_3 ; its relationship to N_A, A, or *d* is not exceptionally well defined. A variety of planar grain size distribution methods have also been developed to estimate the number of grains per unit volume, N_v, from which the average grain volume, V, can be calculated. The relationship between these spatial measures of grain size and the above planar measures is also ill-defined.

It is now common to express grain sizes in terms of a simple exponential equation:

$$\mathbf{n = 2^{G-1}}$$

where:

n = the number of grains per square inch at 100X magnification, and

G = the ASTM grain size number.

This approach was developed and introduced in 1951 with the premiere of ASTM standard E 91, Methods for Estimating the Average Grain Size of Non-Ferrous Metals, Other Than Copper and Their Alloys. Although the N_A, *d*, or L_3, values had been used for many years as measures of grain size, the G values were adopted readily due to their simplicity. As shown in Eq. 1, we can directly relate the number of grains per unit area to G, but the relationship between L_3, and G, or N_V and G are not as clearly defined. This problem is one of many being addressed by ASTM Committee E4 on Metallography.

Measurement Methods

Although Committee E-4 was formed in 1916 for the express purpose of establishing standard magnifications for micrographs, its first standard, E 2-17T, Methods of Preparation of

Micrographs of Metals and Alloys, was partly devoted to grain size measurement. Two basic approaches to measure grain size were being developed at that time. In the United States in 1894, Albert Sauveur published a "planimetric" approach, which was further developed by Zay Jeffries with two 1916 publications. This approach measured grain size in terms of the number of grains visible on a cross section within a fixed area, the number per square inch at 100X, or the number per square millimetre at 1X, N_A. From this value, the average cross-sectional area of the bisected grains can be computed. This is not an average of the maximum cross-sectional area of each grain because the sectioning plane does not intersect each grain at its maximum width.

Many grain size raters expressed the need for simpler ways to estimate the grain size. In some cases, such as heat clearance, grain size measurement is required. In many cases, it is required that G be 5 or greater (i.e., "fine- grained"). Hence, if the grain size is substantially finer than this, a quick method, which may not be as precise as an actual measurement, is adequate. A comparison chart method with examples of grain sizes meets this need adequately, as long as the grain size distribution is normal. Additionally, the specimens should be etched in the same manner as depicted on the chart. If the grain size is near the specification limit, an actual measurement is preferred due to the improved precision. The first grain size comparison chart was introduced in Methods E 2 in its 1930 revision; this chart was for copper.

Note that these methods are applied on the polished surface of the specimen, that is, on a plane that cuts through the three-dimensional grains. Thus, these are planar rather than spatial measures of the grain size. The planimetric, or Jeffries method, defines the grain size in terms of the number of grains per unit area, the average grain area, or the average grain diameter, while the Heyn intercept method defines it in terms of the average intercept length. The comparison

chart method expresses the grain size only in terms of G, except for the copper charts, which use *d*.

International Method

Committee E-4's work on grain size has been followed closely by other industrial countries and the International Organization for Standardization (ISO). Many countries have adopted one or more of the grain size charts of ASTM Test Methods E 112. Some countries have also developed very useful charts. For example, for rating McQuaid-Ehn carburized specimens, most U.S. raters etch the pearlitic matrix dark as depicted in Plate IV of Test Methods E 112. As the sidebar on grain structures demonstrates, it is easier to see the intergranular carbide phase if we use an etchant that darkens the grain boundary cementite. The French grain size standard, NF A04-102, contains a rating chart where the grain boundary cementite was darkened with alkaline sodium picrate. The German SEP 1510 grain size standard also contains a very useful chart. It illustrates non-twinned grains (such as ferrite grains) that are equiaxed or deformed (elongated 2 to 1 and 4 to 1) by cold working. Eq. 1 described the approach used to compute ASTM grain size numbers which, de- veloped in the United States in the late 1940s, was based on English units rather than metric units. Countries that used the metric system at that time developed an alternate equation that produces nearly identical grain size numbers:

$$\mathbf{m = 8(2^{Gm})}$$

where:

m = the number of grains per mm^2 at 1 X, and

G_m = the metric grain size number.

G_m is slightly greater than G but the difference is negligible. Eq. 2 is used in the Swedish (SIS 11 11 01), Italian (UNI 3245), Russian (GOST 5639), French (NF A04-102), and ISO (ISO 643) standards.

The German standard (SEP 15l0) also uses the metric system, but a different equation is employed;

K= 3.7 + 3.33 Log(Z)

where:

K = the photomicrograph serial number (same as G), and

Z = the number of grains per cm^2 at 1OOX.

In this case, K equals G. Japanese standards JIS G 0551 and G 0552 also use the metric system, with a slightly different equation than Eq. 2 (but equivalent) that produces the same values as Eq. 2: (Equation 4)

$$\mathbf{m = 2^{(G_{m+3})}}$$

where m and G_m are defined as before.

APPENDIX E

ELECTRICAL RESISTIVITY

http://www.chipscalereview.com/issues/ES/issues/0998/m.abtewb1.htm

Resistivity is one of the fundamental electrical properties of solder. For most electronics applications, the resistivity of solder is relatively low and its effect on the overall functionality of the circuit is insignificant. Resistivity varies with temperature, composition and microstructure of a given alloy. Metals that are pure with ordered crystal structure of a large grain size have low resistivity at low temperature. Generally, alloys have higher resistance that typically peaks when the elements present are in roughly equal fractions. Because of the dependence of resistivity on microstructure, grain size, dislocation density, etc., measured values differ significantly among both pure metals and alloys of the same composition. Room temperature resistivity values for common solders and packaging materials used for microelectronics applications are shown in Table E.1.

Table E.1: Room Temperature Resistivity Values for Some Pb-Solders Microelectronics Packaging Materials [(Dumoullin 1981)].

Material	**Resistivity (μΩ-cm)**	**Material**	**Resitivity (μΩ-cm)**
63Sn-37Pb	10, 14.4, 15	52Ni-48Fe	43.2
96.5Sn-3.5Ag	10, 12.3	42Ni-58Fe	57
58Bi-42Sn	30, 34.4, 34	Cu-0.6Fe-0.05Mg-	2.65
48Sn-52In	14.7, 30	Cu	1.73
Ag	1.59		
Bi	115		
Sn	10.1		

Electrical resistivity for SAC, SAC-0.25La and SAC0.5La are presented in Figures E.1-E.10 for both as cast and thermally aged specimens. They were calculated using the equipments given in Chapter 3 (Experimental Design).

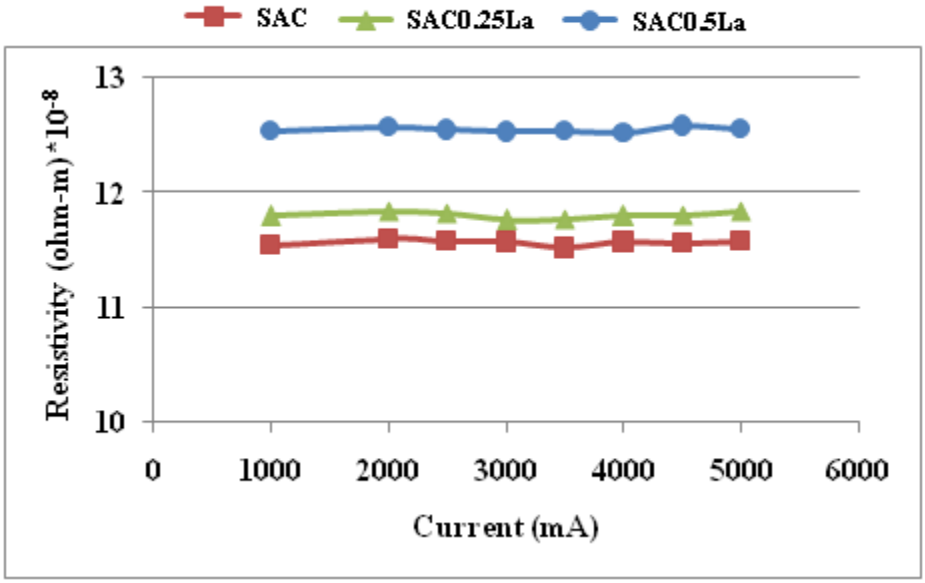

Figure E.1: Electrical resistivity after 10 hours aging at 150°C

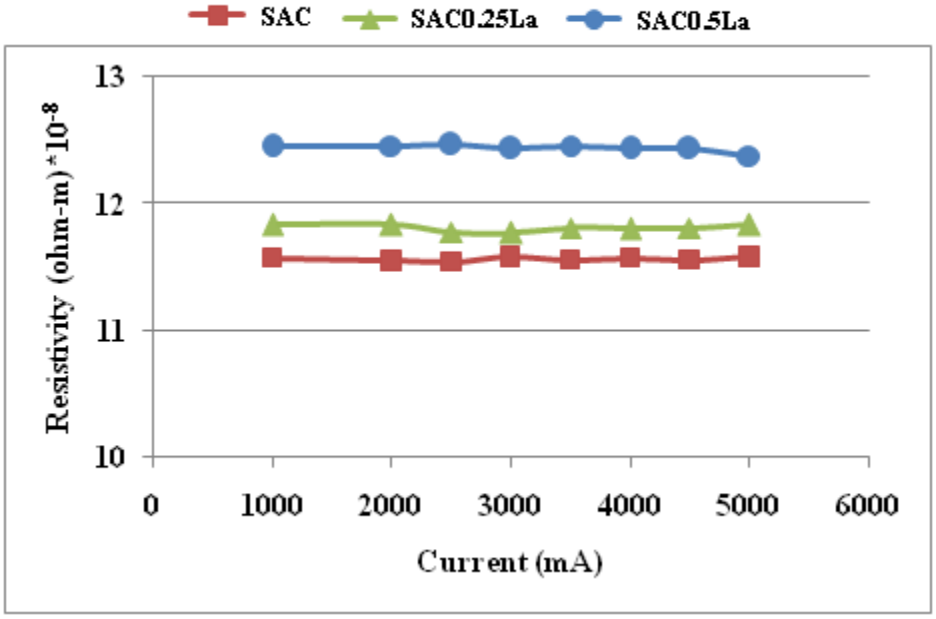

Figure E.2: Electrical resistivity after 25 hours aging at 150°C

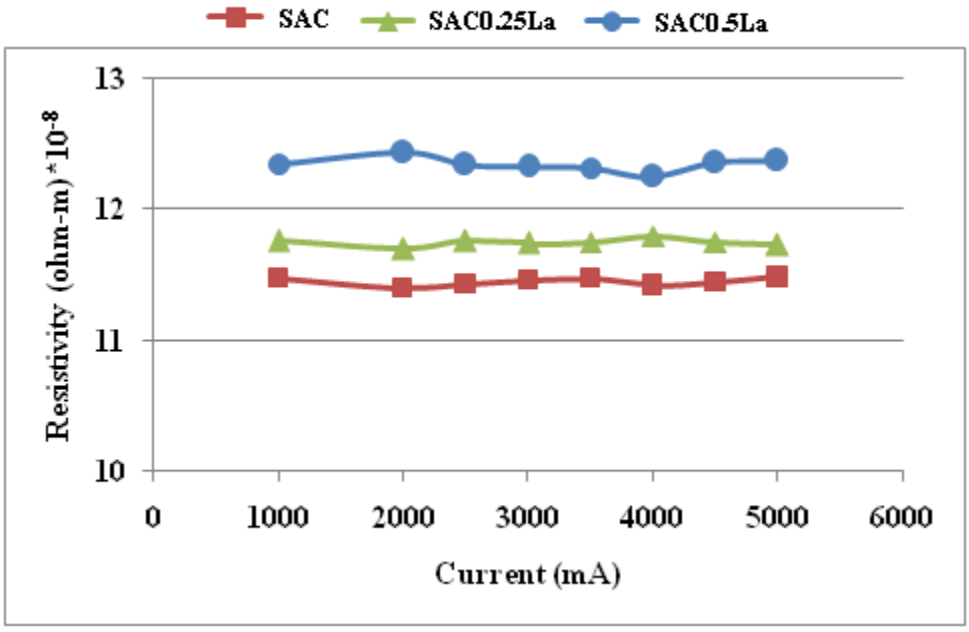

Figure E.3: Electrical resistivity after 50 hours aging at 150°C

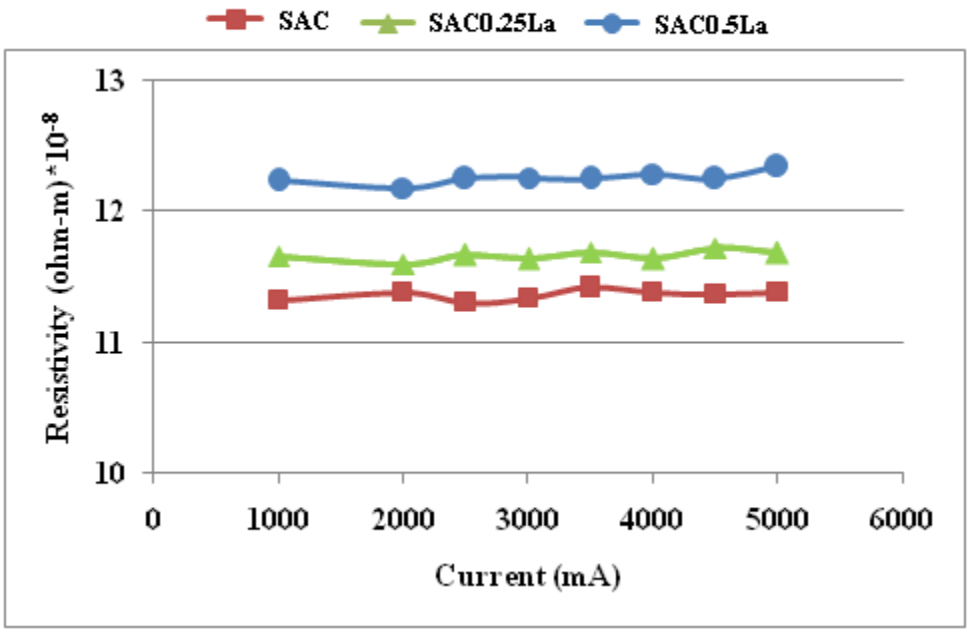

Figure E.4: Electrical resistivity after 100 hours aging at 150°C

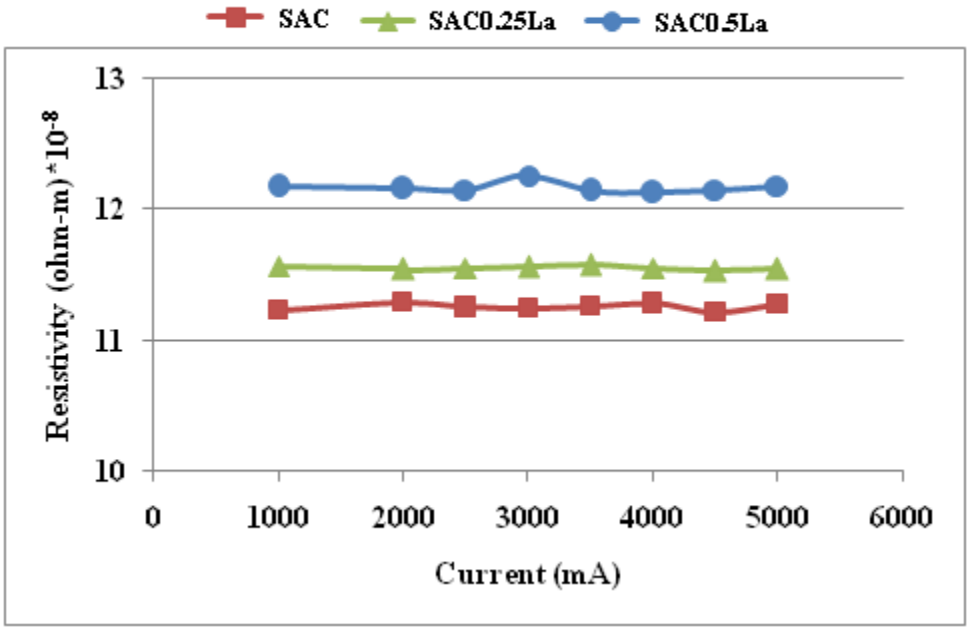

Figure E.5: Electrical resistivity after 200 hours aging at 150°C

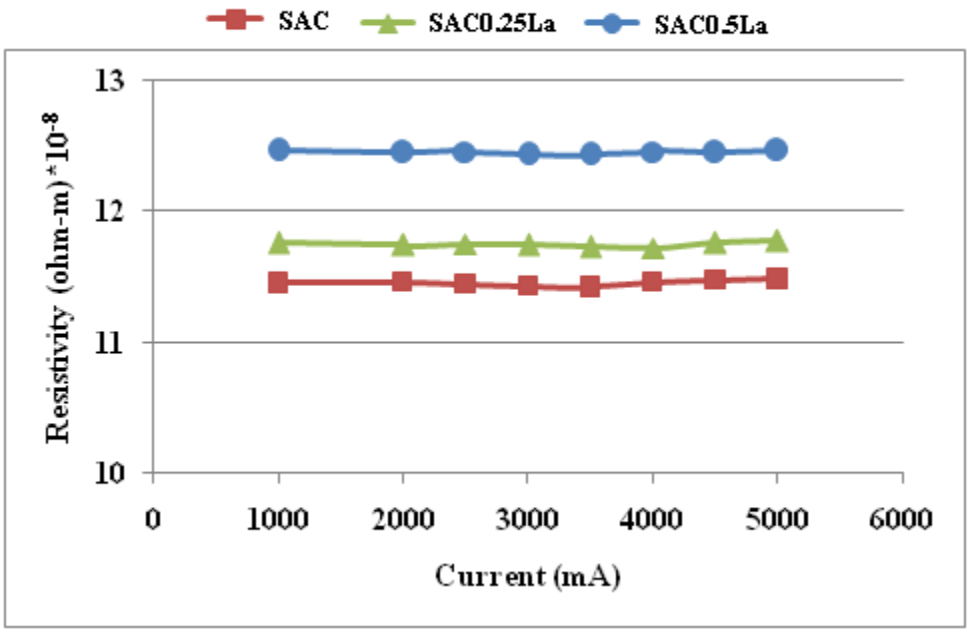

Figure E.6: Electrical resistivity after 10 hours aging at 200°C

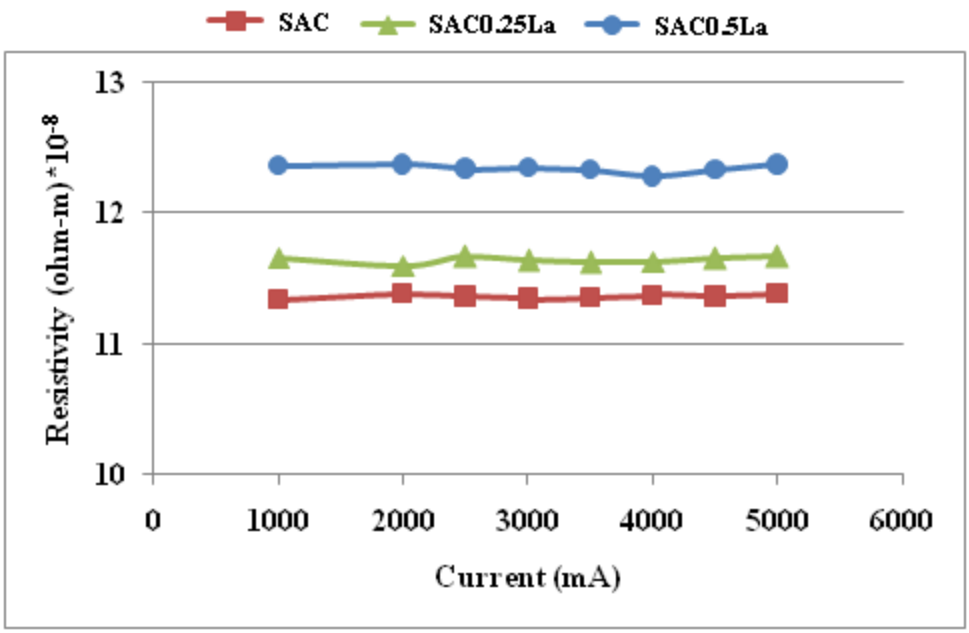

Figure E.7: Electrical resistivity after 25 hours aging at 200°C

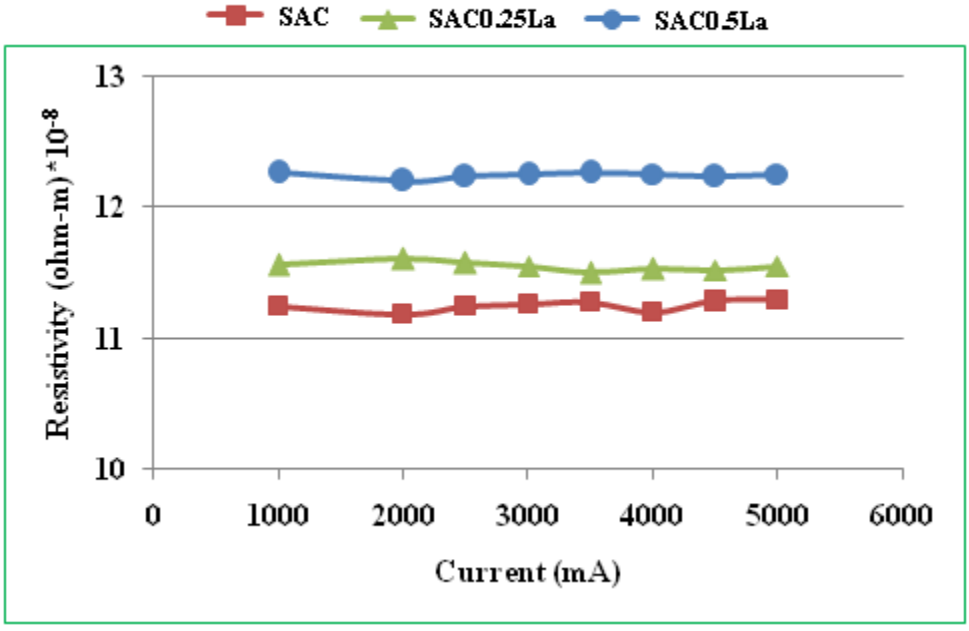

Figure E.8: Electrical resistivity after 50 hours aging at 200°C

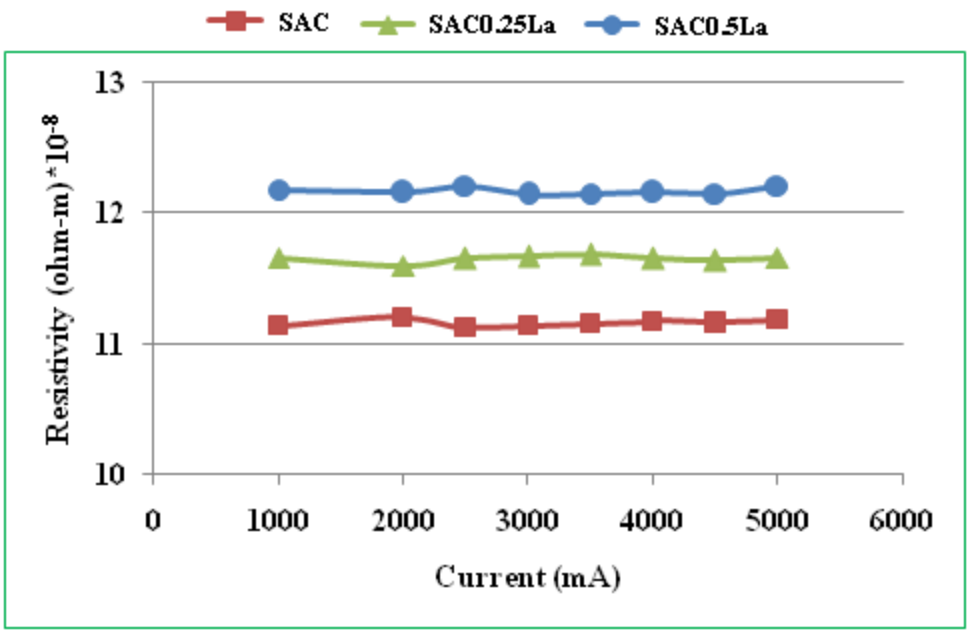

Figure E.9: Electrical resistivity after 100 hours aging at 200°C

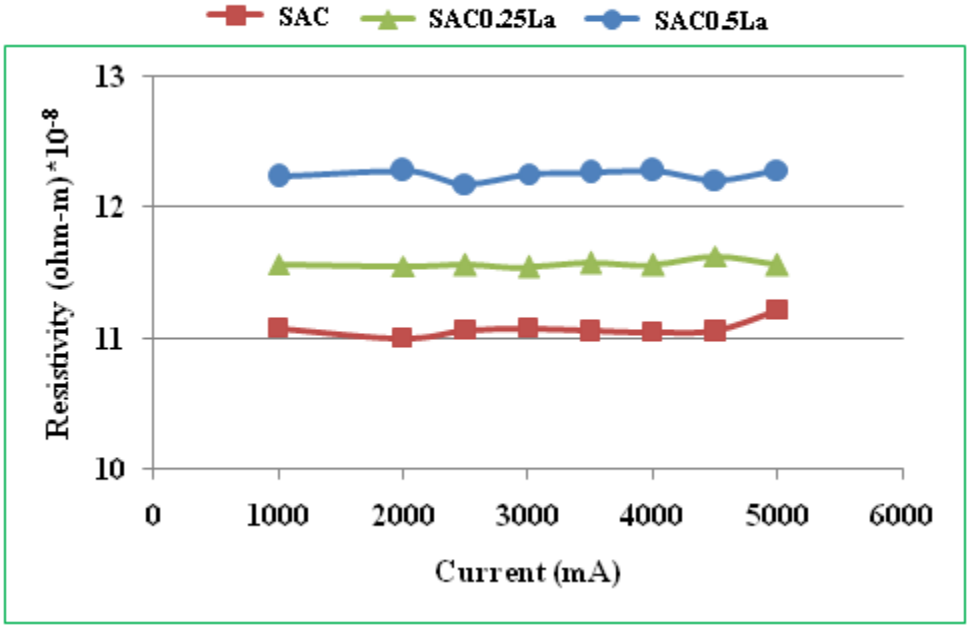

Figure E.10: Electrical resistivity after 200 hours aging at 200°C

REFERENCES

Abtew, M. & Selvaduray, G., 2000. Lead-free solders in microelectronics. *Materials Science and Engineering: R: Reports*, 27(5-6), p.95–141.

Allen, G.L., 1986. Small particle melting of pure metals. *Condensed Matter Physics*, 144(2), p.297–308.

Allen, S.L., Notis, M.R., Chromik, R.R. & Vinci, R.P., 2004. Microstructural evolution in lead-free solder alloys: Part I. Cast Sn–Ag–Cu eutectic. *Journal of materials research*, 19(05), p.1417–1424.

Allen, S.L., Notis, M.R., Chromik, R.R., Vinci, R.P., et al., 2004. Microstructural evolution in lead-free solder alloys: Part II. Directionally solidified Sn-Ag-Cu, Sn-Cu and Sn-Ag. *Journal of materials research*, 19(5), p.1425–1431.

Anderson, I. et al., 2001. Alloying effects in near-eutectic Sn-Ag-Cu solder alloys for improved microstructural stability. *Journal of electronic materials*, 30(9), p.1050–1059.

Baker, H. & Okamoto, H., 1992. ASM Handbook. Vol. 3. Alloy Phase Diagrams. *ASM International, Materials Park, Ohio 44073-0002, USA, 1992. 501*.

Bartelo, J. et al., 2001. Thermomechanical fatigue behavior of selected lead-free solders. Dans *Proceedings, IPC SMEMA Council APEX*.

Bolshakov, A. & Pharr, G., 1998. Influences of pileup on the measurement of mechanical properties by load and depth sensing indentation techniques. *Journal of materials research*, 13(04), p.1049–1058.

Buffat, P. & Borel, J.-P., 1976. Size effect on the melting temperature of gold particles. *Physical Review A*, 13(6), p.2287–2298.

C.M.T. Law et al., 2003. Dans Proceedings of the Materials Science & Technology 2003 Conf.

Cai, Z. et al., 2010. Reduction of lead free solder aging effects using doped SAC alloys. Dans *Electronic Components and Technology Conference (ECTC), 2010 Proceedings 60th*. p. 1493–1511.

Callister, 1985. *Materials Science and Engineering: An Introduction*, Wiley, New York.

Carabello, C.M., Lead-Free solder, New Methodology and Perception.

Chen, M.H., 2003. *Study of Adding Sb into Lead-free Sn-Ag Solder Joints on Metallurgical and Mechanical Properties*.

Chen, T. & Dutta, I., 2008. Effect of Ag and Cu concentrations on the creep behavior of Sn-based solders. *Journal of Electronic Materials*, 37(3), p.347–354.

Chen, Z. et al., 2003. Properties of lead-free solder SnAgCu containing minute amounts of rare earth. *Journal of electronic materials*, 32(4), p.235–243.

Chen, ZG et al., 2002. Study on the microstructure of a novel lead-free solder alloy SnAgCu-RE and its soldered joints. *Journal of electronic materials*, 31(10), p.1122–1128.

Chen, Zhigang, Shi, Y. & Xia, Zhidong, 2004. Constitutive relations on creep for SnAgCuRE lead-free solder joints. *Journal of Electronic Materials*, 33(9), p.964–971.

Cheng, Y.T. & Cheng, C.M., 2004. Scaling, dimensional analysis, and indentation measurements. *Materials Science and Engineering: R: Reports*, 44(4-5), p.91–149.

Choi, S. et al., 1999. Characterization of the growth of intermetallic interfacial layers of Sn-Ag and Sn-Pb eutectic solders and their composite solders on Cu substrate during isothermal long-term aging. *Journal of Electronic Materials*, 28(11), p.1209–1215.

Chollacoop, Dao, M. & Suresh, S., 2003. Depth-sensing instrumented indentation with dual sharp indenters. *Acta Materialia*, 51(13), p.3713–3729.

Chromik et al., 2003. Nanoindentation measurements on Cu–Sn and Ag–Sn intermetallics formed in Pb-free solder joints. *Journal of Materials Research*, 18, p.2251–2261.

Clech, J.P., 2005. Acceleration factors and thermal cycling test efficiency for lead-free Sn-Ag-Cu assemblies. Dans *Proceedings, SMTA international conference, Chicago, IL*. p. 902–917.

Dao, M. et al., 2001. Computational modeling of the forward and reverse problems in instrumented sharp indentation. *Acta Materialia*, 49(19), p.3899–3918.

Deng, X. et al., 2004. Deformation behavior of (Cu, Ag)-Sn intermetallics by nanoindentation. *Acta materialia*, 52(14), p.4291–4303.

Dieter, G.E., 1986. *Mechanical Metallurgy (New York: McGraw-Hill)*,

Dudek, M., Sidhu, R. & Chawla, N., 2006. Novel rare-earth-containing lead-free solders with enhanced ductility. *JOM Journal of the Minerals, Metals and Materials Society*, 58(6), p.57–62.

Dumoullin, J.L., 1981. Oxidation Behavior of solders. *Surface Science*, 104, p.559–568.

Dutta et al., 2004. Impression creep characterization of rapidly cooled Sn- 3.5Ag solders. *Materials Science and Engineering A*, 379, p.401–410.

Dutta, I., 2003. A constitutive model for creep of lead-free solders undergoing strain-enhanced microstructural coarsening: A first report. *Journal of Electronic Materials*, 32(4), p.201–207.

Elmustafa, A.A. & Stone, D.S., 2002. Indentation size effect in polycrystalline F.C.C. metals. *Acta Materialia*, 50(14), p.3641–3650.

Fields, R. & Low, S., 1991. Physical and mechanical properties of intermetallic compounds commonly found in solder joints. *The Metal Science of Joining*, p.165–174.

Fu et al. 2009. Lead-free Solders with Rare Earth Additions. *Lead-free solders Research summary***,** 61(6), p.39-44

Gao, F. et al., 2009. Mechanical properties versus temperature relation of individual phases in Sn-3.0 Ag-0.5 Cu lead-free solder alloy. *Microelectronics Reliability*, 49(3), p.296–302.

Gao, F. & Takemoto, T., 2006. Mechanical properties evolution of Sn-3.5 Ag based lead-free solders by nanoindentation. *Materials Letters*, 60(19), p.2315–2318.

Gebarhardt et al., 1959. The Constitution of the System Ag-Cu-Sn. *Journal of Metallurgy*, 50, p.597–605.

Gibson et al., 1997. Issues regarding microstructural coarsening due to aging of eutectic tin-silver solder. *TMS Annual Meeting, Design Reliability of Solders and Solder Interconnections*, p.97–103.

Goldstein, A.N., 1992. melting in semiconductor nanocrystals. *Science New Stories*, 256(5062), p.1425–1427.

Han Y. D. et al., 2009. A modified constitutive model for creep of Sn–3.5Ag–0.7Cu solder joints. *Journal of Physics D: Applied Physics*, 42(12), p.1–8.

Hao, H. et al., 2008. Microstructure evolution of SnAgCuEr lead-free solders under high temperature aging. *Journal of Electronic Materials*, 37(1), p.2–8.

Henderson, D.W. et al., 2002. Ag3Sn plate formation in the solidification of near ternary eutectic Sn–Ag–Cu alloys. *Journal of Materials Research*, 17(11), p.2775–2778.

Henshall, G.A. & Miller, A.K., 1990. Simplifications and improvements in unified constitutive equations for creep and plasticity—I. Equations development. *Acta Metallurgica et Materialia*, 38(11), p.2101-2115.

Hertzberg, R.W., 1996. *Deformation and fracture mechanics of engineering materials*, Wiley.

Huang, M., Wang, L. & Wu, C., 2002. Creep behavior of eutectic Sn-Ag lead-free solder alloy. *Journal of Materials Research(USA)*, 17(11), p.2897–2903.

Humphrey, W., Dalke, A. & Schulten, K., 1996. VMD: visual molecular dynamics. *Journal of Molecular Graphics*, 14(1), p.33–38, 27–28.

Igoshev, V. et al., 2000. Fracture of Sn-3.5% Ag solder alloy under creep. *Journal of electronic materials*, 29(12), p.1356–1361.

Igoshev, V. et al., 1998. Microstructure changes in Sn-3.5 Ag solder alloy during creep. *Journal of electronic materials*, 27(12), p.1367–1371.

Igoshev, V. & Kleiman, J., 2000. Creep phenomena in lead-free solders. *Journal of electronic materials*, 29(2), p.244–250.

Jin, S., 2003. Rare-earth-enabled universal solders for microelectromechanical systems and optical packaging. *Journal of electronic materials*, 32(12), p.1366–1370.

Kanchanomai, C. et al., 2002. Low cycle fatigue test for solders using non-contact digital image measurement system. *International Journal of Fatigue*, 24(1), p.57–67.

Kang, S.K. et al., 2003. Formation of AgSn plates in Sn-Ag-Cu alloys and optimization of their alloy composition. Dans *Electronic Components and Technology Conference, 2003. Proceedings. 53rd*. p. 64–70.

Kerr, M. & Chawla, N., 2004. Creep deformation behavior of Sn–3.5Ag solder/Cu couple at small length scales. *Acta Materialia*, 52(15), p.4527-4535.

Kim, K., Huh, S. & Suganuma, K., 2002. Effects of cooling speed on microstructure and tensile properties of Sn–Ag–Cu alloys. *Materials Science and Engineering: A*, 333(1), p.106–114.

Korhonen et al., 2004. Mechanical properties of near-eutectic Sn-Ag-Cu alloy over a wide range of temperatures and strain rates. *Journal of Electronic Materials*, 33(12), p.1581–1588.

Lee, J.G., 2002. modeling thermomechanical fatigue behavior of sn-ag solder joints, journal of electronic materials. *Journal of Electronic Materials*, 31(11), p.1152–1159.

Lewis, D. et al., 2002. Determination of the eutectic structure in the Ag-Cu-Sn system. *Journal of electronic materials*, 31(2), p.161–167.

Lifshitz, The Kinetics of Precipitation from Supersaturated Solid Solutions. *Journal of Physics and Chemistry of Solids*, 19, p.35–50.

Loomans, M. & Fine, M., 2000. Tin-silver-copper eutectic temperature and composition. *Metallurgical and Materials Transactions A*, 31(4), p.1155–1162.

Luhua Xu and John H.L. Pang, 2006. Nanoindentation on SnAgCu Lead-Free Solder Joints and Analysis. *Journal of Electronic Materials*, 35(12), p.2107–2115.

Ma, X., Qian, Y. & Yoshida, F., 2002. Effect of La on the Cu-Sn intermetallic compound (IMC) growth and solder joint reliability. *Journal of alloys and compounds*, 334(1-2), p.224–227.

Martin, 2006. Martin a. rist, w. j. plumbridge, s. cooper, " Creep-constitutive behavior of sn-3.8ag-0.7cu solder using an internal stress approach ", *Journal of Electronic Materials* vol. 35, no. 5 (2006)

Mavoori, H., Ramirez, A.G. & Jin, S., 2002. Lead-free universal solders for optical and electronic devices. *Journal of electronic materials*, 31(11), p.1160–1165.

Mayama, T., Sasaki, K. & Ishikawa, H., 2007. A constitutive model of cyclic viscoplasticity considering changes in subsequent viscoplastic deformation due to the evolution of dislocation structures. *International Journal of Plasticity*, 23(5), p.915-930.

Mayo, M. et al., 1992. Nanoindentation of nanocrystalline ZnO. *Journal of materials research*, 7(04), p.973–979.

Mayo, M. & Nix, W., 1988. A micro-indentation study of superplasticity in Pb, Sn, and Sn-38 wt% Pb. *Acta Metallurgica*, 36(8), p.2183–2192.

McCabe, R. & Fine, M., 2002. Creep of tin, Sb-solution-strengthened tin, and SbSn-precipitate-strengthened tin. *Metallurgical and Materials Transactions A*, 33(5), p.1531-1539.

McCabe, R.J., 2000. The creep properties of precipitation-strengthened tin-based alloys. *Journal of Materials*, 52(6), p.33–35.

McCabe, R.J. & Fine, M.E., 1998. Athermal and thermally activated plastic flow in low melting temperature solders at small stresses. *Scripta Materialia(USA)*, 39(2), p.189–195.

Miller, C.M., Anderson, I.E. & Smith, J.F., 1994. A viable tin-lead solder substitute: Sn-Ag-Cu. *Journal of electronic materials*, 23(7), p.595–601.

Min Pei 2007, Effects of Lanthanum Doping on the Microstructure and Mechanical Behavior of a Sn-Ag Alloy, *PhD Thesis*, The Georgia Institute of Technology, 2007

Moon, K.W. et al., 2000. Experimental and thermodynamic assessment of Sn-Ag-Cu solder alloys. *Journal of electronic materials*, 29(10), p.1122–1136.

Nagasawa, H., 2002. Physical Characteristics of Stable Silver Nanoparticles Formed Using a New Thermal-Decomposition Method. *phys. stat. sol*, 191, p.67–76.

Nai, S.M.L., Wei, J. & Gupta, M., 2008. Using carbon nanotubes to enhance creep performance of lead free solder. *Materials Science and Technology*, 24(4), p.443-448.

Noh et al. 2010., Effects of cerium content on wettability, microstructure and mechanical properties of Sn–Ag–Ce solder alloys, *Journal of Alloys and Compounds*, 499 p. 154-159

Oliver, W. & Nix, W., 1982. High temperature deformation of oxide dispersion strengthened al and Al—Mg solid solutions. *Acta Metallurgica*, 30(7), p.1335–1347.

Oliver, W.C. & Pharr, G.M., 1992. Improved technique for determining hardness and elastic modulus using load and displacement sensing indentation experiments. *Journal of materials research*, 7(6), p.1564–1583.

Owen, D.M., 1993. an evaluation of the densification characteristics of nanocrystalline materials. *Nanostructured Materials*, 2, p.181–187.

Pei M. and Qu J., 2007a. Effect of Rare Earth Elements on Lead-Free Solder Microstructure Evolution,". Dans Proceedings - 57th Electronic Components and Technology Conference 2007. p. 198–204.

Pei M. and Qu J., M., 2007b. Effect of Lanthanum Doping on the Microstructure of Tin- Silver Solder Alloys. *Journal of Electronic Materials*, 37 (3), p.331–338.

Ramirez, A.G., Mavoori, H. & Jin, S., 2002. Bonding nature of rare-earth-containing lead-free solders. *Applied physics letters*, 80, p.398.

Rhee, H., Lucas, J. & Subramanian, K., 2002. Micromechanical characterization of thermomechanically fatigued lead-free solder joints. *Journal of Materials Science: Materials in Electronics*, 13(8), p.477–484.

Rist, M.A., Plumbridge, W. & Cooper, S., 2006. Creep-constitutive behavior of Sn-3.8 Ag-0.7 Cu solder using an internal stress approach. *Journal of electronic materials*, 35(5), p.1050–1058.

Sahasrabudhe, S. et al., 2003. Understanding the effect of dwell time on fatigue life of packages using thermal shock and intrinsic material behavior. Dans *Electronic Components and Technology Conference, 2003. Proceedings. 53rd*. p. 898–904.

Senkov et al., 1986. grain growth in a superplastic zn-22% al alloy, *acta metallurgica*, 34, 1986, pp 97–106.

Setty, K., Subbarayan, G. & Nguyen, L., 2005. Powercycling Reliability, Failure Analysis and Acceleration Factors of Pb-free Solder Joints. Dans *Electronic Components and Technology Conference, 2005. Proceedings. 55th*. p. 907–915.

Shi et al., 2002. A New Creep Constitutive Model for Eutectic Solder Alloy". *Journal of Electronic Packaging*, 124(2), p.85–90.

Shi et al., 2008. Effects of small amount addition of rare earth Er on microstructure and property of SnAgCu solder, *Journal of Alloys and Compounds*, 453 p.180–184

Steen, M., Provost, W. & Dhooge, A., 1985. The relationship between microstructure and internal stress in a γ-stengthened Superalloy. *Materials Science and Engineering*, 76(0), p.139-146.

Subramanian, K. & Lee, J., 2004. Effect of anisotropy of tin on thermomechanical behavior of solder joints. *Journal of Materials Science: Materials in Electronics*, 15(4), p.235–240.

Suganuma, K., 2003. *Lead-free soldering in electronics: science, technology and environmental impact*, CRC.

Sun, Y. et al., 2008. Nanoindentation for measuring individual phase mechanical properties of lead free solder alloy. *Journal of Materials Science: Materials in Electronics*, 19(6), p.514–521.

Telang, AA et al., 2002. Orientation imaging studies of Sn-based electronic solder joints. *Journal of materials research*, 17(09), p.2294–2306.

Telang, AU et al., 2004. Grain-boundary character and grain growth in bulk tin and bulk lead-free solder alloys. *Journal of electronic materials*, 33(12), p.1412–1423.

Tsai, I. et al., 2005. Identification of Mechanical Properties of Intermetallic Compounds on Lead Free Solder. Dans *Electronic Components and Technology Conference*. p. 687.

Vander Voort, G.F., 2004. *ASM handbook: Metallography and microstructures*, Asm Intl.

Vianco, 2006. *Fatigue and Creep of Lead-free Solder Alloys: Fundamental Properties*,

Wang, L. et al., 2002. Improvement of wettability and tensile property in Sn-Ag-RE lead-free solder alloy. *Materials letters*, 56(6), p.1039–1042.

Wiese et al., 2003. Microstructural dependence of constitutive properties of eutectic SnAg and SnAgCu solders. *Proceedings - Electronic Components and Technology Conference*, p.197–206.

Wiese, S. et al., 2001. Constitutive behaviour of lead-free solders vs. lead-containing solders-experiments on bulk specimens and flip-chip joints. Dans *Electronic Components and Technology Conference, 2001. Proceedings., 51st*. p. 890–902.

Wu, C., Yu, D., et al., 2002. Improvements of microstructure, wettability, tensile and creep strength of eutectic Sn-Ag alloy by doping with rare-earth elements. *Journal of materials research*, 17(12), p.3146–3154.

Wu, C. et al., 2004. Properties of lead-free solder alloys with rare earth element additions. *Materials Science and Engineering: R: Reports*, 44(1), p.1–44.

Wu, C.M.L. et al., 2002a. Microstructure and mechanical properties of new lead-free Sn-Cu-RE solder alloys. *Journal of electronic materials*, 31(9), p.928–932.

Wu, C.M.L. et al., 2002b. The properties of Sn-9Zn lead-free solder alloys doped with trace rare earth elements. *Journal of electronic materials*, 31(9), p.921–927.

Wu, C.M.L. & Huang, M., 2002. Creep behavior of eutectic Sn-Cu lead-free solder alloy. *Journal of electronic materials*, 31(5), p.442–448.

Wu, C.M.L. & Wong, Y., 2007. Rare-earth additions to lead-free electronic solders. *Journal of Materials Science: Materials in Electronics*, 18(1), p.77–91.

Xia, Z. et al., 2002. Effect of rare earth element additions on the microstructure and mechanical properties of tin-silver-bismuth solder. *Journal of electronic materials*, 31(6), p.564–567.

Xiao, Q., 2004. Aging and creep behavior of Sn3.9Ag0.6Cu solder alloy, *Electronic Components and Technology Conference*, p.1325-1332.

Yang, D.G. et al., 2004. Parametric study on flip chip package with lead-free solder joints by using the probabilistic designing approach. *Microelectronics Reliability*, 44(12), p.1947-1955.

Yu, D., Zhao, J. & Wang, L., 2004. Improvement on the microstructure stability, mechanical and wetting properties of Sn-Ag-Cu lead-free solder with the addition of rare earth elements. *Journal of alloys and compounds*, 376(1-2), p.170–175.

Zhai, Q., Guan, S. & Shang, Q., 1999. *Alloy thermo-mechanism: theory and application*, Metallurgy Industry Press, Beijing.

Zhang, Y., 2010. *The Effects of Aging on the Mechanical Behavior of Lead Free and Mixed Formulation Solder Alloys*. Auburn University.

Zhou et al. 2009. *Investigation on properties of Sn–8Zn–3Bi lead-free solder by Nd addition*. Journal of Alloys and Compounds. 480 p. 903-907

Zhu et al., 1994. Study of Sn-Pb-RE solder. Dans *Materials Research Society Symposium Proceedings*. p. 137–143.

Zhu, S.M., Tjong, S.C. & Lai, J.K.L., 1998. Creep behavior of a β (NiAl) precipitation strengthened ferritic Fe–Cr–Ni–Al alloy. *Acta Materialia*, 46(9), p.2969-2976.

Zou et al., 2009. Nanoparticles of the Lead-free Solder Alloy Sn-3.0Ag-0.5Cu with Large Melting Temperature Depression. *Journal of Electronic Materials*, 38(2), p.351–355.

Zhang Yifei, PhD Thesis, Auburn University 2010.